



# City Research Online

## City, University of London Institutional Repository

---

**Citation:** Ioannou, Eleni (2015). The effects of temperature distortion on aerodynamics and low engine order forced response in axial turbines. (Unpublished Doctoral thesis, City University London)

This is the draft version of the paper.

This version of the publication may differ from the final published version.

---

**Permanent repository link:** <https://openaccess.city.ac.uk/id/eprint/13521/>

**Link to published version:**

**Copyright:** City Research Online aims to make research outputs of City, University of London available to a wider audience. Copyright and Moral Rights remain with the author(s) and/or copyright holders. URLs from City Research Online may be freely distributed and linked to.

**Reuse:** Copies of full items can be used for personal research or study, educational, or not-for-profit purposes without prior permission or charge. Provided that the authors, title and full bibliographic details are credited, a hyperlink and/or URL is given for the original metadata page and the content is not changed in any way.

City University London

School of Mathematics, Computer Science and Engineering

The effects of temperature distortion on  
aerodynamics and low engine order forced  
response in axial turbines

Eleni Ioannou

Submitted for the degree of Doctor of Philosophy

April 2015



**CITY UNIVERSITY  
LONDON**

**CityLibrary**  
Your space  
Your resources  
Your library

**THE FOLLOWING PARTS OF THIS THESIS HAVE BEEN REDACTED  
FOR COPYRIGHT REASONS:**

**p119, Fig 7.2**

# Declaration

I hereby declare that, to the best of my belief, the work presented in the thesis is original and has not been and will not be submitted in whole or in part to another University for the award of any other degree.

Signature:

Eleni Ioannou

## ABSTRACT

The flow entering a high-pressure turbine in a gas turbine engine is characterised by a loss of symmetry due to temperature distortions in both radial and circumferential directions, known as hot streaks. In industrial simulations it is common practice to assume uniform inlet temperature conditions to simplify the aerodynamic analysis. However, hot streaks may have significant impact on the turbine aerodynamics with the redistribution of the hot fluid affecting the development of secondary flows with consequent effects on enhanced local heat transfer and aerodynamic losses. The loss of symmetry has also been linked to the excitation of low-order nodal diameter assembly modes of the downstream rotor blades leading to potential blade failure and thus, should be taken into account during the design process. In today's carbon-constraint environment additional parameters arise as gas turbines are challenged to adapt to variations of the fuel composition driven by the need of efficient and low  $CO_2$  power generation. Introducing syngas, a synthesis gas fuel that is used to power integrated gasification combined cycle (IGCC) power plants, is likely to affect the operating conditions of existing gas turbines leading to the requirement of re-design of components. With particular focus on the turbine hot flow path, the propagation mechanism of hot streaks throughout the turbine will be affected with consequent impact on the turbine aerodynamics and forced response excitation levels originating from the different hot flow patterns.

Motivated by the lack of relevant studies, the current work provides a first step towards the evaluation of the effects of syngas on hot streaks aerodynamics and the induced forced response excitation levels. Using full annulus multi-bladerow unsteady 3D CFD simulations and applying combustor representative hot streak profiles in two different gas turbines, a complete analysis of the hot streaks migration is achieved, with respect to a number of geometric parameters such as the hot streaks shape and injection location in both spanwise and circumferential directions, the coolant configurations as well as the combined effects on the secondary flow development. The aerodynamic analysis indicated the propagation of the hot streaks up to the exit of the turbines under investigation with differences in characteristics depending on design parameters. With respect to the effect of fuel composition variations on the blades temperature levels and the flow pattern is observed between the natural gas and syngas turbine with the syngas showing a more concentrated wake shape. In effect of the syngas different flow pattern, differences are observed in the secondary flows with consequent interaction with the hot streaks. Contrast to initial expectations, the forced response analysis

resulted slightly lower amplitude unsteady force of lower harmonics for syngas compared to natural gas; however, both fuels showed significant levels of the hot streak induced low engine order excitation compared to the burners and stator related blade passing frequency vibration.

# Acknowledgements

Firstly, I would like to express my deepest appreciation to my principal supervisor Professor Naser Sayma, who maintained a high standard at each step of this thesis by providing me with continuous support and expertise knowledge on turbomachinery flows. His kindness, encouragement and suggestions during these years have considerably improved the quality of this thesis, for which I am very grateful. I would like to thank my second supervisor Dr Yevgen Petrov from University of Sussex, who helped me to improve my understanding on relevant aspects of turbomachinery vibration analysis. I would also like to thank Dr Li Shing Wong from Siemens Industrial Turbomachinery for providing the traverse data that has been used at the hot streaks simulation along with relevant advice and suggestions.

There are many people that have accompany me during my long journey of pursuing my thesis both in University of Sussex and City University London, to whom I own my gratitude. I would like to thank Dr Yanling Li, who has been very helpful from the very beginning until the end of my work, as well as my colleagues Adrian Romocea and Dr Pascal Nucara, for all the technical and non-technical guidance during the H2-IGCC project. I would also like to thank Harri Koivisto and Dr Chris Long for all the thoughtful talks at Thermofluids Research Centre during the first half of my study. A special gratitude goes to my colleagues at City University London for their friendship during the final years of this work.

Finally, I would like to direct a very special and personal message of gratitude from the bottom of my heart to my beloved family, for their continuous support, as well as my partner George, who has supported me with endless love, regardless of the late working evenings and weekends prior and during my doctoral degree.

This study has been financially supported by the European Union's 7<sup>th</sup> Framework Programme for Research and Development and coordinated by the European Turbine Network (ETN). The financial support has been a prerequisite for the existence of this study and is hereby gratefully acknowledged.

# Contents

<b>List of Tables</b>	<b>x</b>
<b>List of Figures</b>	<b>xiv</b>
<b>1 Introduction</b>	<b>1</b>
1.1 Background . . . . .	1
1.1.1 The Use of Syngas in Industrial Gas Turbines . . . . .	1
1.1.2 The Effects of Syngas on Turbine . . . . .	2
1.1.3 H2-IGCC Project . . . . .	4
1.1.4 Hot Streaks - Problem Overview . . . . .	5
1.1.5 Unsteadiness and Forced Response Vibration Problems . . . . .	6
1.2 Objectives of the Research . . . . .	9
<b>2 Literature Review</b>	<b>11</b>
2.1 Introduction . . . . .	11
2.2 Hot Streaks Kinematics . . . . .	11
2.2.1 Effects of Hot Streaks on Aerodynamics . . . . .	14
2.2.2 Forced Response and LEO excitation . . . . .	20
2.3 Syngas Operation in Turbine . . . . .	23
2.4 Summary of Review . . . . .	25
2.5 Contributions . . . . .	25
2.6 Thesis Outline . . . . .	26
<b>3 The Numerical Model</b>	<b>28</b>
3.1 Introduction . . . . .	28
3.2 Forced Response Methodology . . . . .	28

3.2.1	Overview . . . . .	28
3.2.2	In-house CFD and Aeroelasticity Solver . . . . .	30
3.2.3	Flow Model . . . . .	31
3.2.4	Structural Model . . . . .	34
3.3	Test Case . . . . .	36
3.3.1	Grid Independence Study . . . . .	38
3.3.2	Comparison Between 3D CFD Results and Through Flow Calculation	43
3.3.3	Grid Independence study - Unsteady 3D CFD simulation with peri- odic boundaries . . . . .	44
3.4	Summary . . . . .	50
<b>4</b>	<b>Hot Streaks Migration and Aerodynamic Effects in 2-Stage HP Axial Turbine</b>	<b>51</b>
4.1	Introduction . . . . .	51
4.2	Hot Streaks Cases Preparation . . . . .	52
4.2.1	HP Turbine Overview . . . . .	52
4.2.2	Boundary Conditions . . . . .	55
4.3	Unsteady Hot Flow Path Analysis - Results and Discussion . . . . .	61
4.3.1	Hot Streak Migration in Blade-to-Blade Plane - Segregation Phe- nomenon . . . . .	61
4.3.2	Radial Hot Streak Migration - Combined Effects . . . . .	69
4.3.3	Effects of Hot Streak Shape . . . . .	78
4.3.4	Combined Effects of 1 <sup>st</sup> Vane Coolant and Potential Interaction . .	80
4.4	Summary . . . . .	82
<b>5</b>	<b>H2-IGCC Project - Gas Turbine Modification Options for Syngas Operation</b>	<b>84</b>
5.1	Introduction . . . . .	84
5.1.1	Baseline Gas Turbine - Overview . . . . .	85
5.1.2	Gas Turbine Modifications - Syngas fuel . . . . .	86
5.2	Summary . . . . .	90
<b>6</b>	<b>Hot Streaks Aerodynamics in 4-Stage Generic Turbine - comparison of fuel con-     ditions</b>	<b>91</b>
6.1	Introduction . . . . .	91
6.2	Hot Streaks Case Setup . . . . .	92

6.2.1	H2-IGCC Turbine Overview . . . . .	92
6.2.2	Boundary Conditions . . . . .	94
6.2.3	Film Cooling . . . . .	97
6.3	Unsteady CFD Analysis - Results and Discussion . . . . .	98
6.3.1	Hot Streaks Migration - Varying Circumferential Inlet Hot Streak Location . . . . .	98
6.3.2	Hot Streaks Interaction with Blades Film Coolant . . . . .	100
6.3.3	Hot Streaks Propagation - Varying Fuel Composition . . . . .	103
6.3.4	Hot Streaks Effects on Stator Thermal Wakes . . . . .	112
6.4	Summary . . . . .	114
<b>7</b>	<b>Investigation of Low Engine Order Excitation of 1<sup>st</sup> Rotor due to Temperature Distortion</b>	<b>116</b>
7.1	Introduction . . . . .	116
7.2	Overview of the Forced Response Model . . . . .	117
7.2.1	Modal Analysis Setup . . . . .	117
7.2.2	Modal Analysis Results . . . . .	120
7.2.3	First Stage Forced Response Analysis Setup . . . . .	125
7.2.4	Forced Response Results . . . . .	126
7.3	Summary . . . . .	129
<b>8</b>	<b>Conclusions and Recommendations</b>	<b>131</b>
8.1	Introduction . . . . .	131
8.2	Meeting the Objectives: Summary of Thesis Achievement . . . . .	131
8.2.1	The aerodynamics of hot streaks in a two-stage HP turbine . . . . .	131
8.2.2	The aerodynamic of hot streaks in the four-stage H2-IGCC turbine with respect to fuel composition . . . . .	133
8.2.3	The effects of fuel composition on the LEO excitation due to inlet temperature non-uniformities . . . . .	134
8.3	Recommendations and Future Work . . . . .	135
8.3.1	Simulation of full annulus unsteady CFD analysis against experi- mental data . . . . .	135
8.3.2	Varied hot flow patterns . . . . .	135

8.3.3	Comparison with other turbulence models . . . . .	136
8.3.4	LEO excitation of the downstream rotor blades . . . . .	136
<b>A</b>	<b>Harmonic Index and Nodal Diameter</b>	<b>149</b>

# List of Tables

3.1	Grid independence study - Average inlet-outlet steady state results . . . . .	40
3.2	Average inlet-outlet results - throughflow model vs. CFD mixing planes . .	43
4.1	Dataset overview and normalised flow conditions . . . . .	52
4.2	Percentage of coolant injection per bladerow with respect to turbine inlet mass flow rate . . . . .	54
4.3	Percentage of temperature distortion applied for the sinusoidal profile . . .	58
5.1	SGT5-4000F characteristics . . . . .	86
5.2	Compositions and properties of selected fuels . . . . .	87
6.1	Geometric parameters for H2-IGCC turbine . . . . .	93
6.2	H2-IGCC turbine inlet-outlet average values - unsteady CFD results . . . .	94
6.3	H2-IGCC turbine coolant properties per bladerow for natural gas and syngas	97
7.1	Alloy IN-738 properties . . . . .	120
7.2	Natural Frequencies for the first 3 modes of the selected NDs . . . . .	123
7.3	Syngas and Natural Gas predicted LEO response for R1 . . . . .	127

# List of Figures

1.1	Campbell diagram illustration . . . . .	7
2.1	Kerrebrock and Mikolajczak segregation effect . . . . .	12
2.2	Schematic illustration of the development of secondary flow in a rotor blade passage [1] . . . . .	14
2.3	Measured (QinetiQ) combustor exit temperature profile in a military engine from Povey and Qureshi [2] . . . . .	20
3.1	Schematic representation of the applied forced response methodology . . . . .	29
3.2	Typical 2D mixed-cell mesh . . . . .	33
3.3	Turbine annulus . . . . .	36
3.4	Computational grid for 1 <sup>st</sup> stator blade . . . . .	38
3.5	Computational domain for 1 <sup>st</sup> stator blade at hub . . . . .	39
3.6	Grid independence study - normalised stagnation pressure and temperature radial profiles at $R1_{ex}$ domain . . . . .	40
3.7	Mach number contours on 1 <sup>st</sup> stator blade - midspan . . . . .	41
3.8	Pressure profile along S1 blades at hub and midspan . . . . .	42
3.9	Comparison between throughflow model and CFD steady state results at $R2_{ex}$ domain . . . . .	44
3.10	Simplified model of the first turbine stage with periodic boundaries . . . . .	45
3.11	Normalised stagnation temperature profile at turbine inlet with circumferential variations . . . . .	46
3.12	Recorded pressure variation at midspan of one first rotor blade . . . . .	47
3.13	Instantaneous temperature contours at the exit plane of stator bladerow . . . . .	48
3.14	Instantaneous temperature contours at the exit plane of stator bladerow . . . . .	49
4.1	Two-stage computational grid and boundaries nomenclature . . . . .	54

4.2	Inlet temperature contour plots provided by Siemens . . . . .	56
4.3	Normalised circumferentially averaged radial temperature profiles at turbine inlet . . . . .	57
4.4	Circumferential temperature distribution and FFT at $S1_{in}$ plane at the spanwise location of HS centre . . . . .	59
4.5	Normalised stagnation temperature contours at the inlet of the turbine - used as boundary conditions . . . . .	60
4.6	Normalised stagnation temperature contour plot of two non-identical simulated inlet hot streaks based on Figure 4.5 (b) . . . . .	61
4.7	Instantaneous normalised stagnation temperature contours through the two-stage turbine at 40% span (hot streak centre) . . . . .	63
4.8	Instantaneous hot streak propagation through R1 blade passage at 40% span	64
4.9	Instantaneous static temperature distribution along hot blades through the 4 bladerows for three different spans . . . . .	66
4.10	S1 exit circumferential normalised stagnation temperature at 40% span . . .	67
4.11	S1 exit circumferential absolute velocity at 40% span . . . . .	68
4.12	S1 exit difference in circumferential absolute velocity at 40% span . . . . .	69
4.13	Spanwise axial absolute velocity distribution at bladerows exit plane for compared inlet temperature profiles . . . . .	70
4.14	Velocity triangles at first stage outlet - effect of hot streaks on flow coefficient	71
4.15	Circumferentially averaged radial flow coefficient difference at the exit of S1 domain . . . . .	72
4.16	$R1_{in}$ instantaneous temperature contours showing hot streak radial spread .	72
4.17	First stage exit - radial hot streak migration . . . . .	74
4.18	Instantaneous normalised stagnation temperature contours at $R1_{ex}$ for different time steps . . . . .	75
4.19	Instantaneous stagnation pressure contours at the exit of 1 <sup>st</sup> stage for three different inlet temperature conditions . . . . .	76
4.20	Instantaneous stagnation temperature contours and velocity vectors on R1 SS blades . . . . .	77
4.21	Spanwise stagnation temperature distribution at the exit of turbine stages for the baseline and sinusoidal HS profile . . . . .	79

4.22	Alteration of hot streak shape at the exit of 1 <sup>st</sup> vane row - baseline case . . .	81
4.23	Alteration of hot streak shape at the exit of 1 <sup>st</sup> vane row - no vane coolant .	81
4.24	Instantaneous total pressure coefficient contours at the exit of 1 <sup>st</sup> vane row .	82
5.1	SGT5-4000F gas turbine, Siemens Power Generation in Berlin . . . . .	85
5.2	Compressor and turbine flow characteristics . . . . .	87
6.1	H2-IGCC syngas turbine modification - 1 <sup>st</sup> stator blade opening by 0.22° .	92
6.2	H2-IGCC four-stage generic turbine geometry based on SGT5-4000F . . .	93
6.3	Stagnation temperature contours at the turbine inlet plane . . . . .	95
6.4	H2-IGCC turbine inlet boundary conditions for CFD simulations . . . . .	96
6.5	Zoom on different hot streak clocking positions at 30% span- NG . . . . .	99
6.6	Stagnation temperature contours along the four stages at 30% span - NG . .	100
6.7	Stagnation temperature contours along R1 blade PS for different inlet tem- perature conditions and fuels . . . . .	101
6.8	Static temperature profile along hot blades of 1 <sup>st</sup> turbine stage at 30% span for natural gas and syngas . . . . .	102
6.9	Spanwise axial absolute velocity distribution at bladerows exit plane for nat- ural gas and syngas . . . . .	104
6.10	Horseshoe vortex system on R1 passage for natural gas and syngas cases . .	105
6.11	Secondary flow development through blade passage [3] . . . . .	106
6.12	Stagnation pressure contour plots at R1 exit for natural gas and syngas . . .	107
6.13	Hot streak propagation through R1 passage for natural gas and syngas . . .	109
6.14	Hot streak propagation through S2 passage for natural gas and syngas . . .	110
6.15	Spanwise stagnation temperature distribution at bladerows exit plane for natural gas and syngas . . . . .	111
6.16	Instantaneous stagnation temperature contours at turbine exit . . . . .	111
6.17	Circumferential stagnation temperature profile and FFT at S1 <sub>ex</sub> plane at 30% section with closer view of one hot streak vane wake and the 19 EO amplitude	112
6.18	Circumferential stagnation temperature profile at S1 <sub>ex</sub> section at 30% with theoretically predicted circumferential profile . . . . .	113
7.1	H2-IGCC 3-stage cooling geometry overview [4] . . . . .	118
7.2	Cross section of the SGT5-4000F gas turbine [5] . . . . .	119

7.3	1 <sup>st</sup> rotor FE sector model . . . . .	119
7.4	Natural frequencies vs. nodal diameters . . . . .	121
7.5	Campbell diagrams for various NDs . . . . .	122
7.6	Mode shapes contours corresponding to the values presented in Table 7.2 . . . . .	124
7.7	Full annulus mode shape for 19 ND and displacement . . . . .	124
7.8	FE to CFD mesh interpolation . . . . .	125
7.9	Comparison of contour mode shape between the FE modal analysis and the interpolated CFD values for the 19 ND . . . . .	126
7.10	Modal force amplitude for compared cases of natural gas and syngas . . . . .	128
A.1	Beam mode shapes . . . . .	149
A.2	Disk mode shapes . . . . .	150
A.3	Campbell diagrams for 1-24 ND . . . . .	154

# Nomenclature

<i>amp</i>	Amplitude
<i>C</i>	Velocity in stationary frame, m/s
<i>C<sub>p</sub></i>	Pressure coefficient
<i>Ma</i>	Mach number
<i>P, p</i>	Pressure, Pa
<i>R</i>	Rotor, Universal gas constant
<i>S</i>	Stator
<i>T</i>	Temperature, K
<i>U</i>	Blade speed, m/s
<i>W</i>	Velocity in relative frame, m/s
1	Bladerow 1
2	Bladerow 2
3	Bladerow 3
4	Bladerow 4

## Abbreviations

<i>BPF</i>	Blade Passing Frequency
<i>CC</i>	Combined Cycle
<i>CCS</i>	Carbon Capture and Storage
<i>CFD</i>	Computational Fluid Dynamics
<i>DOF</i>	Degrees Of Freedom
<i>EO</i>	Engine Order
<i>FE</i>	Finite Element
<i>FFT</i>	Fast Fourier Transform
<i>HCF</i>	High Cycle Fatigue
<i>HP</i>	High Pressure
<i>HS</i>	Hot Streak
<i>IGCC</i>	Integrated Gasification Combined Cycle
<i>LEO</i>	Low Engine Order
<i>LHV</i>	Lower Heating Value
<i>LP</i>	Low Pressure

<i>ND</i>	Nodal Diameter
<i>NG</i>	Natural Gas
<i>PS</i>	Pressure Side
<i>RANS</i>	Reynolds-Averaged Navier-Stokes
<i>SG</i>	Syngas
<i>SS</i>	Suction Side
<i>TIT</i>	Turbine Inlet Temperature
<i>1D</i>	One-Dimensional
<i>2D</i>	Two-Dimensional
<i>3D</i>	Three-Dimensional

*Subscript*

<i>av</i>	Mass average variable
<i>ex</i>	Outlet of the bladerow
<i>in</i>	Inlet of the bladerow
<i>o,t</i>	Total variable
<i>s</i>	Static variable
<i>x</i>	Axial coordinate direction
1	Turbine 1 <sup>st</sup> stage inlet
1.5	Turbine 1 <sup>st</sup> rotor inlet
2	Turbine 1 <sup>st</sup> stage outlet
2.5	Turbine 2 <sup>nd</sup> rotor inlet
3	Turbine 2 <sup>nd</sup> stage outlet
3.5	Turbine 3 <sup>rd</sup> rotor inlet
4	Turbine 3 <sup>rd</sup> stage outlet
4.5	Turbine 4 <sup>th</sup> rotor inlet
5	Turbine 4 <sup>th</sup> stage outlet

*Greek letters*

$\alpha$	Absolute flow angle
$\beta$	Relative flow angle
$\gamma$	Ratio of specific heats

$\theta$	Local tangential angle
$\rho$	Density , $kg/m_3$
$\tau$	Passing period
$\phi$	Flow coefficient

# Chapter 1

## Introduction

### 1.1 Background

#### 1.1.1 The Use of Syngas in Industrial Gas Turbines

During the last decade the development of gas turbines burning syngas together with the introduction of Integrated Gasification Combined Cycle (IGCC) concepts has been considered as one of the most promising solutions for efficient and low- $CO_2$  power generation [6]. IGCC power plants are attractive technological solutions for power production, compared to the natural gas fired Combined Cycle (CC) power plants, providing the opportunity to reduce  $NO_x$  emissions [7], offering  $CO_2$  capture convenience, when combined with Carbon Capture and Storage (CCS) [8], while allowing at the same time the use of low cost fuels such as coal, biomass or solid waste. The implementation of CCS technology has been identified by the European Strategic Energy Technology Plan (SET-Plan) [9] as the only available technology that can capture at least 90% of emissions and hence, contribute towards the targets of global  $CO_2$  reduction.

In IGCC power plants the carbon-based fuel is converted into a synthetic gas (syngas) through a gasification process and then converted into electricity in the combined cycle that consists of a heavy duty gas turbine with Heat Recovery Steam Generator (HRSG) and a steam turbine. The process used for syngas production and the IGCC operation are described in some recent studies including current operating IGCC power plants [10, 11, 12]. The current state-of-the-art IGCC plants [13, 14] provide important knowledge regarding the design parameters that may affect the gas turbine operation.

Generally, syngas differs from natural gas in terms of composition and calorific value; depending on the gasification process the composition and properties of syngas will vary. Hence, addressing syngas fuel in gas turbines, additional complications may arise related to the fuel composition. The syngas coming from the gasifier is primarily a mixture of varying amounts of carbon monoxide ( $CO$ ), carbon dioxide ( $CO_2$ ), hydrogen ( $H_2$ ) and steam. With syngas usually being diluted with  $H_2O$  and  $N_2$ , for  $NO_x$  control, the Low Heating Value (LHV) is about 1/3 of the LHV of natural gas [15]. As the composition variability of syngas is an important parameter for the operation and performance of a gas turbine, most of the published studies have focused on the effects of syngas properties compared to natural gas [16, 17]. Depending on the syngas fuel composition the varying calorific values of the fuel introduces additional design challenges towards the development of existing gas turbines. Once the syngas composition is selected for the IGCC plant operation, with respect to the power plant performance, the modification of the gas turbine and the adoption to the variation of the fuel composition is the next most critical step of the IGCC power plant design process, as that will affect the overall performance of the plant.

### **1.1.2 The Effects of Syngas on Turbine**

In the general case of a syngas fuel, the lower LHV of the fuel means that more syngas is required to be burnt in order to maintain the same power output, compared to the natural gas fired gas turbine, affecting the mass flow rate at the turbine inlet. The volume flow rate of syngas at the turbine inlet is dependent on the syngas composition and the dilution process; in case of undiluted syngas the mass flow rate of the combustion products reduces, resulting lower mass flow rate at the turbine inlet [18]. Typical values of LHV have been published by Kim et al. [19] in a comparative study where the effect of syngas type on the performance of a gas turbine is investigated. In that study the values of three syngas fuel types correspond to 8.62, 10.49 and 37.02 [ $MJ/kg$ ] compared to the natural gas higher value of LHV that is equal to 49.3 [ $MJ/kg$ ]. However, there is not sufficient amount of information available in the literature regarding the syngas variability.

Regardless of the dilution process and the syngas composition, the lower molecular weight of syngas (always compared to natural gas) results higher volume mass flow rate at the inlet of the turbine. In currently operating IGCC power plants natural gas state-of-the art technology is adapted for using syngas. The increase in volume flow rate in case of syn-

gas introduces the need for certain modifications of the existing gas turbine design in order to maintain an existing natural gas burning machine to operate reliably and similarly efficiently with syngas. For a current natural gas fired gas turbine, modifications can be applied either to the compressor or turbine design to operate under syngas conditions. The key challenges related to the implementation of existing gas turbine technology for syngas operation can be summarised as follows:

- Assuming the common turbine choking condition for heavy duty gas turbines, the increased volume flow rate of syngas will lead to increased turbine inlet pressure and thus, reduced demand of air from the compressor. That results in higher compressor back pressure and potential compressor instability problems. The key challenge is an adjustment through which the compressor operation can be unaffected. One possible way is by adjusting the blade stagger angles and hence reducing the mass flow coefficient while operating at nearly the same original performance.
- A second key challenge is related to the turbine operation. Due to the increased volume flow rate, the original turbine could be adjusted to allow the compressor working at the same point by applying geometric modifications. Letting the compressor to work at the same design point as with natural gas, the restaggering of the first stator blades could be adopted for the modified turbine [20].
- The aerothermal effects are related to (i) the increased isentropic enthalpy drop; the difference in thermodynamic properties results lower specific heat ratio ( $\gamma$ ) for syngas fuels, that leads to increased isentropic enthalpy drop and consequently to increased levels of turbine exit temperature [18], (ii) the turbine hot flow path; the lower specific heat ratio ( $\gamma$ ) leads to a difference in velocity triangles, influencing the axial velocity component and thus the hot flow path, and (iii) the heat transfer rate; the higher water content of combustion products is another important aspect resulting in higher heat transfer rate on the blades surfaces. Hence, additional challenges are addressed towards the turbine cooling system design and the improvement of understanding of the temperature redistribution in the turbine, that is critical to allow for the selection of appropriate materials and coatings.
- A final challenge that is introduced is related to the variations of the hot streak profile at the turbine inlet that may affect the low engine order forced response excitation of

the downstream turbine rotor blades. In that case, the issues associated with conventional gas turbines also apply to syngas machines with the added parameter of fuel composition.

This study is motivated by the need of adjustment of an existing gas turbine fuelled by natural gas to these changes providing reliable and highly efficient operation of the turbine section as part of the H2-IGCC project which is coordinated by the European Turbine Network (ETN).

### **1.1.3 H2-IGCC Project**

The main objective of the H2-IGCC project (co-funded by the European Union's 7<sup>th</sup> Framework Programme for Research and Development and coordinated by the European Turbine Network), is to provide reliable and efficient technical solutions for the next generation IGCC power plants burning hydrogen-rich syngas fuel, by the implementation of current state-of-the-art gas turbine technology [21]. The project brings together 24 partners from 10 countries to deal with specific technical challenges which are divided into four subprojects, the combustion, the materials, the turbomachinery and the system analysis which evaluates the optimised compatibility between the combustion technology, the materials and the turbomachinery requirements.

Among the partners, Roma Tre University, RWTH Aachen University, Cenaero and City University of London <sup>1</sup>contributed towards researching technical solutions related to the turbomachinery challenges. The modified compressor and turbine design has to cope with the increased volume flow rate, the increased isentropic enthalpy drop and consequent higher turbine exit gas temperature and heat transfer rates. More specifically, Roma Tre University provided the throughflow model for the generic gas turbine, leading to the definition of the number of stages, annulus line and blade profiles at mid-span to all stages plus a compressor characteristic [22]. Based on this data University of Sussex produced a 3D compressor design that was done by extending the 2D model along the span taking into account the correct stagger of the blades. The design was iteratively modified to achieve the required performance using 3D CFD computations for single passage multi-bladerow analysis with mixing planes.

---

<sup>1</sup>transferred by University of Sussex

RWTH Aachen University was responsible for the definition of a representative expander geometry to be used by all the project partners as a reference for the analysis. Based on the annulus design and the thermodynamic inlet and outlet conditions provided by the through-flow analysis the turbine blades have been designed [23]. For the current work, the boundary conditions have been set for the case of natural gas, based on the CFD results of RWTH Aachen University. The initial CFD calculations that have been performed using the in-house CFD solver, for different grids, provided converged solutions and comparable results with RWTH and Roma Tre Universities. CENAERO produced a preliminary design for the cooling system which can be used as a generic baseline geometry. The work presented in this thesis is aimed to investigate the effects of syngas on the temperature distribution through the four-stage turbine with respect of the aerodynamics and the forced response vibration problem as part of the H2-IGCC project, using the generic gas turbine and the modified syngas gas turbine geometries as those have been provided by RWTH Aachen University.

#### **1.1.4 Hot Streaks - Problem Overview**

It is well known that the flow exiting the combustor in gas turbines contains both radial and circumferential temperature gradients, known as hot streaks. First turbine stages experience those temperature gradients which can propagate downstream creating local hot spots on blades' surfaces affecting the local heat transfer [24, 25, 26, 2]. Those localised peak temperature areas can be crucial for the turbine blade life, therefore the temperature tolerance of the first bladerow is generally based on higher temperature than the mean Turbine Inlet Temperature (TIT) which in turn, results in performance costing cooling flow in the turbine [27, 28].

Additionally, due to the complex nature of the flow and the relative motion of the adjacent bladerows, these periodic flow disturbances can also affect the performance of the downstream turbine stage [29, 30], as well as the blade failure due to forced response excitation [31, 32]. In respect to the effects of the fuel composition (when switching from natural gas to syngas) on the turbine flow path, the ability to understand the temperature migration pattern in a turbine and identify those areas of localised high temperatures and enhanced local heat transfer is essential in order to improve cooling effectiveness and reduce cooling losses. The enhanced heat transfer issues that arise from burning syngas may affect the migration pattern through the turbine and the combined aerodynamic effects through the

turbine stages.

Despite the large number of numerical studies on the effects of temperature redistribution on the turbine, it is difficult to draw general conclusions that could be applied to turbine design due to a number of design parameters that have impact on the hot streak kinematics and hence, on the aerodynamics and aeromechanics of the turbine. Due to the lack of full annulus combustor measurements most of the published studies follow simplified approaches for the hot streaks simulation. The simulation of realistic non-identical hot streaks is expected to result differences in the hot streak propagation and hence, one issue that the current study is dealing with is the application of a combustor-representative hot streak profile. The numerical investigation of the hot streak shapes and the effects on aerodynamics was conducted on the SGT300-2S two-stage turbine based on traverse data provided by Siemens.

### **1.1.5 Unsteadiness and Forced Response Vibration Problems**

The periodic circumferential temperature variations at the turbine inlet introduce additional unsteadiness to the turbine flow that may lead to potential excitation problems of the downstream blade rows. Unsteadiness in turbomachinery can arise from different sources generally related to circumferential variation in the flow and can be classified in the following: 1) potential interaction, that is related to pressure fields and depends on the axial gap between the blade rows and the Mach number; 2) vortical perturbations, which are related to blade wakes and streamwise vortices that are convected through the stages and can influence the surface pressure, heat transfer and boundary layer nature of the downstream blades; and 3) entropic perturbations, related to density fluctuations and thus to temperature fields [33]. The effects of all three types have been widely investigated over the past years and a thorough review can be found in AGARD manual [34].

Based on the forcing function acting on the blade, excitation problems in gas turbines can be classified into flutter and forced response problems; only the forced response related problems will be discussed here. In turbine forced response problems, the unsteady loading arises from upstream or downstream fluctuations in the flow being periodically applied to the blades. When the frequency of the exciting force coincides with a blade natural frequency, resonant vibrations result inducing High Cycle Fatigue (HCF), affecting turbine blade life. Such conditions are characterised by the growth of fatigue cracks in blades due to the large number of alternating stress cycles and should be avoided during the operation of the tur-

bine. Hence, prime consideration of the structural dynamics is the prediction of the natural frequencies of bladed disk assemblies in order to design the machines to operate outside resonant conditions and prevent dangerous vibrations.

That resonant condition was early described by Campbell [35], who identified the characteristics of vibrational modes of steam turbine bladed disks. A simple tool that has been used for that purpose, shown in Figure 1.1, is Campbell diagram that predicts where the blades natural frequencies coincide with the excitation frequencies. Such resonant conditions are named crossing points. The natural frequencies (Hz) on vertical axis are plotted against turbine speed (rpm) on the horizontal axis. The diagonal lines represent the sources of excitation. The excitation frequency of the flow fluctuations, related to upstream and downstream stator blades as well as burner cans, is normally proportional to the speed of rotor and is denoted by the Engine Order (EO). For example, in the presence of 40 upstream vanes, the blade passes downstream encounters a high and low pressure region, hence the excitation frequency is said to be a 40 – EO excitation.

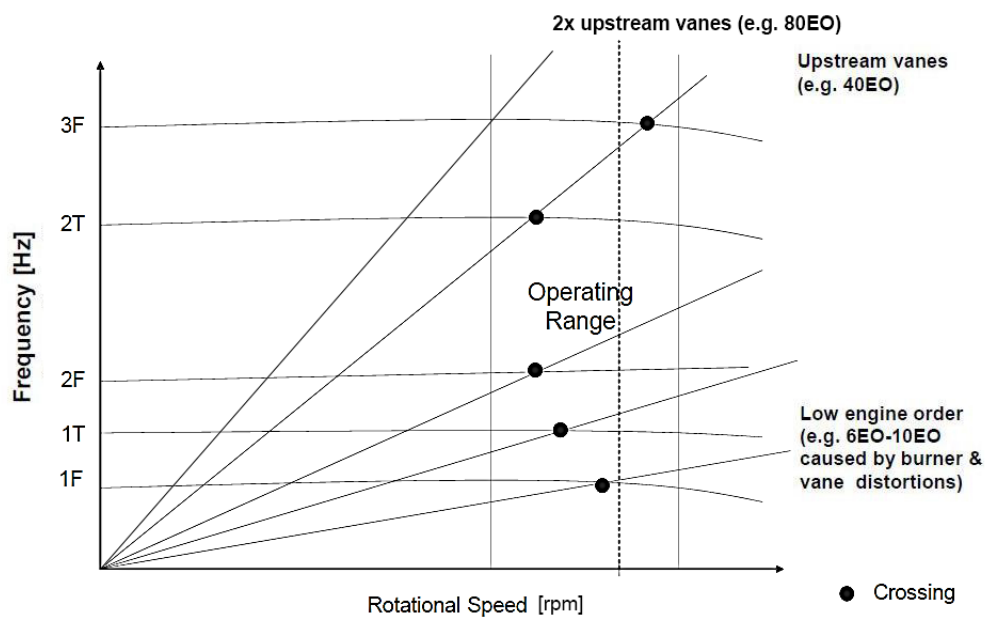


Figure 1.1: Campbell diagram illustration

The unsteady force arising from the flow interaction between stationary and moving blades, known as Blade Passing Frequency (BPF) excitation, is a well-defined problem and the accurate prediction of the excitation levels is part of the design phase. In order to describe aeroelastic phenomena in turbomachinery, Computational Fluid Dynamics (CFD) codes in

combination with standard Finite Element (FE) models constitute an effective way to predict vibration-free operating ranges. The Campbell diagram can be obtained by a FE analysis through a modal analysis that model describes the structure's behaviour without any external force or excitation. Natural modes and frequencies can then be defined by the physical geometry of the component, as natural modes describe the patterns of vibration and natural frequencies are the frequencies of the natural modes. Since periodic excitations due to rotor blades passing stationary blades are known a priori, the turbine rotors can be designed such that assembly mode frequencies do not intersect excitation EOs at the rotational speed, as shown in Figure 1.1.

Another source of excitation forces is related to variations in the flow around the annulus and results in Low Engine Order (LEO) forced response problems. In case of LEO excitation, the unsteady aerodynamic force is composed of harmonics lower than BPF, hence the term LEO forced response. The unsteady harmonic forcing distribution acting on the rotor blade is caused by any loss of symmetry arising from manufacturing variability and is therefore somewhat random in nature; examples of which are the combustor exit temperature profile, the inherent non-uniform spacing between stator blades (or throat width variation) and effects due to burner blockages. LEO is difficult to predict as the sources of flow variation may vary between different engines.

Once a resonance is identified, the blade response at that condition needs to be estimated solving the forced response problem. The forced response aeroelasticity analysis can be numerically conducted in fully-coupled or uncoupled way. In coupled forced response systems the structural mode shapes, resulting from the modal analysis, are interpolated on the aerodynamic mesh which moves at each time step during the solution process in order to accommodate the structural motion by exchanging the boundary conditions at the fluid-structure interface. The frequency of the motion is determined by the natural frequency of the corresponding mode. The advantage of the fully-coupled method is the automatic inclusion of the aerodynamic damping. However, unless the change in aerodynamic damping is likely to be important, the forced response analysis may be simplified and solved in uncoupled way, where the unsteady force and the blade motion are considered separately. This simplification still allows the calculation of the aerodynamic damping from a separate flutter analysis and is valid unless the unsteadiness arising from the blade motion is significant such as in case of fan assemblies. Further discussion and comparison between the two methods

has been published by Breard et al. [36] and Vahdati et. al [37]. In the current study blade mode shapes are assumed to remain unchanged by the aerodynamic force, thus the FE modal analysis is solved independently to the CFD analysis, where mode shapes are interpolated into the fluid mesh.

In the past 30 years there has been an effort leading to significant progress in understanding the basic mechanisms of propagation of the hot fluid into the first turbine stage and aerodynamic effects. The increase in computer power has allowed a great progress to be made in the field of Computational Fluid Dynamics (CFD) improving in such way the general understanding of the complicated flow field in turbomachinery. However, due to the significant computational time required, some of the current industrial design practices are still based on steady state CFD codes. Hence, unsteady flow phenomena, such as the temperature variation at turbine inlet, are usually absent in most of the CFD simulations, and ideal uniform inlet temperature conditions are generally assumed. In spite of the considerable amount of studies on the hot streak kinematics it is difficult to interpret the results of those studies in a way that may be applied to turbine design due to the complex nature of the flow field in which a number of design parameters have impact, such as combustor design (hot streak shape and location in radial and circumferential direction), temperature ratio of the hot to the cold gas, blade count and coolant injection. Due to the dependency of the hot streaks on the combustor type, ideal hot streak profiles have been simulated in most of the cases due to the lack of published experimental combustor measurements. One other important aspect is related to the effects of hot streaks on forced response excitation; however, it has not been widely investigated and only a few studies are reported in the open literature [31, 32]. With the use of syngas, additional complications may arise related to the fuel composition, affecting the turbine hot flow path and the rotor blades vibration and thus major challenges need to be overcome to account for the aero-thermal aspects involved in order to secure the efficient and reliable performance when switching to syngas fuel operation.

## **1.2 Objectives of the Research**

As part of the H2-IGCC project, this work intends to present the detailed hot flow path in two different gas turbines, an existing and a modified one, with particular focus on the variation in fuel composition (natural gas and hydrogen-rich syngas). The overall objective is to predict,

via numerical simulations, the hot streaks propagation mechanism with regard to the turbine aerodynamics and LEO excitation in the two axial HP turbines. The specific objectives of this thesis are:

- To develop a better understanding of the propagation mechanism of the hot streaks through a HP turbine considering a number of parameters such as, the coolant injection, the potential interaction between bladerows, the hot streak shape and location injection. The Siemens SGT300-2S/Athena turbine has been included in the analysis for that scope, focusing on the simulation of hot streak profiles which are representative of real combustor exit conditions.
- To assess the impact of the fuel composition on the flow temperature levels in a four-stage heavy-duty turbine and the aerodynamics of hot streaks when switching from natural gas to syngas fuel.
- To evaluate the effect of syngas on the potential LEO excitation of the first rotor blade in modified turbine geometry originally designed to burn natural gas, as well as the magnitude of the LEO excitation compared to the BPF excitation levels.

# Chapter 2

## Literature Review

### 2.1 Introduction

This chapter provides a literature review of some of the previous work on the hot streak problem. The review has been listed according to the effects of the problem under investigation and is generally chronologically arranged to provide some sense of the progress that has been made through the years as well as of the contribution of the current work. Until now, the focus has been primarily on the effects of temperature distortion on turbine aerodynamics. As it will be seen, the hot streaks can also exhibit effects on forced response vibrations. Summarising the current state of the literature the need to implement realistic inlet temperature profiles than what is commonly used in numerical simulations is highlighted in order to capture the unsteady effects in turbines. Moreover, the fuel flexibility in gas turbines leads to new challenges that are rarely studied. The effects of syngas on turbine design are discussed in the last part of the literature review.

### 2.2 Hot Streaks Kinematics

Knowledge of the temperature migration pattern in a turbine is essential in order to maintain high turbine performance - through high TIT - avoiding at the same time the heat and mechanical loads and related High Cycle Fatigue (HCF) problems. The dominant mechanism of the temperature redistribution into the stages, in the blade-to-blade plane, was first described by Kerrebrock and Mikolajczak for high-speed compressors [38]. For the case of rotor wake/stator interaction in a compressor stage the temperature wakes passing through

the stators are transported towards the Pressure Side (PS) of the stator passage. That happens as a result of the difference of the absolute velocity at the inlet of the rotor, due to the temperature difference and is known as segregation effect for wakes and hot streaks. The relationship between the absolute velocity,  $C$  and the static temperature,  $T$  is described by the definition of the Mach number,  $Ma$ :

$$Ma = \frac{C}{\sqrt{\gamma RT}} \quad (2.1)$$

where  $\gamma$  is the ratio of specific heats, and  $R$  is the gas constant. According to Equation 2.1 the only variable for a hot streak entering the rotor frame is the increased temperature when compared to the neighbouring cold streak. Hence, a difference in absolute velocity induces a relative slip velocity between the hot and cold fluid entering at the rotational frame. The turbine velocity triangles in Figure 2.1 show how the direction of the relative velocity at rotor inlet differs between the hot and the cold fluid, with the hot fluid moving towards the rotor PS. Kerrebrock and Mikolajczak also performed an analytical study to describe the stagnation temperature excess in the wake at stator exit. This analysis will be discussed further in Chapters 4 and 6, with respect to the thermal wakes at stator exit.

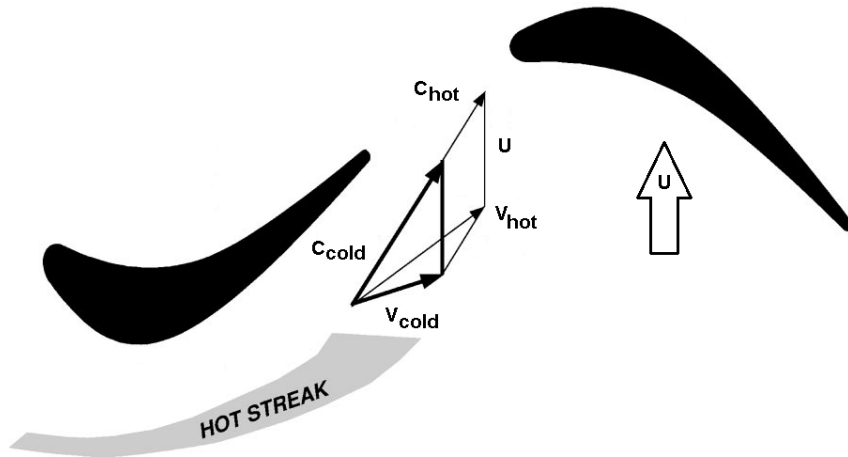


Figure 2.1: Kerrebrock and Mikolajczak segregation effect

An initial study of the effects of inlet flow distortion in turbine stationary blade rows was done by Munk and Prim [39]. It was theoretically shown that the inlet total temperature variation leaves the stator streamline pattern unaffected in the absence of inlet stagnation pressure,  $P_{o,in}$  gradients. Early experimental studies were performed by Schwab et al. [40] at NASA Lewis Research Centre and a few years later by Butler [41] on the Large Scale

Rotating Rig (LSRR) [42]. Schwab studied the effects on performance in an axial turbine stage when a radial non-uniform inlet temperature profile is applied, while Butler carried out a number of hot streaks experiments in a large-scale low speed axial turbine to confirm the tendency of separation of hot and cold fluid when entering the rotational frame. During this experiment one hot streak was injected at 40% span aligned with the mid-passage between two stator blades. Sensing the  $CO_2$  that was used to describe the flow path, hot streaks were convected through the stationary frame indicating no significant movement. Entering the rotational frame the hot and cold gas separated, following the segregation effect. The result is the preferential heating of rotor PS, with the hot fluid moving towards the PS of the rotor and the cold towards the Suction Side (SS). Butler's experimental results indicated no change to the streamline pattern in the stationary frame for uniform  $P_{o,in}$  confirming the theory first described by Munk and Prim [39] and Lakshminarayana [43]. However, in addition to the segregation effect, some 3D effects were observed such as a spanwise migration of the flow, especially on the PS of the rotor. That effect was attributed to the increase in secondary flow due to temperature gradients. Further discussion on the effects on secondary flow is presented in Section 4.3.2.

Early computations aimed to simulate the hot streak kinematics as was described in Butler's experiment. The first numerical simulation was conducted by Rai [44] using a 2D Navier-Stokes analysis for a single-stage axial turbine. The airfoil geometry used is the same as that of Butler's experiment and the comparison indicated qualitative agreement between them, taking into account the simplifications of the numerical analysis and suggesting the need of a 3D analysis in which the geometry and inlet flow conditions would be more realistic. 3D analysis was performed by Dorney [45] for 1 stator/1 rotor capturing most of the flow physics of hot streaks migration in a turbine stage. The influence of secondary flows was also simulated with good accuracy compared to Butler's experimental results. Dorney's 3D simulation confirmed the inability of the 2D simulation to predict the increased rotor surface temperature. Sharma's assessment on unsteady flows provided a comparison between Butler's experiments, 2D numerical approaches and 3D unsteady simulations [29]. Results from both experimental and unsteady numerical simulations indicated the preferential heating of rotor PS due to the presence of temperature distortions when the hot streak is aligned at the mid-passage at the inlet of the stator blades. The kinematics of hot streaks in the radial direction are related to the secondary flows into the rotor passage and are discussed in the

following section through relevant published studies.

## 2.2.1 Effects of Hot Streaks on Aerodynamics

Secondary flow is produced when a streamwise component of vorticity is developed from the deflection of a flow with velocity or density gradients [46, 47]. The impact on vorticity production due to temperature non-uniformities was early investigated analytically by Lakshminarayana [43] and later computationally by Hermanson and Thole [48] who showed that zero vorticity is produced in a turbine stator when inlet stagnation temperature non-uniformities are not accompanied by gradients in Mach number and stagnation pressure, in order to predict the thermally driven secondary flow in a turbine stator and rotor bladerow.

Based on secondary flow theory the streamwise component of vorticity for compressible, inviscid flow is given by Equation 2.2:

$$\frac{\partial}{\partial s} \left( \frac{\omega_s}{\rho C_s} \right) = \frac{2\omega_n}{\rho C_s R} + \frac{1}{\rho^2 C_s^2 T} \frac{\partial T}{\partial b} \frac{\partial p}{\partial n} \quad (2.2)$$

where  $C_s$  and  $R$  correspond to the inlet streamwise velocity component and the radius of the curvature of the streamline, respectively, while  $\omega_s, \omega_n, \omega_b$  are the components of vorticity in the streamwise, normal and binormal directions as shown in Figure 2.2, with  $\omega_n = \partial C_s / \partial b$ .

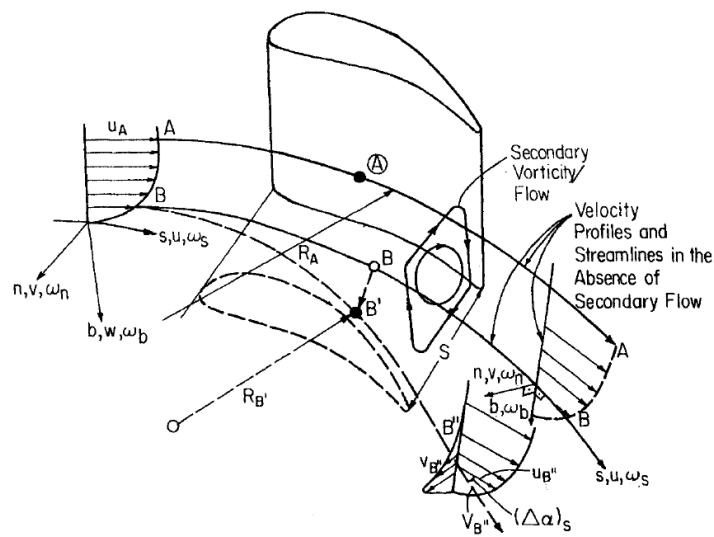


Figure 2.2: Schematic illustration of the development of secondary flow in a rotor blade passage [1]

It is clear from Equation 2.2 that secondary flow can develop under two conditions: (i) when there is a normal component of vorticity at the inlet plane ( $\omega_n$ ) and (ii) when there is a radial static temperature gradient at the inlet. Since the pressure gradient,  $\partial p/\partial n$ , is always non zero in a curved streamline, then secondary flow develops in a bladerow when there is static temperature gradient at the inlet. Lakshminarayana expressed the streamwise vorticity also in terms of stagnation temperature, which after simplifications is given by Equation 2.3:

$$\frac{\partial}{\partial s}\left(\frac{\omega_s}{\rho C_s}\right) = \frac{2\omega_n}{\rho C_s R}\left(1 + \frac{\gamma-1}{2}Ma^2\right) - \frac{|\nabla T_o|\cos\beta}{\rho TR} \quad (2.3)$$

where  $\beta$  is the angle between the  $|\nabla T_o|$  and binormal direction ( $b$ ). Providing that there are Mach number gradients, variation of stagnation temperature in the radial direction will produce additional secondary flow in a bladerow, while in the absence of Mach number gradients the terms of normal vorticity  $\omega_n$  and  $|\nabla T_o|$  cancel each other and secondary flow remains unchanged. This condition is not representative of the turbomachinery environment; however, is used as an assumption providing a mean of controlling the parameters that contribute to the generation of secondary flow and in turn, simplify the analysis.

Since, additional secondary flows cannot develop when the stagnation pressure gradient is zero, the fixed temperature profile in the stationary frame, also mentioned by Butler et al. [41], is explained when hot streaks are present with uniform  $P_{o,in}$  boundary conditions. However, in the rotor frame, the difference in rotor relative inlet velocity between the hot and cold streak, due to segregation effect, produces stagnation pressure gradients at rotor inlet, leading to additional generation of secondary flows. A 3D Euler solver was used by Shang and Epstein [49] who investigated the individual effects of wakes and turbine inlet temperature gradients on the production of secondary flows for low aspect ratio multi-stage turbines. Boyle and Giel [50] investigated the effects of hot streaks confirming the experimental measurements of Shang, using a steady state 3D Navier-Stokes analysis when CPU time requirements were still quite high for such analyses. In a more recent numerical study Hermanson and Thole [51] used similar temperature gradient to that used by Boyle, in order to investigate the effect of non-uniform inlet conditions on the secondary flow fields focusing also on the relationship between  $P_{o,in}$  and secondary flow generation. The results demonstrated the need to consider more realistic turbine inlet profiles due to the effect of pressure gradient on the magnitude of secondary flows.

Prasad and Hendricks [52] studied the mechanisms that drive hot streak transport in turbine rotor with respect to secondary flows. It was found that the variation in flow density due to the temperature variation drives the variation in the secondary flows in the rotor passages. Later CFD simulations [53, 54] confirmed the additional secondary flow production due to hot streaks and the impact of that on the spanwise migration of hot fluid on the PS and SS of rotor blade. Ong and Miller [54] also investigated the combined effects of blade row interaction and thermally driven interaction on the hub endwall secondary flow production in rotor passage, showing relatively weak contribution of the hot streaks on the hub passage vortex enhancement compared to the stator wake. However, those are general trends and are quite dependent on specific conditions in different turbines. The major effect of the enhanced secondary flow in rotor passage is the distortion of the hot streak profile on the rotor PS, the magnitude of which is dependent on the turbine and combustor design, and the compression of the hot flow streamlines on the rotor SS, the importance of which is highlighted in terms of performance and coolant effectiveness. As has been shown in an experimental study by Jenkins et al. [55], the much steeper temperature gradients that result on rotor SS enhance the combined effects of film cooling and high turbulence levels on that blade surface. That may lead to a significant attenuation of peak temperature (by about 74%), leaving a substantial hot streak on the rotor PS.

In terms of performance, Lewis [56] showed that the effect of spanwise total temperature redistribution may have significant impact on aerodynamic performance in axial turbines. However, according to Adamczyk [57], unlike spanwise redistribution, there is no evidence suggesting that circumferential redistribution impacts on aerodynamic performance. This is confirmed by a more recent study where the effects of hot streak inlet profile on turbine performance were investigated [58] taking into account different circumferential hot streak positions at the turbine inlet. Zilli et al. [58], used a Gaussian distribution superimposed on a radial profile in order to simulate the hot streak profile. Applying 3D CFD tools the analysis was performed for two fuel injector positions, one where the hot streak was aligned with the stator mid-passage, which was defined as unclocked position, and one where the hot streak was aligned with the stator Leading Edge (LE), and this was defined as clocked position. Comparative CFD results between the two clocking positions and a case of radial inlet temperature redistribution indicated quite small variations in terms of performance, with the most favourable to be the case of the clocked hot streak position, and the worst

case the one when only radial inlet temperature variation is applied. Since the variations of performance have been found to be very small, attention turned mainly to the effects of total temperature redistribution on the formation of hot spots on blades' surfaces which may impact the blade life.

In order to investigate the most favourable hot flow migration pattern through the turbine stages in terms of heat transfer the effects of hot streak shape and injection location have been studied. With respect to the circumferential injection location at turbine inlet, there are various numerical studies dealing with the sensitivity of the hot streak propagation through the turbine [59, 60, 61, 62, 63, 53, 64]. As a general outcome of those studies, the segregation effect was confirmed to be the dominant hot streak transport mechanism on the blade-to-blade direction along the turbine, in case that the hot streak was aligned with the mid-passage between two stator blades (unlocked position). This is because the hot and cold streaks are not interacting with each other and hence, convect towards rotor PS and SS, respectively. In case of clocking the hot streak position and align the hot flow injection with the stator LE, the hot and cold streak are in phase and the movement depends on the relative strength of the two mechanisms. As long as the temperature difference between the two streaks (hot and cold) remains quite high, the cross-passage movement is driven by the hot streak, but the preferential heating of the rotor PS may be weakened. However, if the temperature difference is not high enough then the effect of rotor PS preferential heating may disappear or even be reversed.

In terms of coolant effectiveness, the clocked hot streak position leads to reduced peak temperatures on rotor PS. At the same time the alignment of the hot streak with the stator LE results increased thermal load on stator blades, thereby higher cooling flow rate is necessary in order to control the effects on stator blades surfaces heat load. Basol et al. [53] presented a more detailed study showing that by clocking of the hot streak even by less than  $6^\circ$  towards the stator PS the heat load of the rotor blade tip could be substantially reduced. Although there have been numerous studies on the effects of hot streak clocking positions, that design philosophy only applies for integer hot streaks/stator blades ratios. For non-integer ratios a combination of clocked and unlocked hot streak positions is unavoidable, hence a full annulus simulation would provide a more accurate description of the combined effects on hot streak migration.

A study on the effects of hot streaks focused on turbine blade heat load was performed

by An et al. [62], taking into account the interaction with the Trailing Edge (TE) coolant injection and applying 3D unsteady numerical simulation for a 2 stators/4 rotors configuration. Six different hot streak positions were investigated circumferentially relative to the LE of the stator blades in order to evaluate the effect on heat transfer characteristics. The study pays more attention to the transient variation of heat load to describe the unsteady effects of the hot streaks. An altered hot streak was observed at the exit of stationary frame in terms of shape and maximum temperature values, affecting in such way the fluctuation range of heat load at rotational frame. The alteration of hot streak shape at the exit of the first stationary frame was indicated as a result of cut-back slot ejection. Pyliouras et al. [65] suggested an optimised coolant configuration for individual blades with respect to the first stator bladerow coolant, as the temperature difference between the hot and cold sections on stator blades was found to be up to +/- 400 K. According to that study, Pyliouras et al. [65] concluded that designing the coolant scheme for each stator blade equally, considering only the highest temperatures, results in a waste of cooling on blades not aligned with the hot streak.

A more recent numerical study performed by Simone et al. [66] on the hot streak effects on thermal loads in HP turbine summarised some significant design parameters that are worth to be mentioned as they also account for the contribution of this thesis. Regarding CFD methods, the importance of the exact blade count ratio is mentioned, in case that there is no common divisor between stator and rotor blades, as scaling methods will alter the solidity and result in different alignment positions between hot streak and stator blades (clocking), with a consequent alteration of the hot flow path. In such case full annulus analysis should be performed to capture the accurate transport mechanism of the hot fluid into the turbine. Regarding design parameters, the need for realistic temperature profiles was also pointed out by Simone; he suggested that the propagation of the distortions further downstream the first HP turbine stage should be considered to investigate the segregation effect taking place also on second stator blades, when a representation of a real machine temperature profile is used. This is of great importance for the accurate interpretation of the hot streak propagation into the turbine and will be further investigated in this thesis. The need to investigate further the hot streak migration pattern into the second turbine stage was also pointed out earlier by Dorney et al. [67] and it is taken into account in this thesis where the hot streak propagation is investigated up to the exit of the turbine.

Only a few studies deal with the combustor design impact including both the hot streak

shape and the spanwise location of hot streak injection, in respect of the effects of an accurate hot streak profile simulation. Those could provide useful information for the interpretation of the results as will be presented in this thesis, since different turbine designs have been investigated, using hot streak shapes in a way that will have the optimum effect on heat load distribution on turbine blades. In order to investigate the effects of spanwise hot streak injection a study was conducted by Roback and Dring [59] in relation to the combustor design. According to Roback and Dring, the radial migration of the hot streak into the rotor passage was found to be dependent on the radial hot streak location at turbine inlet. With the hot streaks injected in various locations, accumulation of the hot fluid was recorded towards both hub and tip regions in rotor passage, expressing the dependency of the radial migration of the hot streak on the location of the radial injection. With respect to the shape of the hot streak most researchers consider ideal hot streak shapes due to the lack of published experimental data. They typically used parabolic functions in order to simulate the inlet temperature profile.

One of the first numerical studies dealing with the effect of hot streak shape in an un-cooled turbine stage was performed by Dorney and Burlet [68] using circular and elliptical hot streaks of varying sizes. Based on that study the elliptical shape hot streaks were mixing more rapidly due to the larger area exposed to the cold surrounding fluid. Regarding the size of the hot streak, the larger surface area exhibited higher interaction with the secondary flows near the hub, thus higher losses, resulting in an additional high temperature region. However, the authors mentioned the need to include cooling injection in a future analysis, as that would have affected the interaction with secondary flows and the distortion of the hot streak. Basol et al. [53] also investigated the effects of hot streak shape, using elliptical hot streak shape in various rotation angles. This practice can be considered as a way of hot streak clocking (relative circumferential position) with similar findings. Finally, more extensive studies on combustor representative hot streak profiles were performed by Povey et al. [69, 28, 2]. In his last study Povey et al. [2] presented a review of six combustor simulators; this is the most recent and significant published work that has been conducted in order to provide realistic data that could be used to describe engine-representative hot flow path in axial turbines. A whole-field combustor exit temperature profile was presented showing the radial and circumferential variations between the hot streaks as shown in Figure 2.3, with a maximum and minimum value of temperature ratio corresponding to 1.14 and 0.84, respectively.

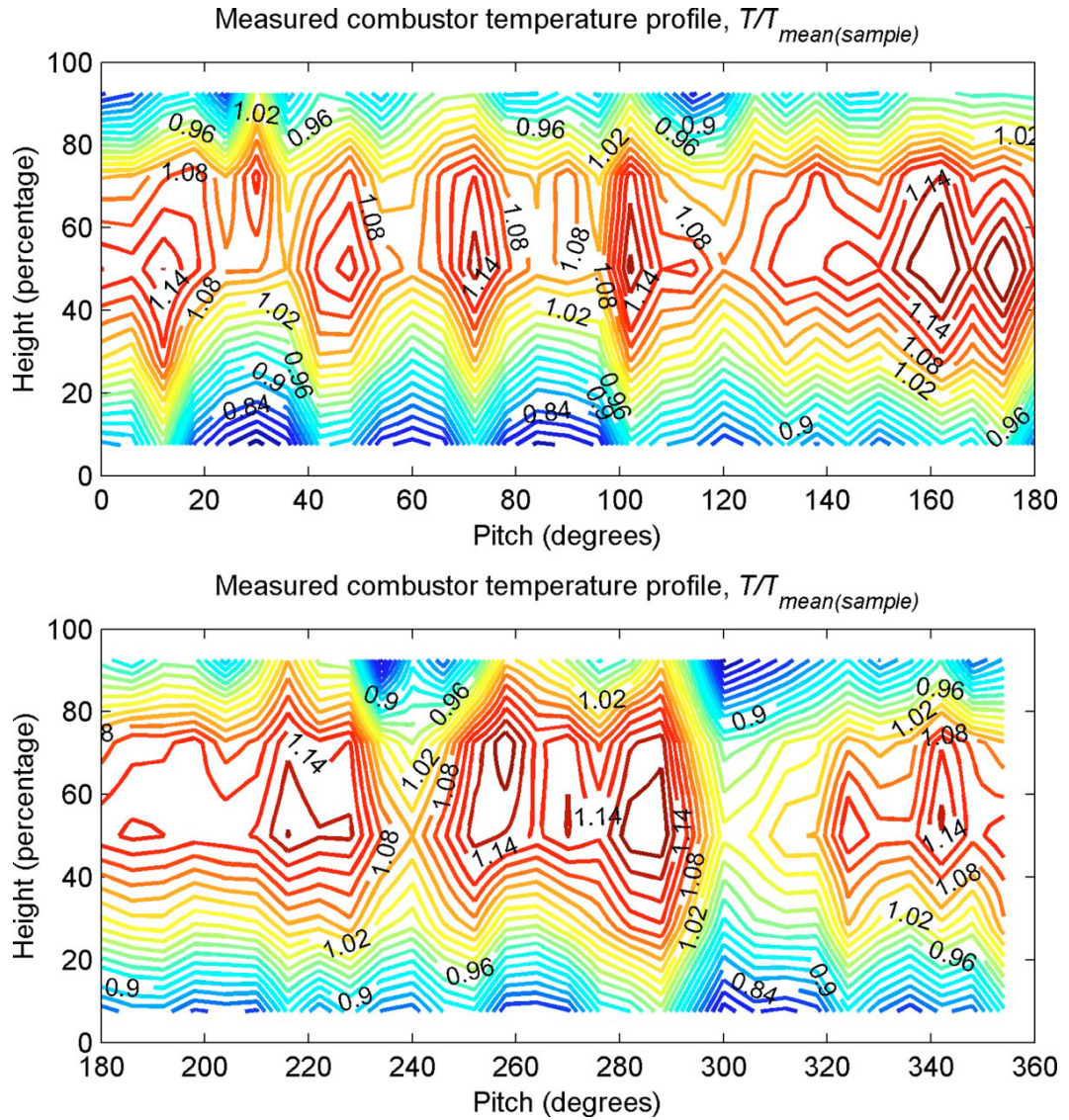


Figure 2.3: Measured (QinetiQ) combustor exit temperature profile in a military engine from Povey and Qureshi [2]

## 2.2.2 Forced Response and LEO excitation

Excitation problems in gas turbines arise from time-varying excitation forces from upstream or downstream disturbances. Compared to the BPF excitation, LEO is far less studied and more difficult to predict due to the unknown controlling parameters a priori that are related to sources of flow variation. Greitzer et al. [70] classified the unsteadiness into three regimes, including LEO excitation and rotating stall in the regime of large scale phenomena, meaning that the length scale of the excitation is roughly an order of magnitude larger than the blade passage. Unsteadiness associated with the wake and boundary layer turbulence and transition corresponds to small scale unsteady phenomena while medium scale is related to the passage

flow structure such as potential interaction and tip clearance vortices.

However, only little work is published regarding the understanding of the large scale unsteady phenomena such as the LEO forced response. An aeromechanical approach with forced response analysis, as has been described above, is necessary in order to investigate the mechanical effects arising from unsteady blade forces that have been generated by flow non-uniformities. Sayma et al. [71] investigated the effects of non-uniform spacing between stator blades on LEO excitation, which is believed to be the most common source of low harmonics. Using a well-defined pattern, the 4<sup>th</sup> and 8<sup>th</sup> EO excitations were produced and the final modal displacement amplitude was found to be dependent on the variation of the throat width. The same analysis was also presented by Elliott et al. [72] finding the aerodynamic force to be linearly proportional to the amount of throat width variation. Rzadkowski et al. [73] performed a 3D numerical study comparing effects of LEO and BPF excitation. In that study, the LEO excitation that was caused by general unsteadiness in the flow was shown to be higher in comparison to higher order excitation frequencies.

Joecker et al. [74] presented a comparison of numerical models that have been used to predict LEO excitation problems in order to evaluate computational approaches that would save time avoiding to compute the whole annulus turbine stage. A variation of stator throat width was used to produce a 5<sup>th</sup> EO excitation force, which when was compared against experimental results the sector model yielded inadequate results. The same source of LEO excitation was studied by Vahdati et al. [37] performing multi-blade row forced response analysis for gradual blockage in second stage of an axial compressor. The results indicated a small effect on the main BPF but the amplitude of the LEO harmonic were found to increase as the amount of blockages increases. A more recent numerical study on LEO excitation was performed by Aschenbruck et al. [75] considering geometrical variances as a source of low harmonics. Two geometric variations were implemented, one alternating the thickness of stator TE and another varying the stagger angle of every other blade, resulting in a non-linear relation between the amount of the geometry defect and the excitation response of the blades. The modifications were based on geometry defects measured on real blades and the variation of the stagger angle was found to be the largest contributor to forced response.

In general, the numerical studies of hot streaks have been conducted for aerodynamic considerations in HP first turbine stage rather than forced response analysis. Hence, forced response studies for LEO excitation due to turbine inlet temperature distortions are very

sparse in the open literature, though the effects of turbine inlet temperature distortions on the forced response vibration have been pointed out in few studies [54, 65] but have not been further investigated. The first attempt to predict the effect of temperature distortions on the LEO excitation was presented by Manwaring and Kirkeng [31] for a Low Pressure (LP) turbine based on temperature measurements at the exit of the HP turbine (inlet to LP turbine). Focusing on the fifth stage, they considered both entropic, due to temperature distortions, and vortical waves, due to total pressure variations, showing equally important impact on the determination of the unsteady loading. Further calculation of the blade stresses and comparison with measured data on the fifth LP turbine stage blade exhibited good agreement. Hence, the study concluded that incorporation of the forced response analysis, due to the turbine inlet flow variations, in the design process is needed in order to ensure acceptable tolerances on the blade vibrations.

Only two more recent numerical studies have been published investigating the aeromechanical effects of hot streaks with particular interest on the LEO excitation effects [76, 32]. Breard et al. [76] investigated the effects of temperature distortion, that is caused due to fully or partially blocked burners, using whole annulus 3D CFD simulations and a representative temperature distribution profile. Additional individual sources of LEO excitation were included in the same study, among those are variations of stator throat width which arise from non-identical stator blade passages, variation of the flow exit angle due to manufacturing and assembly tolerances, as well as cooling non-uniformities between the blades. Combined effects were also considered, since in reality most of the sources of LEO coexist meaning that some of the individual parameters will either cancel each other or produce much larger forcing by superposition. Comparison between the effects of each excitation source was found to be difficult because the quantification of the parameter variation levels is not straightforward, while additional difficulties arise when determining the combined effects by linear superposition. Breard et al. concluded that the total excitation forcing can be quite different in magnitude compared to the individual components depending on the phase difference between them.

Finally, Mayorca et al. [32] investigated the excitation levels of the fourth stage of an industrial gas turbine with respect to burner cans induced forced response. Applying 3D CFD simulation and scaling method between the stages the excitation levels due to temperature distortion found to be of considerable strength at the downstream LP rotor blades due to the

fact that the hot streaks were not highly mixed out through the turbine. However, Mayorca et al. found no contribution of the total temperature inlet profile on the BPF excitation on rotor blades. The result is attributed to the possible large interaction between cooling flows, viscous and potential field effects as well as to the effect of scaling the bladerows. More specifically, the blade count modification is expected to result in a different distribution of the temperature profile development along the turbine stages in a way that is proportional to the level of bladerow scaling and in different set of EOs arising from the blade count difference excitation.

For forced response predictions, whole annulus models need to be used to accurately describe the phenomenon due to the lack of cyclic symmetry, as an accurate representation of the temperature profile at the combustor exit contains random differences between the hot streaks in radial and circumferential directions. Moreover, in the case of non-integer hot streaks/blade count ratio, scaling effects would affect the temperature distribution with the effects being proportional to the level of blade count modification. The effects of geometrical scaling on the prediction of aerodynamic forcing have been presented in a very recent study by Mayorca et al. [77]. In order to accurately model the effects of the hot streaks on the LEO excitation an aeroelasticity model described by Sayma et al. [71] and Vahdati et al. [78] will be used in the current research for the forced response analyses.

## **2.3 Syngas Operation in Turbine**

With regard to the turbine, there may be many limitations depending on the gas turbine technology and fuel under consideration. Chemical composition variability and syngas heating values address considerable issues about the turbine aerodynamic, thermal and mechanical design. A Siemens study [79] addressed the effect on increased volume mass flow rate due to the low calorific value resulting in raised Mach numbers. Moreover, due to noticeable fraction of non-combustibles, such as steam,  $CO_2$  and  $N_2$ , performance issues of the combined cycle arise. The higher steam concentration of the expansion gas increases the rate of heat transfer to the blades leading to maximum allowable turbine inlet temperature and hot gas path cooling. Discrepancies found in the composition of the fuel (syngas type) will affect the content of water vapour in the combustion gas and hence the heat transfer characteristics [80, 15, 81, 19, 82]. A syngas fuelled machine will exhibit increased water vapour

in the gas turbine exhaust gases (the amount being dependent on syngas type) that is linked to enhanced heat transfer and increased blade metal temperature. With regard to the fuel composition, the effects of undiluted syngas on the volume mass flow rate were discussed by Chiesa et al. [18]. He also mentioned the consequences of the increased volume flow rate on the hot flow path due to the influenced flow velocity and hence the altered velocity triangles. The work of Chiesa et al. [18] is considered in the thesis as not many published studies deal with hydrogen-rich syngas fuel in gas turbines.

The overheating of the turbine metal for syngas fuel was investigated by Chacartegui et al. [82], Sabau and Wright [83]. In particular, Chacartegui showed about 7 – 25 °C higher metal temperature of the blades compared to natural gas. Maurstad et al. [80] suggested a combination of air cooling and blade thermal barriers coating for syngas fuel while GE recommended decreasing the turbine inlet temperature by a certain amount if it is desirable to maintain 100% of the design lifetime. According to that study, the higher the volume percentage of water vapour, the more the turbine inlet temperature needs to be reduced. In order to modulate the turbine parameters and avoid blade failure, an assessment of the turbine blade temperature due to the fuel change is necessary as the higher heat transfer rates may address the need of improved coolant schemes.

The effects of syngas on the turbine aerodynamics were also investigated by Colantoni et al. [84]. Compared to natural gas and for same firing temperature, Colantoni also investigated the flow path overheating when using syngas, without taking into account though 3D effects such as the hot streak propagation or secondary flow. Those effects were investigated for a syngas firing gas turbine in a very recent study by Wang and Yuan [85]. Wang and Yuan [85] performed a 3D CFD analysis to study the combined effects of hot streaks and gas species non-uniformities on the turbine aerodynamics. Applying sinusoidal profile to simulate both hot streaks and water steam concentration aligned with stator mid-passage, the impact of secondary flow and species concentration on the radial migration of the hot streak into a one-and-half stage turbine was shown, especially on the rotor PS where water steam was carried along with the hot streak.

## 2.4 Summary of Review

A summary of the literature review is presented here with attention paid to the effects that are relevant to the current thesis and whose importance needs to be highlighted. For natural gas fuelled turbines, the flow path of the hot streak has been widely investigated as presented in the literature review in Section 2.2 for aerodynamics considerations. With respect to coolant efficiency, most of the studies have been limited to the first turbine stage, that is the hot turbine section, and thus multi-stage turbine simulation have not been conducted in order to investigate the propagation of the hot streaks up to the exit of the turbine. Apart from the effects on the turbine aerodynamics, the impact on the downstream blade vibration has been mentioned but not studied extensively. Only a few publications can be found in the open literature mentioning the importance of an aeroelasticity analysis being performed as part of the design process, focused on the LEO excitation. Finally, the recent trend towards environmentally friendly and low cost fuels, such as syngas, leads to new concerns regarding the effects of fuel composition on the hot streak propagation; only one recent study deals with the effects of the fuel composition on the hot streak redistribution mechanism [85].

Regarding the simulation tools, the need of unsteady CFD simulations has been highlighted in order to accurately capture the effects of propagation of the hot streak in the turbine, as the nature of the problem is inherently unsteady. Moreover, an accurate modelling of the turbine stage geometry by using the exact hot streak/stator/rotor blade count ratio is rare in the literature; current CFD simulations still use scaling methods of the count ratio with effects on the accuracy of the hot flow field description. Finally, regarding the simulation of the turbine inlet conditions, data of combustor representative hot streak profiles are not widely found in open literature due the scarcity of experimental studies and the diversity of combustor designs, hence most researchers have considered ideal hot streak shapes for the numerical analysis.

## 2.5 Contributions

The use of syngas in industrial gas turbines addresses the need for design modifications to existing engines. For natural gas fuelled turbines, the hot flow path has been widely investigated; however, additional complications may arise related to the fuel composition, when switching to syngas operation, regarding the turbine hot flow path and the rotor blades

vibration; hence further research on the kinematic behaviour of hot streak migration pattern through the turbine stages needs to be done. Moreover, the lack of experimental data and the hot streak shape dependency on the combustor type lead to additional challenges regarding the realistic representation of the turbine inlet temperature conditions in order to enhance the understanding of the temperature redistribution phenomenon as well as the effects on the potential excitation mechanism of the downstream rotor blades.

For the current thesis the aerodynamic and forced response effects of turbine inlet temperature distortions are presented as necessary part of the design phase, with respect to fuel flexibility in gas turbine, based on the turbine modifications provided by other H2-IGCC project partners. A realistic hot streak profile for a natural gas fired gas turbine was provided by Siemens to simulate combustor representative temperature conditions. To the best knowledge of the author there are no data available in open literature for the effects of firing syngas on the hot streak propagation and LEO excitation for the whole turbine applying combustor representative hot streak profile, and this is the main contribution of this thesis. The final results suggested safe operation of the syngas turbine in terms of LEO excitation, while important differences in hot streaks propagation observed between different turbine designs that intent to enhance the understanding of the phenomenon with respect to coolant effectiveness.

## **2.6 Thesis Outline**

This section outlines the organization of the thesis in the remainder 6 chapters after the introduction and literature survey that have been presented in Chapters 1 and 2, respectively. In Chapter 3 the in-house numerical model used for the forced response and aerodynamics analysis is presented along with a grid independence study. Chapter 4 and 6 constitute one of the two main objectives of the thesis and present the investigation of the effects of hot streaks on the turbine aerodynamics. Chapter 4 addresses the aerodynamic effects of hot streaks on the SGT-300 two-stage HP turbine with respect to the propagation mechanism and the interaction with the flow features. Chapter 5 sets the background of the H2-IGCC project focusing on the turbomachinery challenges part of which is related to the current work. In Chapter 6 the hot streaks aerodynamics are analysed with respect to the fuel composition for the purposes of the H2-IGCC project. The effects of syngas on the kinematics of hot streaks are discussed with particular focus on the turbine cooling. The evaluation of the LEO

excitation of the first rotor bladerow for the H<sub>2</sub>-IGCC turbine is the second main objective of the thesis and is investigated in Chapter 7 with regard to the fuel composition. The thesis is concluded with Chapter 8 where an overall discussion of the results is given, as well as recommendations for further research.

# Chapter 3

## The Numerical Model

### 3.1 Introduction

A numerical approach has been used for the aerodynamic and aeroelasticity analysis in this thesis based on CFD and FE methods. This chapter consists of two parts; an overview of the aeroelasticity model that is presented in Section 3.2 followed by a grid independence study in Section 3.3 including also a comparison of the steady state CFD results against the throughflow model analysis. Finally, Section 3.4 summarises the key points of the chapter.

### 3.2 Forced Response Methodology

#### 3.2.1 Overview

There have been a number of numerical methods developed for the simulation of unsteady flows in a gas turbine environment. For the purposes of the current work the aeroelasticity model applied to solve the hot streaks induced forced response problem has been previously described by Sayma et al. [71, 86, 87], an overview of which will be given here. The forced response numerical model involves two different fields, fluid and structural. For the current study the two parts are solved in an uncoupled way. The aerodynamic part is provided by an unsteady RANS CFD solver while the structural part is based on a standard linear FE model. A schematic diagram of the current approach is shown in Figure 3.1 and can be described through the following steps:

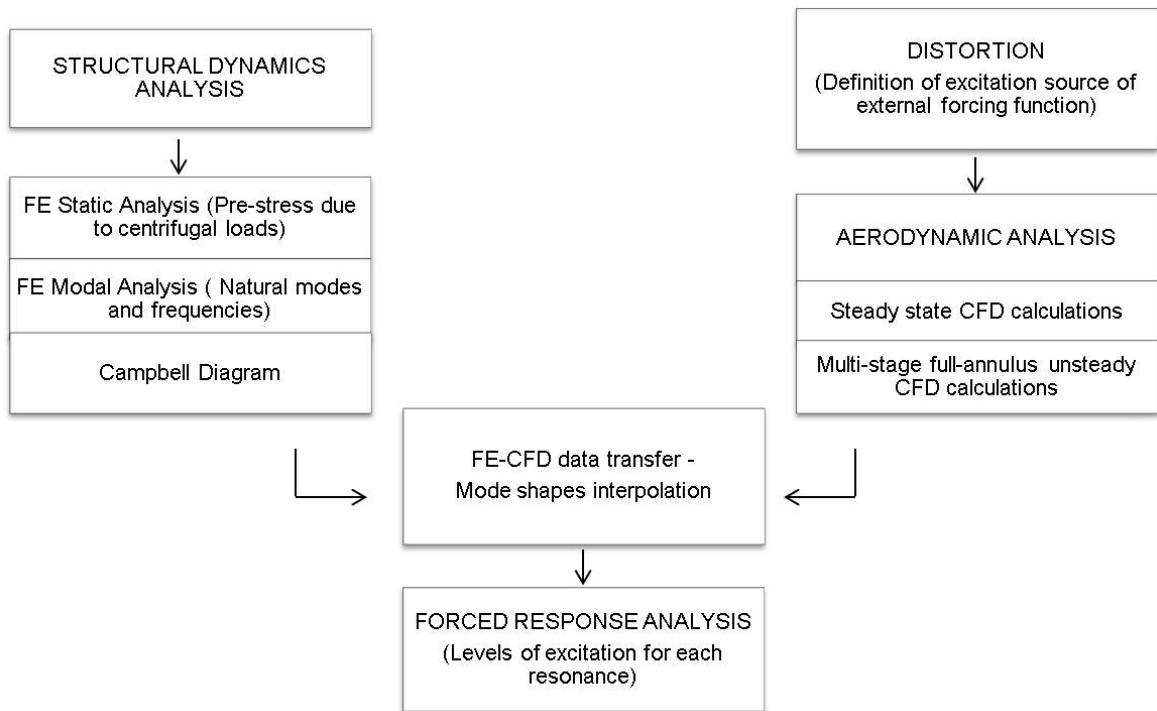


Figure 3.1: Schematic representation of the applied forced response methodology

1. Steady state computation of a single passage for each one of the bladerows.
2. Expand the solution to form the full annulus multi-stage model.
3. Prestress the blade under investigation performing a static analysis.
4. Perform a linear prestressed modal analysis to obtain the mode shapes and natural frequencies of the blade under investigation.
5. Anticipate the critical frequencies from inspection of the Campbell diagram for the operating speed.
6. Interpolate the mode shapes from the structural mesh onto the aerodynamic mesh.
7. Apply the source of unsteadiness on the CFD model, that is representative of the temperature distortion in the current study.
8. Solve the unsteady forced response model by using the results of step 2 as initial condition, the mode shapes of step 6 and the unsteady forcing source applied at step 7. Using the steady state solution as the initial condition, the unsteady calculations are performed with sliding planes between bladerows.

9. Extract the levels of excitation for each one of the mode shapes and the aerodynamic flow features through the turbine stages.
10. Calculate the modal force in a post processing step based on the results obtained at step 9.

### **3.2.2 In-house CFD and Aeroelasticity Solver**

The forced response methodology has been described above while in this section the specific details of the aeroelastic model are given. The in-house CFD code, SURF, is used in the current work for the unsteady aerodynamics and forced response computations. The code that has been described by Sayma et al. [88, 87, 86] is a finite volume, URANS compressible flow solver. In SURF the flow equations are discretised using a second-order accurate time-implicit scheme for unsteady flow calculations and an outer Newton iteration procedure is used where the time step is fixed throughout the solution domain. The selection of an optimum number of time step, in terms of computational cost, is based on the physics of the phenomenon under investigation. For forced response calculations the time step is controlled by the blade passing frequency and is chosen so that a complete cycle of vibration is captured. For the sliding planes between the bladerow boundaries the solution is updated at the interface at each time step by interpolating the variables in the stator computational domain to get the rotor fluxes and in the rotor domain to get the stator fluxes [89, 88].

The aerodynamic meshing approach that has been reported by Sayma et al. [86] and by Sbardella et al. [90], combines the advantages of both structured and unstructured grids providing geometric flexibility. A structured body fitted grid is applied near the blade to resolve the large gradients normal to the wall effectively while an unstructured grid occupies the interface between the structured mesh around the blades as shown in Figure 3.2. The one-equation Spalart-Allmaras turbulence model [91] is employed for the CFD simulations and the standard wall function with slip condition is used in these computations.

The structural modelling is based on a linear modal analysis that is the standard method followed to solve part of the forced response problem when the elements of the stiffness matrix are constant. The structural analysis provides the mode shapes and eigen-

frequencies of the blades using a FE model of the structure. The FE software used in this analysis was chosen to be ANSYS, a typical commercial package. The mode shapes are interpolated from the structural mesh to the aerodynamic mesh to complete the forced response calculations.

### 3.2.3 Flow Model

For the sake of completeness the formulation of the CFD code is described in this section. The unsteady, compressible, 3D RANS equations can be solved in a relative reference frame for a blade rotating about the x-axis with angular velocity  $\omega$ . Assuming a given control volume  $\Omega$  with boundary  $\Gamma$ , the governing equations can be written in conservation form as:

$$\frac{d}{dt} \int_{\Omega} V d\Omega + \oint_{\Gamma} (F_i - G_i) n d\Gamma = \int_{\Omega} S d\Omega \quad (3.1)$$

where the unit vector normal to the surface is represented by  $n$ , while  $U$ ,  $F$  and  $G$  are vectors given by:

$$U = \begin{pmatrix} \rho \\ \rho u_i \\ \rho e \end{pmatrix} \quad (3.2)$$

$$F = \begin{pmatrix} \rho(u_j - w_j) \\ \rho u_i(u_j - w_j) + p\delta_{ij} \\ \rho e(u_j - w_j) + p u_j \end{pmatrix} \quad (3.3)$$

$$G = \begin{pmatrix} 0 \\ \sigma_{ij} \\ (u_k \sigma_{ik}) + \kappa \frac{\partial T}{\partial x_i} \end{pmatrix} \quad (3.4)$$

with  $U$  representing the vector of the conservative variables,  $F$  and  $G$  the inviscid and

viscous flux vectors respectively, where the viscous term  $G$  is put into non-dimensional form. The first row of the vectors corresponds to the continuity equation, the second to the momentum equation, while the third is the energy equation. In Equation (3.1)  $S$  contains the terms of Equation (3.1) due to the rotation of the non-Newtonian reference frame and is given by:

$$S = \begin{pmatrix} 0 \\ 0 \\ \rho \omega u_2 \\ \rho \omega u_3 \\ 0 \end{pmatrix} \quad (3.5)$$

In Equations (3.2) - (3.3)  $\rho$  is the fluid density,  $p$  is the static pressure,  $e$  is the specific internal energy,  $u_i$  is the absolute flow velocity vector and  $w_j$  is the grid velocity in the reference frame and  $\delta_{ij}$  represents the Kronecker delta function. In Equation (3.4)  $\kappa$  is the effective thermal conductivity,  $T$  is the static temperature and  $\sigma_{ik}$  is the viscous stress tensor given by:

$$\sigma_{ij} = \mu \left( \frac{\partial u_i}{\partial x_j} + \frac{\partial u_j}{\partial x_i} \right) - \frac{2}{3} \delta_{ij} \mu \frac{\partial u_k}{\partial x_k} \quad (3.6)$$

where  $\mu$  is the sum of the molecular and eddy viscosity. The eddy viscosity assumption is used in one-equation turbulence models such as the Spalart-Allmaras where only one additional equation is needed to model the turbulence viscosity transport. One-equation models have shown efficient behaviour in complex turbomachinery flows, where the use of unstructured grid becomes very popular due to the advantage of flexibility that offers. For the current study the one-equation Spalart-Allmaras turbulence model is employed for the CFD simulations, as the only available in the code, and the standard wall function with slip condition is used in these computations.

The equation set is completed with the perfect gas relation:

$$p = (\gamma - 1) \rho \left( e - \frac{c^2}{2} \right) \quad (3.7)$$

where  $\gamma$  is the the fluid specify heat ratio. An edge-based discretisation method described by Sayma et al. [86] is employed to solve Equation 3.1 on a computational domain that has been discretised in volumes. Based on this approach, the grid is treated by the solver as a set of node pairs connected by edges, a 2D mesh representation is shown in Figure 3.2. For clarity this is illustrated on a 2D mesh, although the formulation is applicable to 3D cells. Assuming that node  $I$  is connected to the surrounding nodes  $J_1, \dots, J_n$ , the side weight  $\eta_{IJ_1}$  is obtained by the summation of the two dual median lengths around the side times their normals. According to the example shown in Figure 3.2 it will be  $\eta_{IJ_1} = \vec{AB} + \vec{BC}$ . The inviscid fluxes  $F_{IJ_s}$  are treated using a central difference formulation with a suitable artificial dissipation based on an upwind scheme. The viscous fluxes are expressed using the edge weights  $\eta_{IJ_1}$  and by evaluating the required gradients of the primitive variables at the mesh nodes.

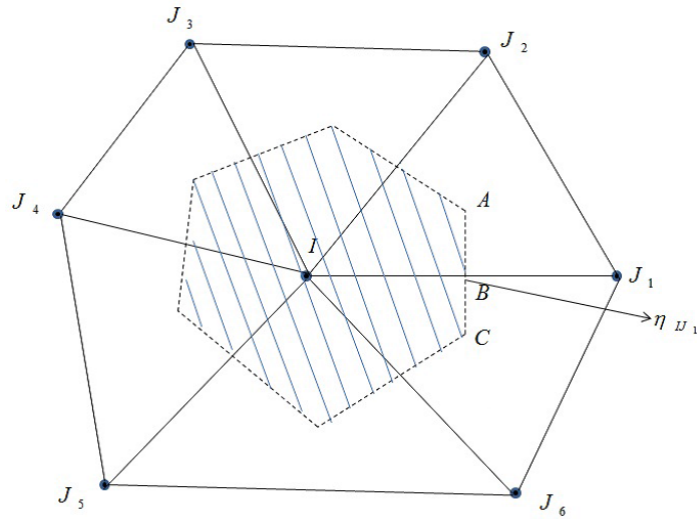


Figure 3.2: Typical 2D mixed-cell mesh

The system of equations is advanced in time using first order, implicit time integration. Steady flow calculations are achieved by using a point relaxation procedure with Jacobi iterations. While unsteady, time-accurate flow computations are treated using a scheme with Jacobi iterations and a dual time stepping allowing relatively large time steps for the external Newton iterations ensuring time accuracy [92].

### 3.2.4 Structural Model

Assuming a linear behaviour of the blade motion, the global aeroelasticity equation of motion can be written as:

$$[M]\ddot{x} + [C]\dot{x} + [K]x = F(t) \quad (3.8)$$

where the mass  $M$ , damping  $C$  and stiffness  $K$  matrices are constant while the unknown displacement  $x$  varies with time as well as the aerodynamic force  $F(t)$ . The modal analysis describes the way in which the bladed disk will vibrate naturally, numerically this solution is achieved by performing a free response analysis considering  $F(t) = 0$  in Equation 3.8. By solving the free vibration problem the modal analysis provides the natural modal properties (natural frequencies  $\omega_r$  and mode shapes  $\phi_r$ ) of the blades using a FE model of the structure,  $r$  being the mode index.

Transforming the system into mass normalised modal space through the coordinate transformation  $x = \Phi q$  [?], with  $q$  being the vector of principal or modal coordinates and  $\Phi$  the mass-normalised mode shape matrix, allows Equation 3.8 to be written as:

$$\Phi^T M \Phi \ddot{q} + \Phi^T C \Phi \dot{q} + \Phi^T K \Phi q = \Phi^T F(t) \quad (3.9)$$

For full assembly calculations, assuming that the disk is rigid, the mass-normalised mode shape matrix can be evaluated for a single blade and expanded to the full assembly. For symmetric structures, the method has the capability of modelling a bladed disk based on cyclic symmetry. Due to the rotationally periodic nature of the assembly, bladed disks can be represented by a single subpart which is repeated at equal angles around the rotation axis.

Using the orthogonality properties of the mass, damping and stiffness matrices with respect to  $\Phi$ , and assuming proportional damping, the equations of motion decouple, reducing to:

$$\ddot{q}_r + [diag(2\zeta_r \omega_r)] \dot{q} + [diag(\omega_r^2)] q = \Phi^T F(t) = \Theta_r(t) \quad (3.10)$$

where  $\omega_r$  and  $\zeta_r$  are the natural frequency and modal damping for mode  $r$  and  $\Theta_r(t)$

the modal force, is the projection of the aerodynamic load vector  $F(t)$  onto the mode shape vector  $\phi_r$ . This can be expressed as:

$$\Theta_r(t) = \sum_{j=1}^{nodes} \phi_{rj}(\Delta A_j n_j) p_j(t) \quad (3.11)$$

where  $j$  is the node index,  $\Delta A_j$  is the blade surface element area associated with node  $j$ ,  $n$  is the normal unit vector on the blade's surface and  $p(t)$  is the vector of pressures.

In this form the aeroelastic equation of motion can be solved; once the modal force is calculated, that represents the strength of the unsteady excitation force in a particular mode of vibration, can be expressed in the frequency domain by Fourier analysis in order to separate the signal into discrete harmonics. A Fourier transform of the time-varying force will give the amplitude of the unsteady force associated with the corresponding mode of vibration. At the node that exhibits the highest displacement, the maximum resonant amplitude for a given mode  $r$ , is calculated using Equation 3.12:

$$X_{max} = \frac{AQ\Phi_{max}}{\omega_r^2} \quad (3.12)$$

where  $A$  is the amplitude of the modal force resulting from the Fourier transform,  $\Phi_{max}$  and  $\omega_r$  is the value obtained for the maximum modal displacement and the corresponding natural frequency respectively, resulting from the modal analysis, and  $Q$  is the damping factor representing the sum of aerodynamic and structural damping. If the forced response analysis is conducted in coupled way, the aerodynamic damping is computed inherently during the computation. In the current work uncoupled method is employed considering the unsteady flow and the blade motion separately. In that case the aerodynamic damping could be calculated from a separate flutter analysis while the specification of the structural part of  $Q$  in this study is obtained from published literature.

### 3.3 Test Case

The Siemens 5.2 MW SGT-100-1S turbine is a two-stage HP turbine with a non-integer stator-rotor count ratio of 2:3.05 and 2.6:3.05 and a design rotational speed of 17,500 rpm. In Figure 3.3 a view of the annulus line and the blade locations within the throughflow model are displayed with the location of the first rotor domain shown with blue colour, on which a mesh independence study is carried out next. A sample of the computational grid of the first stator is shown in Figure 3.4 in the radial and blade-to-blade direction.

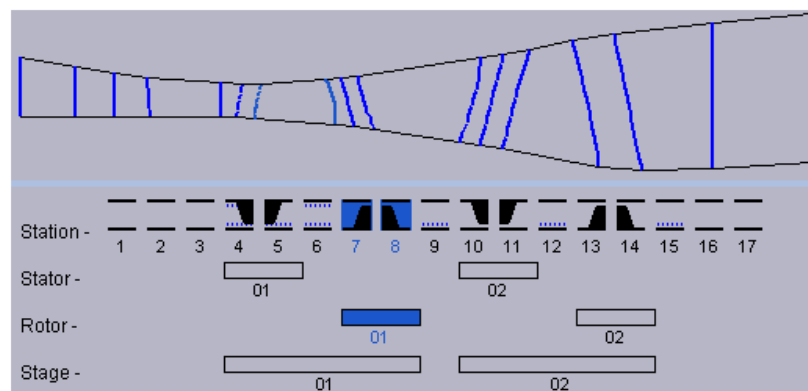
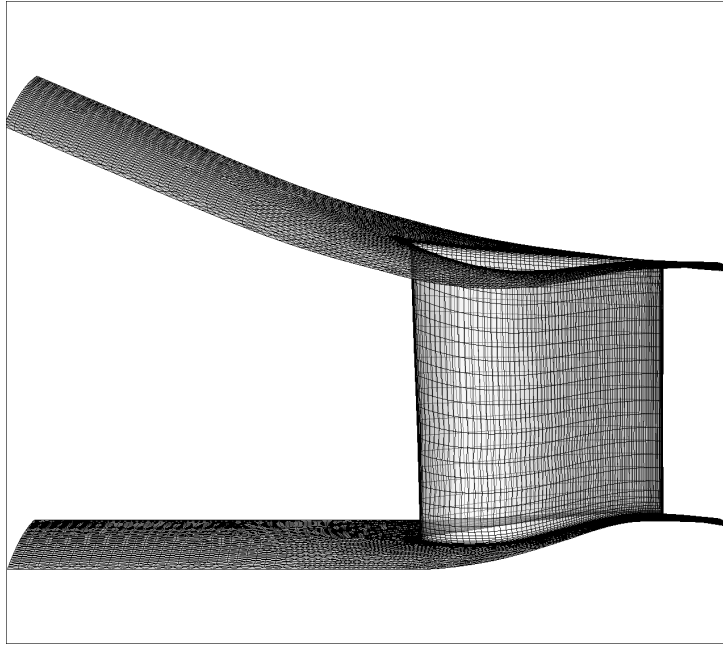
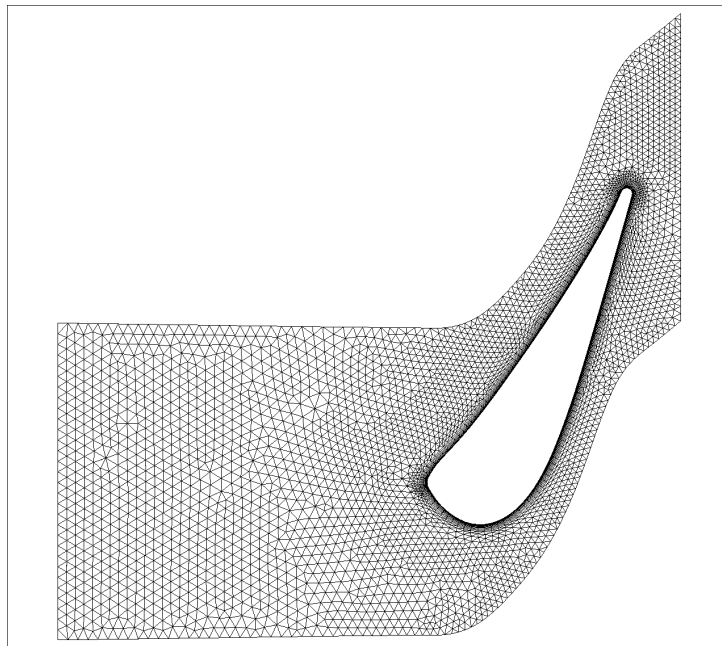


Figure 3.3: Turbine annulus

The boundary conditions for the single bladerow 3D steady flow simulations were defined based on the throughflow model provided by Siemens. The steady state analysis, that can be then used as initial condition for the unsteady simulation, is based on the mixing plane approach assuming the flow to be mixed out at the mixing plane before entering the next bladerow. The steady state analysis was carried out on an 800,000 point mesh using all the four bladerows and convergence to steady state conditions was achieved after about 2000 time steps. The second and more realistic type of multi-bladerow CFD methods applied to calculate the unsteady flow field into the machine, is based on the sliding planes approach [93]. During the unsteady procedure the interface between the bladerows is treated as a sliding boundary and flow data are exchanged between the two non-overlapping meshes that move relative to each other, rescaling the pitch/chord ratio of the rotor blade row. Such analysis is applied for all the hot streaks simulation and discussed in the next chapters.

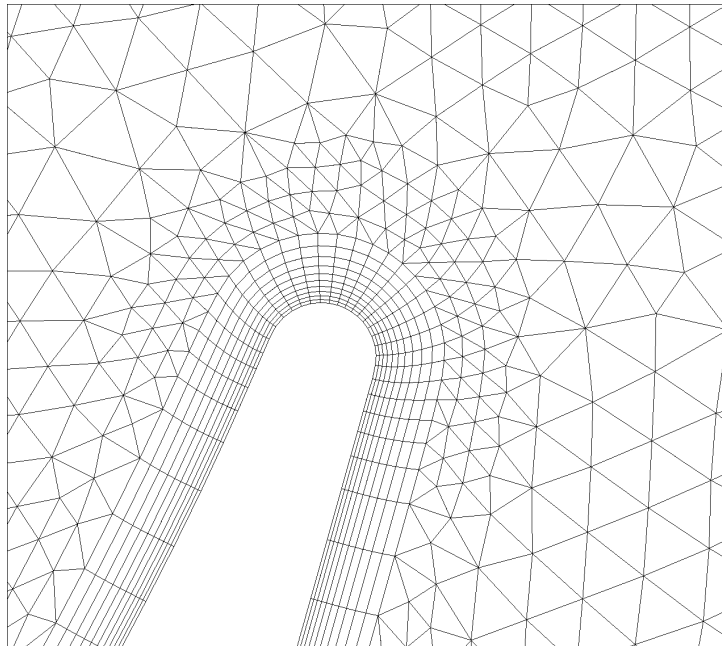


(a) Stator blade



(b) Mid span

A distributed source point based cooling model was used to inject 7% coolant flow of the turbine inlet mass flow rate into the main flow from the trailing edge region of the first stator. In order to simulate the cooling injection the applied local source term method uses a uniformly distributed source term treatment which mimic the behaviour of coolant injectors. The source terms are applied as a patch in the area corresponding to the cooling holes [94] as shown in Figure 3.5 for three different mesh densities.



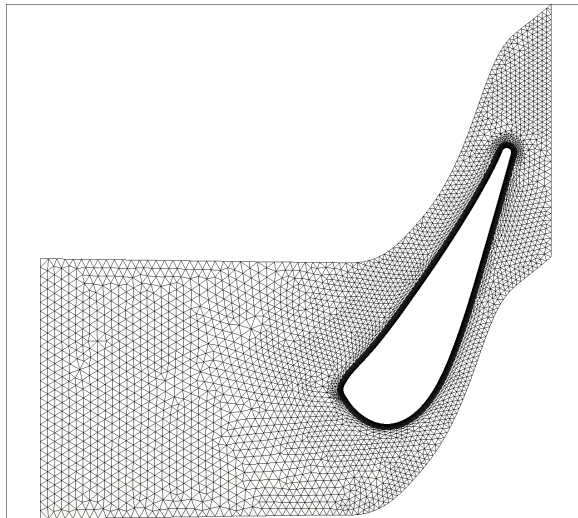
(c) Trailing edge

Figure 3.4: Computational grid for 1<sup>st</sup> stator blade

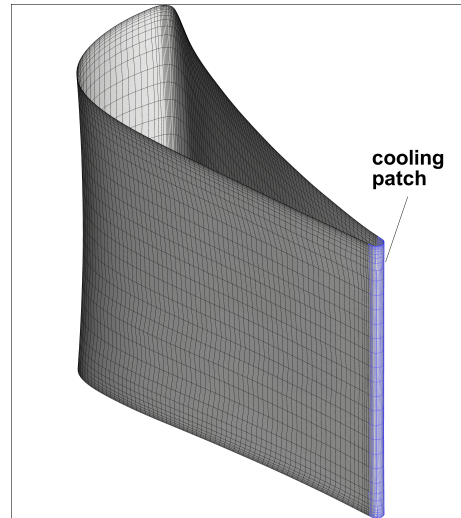
A leakage flow consisting of about 4.5% of the mass flow rate was included in the hub and tip region of the first rotor domain, downstream of the blade. A more accurate method to simulate the cooling flows would consider a full meshing approach where the cooling holes are included in the computational domain. However, the increased computational cost, due to the high number of points, along with the meshing process, which can be time-consuming, led to the choice of the local source term method which has been proved to provide adequate results for complex 3D geometries [95].

### 3.3.1 Grid Independence Study

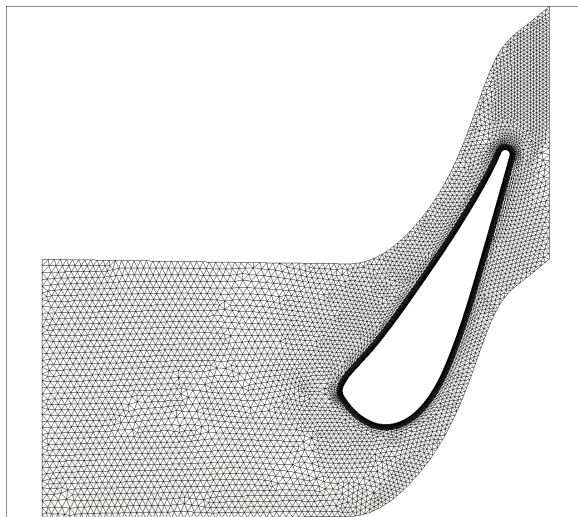
In order to investigate the grid independence on the numerical solution, a grid dependency study was conducted using three different grids for the first of the two stages and results are presented for Rotor 1, at design point. Starting from a relatively coarse grid the number of control volumes has been gradually increased for each type of grid in both blade-to-blade and radial direction.



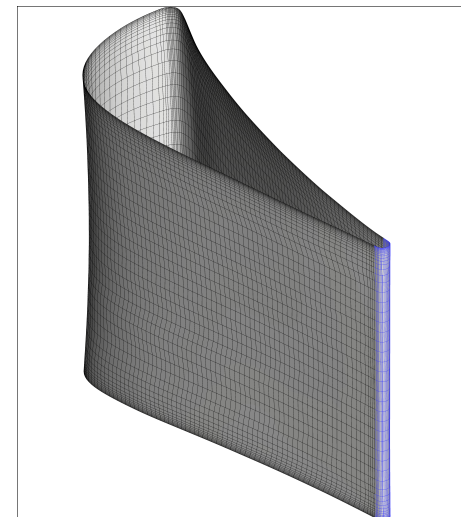
(a) Coarse mesh - Hub



(b) Coarse mesh - 35 radial layers



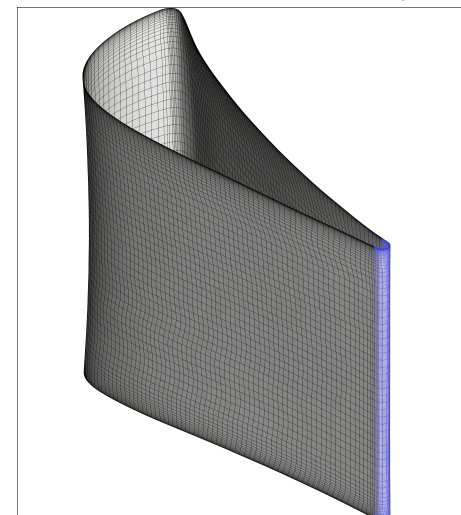
(c) Medium mesh - Hub



(d) Medium mesh - 50 radial layers



(e) Fine mesh - Hub



(f) Fine mesh - 70 radial layers

Figure 3.5: Computational domain for 1<sup>st</sup> stator blade at hub

The two-stage mixing plane simulation for three different grids gives the grid independent solution that will be used as initial case for the unsteady simulation. In these 3D steady state simulations two mesh refinements are presented compared to the coarse grid. An example of the three grids used to discretise the first stator blade on the blade-to-blade plane is shown in Figure 3.5. The total number of points corresponds to 200k, 400k and 800k for the coarse, the medium and the fine grid, respectively. All three simulations use the same initial conditions based on the throughflow model.

## Results

The results presented in that section refer to the first HP turbine stage where the coolant model has been implemented. Table 3.2 presents the outlet normalised average values for the three grids at the exit plane of the first rotor row (Station 9 in Figure 3.3), showing an overall good agreement between the three cases. The normalisation is based on the corresponding inlet mass averaged values for the current turbine.

Case	No. of points	Radial levels	$P_{o,out}/P_{av}$	$T_{o,out}/T_{av}$	$\dot{m}_{out}$ [kg/s]
Coarse mesh	200k	35	0.9811	0.563	1.07
Medium mesh	400k	50	0.9818	0.569	1.072
Fine mesh	800k	70	0.9821	0.571	1.078

Table 3.1: Grid independence study - Average inlet-outlet steady state results

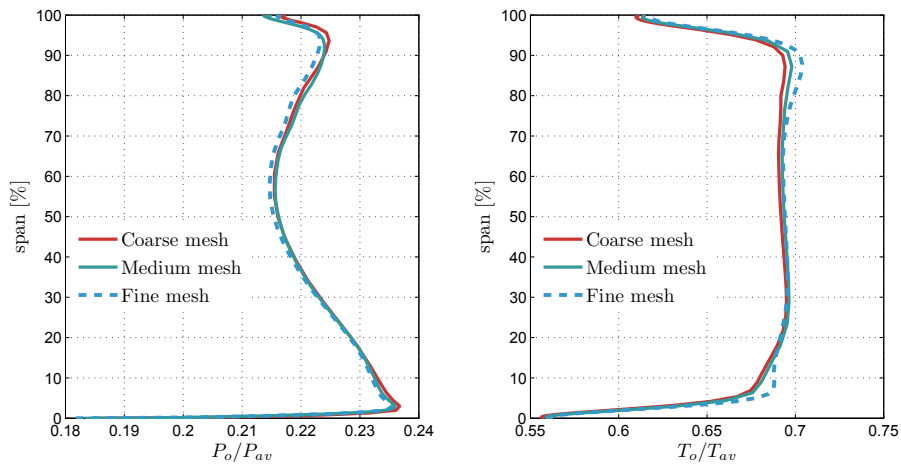


Figure 3.6: Grid independence study - normalised stagnation pressure and temperature radial profiles at  $R1_{ex}$  domain

In Figure 3.6 the radial profile of the normalised total pressure and temperature is shown for the outlet plane of the first stage. Due to industrial confidentiality the values displayed have been normalised based on the inlet average conditions. All three grids capture the same profile with an exception of the fine mesh on the area close to the hub and tip with regard to the temperature distribution. However, the differences that the three grid densities exhibit in the radial distribution can be considered negligible and hence, the 35 radial levels of discretisation are acceptable without further refinement in the radial direction.

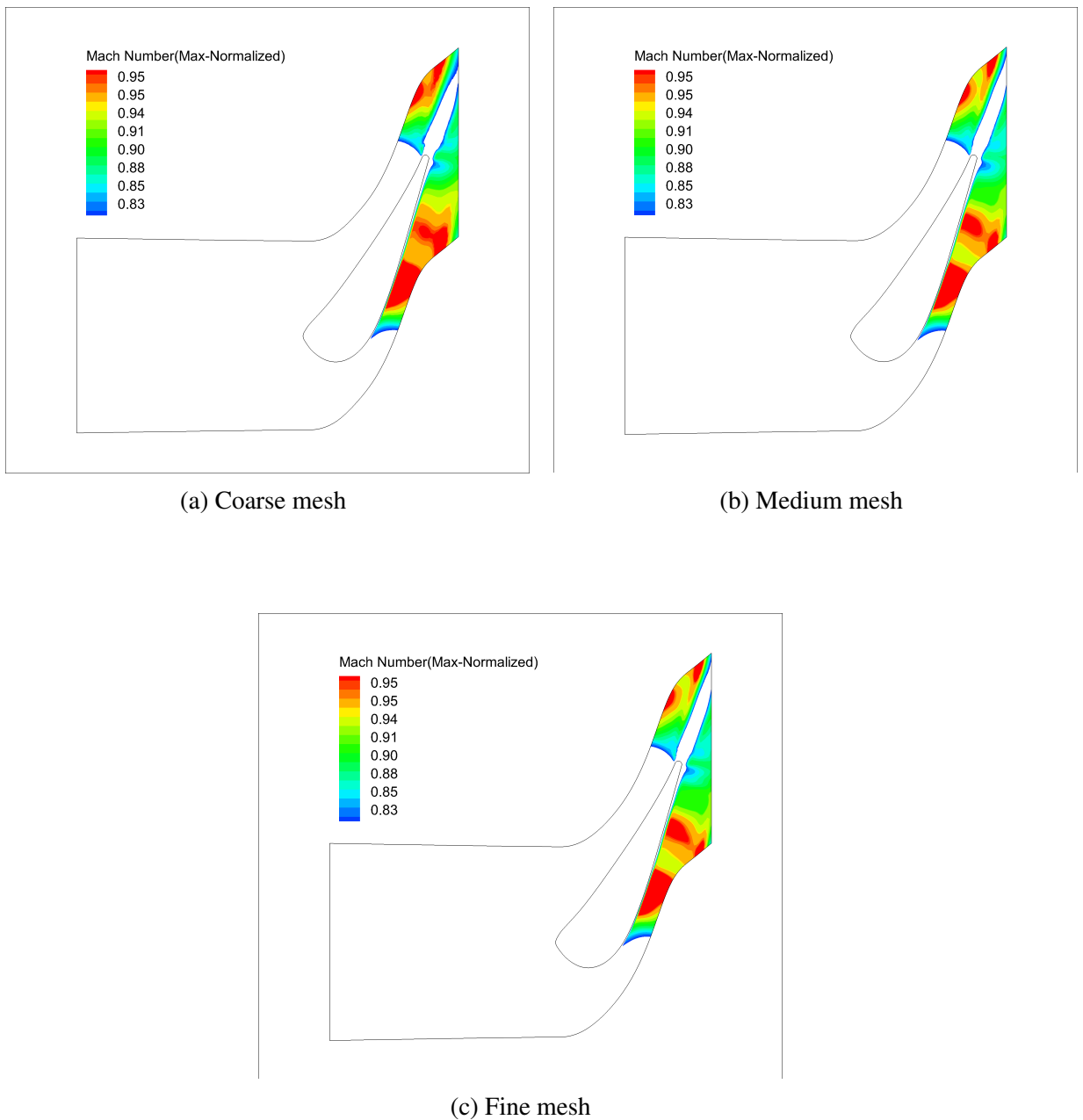


Figure 3.7: Mach number contours on 1<sup>st</sup> stator blade - midspan

Plots of the normalised Mach number contours are shown in Figure 3.7 for the first stator at midspan. The two shocks, one on the suction side and one on the pressure side near the trailing edge have been captured for all the three grids. The mesh refinement leads to a slightly more distinctive areas of high Mach numbers. However, the analysis that follows in the next sections is unsteady and analysis of this type is expected to demonstrate more accurate predictions of the unsteady flow features such as the shock waves. Thus, the fact that the coarse and medium mesh used for this steady state simulation capture the flow phenomena makes them a good compromise between computational cost and accuracy.

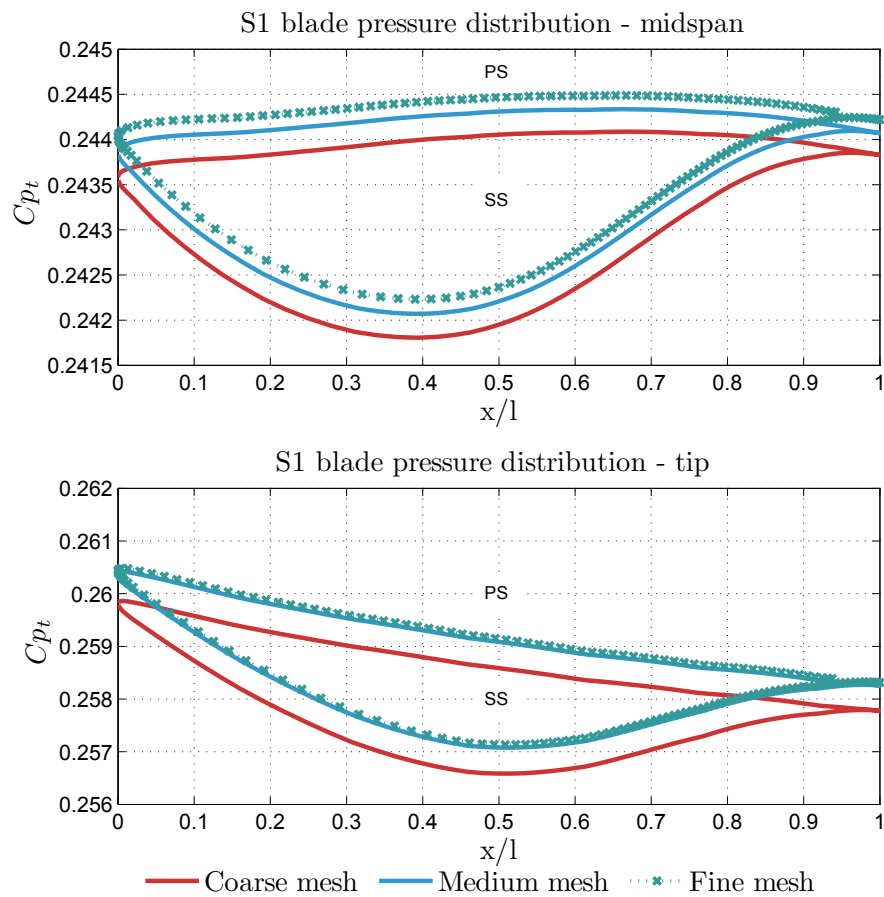


Figure 3.8: Pressure profile along S1 blades at hub and midspan

Figure 3.8 shows a comparison of the total pressure coefficient distribution along the first stator blade at tip and midspan for each mesh refinement. The total pressure coefficient used throughout the thesis is defined by Equation 3.13 and is used as indication

of pressure losses to provide comparable values against future experimental work.

$$Cp_t = \frac{P_t - P_{s,ex}}{P_{t,in} - P_{s,ex}} \quad (3.13)$$

Comparison of the medium and fine mesh results quite close match between the flow features along the blade surface; hence, a representative of the medium mesh will be used as a baseline for the unsteady calculations presented in the thesis.

### 3.3.2 Comparison Between 3D CFD Results and Through Flow Calculation

A comparison between the steady CFD results and the through flow model is presented in this section in order to ensure that the applied numerical tool produces accurate results. As discussed in the first section of this chapter, SURF offers two distinct methods for solving the flow equations, the steady and unsteady approach. The code has been validated against experimental data for unsteady aeroelasticity simulations [78, 88]. In addition to previous validation studies, a simple steady state analysis where averaged outlet values are compared against throughflow model results has been included here.

#### Results

For the purpose of the comparison between the two models, the inlet and outlet average values of mass flow rate, total pressure and temperature are presented in Table 3.2 showing very good agreement between the steady CFD analysis and the throughflow model.

	$\dot{m}_{in}$	$\dot{m}_{ex}$	$P_{o,in}$	$P_{o,ex}$	$T_{o,in}$	$T_{o,ex}$
Throughflow model	1	1.127	1	0.786	1	0.56
CFD	1.01	1.13	1	0.771	1.002	0.57

Table 3.2: Average inlet-outlet results - throughflow model vs. CFD mixing planes

A comparison of stagnation pressure and temperature radial distributions is shown in Figure 3.9 at the exit plane of the HP turbine (station 17 in Figure 3.3). The results show good agreement with the throughflow model in terms of temperature and are in a fair agreement in terms of pressure between 10% and 90% span, before and after which the pressure difference increases. That difference is not unexpected as throughflow calculations do not capture the secondary and tip leakage flows near the endwalls. The temperature profile is of high importance as it seems to be captured very well and the results appear to be compatible with the data provided by the industry confirming the validity of the coolant injection model which has been incorporated into the code for the purposes of the current work.

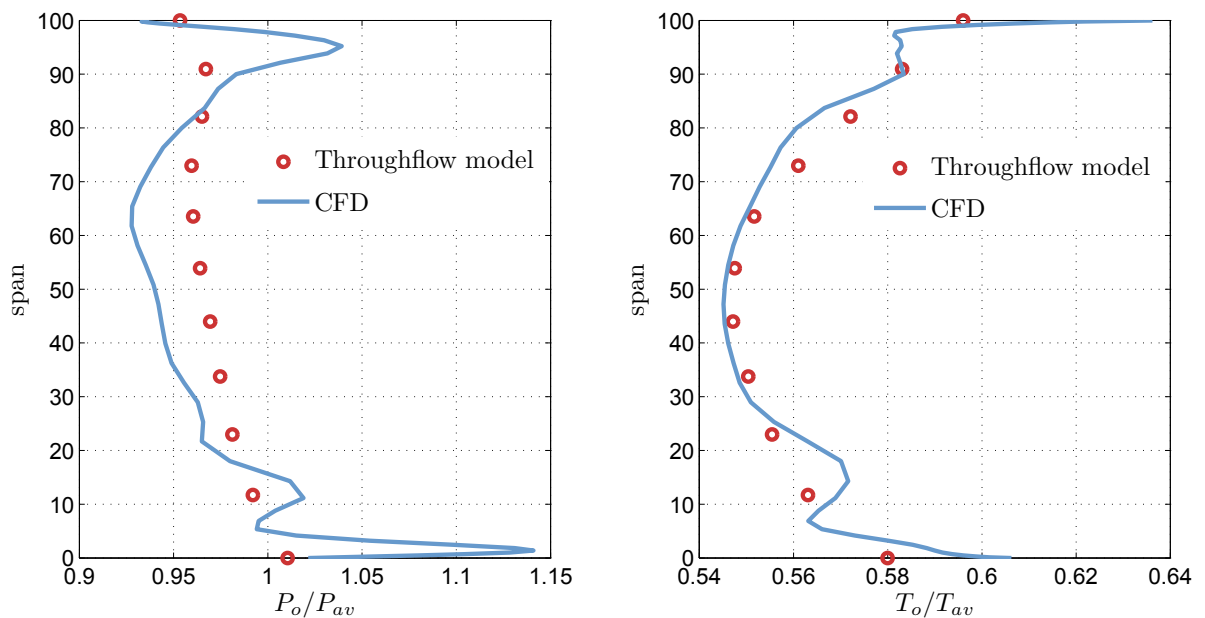


Figure 3.9: Comparison between throughflow model and CFD steady state results at  $R2_{ex}$  domain

### 3.3.3 Grid Independence study - Unsteady 3D CFD simulation with periodic boundaries

In order to get confidence on the unsteady simulations a mesh independence study was performed for the coarse and medium mesh densities, using scaling methods for the first turbine stage. A simplified model consisting of 4 stator and 6 rotor blades was used for the purposes of evaluation of the mesh density. A simple non-uniform

temperature profile was applied at the turbine inlet providing variations only in the circumferential direction. The temperature ratio of the maximum over the average inlet value corresponds to 1.12. Figure 3.10 shows the model of the first stage, including the inlet stagnation temperature profile and the cooling patches used for stator and rotor blades coolant. As mentioned above, a sourced point based cooling model was used to inject coolant into the main flow from the first stator TE and the first rotor hub and tip at the temperature of 672.1 K. The total amount of coolant corresponds to 11.4% of the turbine inlet mass flow rate.

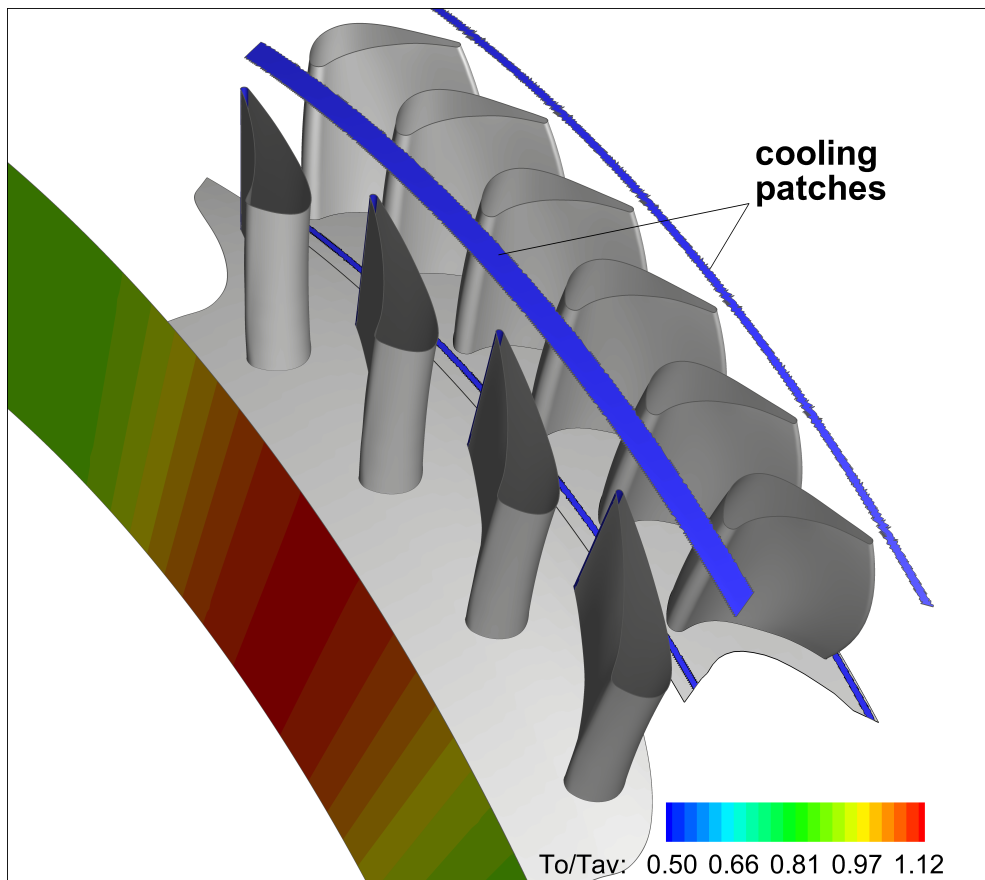


Figure 3.10: Simplified model of the first turbine stage with periodic boundaries

The simulated inlet temperature profile consists of ten circumferential temperature variations over the entire inlet cross-section and was simulated through a trigonometric function (Equation 4.2) in order to get a sinusoidal profile enforcing periodicity.

$$T_o(\theta) = T_o(1 + A * \sin(ND * \theta)) \quad (3.14)$$

where  $T_o$  is the specified average total temperature for a given spanwise location,  $\theta$  is the circumferential coordinate,  $A$  corresponds to the amplitude and the Nodal Diameter (ND) corresponds to the number of distortions applied, which are ten in this case. A constant percentage of distortion was applied along the span and is equal to 0.012%. Figure 3.11 shows the inlet boundary conditions in normalised stagnation temperature values.

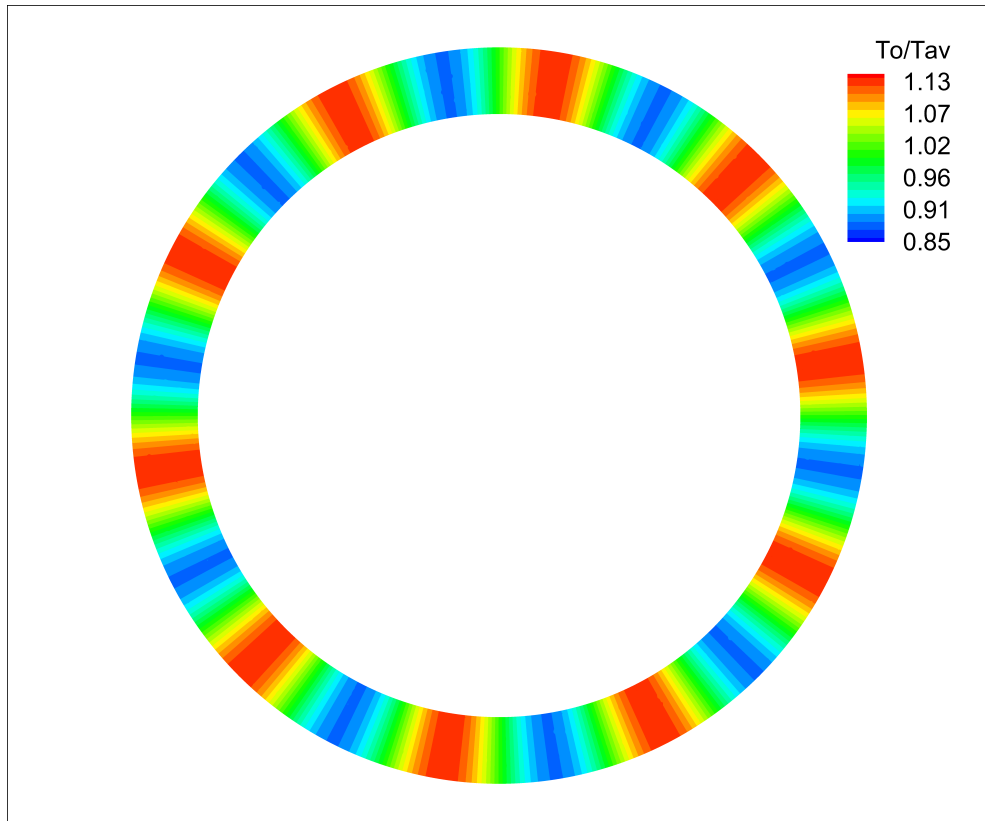
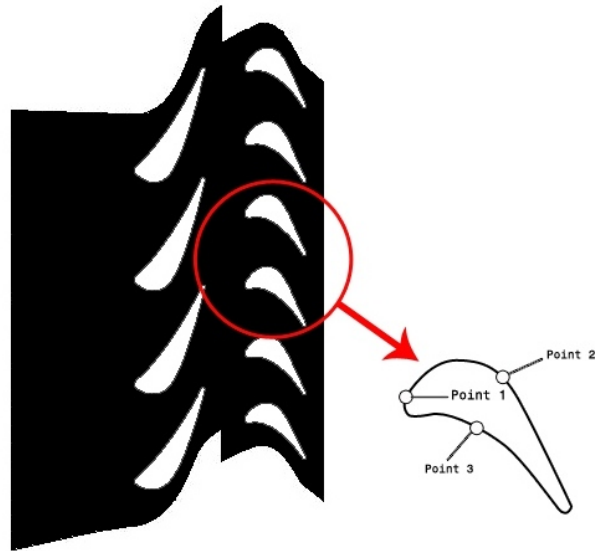


Figure 3.11: Normalised stagnation temperature profile at turbine inlet with circumferential variations

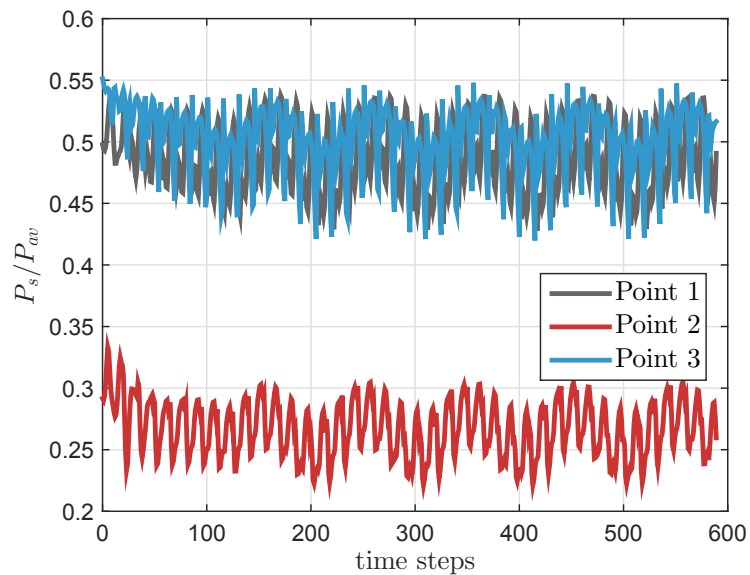
## Results

The steady state solution presented in the previous section of this chapter was used as initial condition for the unsteady CFD simulation. A considerably large number of 200 time steps was set as the rotor passes one stator passage. However, due to the high computational cost, a reduced time step number is preferred to be considered for the full annulus multi-bladerow simulations which are presented in the following chapters. In order to ensure convergence the variation of static pressure was recorded for three points on the rotor blade surface as shown in Figure 3.11 (a). The values of static

pressure have been normalised as previously, based on the average inlet conditions. As shown in Figure 3.12 (b) periodicity was reached after approximately 150 time steps. The simulation was performed in a serial environment for a total number of 2000 time steps that corresponds to a quarter of one full revolution.



(a) Schematic representation of the recorded points

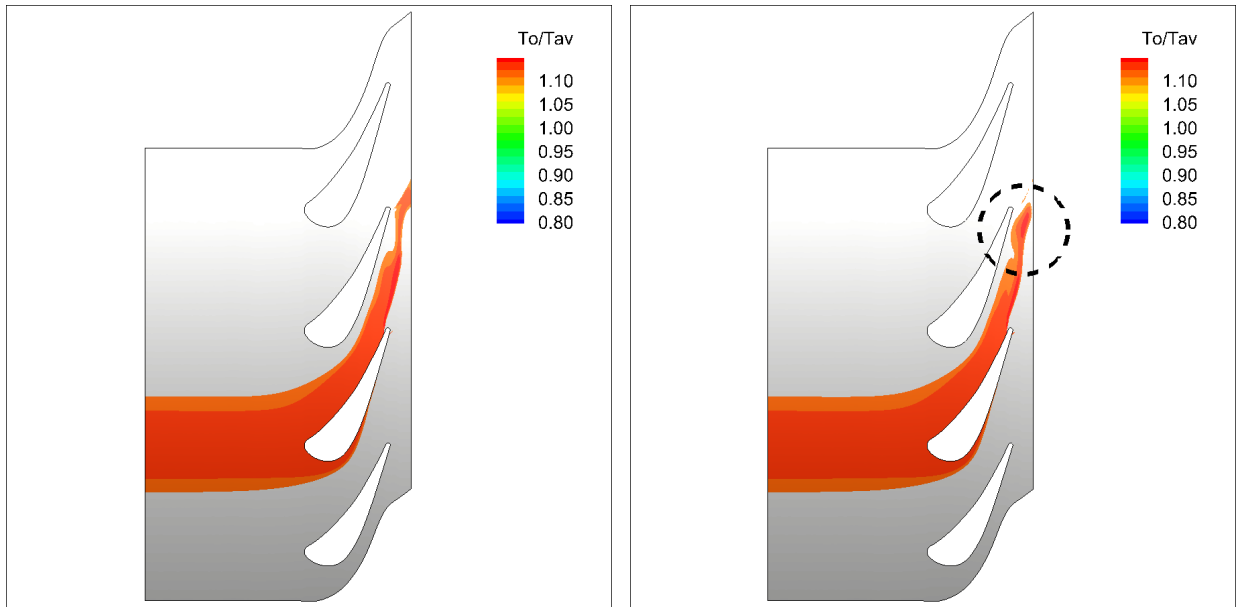


(b) Normalised static pressure variation monitored at LE, PS mid-chord, SS mid-chord

Figure 3.12: Recorded pressure variation at midspan of one first rotor blade

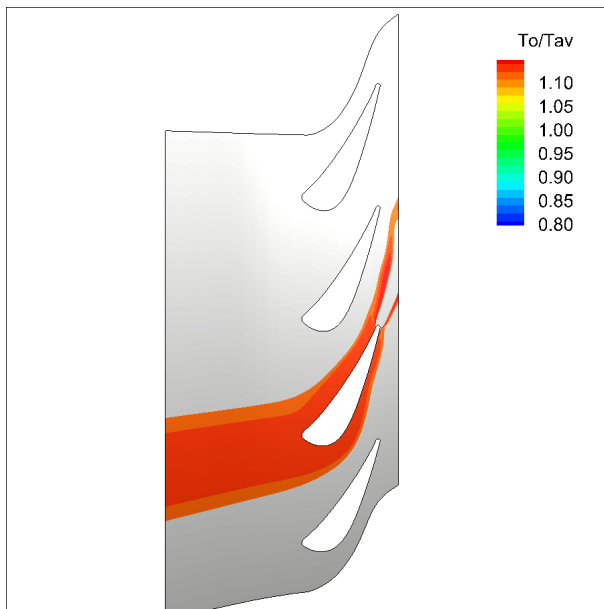
Figure 3.13 shows the instantaneous normalised stagnation temperature contours at

hub and tip of the first stator bladerow after 2000 time steps. The contours are plotted for values of  $T_o/T_{av}$  higher than 1.1 to identify the small variations due to the mesh density difference. Between the coarse and fine mesh small differences can be observed after the stator TE when the hot fluid interacts with the downstream bladerow, while not considerable differences are observed near the hub between the two grids.

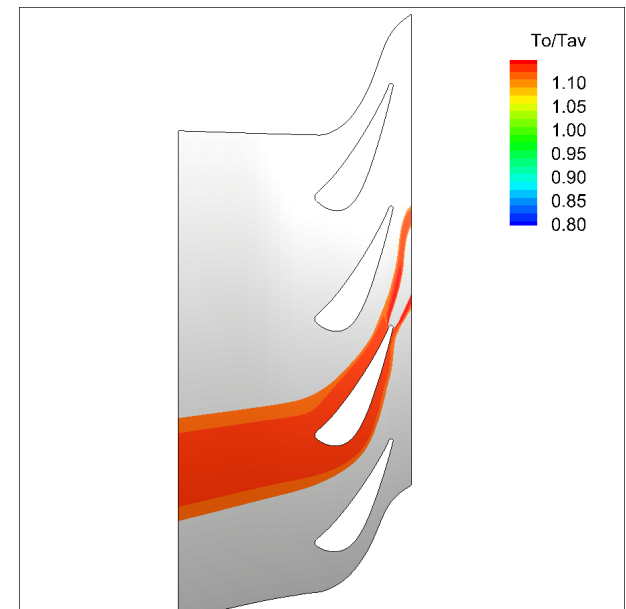


(a) Normalised stagnation temperature contours at stator hub - coarse mesh

(b) Normalised stagnation temperature contours at stator hub - medium mesh



(c) Normalised stagnation temperature contours at stator hub - coarse mesh

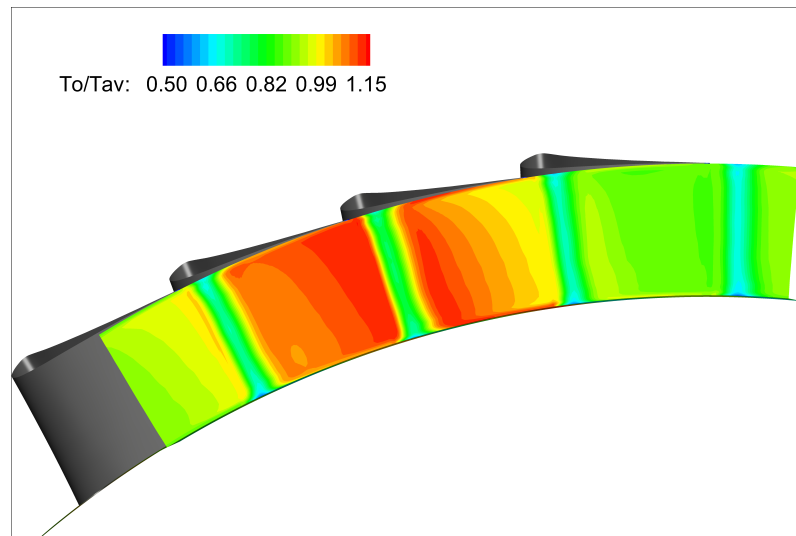


(d) Normalised stagnation temperature contours at stator hub - medium mesh

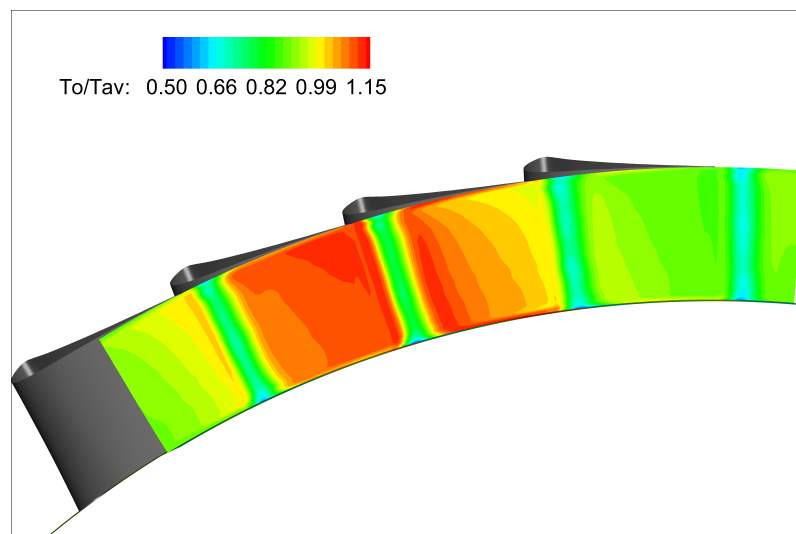
Figure 3.13: Instantaneous temperature contours at the exit plane of stator bladerow

At the outlet plane of the stationary bladerow the normalised stagnation temperature

contours are shown in Figure 3.14 for the same instant. Small variations in temperature distribution are observed for the peak temperature values with the coarse mesh resulting into a more uniform temperature distribution along the span and slightly higher magnitude. However, the differences are considered quite small to make the grid refinement necessary for the full annulus unsteady simulations which are presented in the next chapters.



(a) Normalised stagnation temperature contours at stator exit - coarse mesh



(b) Normalised stagnation temperature contours at stator exit - medium mesh

Figure 3.14: Instantaneous temperature contours at the exit plane of stator bladerow

## 3.4 Summary

In this chapter an overview of the methodology and the CFD code that is used for the analysis presented in this thesis has been given followed by a test case. Based on the steady state results of the grid verification in Section 3.3.1, a medium grid density with 35 radial levels of discretisation has been chosen to ensure grid independent solution while keeping a minimum of the computational resources. A comparison between the steady CFD results and the throughflow model has also been presented in order to ensure that the applied numerical tool produces accurate results. In addition, a test case is presented using unsteady simulations where circumferentially non-uniform stagnation temperature profile is applied at the turbine inlet for a scaled geometry of the first turbine stage. The results have been presented for two mesh densities, the coarse and medium, showing not significant variations in terms of the hot flow distribution through the stator bladerow.

# **Chapter 4**

## **Hot Streaks Migration and Aerodynamic Effects in 2-Stage HP Axial Turbine**

### **4.1 Introduction**

The full annulus unsteady CFD analysis of the hot streaks aerodynamics in the SGT-300-2S two-stage turbine is presented in this chapter. In section 4.3.1 the propagation of hot streaks on the blade-to-blade direction is discussed separately trying to identify the individual mechanisms of the hot streaks kinematics. In section 4.3.2 the combined effects of hot streaks and stator coolant injection are taken into account to describe the hot streak migration and interaction with the flow. Emphasis is given on the shape and the spanwise location of the hot streak with respect to the impact on the hot flow propagation. Applying the classic hot streak migration theory, the importance of simulating realistic hot streak shapes is underlined by the comparison of standard sinusoidal and combustor representative hot streak profiles. Highlighting the significance of advanced CFD methods the analysis provides a better understanding of the hot streak migration pattern.

## 4.2 Hot Streaks Cases Preparation

### 4.2.1 HP Turbine Overview

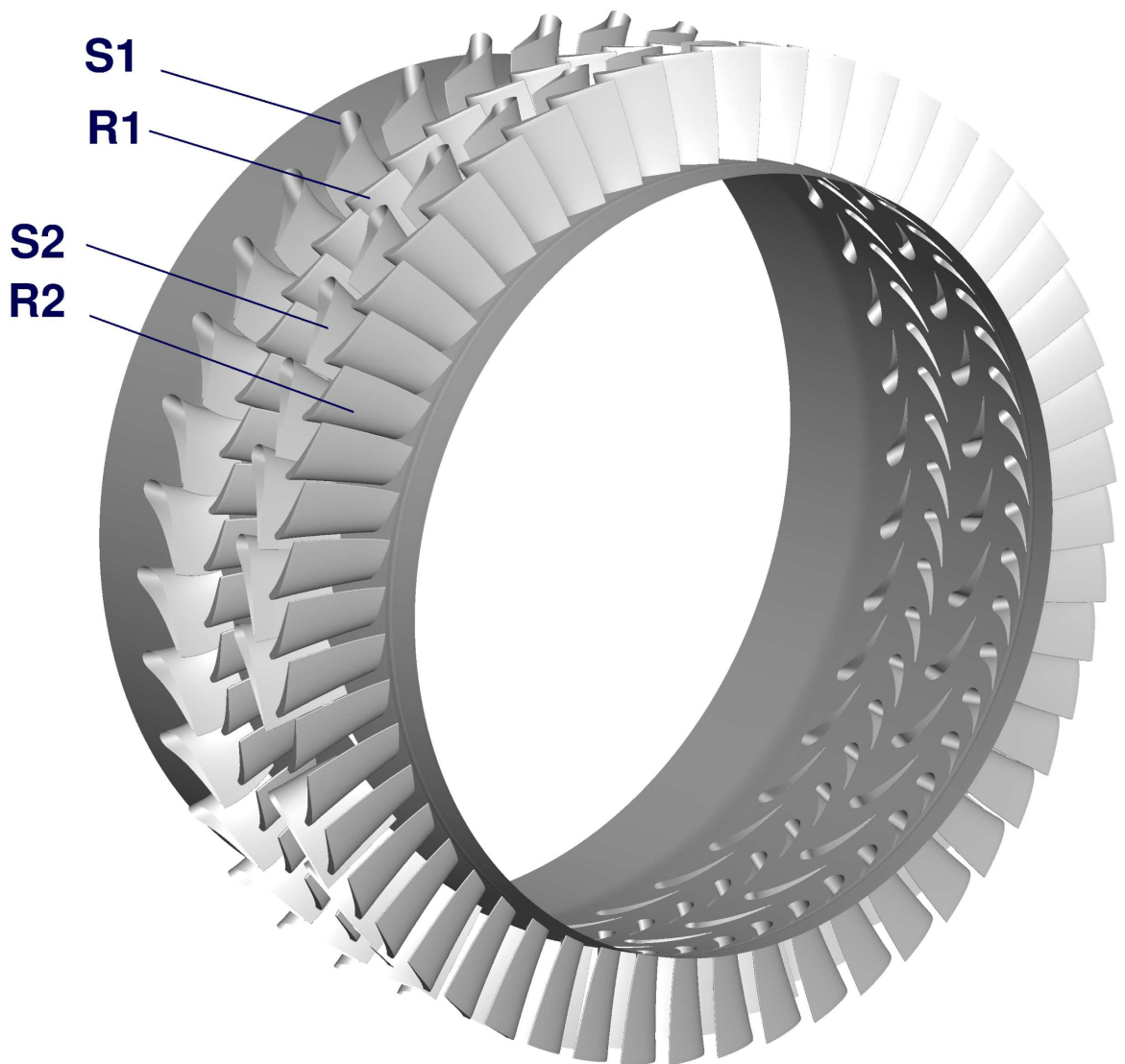
A two-stage axial turbine is used for this study, the main design parameters of which are given in Table 4.1 in normalised form due to industrial confidentiality as has been mentioned in Chapter 3. The geometry and operating parameters were provided by Siemens Industrial Turbomachinery Ltd. As there is no common integer factor between the number of stator and rotor blades, a common approach in order to perform computationally cheap unsteady simulations in a case like this, would be to apply a geometrical scaling method changing the solidity of one of the bladerows. Due to the significant computational cost even most recent unsteady simulations still use scaled geometries in order to reduce computational time. However, this method has been found to give some discrepancies in the prediction of unsteady flow features through a turbine and further verification of the results would be necessary[96, 97, 77]. Thus, this approximation is avoided here by running 3D CFD simulations in a multi-bladerow whole-annulus environment. Both stages have been simulated with the real blade configuration in order to investigate whether the hot gases are convected into the second stator/rotor passage and how they affect the aerodynamics throughout the turbine.

Parameter	Value
S1/R1	1/1.5
S2/R2	0.95/1.5
Rotational speed [rpm]	13996
$P_{s,out}/P_{o,in}$	0.262

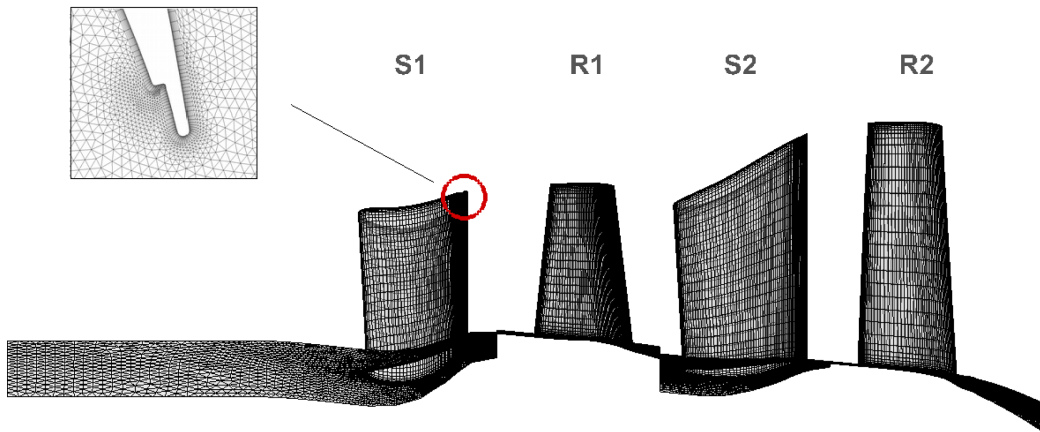
Table 4.1: Dataset overview and normalised flow conditions

The computational grid for the whole turbine contained about 30 million points and the number of 80 physical time steps was set per rotor blade passing. That means 2720 time steps are needed for one full revolution for the current turbine. The results presented in this chapter correspond to two full revolutions with the total wall clock time of about 5 days for a simulation performed in a parallel environment of 48 Intel

Xeon cores of 1.95 GHz. In order to obtain accurate predictions of time-dependent flows it is essential to find a combination of an appropriate grid and time step. A time step sensitivity study was performed for two different values of 80 and 200 time steps for a simple unsteady simulation with inlet temperature gradients, as shown in Section 3.3.3. The final choice of 80 time step was found to be high enough to describe the hot streak aerodynamics, as well as the forced response problem. Based on the literature, a common choice of 40 time steps per blade passing has been found to describe the hot streak migration [98, 85].



(a) Full annulus two-stage SGT-300 turbine geometry



(b) Two-stage blade passage computational grid

Figure 4.1: Two-stage computational grid and boundaries nomenclature

For the current simulations all the airfoils were cooled using cooling patches at discrete locations. The coolant properties are presented in Table 4.2 in percentages of the inlet mass flow rate. Figure 4.1 shows the two-stage HP turbine geometry as well as the computational grid of one blade passage. In Figure 4.1 (b) the grid around the TE slot that is used to simulate the stator TE coolant injection is also shown in detail. Six hot streaks have been modelled circumferentially for the full annulus analysis; the details are presented in the following section where the boundary conditions are discussed further.

Bladerow	Coolant Injection [%]
S1	7.114
R1	4.016
S2	2.540
R2	1.621

Table 4.2: Percentage of coolant injection per bladerow with respect to turbine inlet mass flow rate

## 4.2.2 Boundary Conditions

An objective of this work is to consider the contribution of the hot streak shape on the kinematics of hot streaks propagation through the stages of a HP turbine. Hence, this chapter highlights the differences in hot streak propagation and the effects on turbine aerodynamics with respect to three different inlet temperature profiles, a uniform, a radial, and a profile consisting of six hot streaks circumferentially positioned corresponding to the six combustor burners. A common approach for hot streaks simulations is to maintain the stagnation pressure,  $P_o$ , of the hot fluid the same as in the main flow to isolate the effects of hot streaks on the enhancement of secondary flow. Following that approach, the hot streaks have been modelled with the absence of total pressure gradients at the turbine inlet.

### Spanwise Temperature Variation

The two parameters with major influence on the propagation of hot streaks are the maximum over the average inlet temperature ratio and the hot streak shape that depends on the combustor design and fuel choice. Any variation in terms of hot streak shape and injection location is expected to produce some differences between the corresponding CFD results. This information is very limited in open literature because of the lack of such data and due to that wide variation in the inlet temperature profiles between engines. Thus, ideal shapes have been widely used in literature with identical circumferentially applied hot streaks; however, measured temperatures at the exit of combustors exhibit only approximately symmetric circumferential variations and non-identical hot streak shapes, with relatively cool regions at the hub and casing end walls [2].

For the turbine considered in this study the boundary conditions for the hot streak profiles were established based on two sets of traverse data provided by the industrial partner. Those sets consist of contour plots of total temperature values at different spanwise locations as shown in Figure 4.2. In the first case (Figure 4.2 (a)) a hot streak profile was provided with the peak temperature radially located at about 20% of the span from the hub endwall to the tip endwall. After further discussion on the first configuration (Figure 4.2 (a)) and interpretation of initial CFD results, an updated

temperature profile was provided by the industrial partner shown in Figure 4.2 (b). Based on the data shown in Figure 4.2 (b) another hot streak profile was simulated, the so-called baseline, with a peak temperature located between 40-50% spanwise. For the second set of data, additional total temperature values were provided at different radial locations along with the contour plot. The extra information allowed a more realistic simulation of the hot streak profile compared to the first set of data.

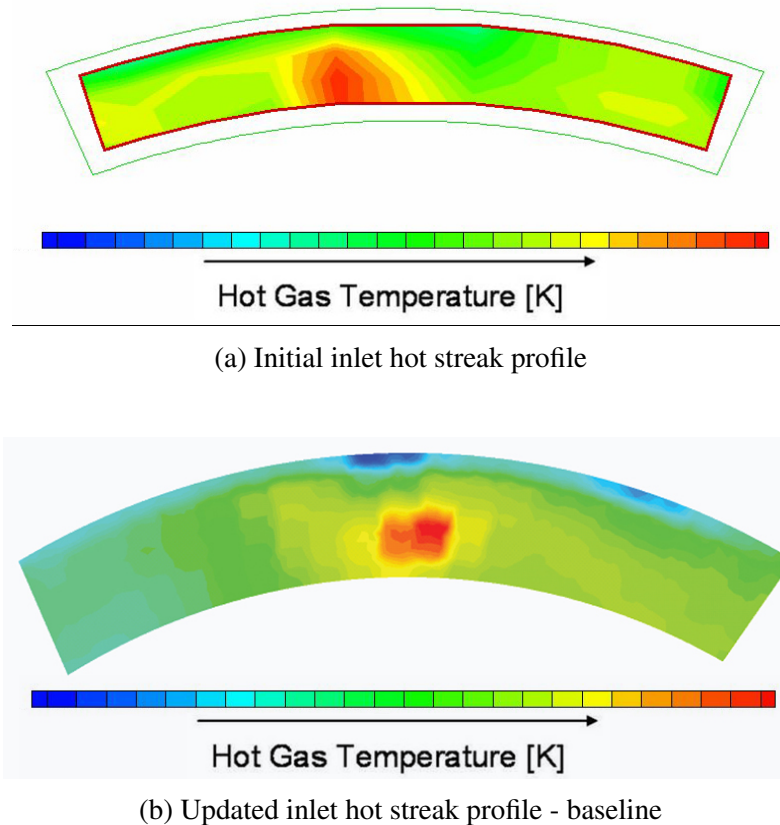


Figure 4.2: Inlet temperature contour plots provided by Siemens

Two additional cases were simulated for the purposes of this study, one with a purely radial variation of the temperature profile and one with uniform inlet temperature boundary conditions. Those are used for comparative purposes against the simulated hot streak profiles as they represent the common approach used in industry in which temperature non-uniformities in both radial and circumferential direction are not usually taken into account during simulations. Figure 4.3 summarises the circumferentially averaged normalised radial temperature profile of the four different inlet boundary conditions used for the current turbine where the uniform temperature profile corresponds to average temperature of the baseline hot streak profile. Throughout

the analysis different cases are compared on a non-dimensionalised basis where the normalised values are divided over the corresponding mass averaged stagnation values at turbine inlet.

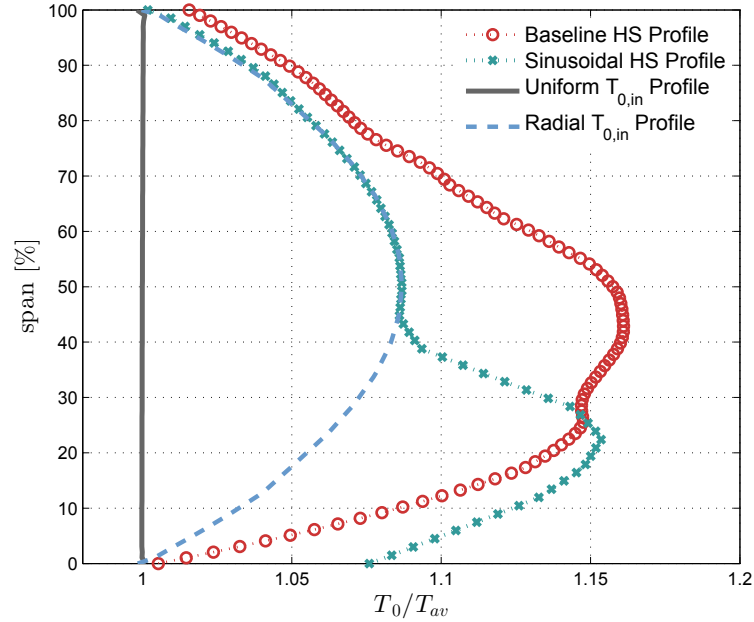


Figure 4.3: Normalised circumferentially averaged radial temperature profiles at turbine inlet

### Circumferential Temperature Variation

Regarding the circumferential temperature variation over the entire inlet cross-section, a sinusoidal profile was used to simulate the first set of data (Figure 4.2 (a)), enforcing periodicity through a trigonometric function (Equation 3.14), with one hot streak periodicity having  $30^\circ$  circumferential angle same as in Chapter 3. The simulated profile (Figure 4.5 (a)) consists of six elliptical and identical between each other hot streaks. The percentages of inlet distortion in the spanwise direction, and hence the amplitude, are calculated based on the definition of the Overall Temperature Distribution Factor (OTDF) [28] that was provided by the industrial partner to be about 20%. The OTDF is used as measure of the variation of the hottest gas streak from the mean temperature and is given by Equation 4.1:

$$OTDF = \frac{T_{max} - T_{av,area}}{\Delta T_{comb}} \quad (4.1)$$

where  $T_{av,area}$  is the mean temperature,  $T_{max}$  is the maximum local temperature at combustor outlet and  $\Delta T_{comb}$  is the temperature rise across the combustor. By specifying the value of OTDF, the average combustor and turbine inlet temperature the value of maximum temperature was determined based on which the percentage of temperature distortion was estimated. Table 4.3 shows the percentage of distortion applied along the span.

Span [%]	A [%]
0	0.0693
12	0.0848
18	0.0975
25	0.0768
35	0.0378
40	0.0005

Table 4.3: Percentage of temperature distortion applied for the sinusoidal profile

In order to represent more realistic hot streak profiles additional total temperature values were provided for the second and baseline case. More concentrated and non-identical hot streak shapes were simulated with the percentage of distortion slightly varying between each hot streak (Figure 4.5 (b), 4.6) such that the hot streak profile also has circumferential variation.

Regarding the baseline hot streak profile, a MATLAB script was used to produce the varying temperature values, where the input values are based on data provided by the manufacturer. The added benefit for the baseline configuration is that in a realistic turbine environment, hot streaks would exhibit both radial and circumferential variations. Such differences would affect the propagation of hot streaks through the turbine stages and their simulation would enhance the quality of the analysis and lead to a better understanding of the propagation mechanism under more realistic conditions than usually met in the literature.

The non-uniform inlet temperature profile in the circumferential direction is shown in Figure 4.4 to help illustrate the inlet conditions. The distribution is presented at 30% and 40% span for the sinusoidal and the baseline case, respectively, where peak temperature is set. The Fast Fourier Transformation (FFT) shows a clear dominance

of the six Engine Order (EO). The term Engine Order is used throughout this study to describe the amplitudes of the frequency components which are determined by the multiples of the rotational speed. In Figure 4.4 the presence of different EOs with lower amplitudes can also be noticed for the baseline profile, that is related to the random variations between the six hot streaks.

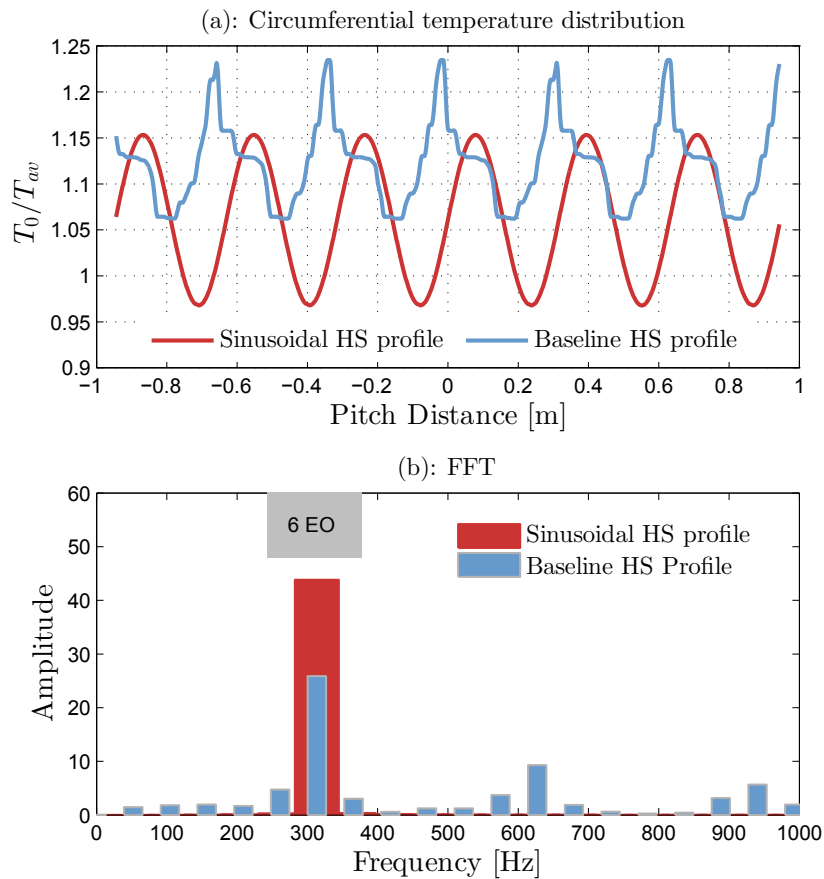


Figure 4.4: Circumferential temperature distribution and FFT at  $S1_{in}$  plane at the spanwise location of HS centre

Based on the temperature profile provided by the industrial partner the peak to average temperature ratio is close to 1.15 for the first case and 1.23 for the baseline one as shown in Figure 4.4. An accurate comparison between different hot streak shapes should be made using the same temperature ratio (peak to average temperature) and same hot area; however, in that case the temperature differences between the hot streak shapes are not noticeable, thus comparison between the two configurations is considered to be acceptable for the purposes of that study.

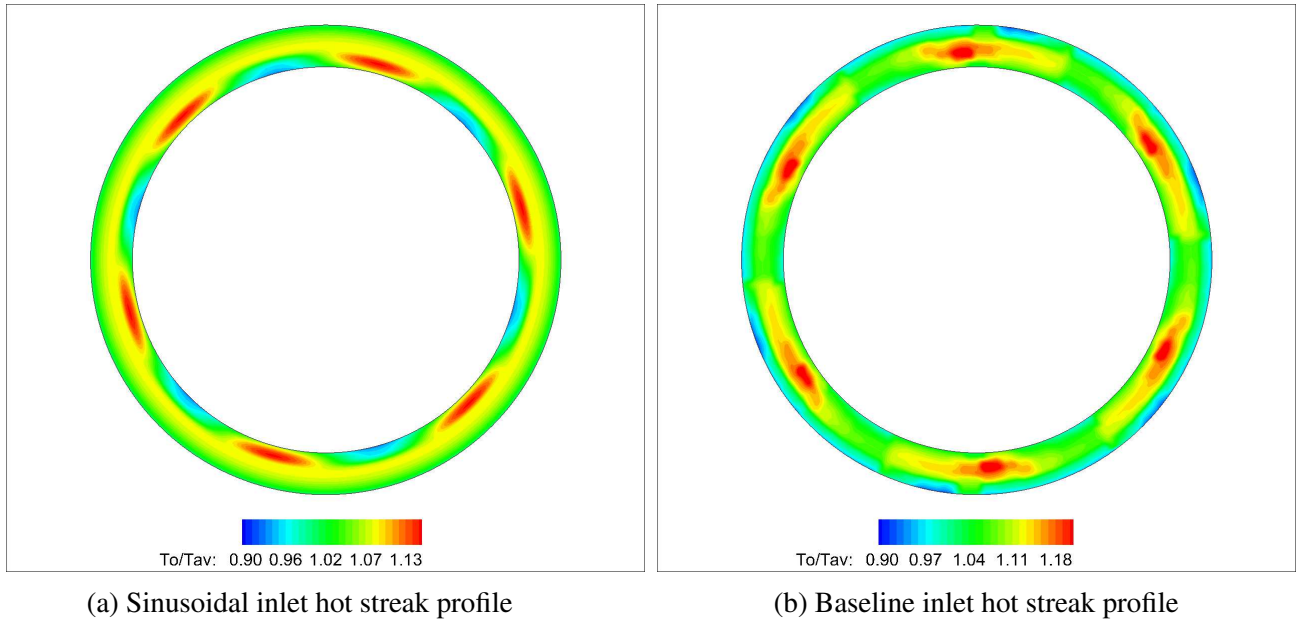


Figure 4.5: Normalised stagnation temperature contours at the inlet of the turbine - used as boundary conditions

After establishing the inlet temperature profiles the procedure is as follows:

- Applying uniform inlet stagnation temperature conditions in order to get a converged steady state solution that will be used as initial condition for the unsteady simulation.
- Generating the inlet boundary conditions as shown in Figure 4.5, with the sinusoidal inlet profile shown in Figure 4.5 (a) and baseline one shown in Figure 4.5 (b). Most engines in reality would exhibit some differences between the hot streaks, thus, in the second approach (baseline) small variations are randomly applied between each hot streak. An example of two hot streaks applied in the current analysis is shown in Figure 4.6, where variations on the temperature contours can be seen in radial and circumferential direction.
- Building the full annulus for each blade row and generate the unsteady solution for the whole machine by employing the hot streak boundary plane at the inlet to simulate the flow non-uniformities.

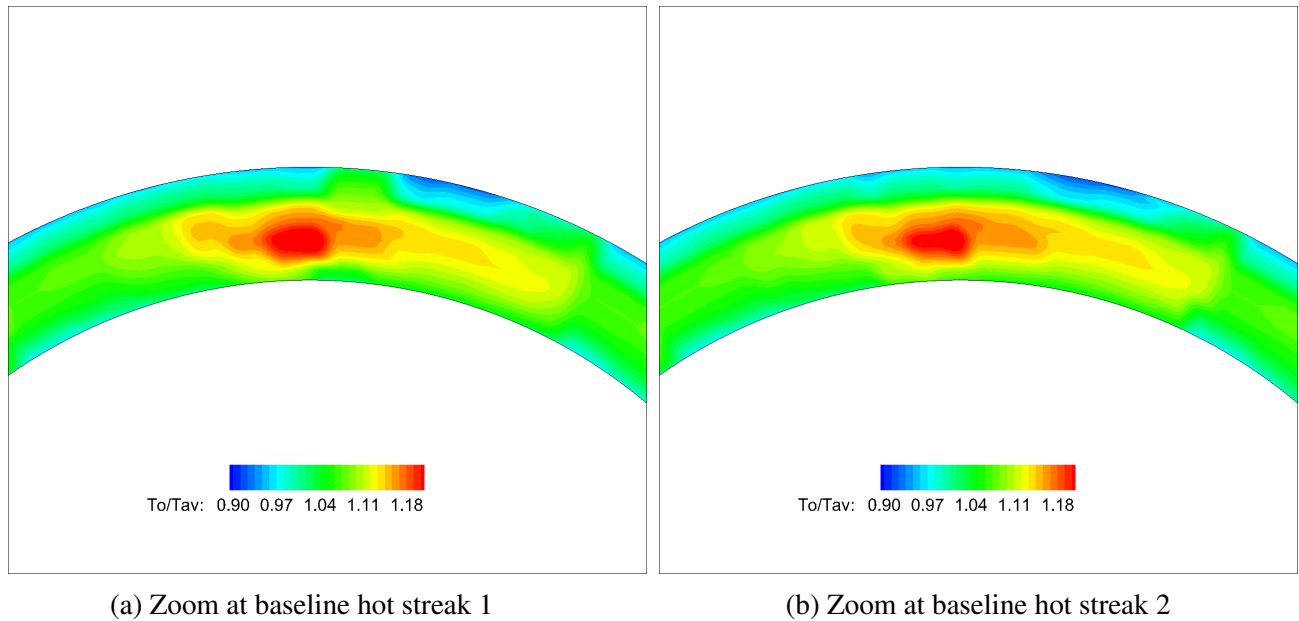


Figure 4.6: Normalised stagnation temperature contour plot of two non-identical simulated inlet hot streaks based on Figure 4.5 (b)

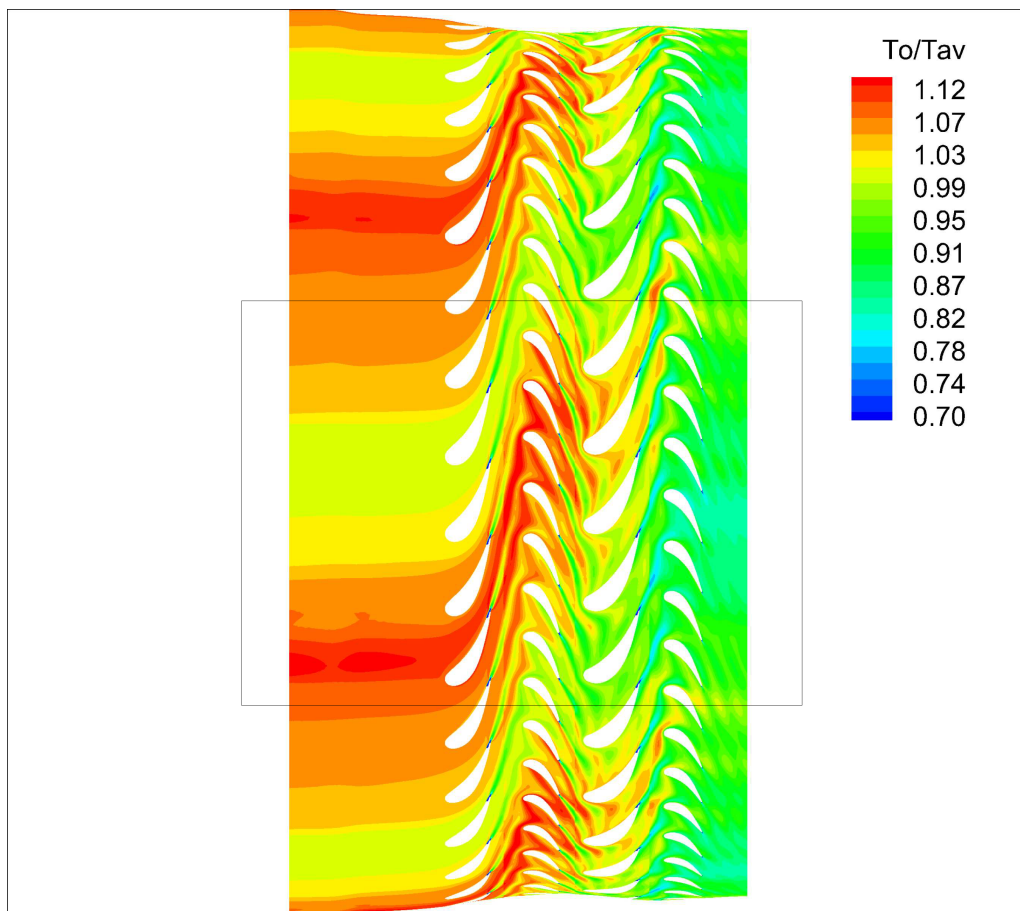
## 4.3 Unsteady Hot Flow Path Analysis - Results and Discussion

### 4.3.1 Hot Streak Migration in Blade-to-Blade Plane - Segregation Phenomenon

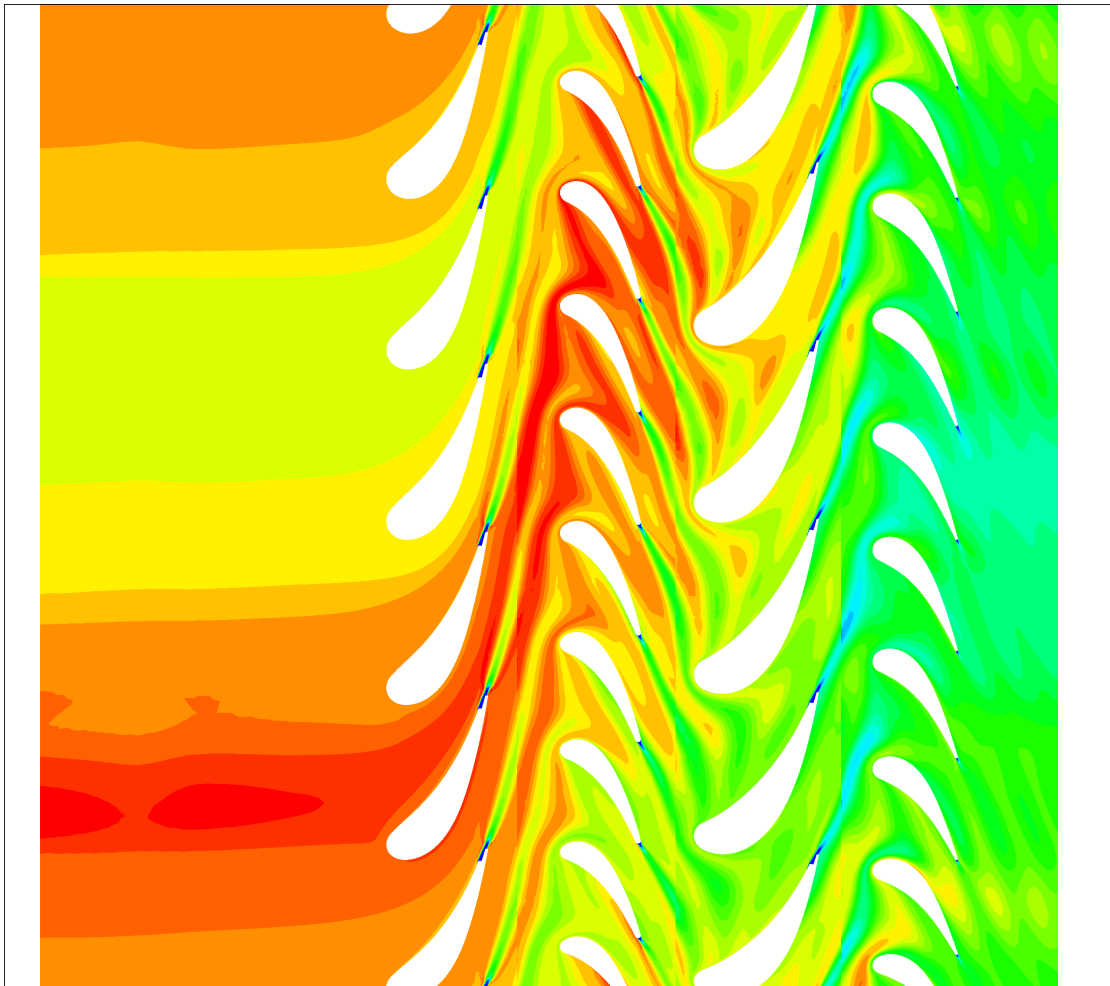
The migration pattern of the hot streaks into the turbine is characterised by 3D flow features. The discussion in this section starts with a 2D consideration in the circumferential and axial direction, followed by a complete 3D analysis, in order to provide an understanding of the distinct and combined effects of hot and cold flow accumulation through the turbine stages. In the blade-to-blade plane, the CFD analysis of the full annulus and multi-stage HP turbine describes the flow field based on the segregation effect which is one of the dominant mechanisms of the hot streak redistribution in axial direction [38] as has already been described in Chapter 2.2. The segregation effect describes how the difference in rotor relative velocity between the hot and cold fluid at stator exit, that is introduced by the hot streaks, results in the preferential heating of the first rotor blade PS. The mechanism is discussed in this section through the

interpretation of the unsteady CFD results for the baseline case.

In Figure 4.7 the normalised stagnation temperature contours are used to display the propagation of the hot fluid through the four bladerows at 40% span, that coincides with the inlet peak temperature spanwise location. A closer view of the hot flow path is shown in Figure 4.7 (b). The tendency of the hot fluid to accelerate towards the first rotor PS when leaving the first stationary frame can already be seen. However, what is noticeable about the propagation mechanism is that the effect is not limited to the first rotor bladerow but it extends to the downstream bladerows as well. The significance of that observation is due to the lack of published data for a complete flow path up to the exit of a turbine. So far, the analysis of the propagation of hot streaks under the effect of the segregation mechanism found in the literature has been limited to single or 1 and 1/2 turbine stages.



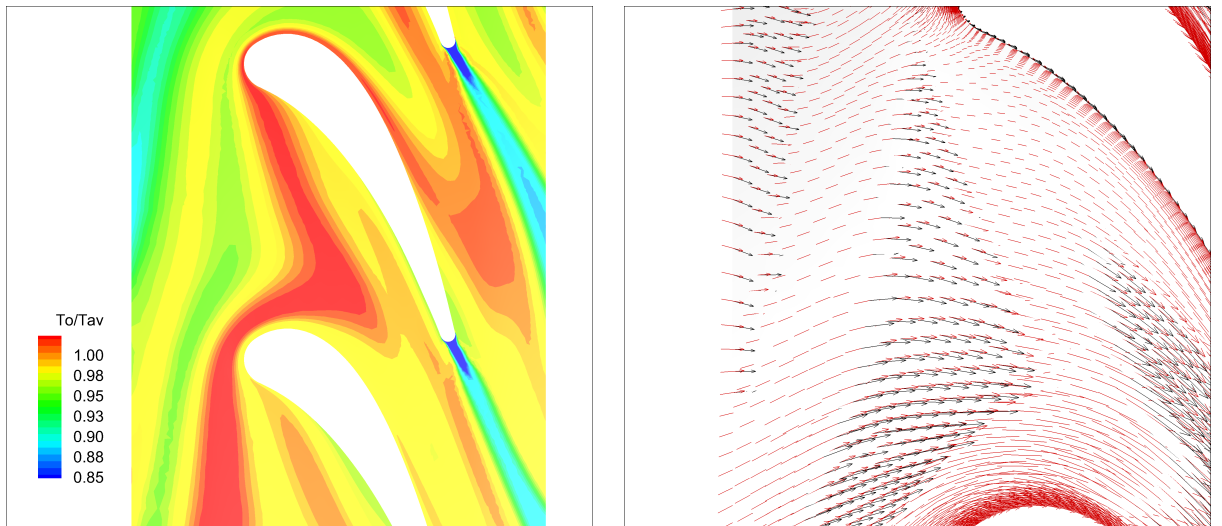
(a) Instantaneous normalised stagnation temperature contours at 40% span



(b) Instantaneous normalised stagnation temperature contours-zoom in one hot streak propagation

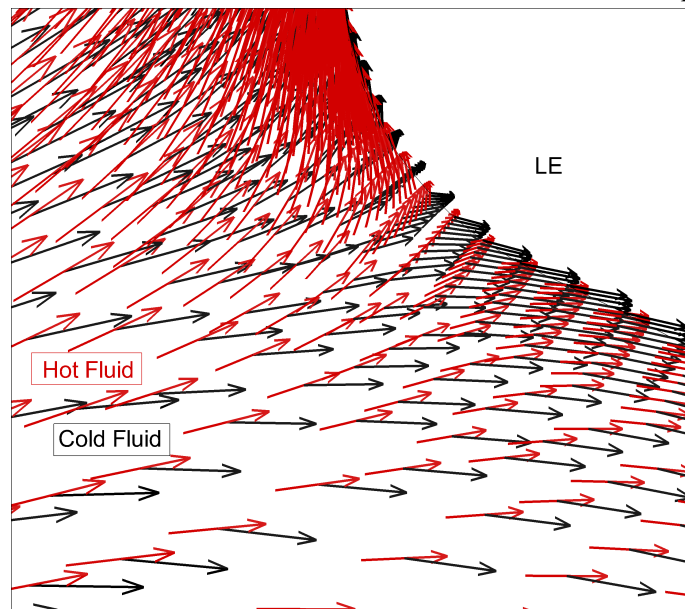
Figure 4.7: Instantaneous normalised stagnation temperature contours through the two-stage turbine at 40% span (hot streak centre)

The effect on first rotor blade is better described in Figure 4.8 where the velocity vectors are plotted in combination with the normalised stagnation temperature contours at 40% span. A closer view of the velocity vectors is shown around the rotor LE and towards the PS area of the hot fluid acceleration. In the same figure, the velocity vectors of a case with uniform inlet temperature conditions are also plotted and are named as cold fluid, since no hot streaks are applied for this case. Hence, the red lines correspond to the baseline HS case and describe the movement of the hot fluid while the black vectors correspond to the case of uniform inlet temperature conditions showing the direction of the fluid in the absence of hot streaks.



(a) Instantaneous normalised stagnation temperature contours at R1

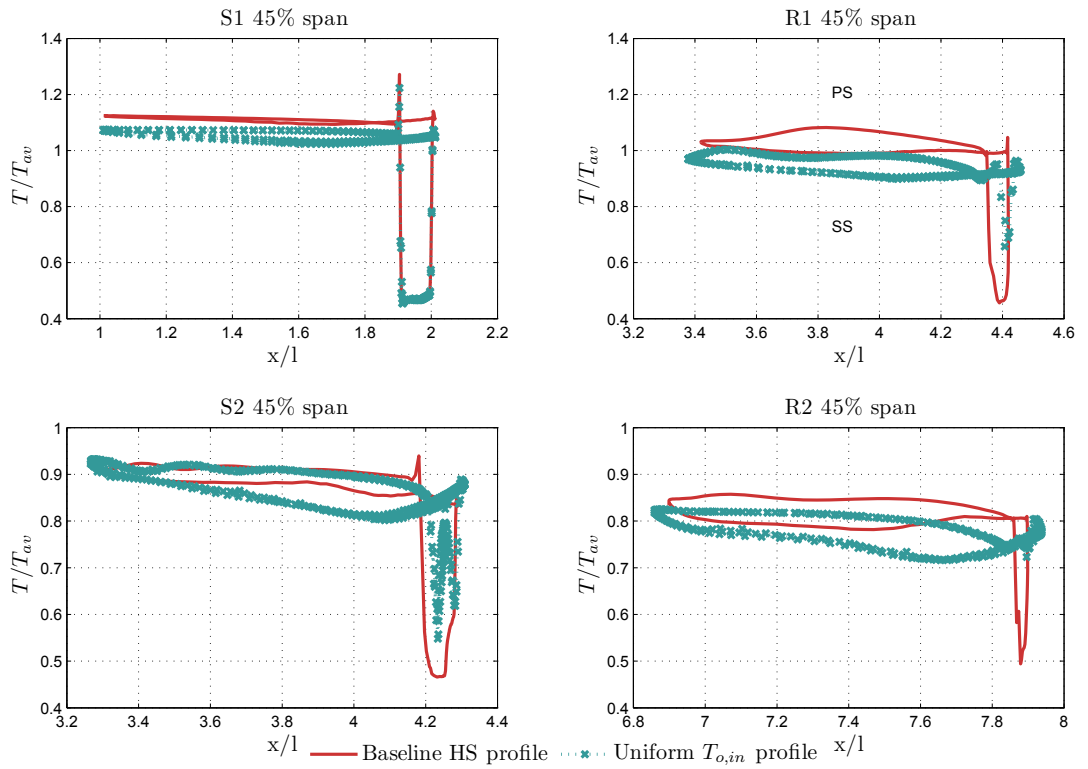
(b) Comparison between velocity vectors at R1 for HS and uniform inlet temperature conditions



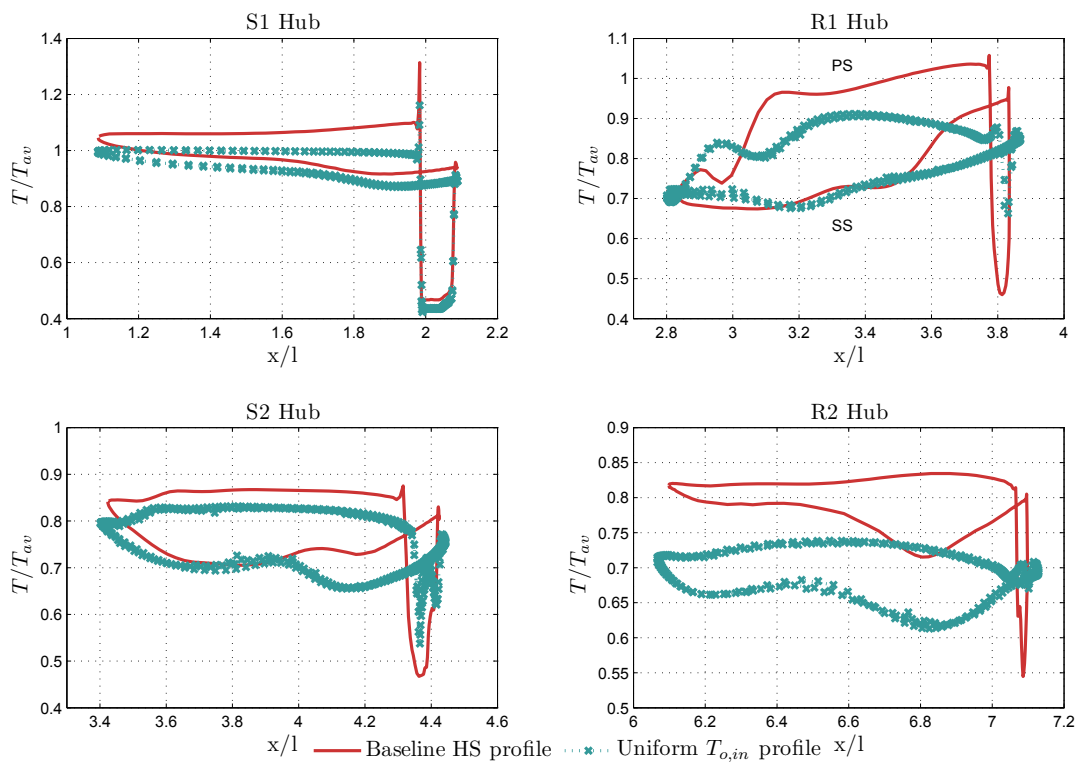
(c) Comparison between velocity vectors at R1 for HS and uniform inlet temperature conditions - close view around R1 LE

Figure 4.8: Instantaneous hot streak propagation through R1 blade passage at 40% span

Figure 4.9 shows the instantaneous normalised static temperature distribution along one "hot" blade of each bladerow referring to the baseline hot streak case and the case of uniform inlet temperature conditions. The results are plotted for three different span locations, hub, tip and 45% span, that is in line with the peak inlet temperature radial location. "Hot" blades have been named those through which the hot streak passes at that instant, after two full revolutions.

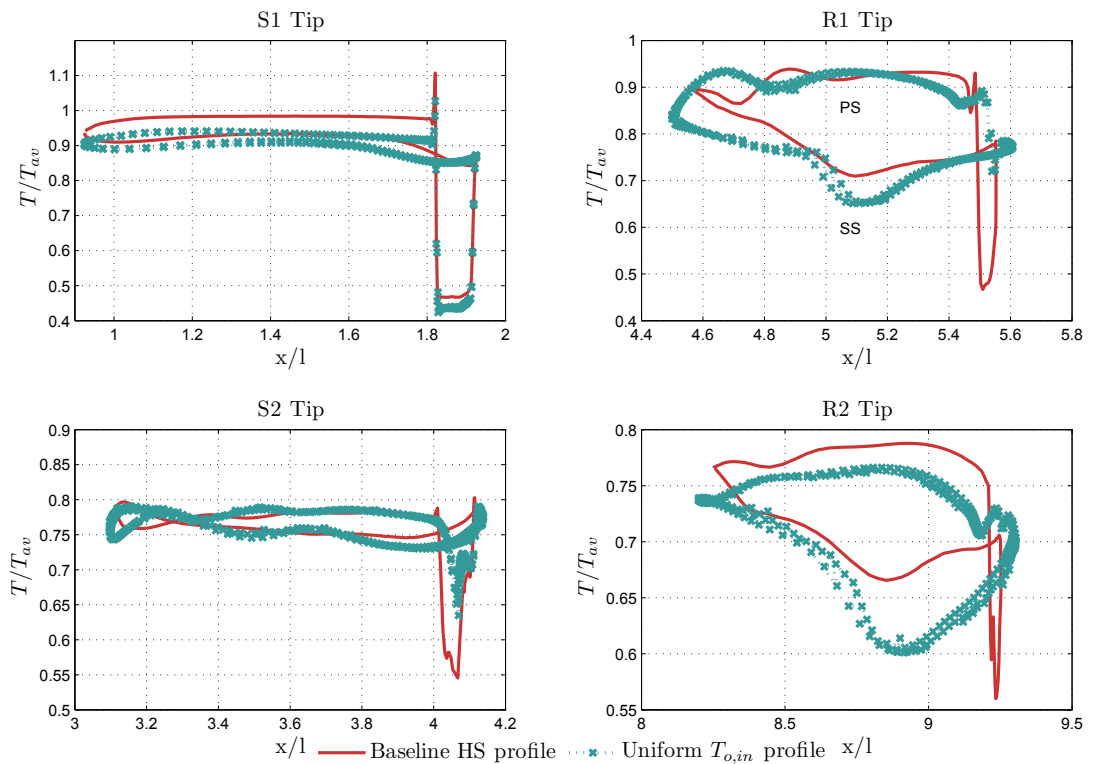


(a) Static temperature profile along hot blades at 45% span - Baseline case



(b) Static temperature profile along hot blades at hub - Baseline case

In the blade-to-blade plane, the temperature distribution generally confirms the tendency of the highest temperature flow to convect to the blades PS and the colder flow towards SS following the kinematics as have been described in the previous section, without any distortion of the hot streak observed along the first stator that is in agreement with previous studies [39, 43] when zero total pressure gradients are assumed at the turbine inlet.



(c) Static temperature profile along hot blades at tip - Baseline case

Figure 4.9: Instantaneous static temperature distribution along hot blades through the 4 bladerows for three different spans

Comparison against the case of uniform inlet temperature conditions shows a higher impact of the segregation phenomenon at the rotational frame near the hub and tip (Figures 4.9 (b) - (c)), while close to the midspan (Figure 4.9 (a)), where the hot streak centre is, the temperature levels remain quite close between the rotor PS and SS. The difference in magnitude of the segregation phenomenon along the span can be explained through the effect of hot streaks on the generation of additional secondary flows [99, 53] as well as the effect of vane coolant on the rotor SS. The enhanced secondary flow at the hub near the blade SS pushes the hot streak towards the midspan

where the temperature difference between PS and SS decreases as shown in Figure 4.9 (a). The impact of secondary flow will be discussed further in this chapter. Another observation related to the radial hot streak migration is related to the hub region of first rotor where the temperature close to the LE is lower compared to the TE. That comes as a result of the radial spread of the hot streak and the migration towards the hub of the rotor PS as it moves towards the rotor LE.

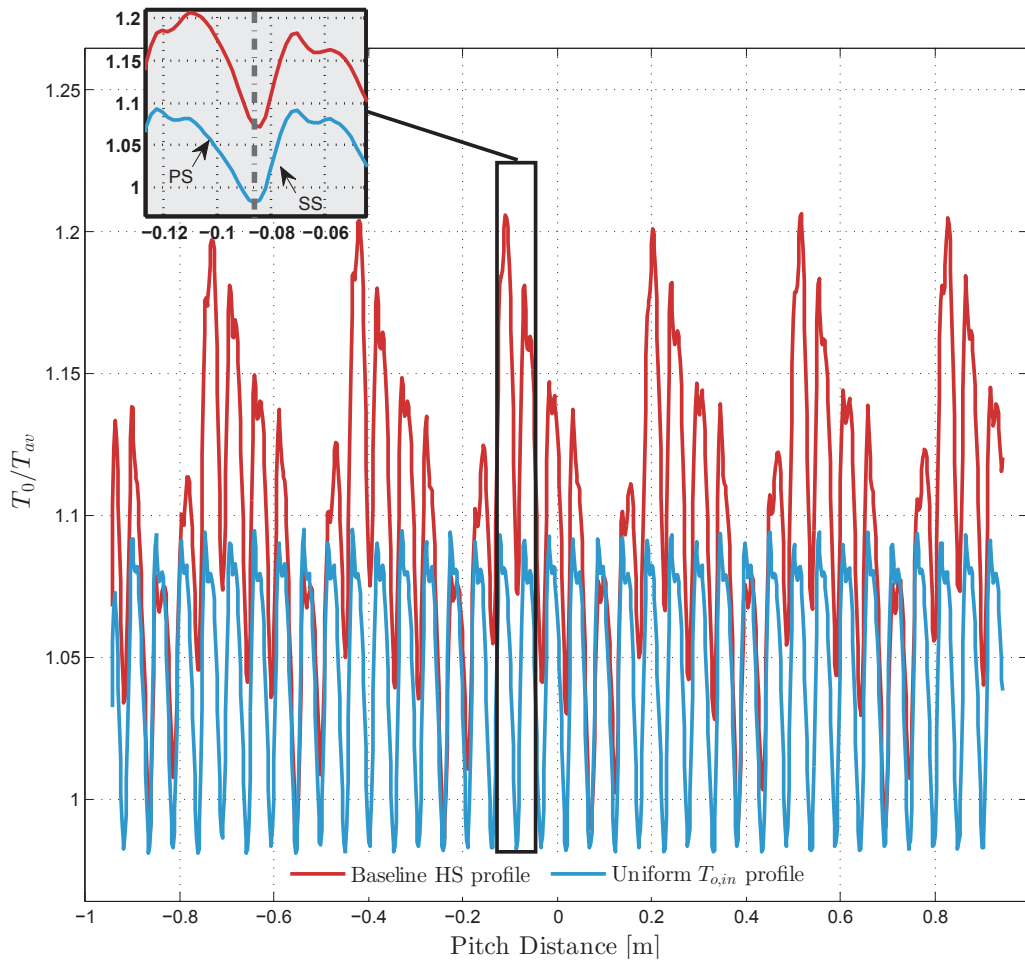


Figure 4.10: S1 exit circumferential normalised stagnation temperature at 40% span

Apart from the velocity deficit in the axial direction, as a result of the temperature difference between the hot streak and the main flow, variations are also observed in the circumferential direction. To illustrate the effects of hot streaks on the variation of circumferential values, the normalised stagnation temperature and absolute velocity at the exit of first stator are plotted in Figures 4.10 and 4.11, respectively, at 40% span for the baseline hot streak profile. Figure 4.10 indicates the effect of hot streaks on the

temperature wake at the exit of first stator blades. Compared to the case of uniform inlet temperature conditions, the hot streaks result in increased stagnation temperature values for both the stator PS and SS. However, the behaviour of velocity in Figure 4.11 is not similar to the stagnation temperature wake. For the first vane exit, larger circumferential increase occurs, in terms of absolute velocity, close to the PS of the stators TE. This is in agreement with the segregation effect as in the circumferential direction the HS with high velocity tends to move towards the rotor PS. Additionally, the stator TE coolant injection should decrease the velocity of hot streak SS branch; the combined effects of stator coolant injection and hot streak will be discussed later in this chapter.

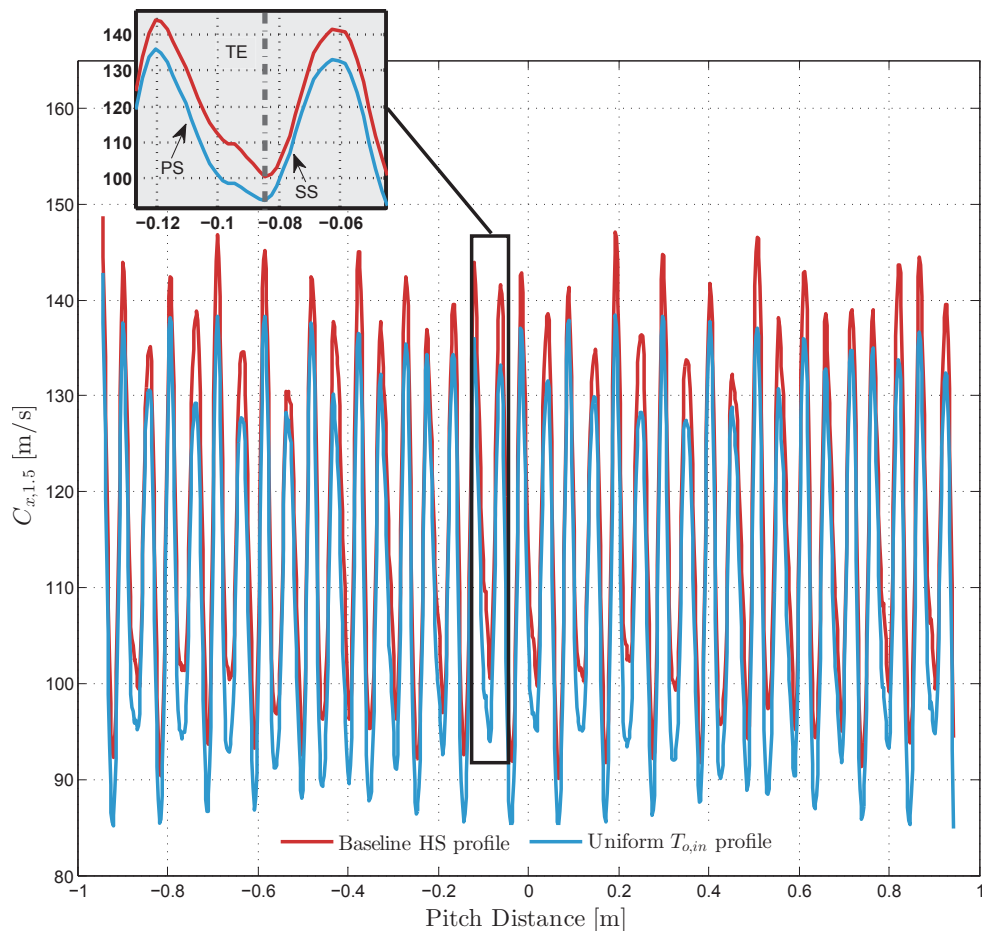


Figure 4.11: S1 exit circumferential absolute velocity at 40% span

Based on Figure 4.11 the axial absolute velocity difference between the HS case and the uniform inlet temperature conditions in the circumferential direction at the exit of

first stator is plotted in Figure 4.12. The average of the absolute velocity difference at 40% span corresponds to 6 m/s.

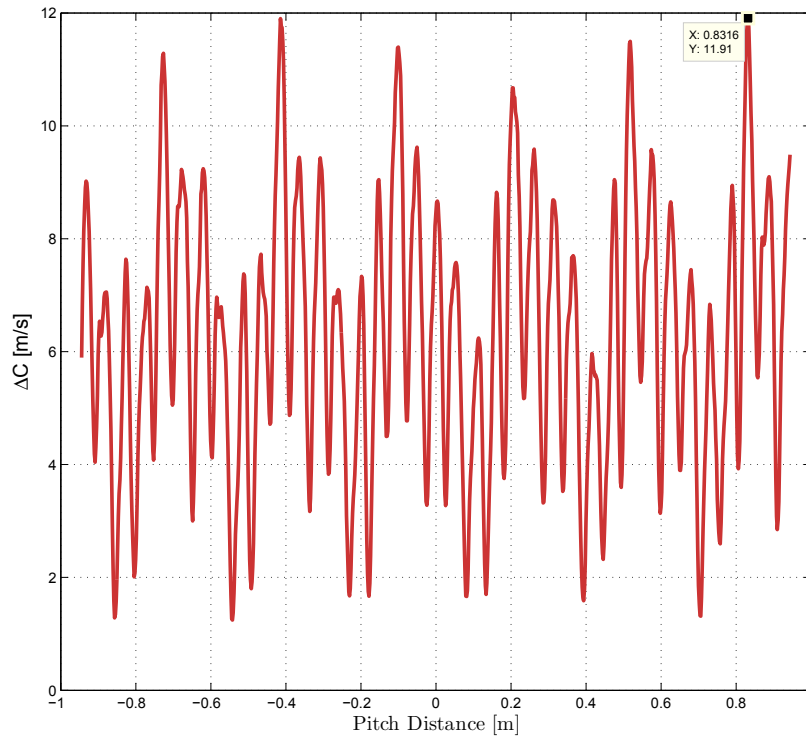


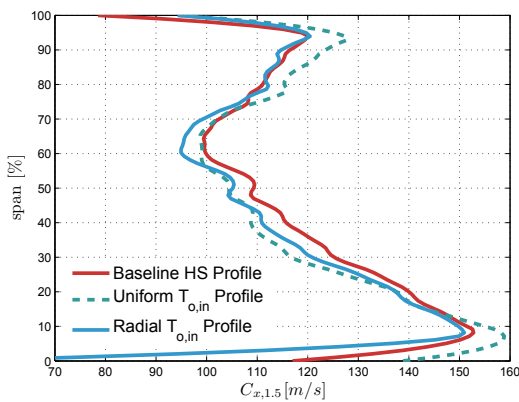
Figure 4.12: S1 exit difference in circumferential absolute velocity at 40% span

### 4.3.2 Radial Hot Streak Migration - Combined Effects

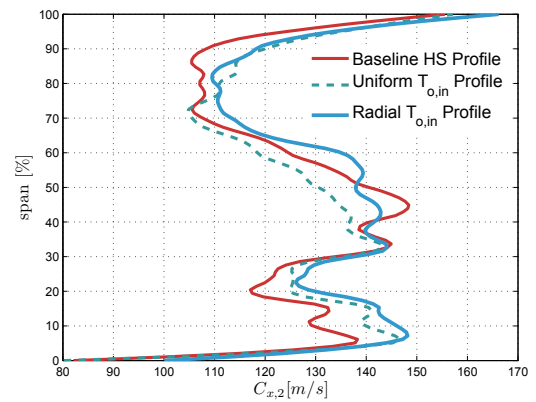
So far, the kinematics of hot streaks on the axial and circumferential direction have been discussed. However, the turbine flow field involves combined effects including coolant injection, secondary flows and hot streaks propagation and they all have an impact on the 3D kinematics of hot streaks. Focusing on the radial hot streak migration, the circumferentially averaged absolute velocity at each one of the bladerow exit planes is presented in Figure 4.13.

The spanwise profiles were extracted at the absolute frame of reference assuming to be the same regardless the reference frame. The spanwise location of higher absolute axial velocity at first stator exit coincides with the position of the hot streak, while the opposite effect is shown at hub and tip where the absolute velocity is lower for both cases of inlet temperature non-uniformities compared to the uniform inlet temperature

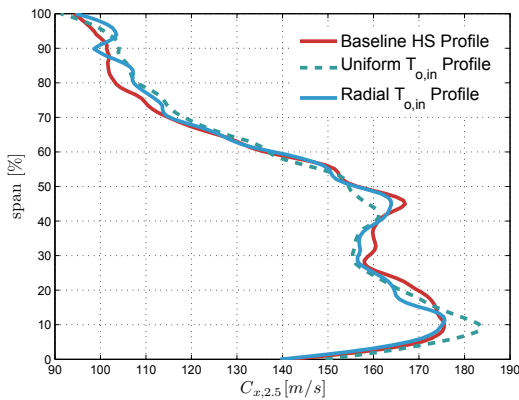
profile. Similar observation can be made at the exit plane of first rotor row for the case of inlet hot streak profile; however, in case of radial inlet temperature distortion the flow turning at hub and tip follows the behaviour of the flow with uniform inlet temperature conditions. Attenuation of the effects of temperature distortion on the flow turning is observed at the exit plane of second stator as shown in Figure 3.13 (c). The divergence in the velocity distribution at the exit planes of the bladerows in combination with the stagnation pressure gradients results in enhanced secondary flow as will be shown next.



(a) Circumferentially averaged radial absolute velocity at the exit of S1 domain



(b) Circumferentially averaged radial absolute velocity at the exit of R1 domain



(c) Circumferentially averaged radial absolute velocity at the exit of S2 domain

Figure 4.13: Spanwise axial absolute velocity distribution at bladerows exit plane for compared inlet temperature profiles

At 40% span, where the hot streak centre was set for the baseline case, the effect of the velocity increase on the flow coefficient is investigated next. When the hot streak profile is applied at the turbine inlet and stator exit absolute velocity,  $C_x$ , increases, as discussed previously, the flow coefficient  $\phi = C_x/U$  increases proportional to  $C_x$  for a

given blade geometry. The simplified velocity triangles in Figure 4.14 help to describe the effect on flow coefficient for the first turbine stage. The term cold streak is used again to refer to the flow in the absence of hot streaks.

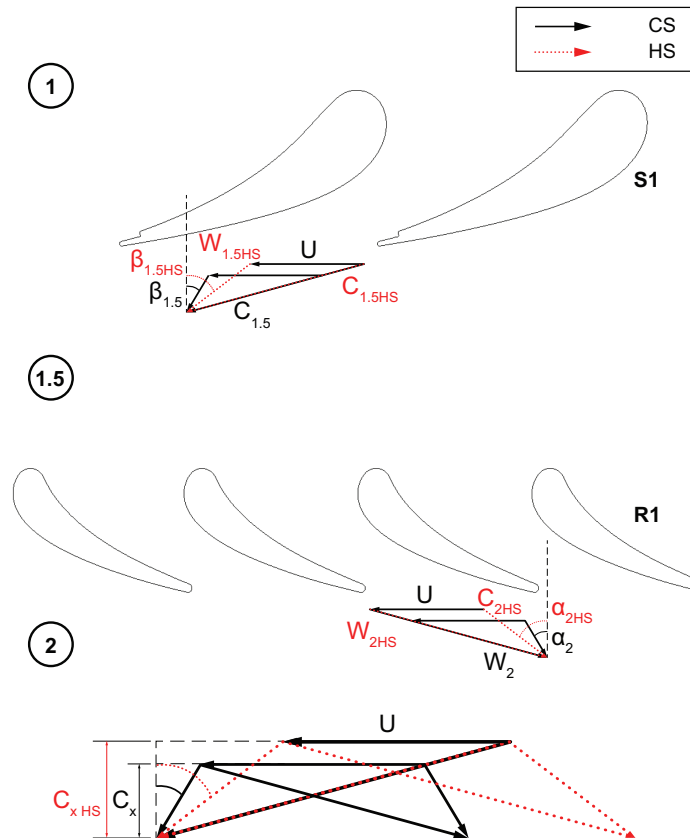


Figure 4.14: Velocity triangles at first stage outlet - effect of hot streaks on flow coefficient

Based on the velocity difference, Figure 4.15 shows the radial variation of flow coefficient as a result of the hot fluid at the exit of first stator. The increase of flow coefficient indicates positive incidence; Dorney et al. [100] related the effect of the difference in flow coefficient on the incidence at rotor inlet. In addition, as a design parameter, the flow coefficient has been chosen to yield the best stage efficiency, increased  $\phi$  is related to increased losses due to the higher flow velocities. Hence, the effect should be taken into account during the design process and uniform inlet temperature profiles should be avoided. This conclusion is further enhanced by the results presented in the following section where the effects of hot streaks on secondary flow are described.

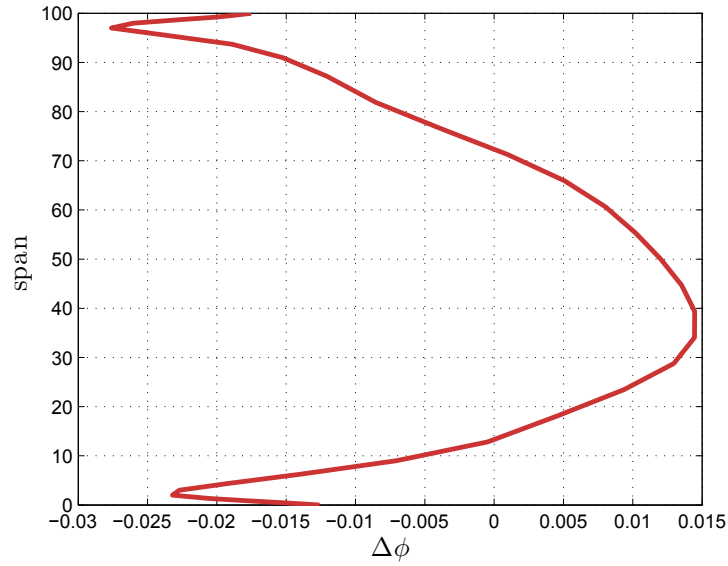
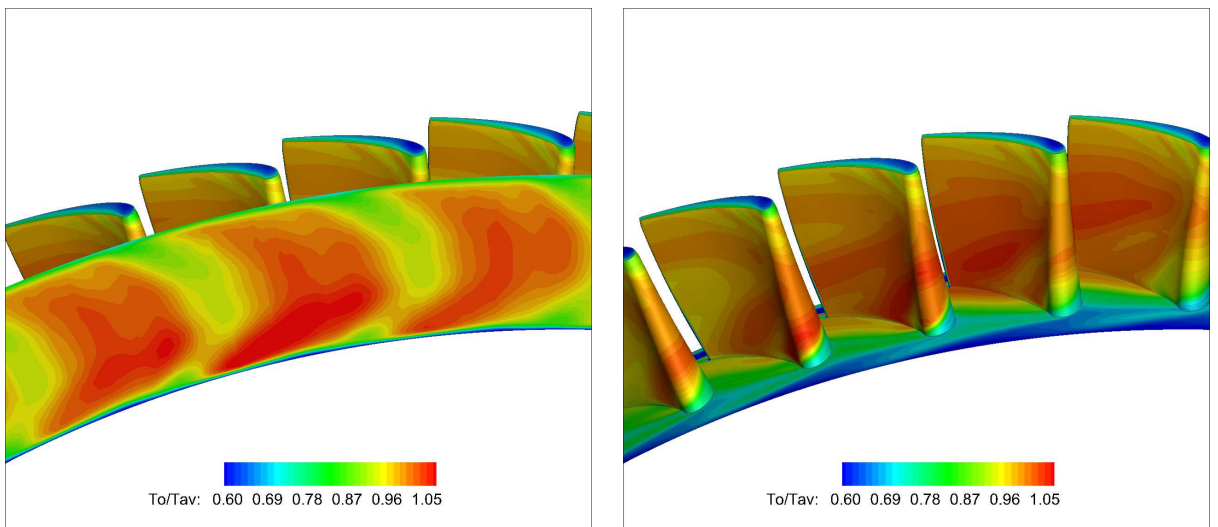


Figure 4.15: Circumferentially averaged radial flow coefficient difference at the exit of S1 domain



(a) Instantaneous stagnation temperature contours at  $R1_{in}$

(b) Instantaneous stagnation temperature contours along the PS of R1 blades

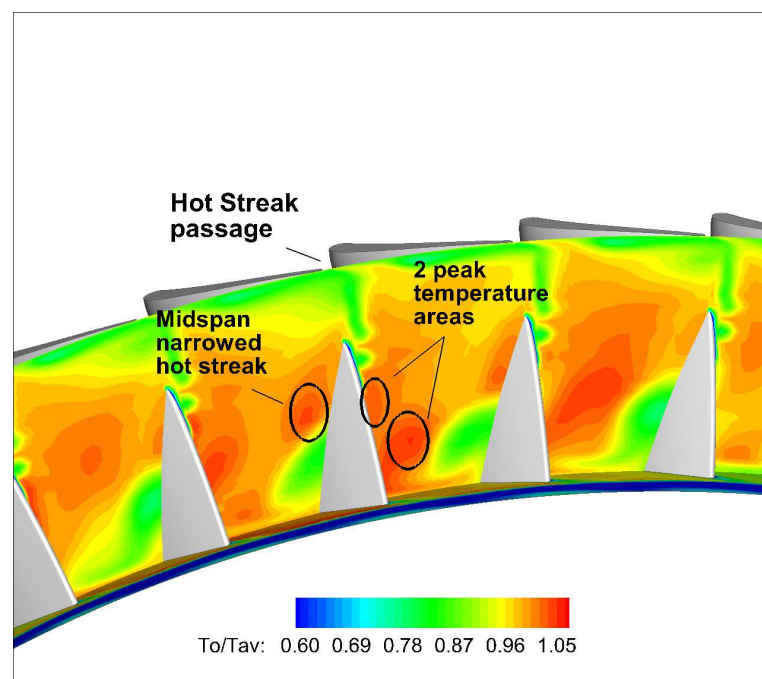
Figure 4.16:  $R1_{in}$  instantaneous temperature contours showing hot streak radial spread

In addition to the difference in flow angles between the hot and cold fluid, the inlet temperature non-uniformities produce radial and circumferential gradients in the rotor relative inlet conditions and hence introduce additional secondary flows that affect the radial migration of the hot streaks. Due to those effects the hot fluid that convects towards the PS spreads radially along the blade surface, while the part of hot fluid that

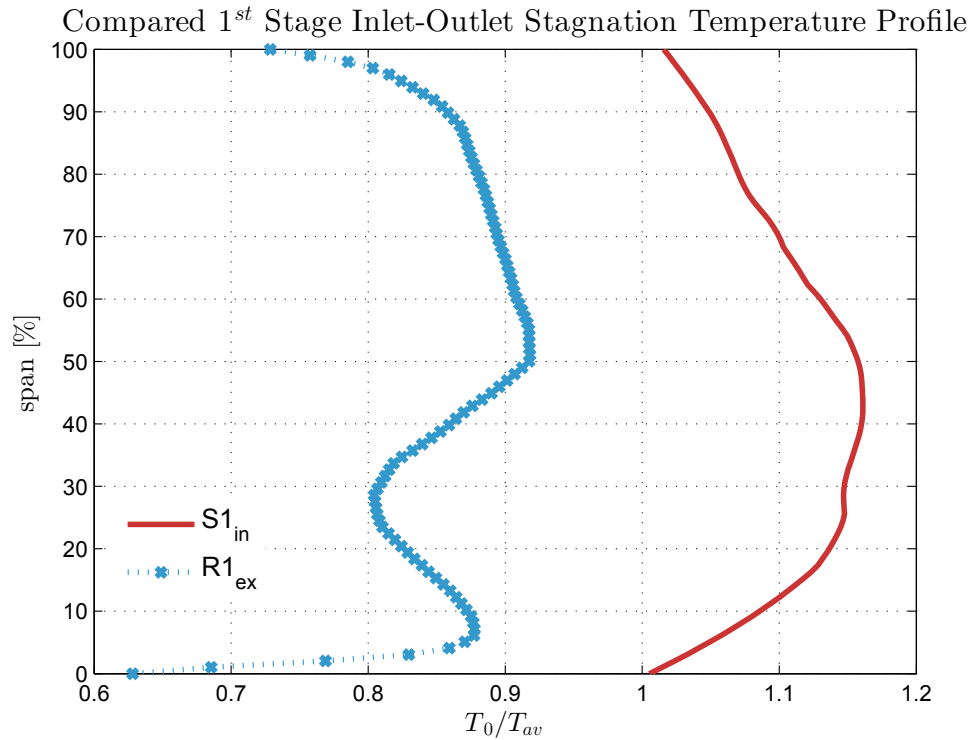
convects towards SS narrows around the blade midspan.

Observation of the normalised temperature contours of first rotor row in Figure 4.16 describes the radial migration of the centre of the hot streak as it enters the rotational frame. The radial migration of the hot fluid on the rotor PS is shown for an instant time after two revolutions in Figure 4.16 (b). The hot fluid propagates towards the hub as it moves towards the rotor LE.

The normalised stagnation temperature contour plots show the propagation of the hot streak through the first rotor blades passage in Figure 4.17 (a). The 3D effects are obvious with the radial spread of the hot streaks resulting in two distinct peak temperature areas that propagate close to the rotor PS and one close to the midspan of rotor SS (segregation effect). The circumferentially averaged temperature distribution at the exit of the first stage (Figure 4.17 (b)) confirms the two temperature peaks with the hot streak centre located between 50-60% span (compared to the inlet 40-50% span). Figure 4.18 shows the normalised stagnation temperature contours at the exit of first rotor for six different instants, each one corresponding to one hot streak passage. The contour plots confirm the previous discussion showing the midspan and close to hub high temperature areas at the exit of first stage as have been marked for the first instance.



(a) Instantaneous stagnation temperature contours at  $R1_{ex}$  domain



(b) Circumferentially averaged stagnation temperature profile at 1<sup>st</sup> stage inlet-outlet

Figure 4.17: First stage exit - radial hot streak migration

To identify the additional vorticity due to the combined effects of hot streaks and coolant injection, the instantaneous normalised stagnation pressure contour plots are presented in Figure 4.19 for the exit plane of first rotor for one hot streak position (the location is in agreement with the hot streak shown in Figure 4.17 (a)). In an attempt to separate the individual effects of the vane cooling and hot streak on the production of secondary flows three different cases are shown here, one for the baseline case (a), one for the case of radial inlet temperature profile (b) and one for the case of uniform inlet stagnation temperature conditions (c). Focusing on the specific blade passage where the hot streak is convected for that instance (can be seen in Figure 4.17) the worst conditions in terms of secondary flow losses are observed for the baseline case (Figure 4.19 (a)). The combination of hot streak and vane coolant result in a stronger lower passage vortex close to rotor SS. The radial temperature profile also enhances the secondary flow, while the absence of temperature variations in Figure 4.19 (c) exhibits the most favourable case in terms of secondary flow losses.

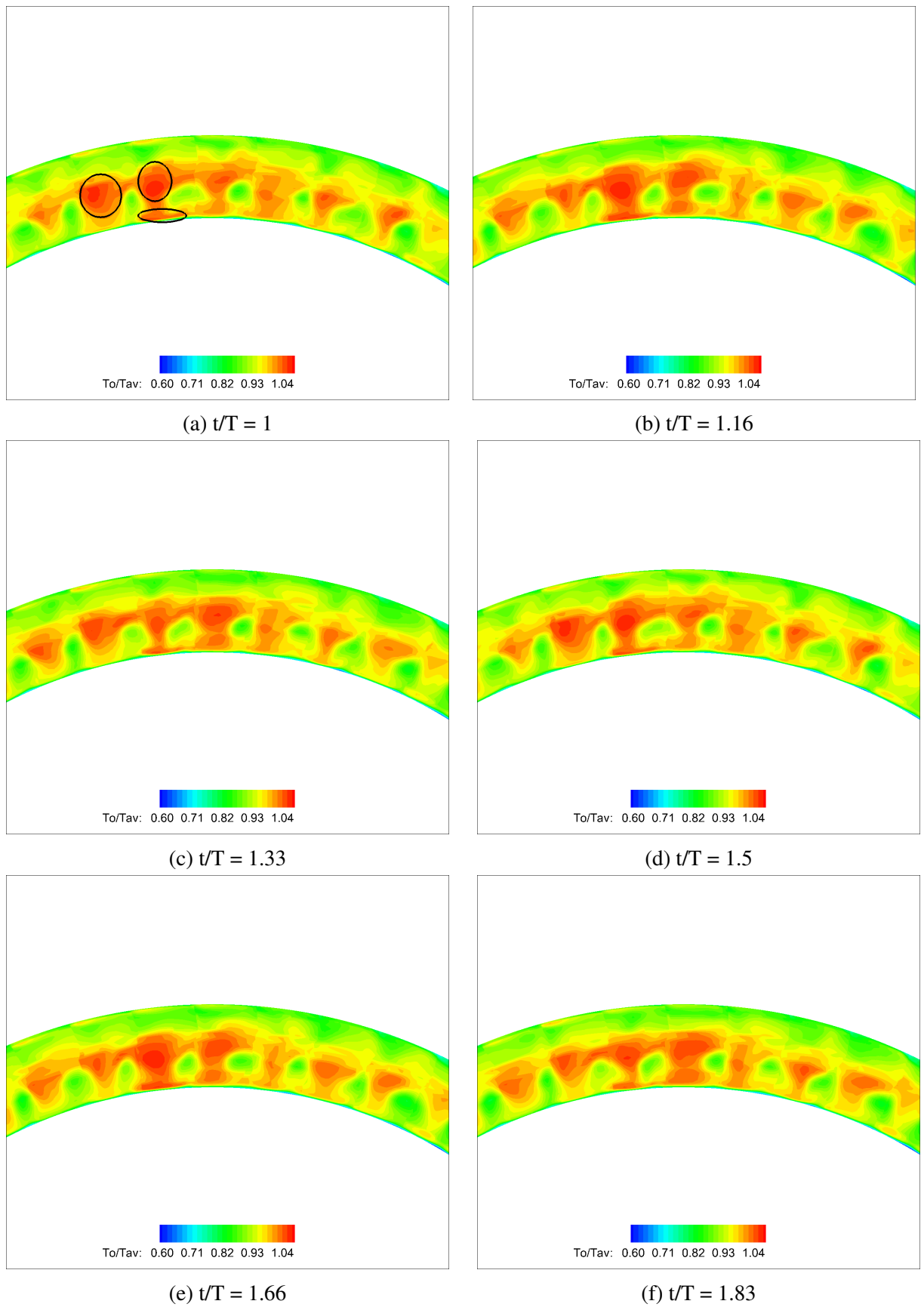
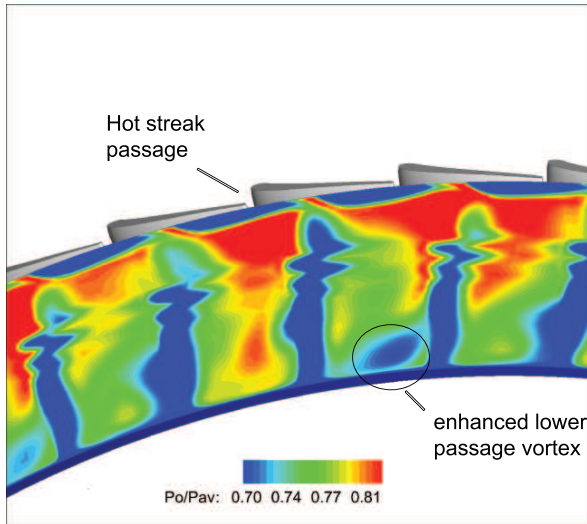
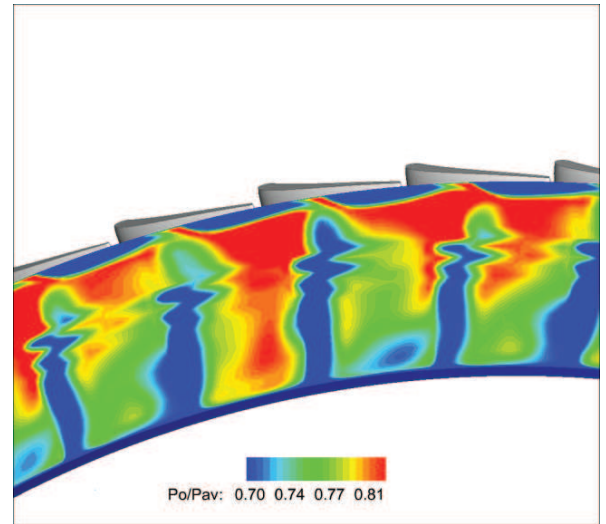


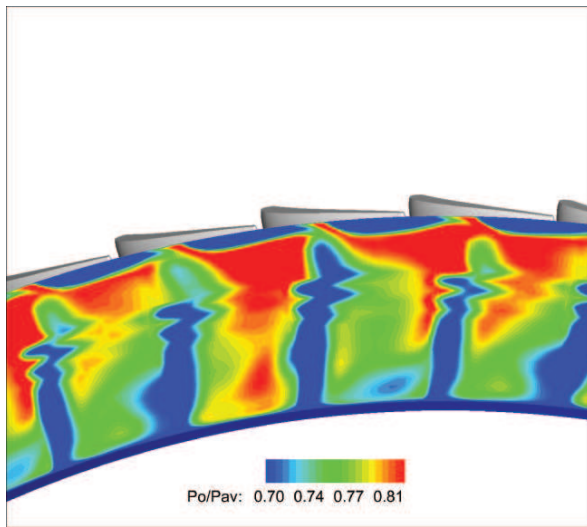
Figure 4.18: Instantaneous normalised stagnation temperature contours at  $R1_{ex}$  for different time steps



(a) Normalised stagnation pressure contours at  $R1_{ex}$  for the baseline case



(b) Normalised stagnation pressure contours at  $R1_{ex}$  - radial inlet temperature profile



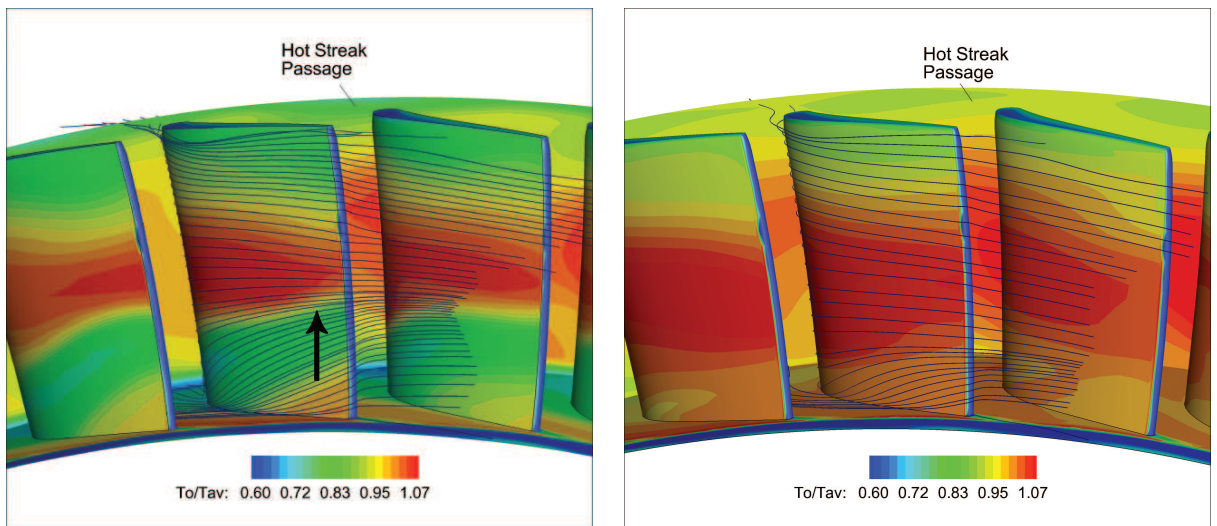
(c) Normalised stagnation pressure contours at  $R1_{ex}$  - uniform inlet temperature

Figure 4.19: Instantaneous stagnation pressure contours at the exit of 1<sup>st</sup> stage for three different inlet temperature conditions

When the hot streak enters the rotational frame additional secondary flows are introduced due to the relative total pressure gradients upstream of the rotor the inlet flow angle radial distribution [43]. This results to streamwise vorticity within the rotor passage due to the upstream vane passage and due to density gradients at the inlet of the rotor bladerow. As discussed about radial hot streak migration, one of the two peak temperature areas formed into the rotor passage migrates towards the hub, interacting as shown here, with the lower passage vortex and resulting in lower total pressure. Compared with the baseline case, in case of radial inlet temperature profile (Figure

4.19 (b)) the effect is less significant, while uniform inlet temperature profile (Figure 4.19 (c)) shows the least impact on the magnitude of lower passage vortex.

The results are in agreement with a previous study of Hermanson and Thole [51] where the effects of spanwise inlet temperature variations alone (1D) and both radial and circumferential inlet temperature varying profiles (2D) on the secondary flow development were investigated showing a minimum effect of the radial temperature distortion compared to the inlet hot streak profile. The resulting velocity profile at stator exit, as shown in Figure 4.13 (a), indicates higher flow turning between 30-60% span and hence, additional unsteadiness and enhancement of the secondary flow into the first rotor passage, demonstrating the effect of circumferential varying inlet temperature gradients and the need to consider realistic turbine inlet temperature profiles.



(a) Stagnation temperature contours at R1 SS - baseline case (b) Stagnation temperature contours at R1 SS - No vane coolant

Figure 4.20: Instantaneous stagnation temperature contours and velocity vectors on R1 SS blades

The additional secondary flow that is produced nearby the first rotor SS is responsible for the redistribution of hot fluid on rotor SS. He et al. [61] has also related the hot streak radial migration to the rotor passage secondary flow. In that study radial migration is observed close to the hub where a stronger secondary flow due to a passage-vortex is more visible than that near the tip. Roback and Dring [59] studied the effects of spanwise hot streak location on the radial migration into the rotor passage. For different injection locations in the radial direction the accumulation of hot streak

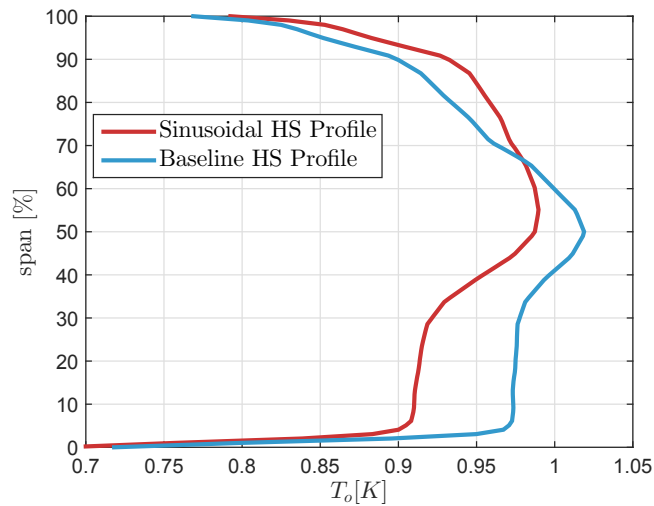
towards both the rotor hub and tip has been observed. The formation of two distinct peak temperature areas at the outlet of first rotor as a result of the radial migration into the rotor passage has been also mentioned in literature [101, 68] that is in agreement with our observations.

Focusing on rotor SS further examination for the cases of cooled and uncooled vanes is shown in Figure 4.20 where the instantaneous stagnation temperature distribution around the rotor SS and the velocity vectors are shown. The figure indicates the contribution of the vane cooling on the enhancement of secondary flow on the rotor SS as has already been discussed. In terms of the hot fluid movement, the lower velocity cold gas convects towards the SS pushing the hot streak towards the midspan where the peak temperature alongside the SS of first rotor blades was observed (Figure 4.9 (a)). For the case of vane cooling injection, it can be noticed that additional secondary flow is introduced in the region of hub and as a result the hot gases narrow around the midspan. The observation of those hot spots on the blade surfaces indicates areas of local heat transfer enhancement and is of great importance for the blade cooling.

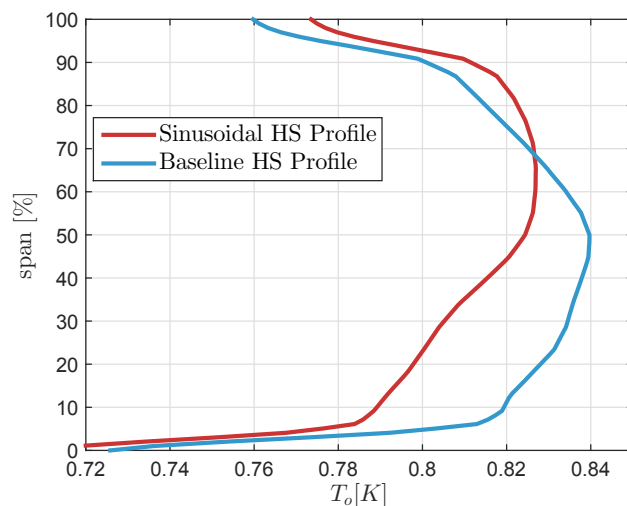
### **4.3.3 Effects of Hot Streak Shape**

The effects of the hot streaks shape on their propagation through the turbine are also discussed by referring to the exit of each stage. In Figure 4.21 the circumferentially averaged radial distribution of the stagnation temperature along the exit plane of each turbine stage shows a higher magnitude of the hot streak for the baseline hot streak profile. In terms of radial migration the hot streak remains more concentrated at the exit plane of the first stage for the baseline case compared to the sinusoidal inlet temperature profile with the two temperature peaks being located close to 50% span, when the inlet hot streak centre was set between 20-30% span for the baseline profile and 40-50% span for the sinusoidal hot streak profile. That shows a significant impact of the baseline profile on the secondary flow which consequently results in radial migration of the hot fluid along the first rotor passage up to the exit of the stage. At the exit of the turbine plane (Figure 4.21 (b)) the sinusoidal hot streak profile exhibits higher mixing with the peak temperature area being located near the tip while the baseline case is spread along the span.

With respect to the hot streak shape, Dorney [68] compared elliptical and circular hot streak profiles, with the elliptical resulting enhanced mixing as it propagates. In case of elliptical profiles the circumference per unit area is bigger, thus more of the hot fluid is exposed to the surrounding colder fluid. As expected, the sinusoidal inlet profile resulted in less significant temperature gradients underestimating the impact of hot streaks up to the turbine exit. Here, the importance of applying realistic hot streak profile for the CFD analysis needs to be highlighted through the comparison of ideal and more realistic hot streak shapes to provide a better understanding of the magnitude of the unsteady aerodynamic effects.



(a) Circumferentially averaged radial stagnation temperature at the exit of R1 plane



(b) Circumferentially averaged radial stagnation temperature at the exit of R2 plane

Figure 4.21: Spanwise stagnation temperature distribution at the exit of turbine stages for the baseline and sinusoidal HS profile

#### **4.3.4 Combined Effects of 1<sup>st</sup> Vane Coolant and Potential Interaction**

The radial migration has already been discussed and further discussion on the circumferential alteration follows here. The hot streak shape at the exit of first stator, as already has been shown in Figure 4.16, has been radially and circumferentially changed compared to the inlet profile. The instantaneous stagnation temperature contours for the baseline case in Figure 4.22 illustrate that variation on the flow pattern at the outlet of the first bladerow. In order to investigate the influence of the coolant injection on the hot streak shape, a comparison between a cooled stator bladerow and an additional case without any cooling injected at stator blades are presented in Figure 4.23. The contours at the exit of the uncooled stationary frame reveal a different shape of the hot streak as compared to the case where hot streak and stator coolant co-exist. For the cooled stator blades Figure 4.22 indicates some lower temperature areas in the spanwise direction caused by the coolant injection at the stator TE resulting in a chopped hot streak shape at the outlet plane of first stator. A case of combined hot streak and coolant injection at the stator TE has been mentioned in the literature [62]. The existence of coolant may affect the migration pattern and needs to be taken into account for the hot flow path analysis.

However, apart from the cooling flow, additional sources of interaction with the hot streaks are investigated, since the comparison of the inlet and outlet profiles also reveals a change in the circumferential direction even in the absence of stator cooling (Figure 4.23) indicating some flow mixing. That could be due to the influence of the downstream potential interaction of the rotor on the stator flow field. The movement of the hot streak in the tangential direction has been described by Shang and Epstein [49] as a "woobling" effect altering the shape of the hot streak in circumferential direction at the rotor blade passing frequency and has also been confirmed by more recent studies [27].

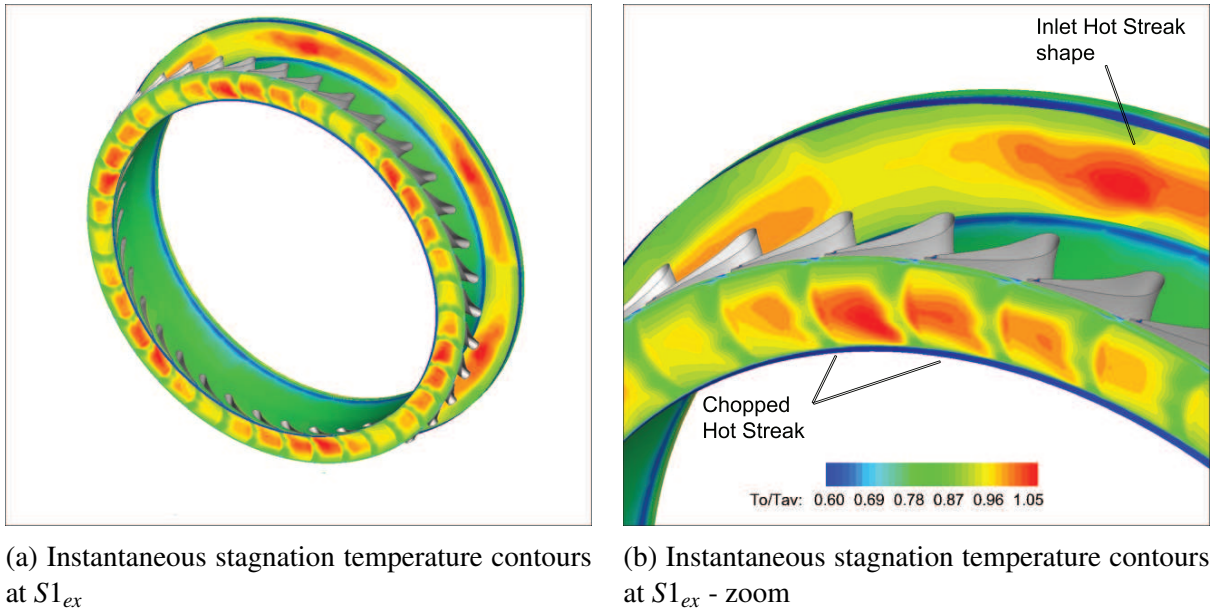


Figure 4.22: Alteration of hot streak shape at the exit of 1<sup>st</sup> vane row - baseline case

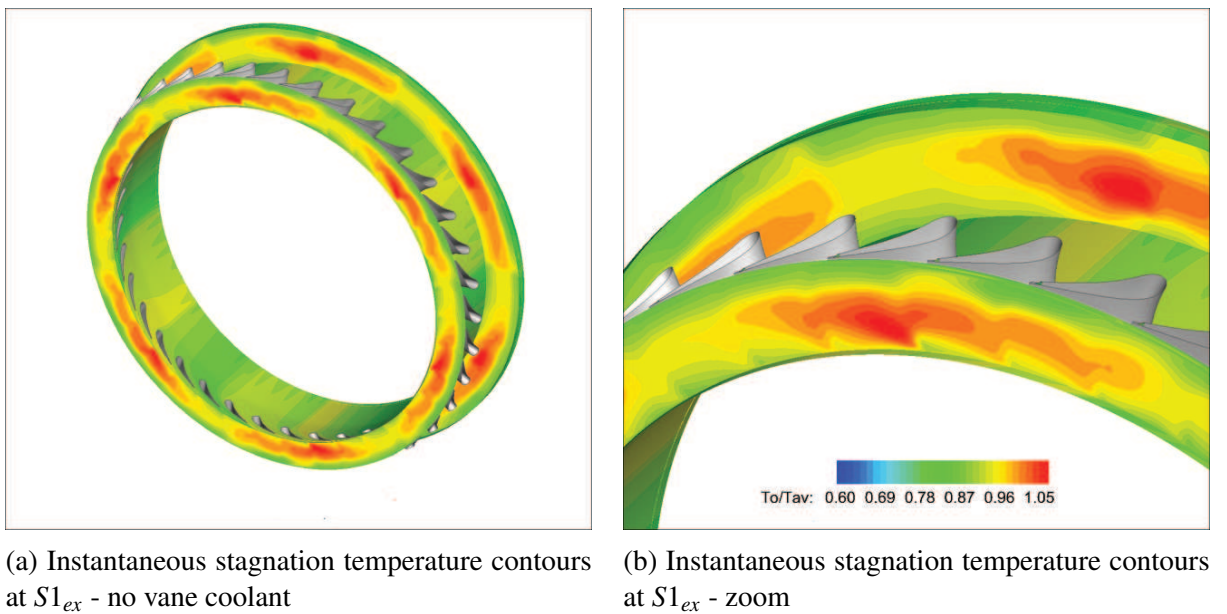


Figure 4.23: Alteration of hot streak shape at the exit of 1<sup>st</sup> vane row - no vane coolant

In order to describe the effect of potential interaction an additional case has been investigated using only the first stator row. The contour plots of the instantaneous total pressure coefficient for the baseline case and the case with only the stator row are shown in Figure 4.24. The total pressure coefficient has been calculated using the turbine inlet condition as the reference condition based on Denton [102]. The effect of the

adjacent rotor row is shown in Figure 4.24 (a), where a region of minimum pressure coefficient is periodically strengthened. Comparison with Figure 4.24 (b) implies that the origin of this low pressure region is the relative motion of stator and rotor row. As the potential interaction is a phenomenon that is dependent on the axial distance from stator TE to rotor LE and the Mach number, the interaction between first stator and rotor blades for this turbine could be related to the high Mach number in the first vane row. The loss of stagnation pressure that is related to the bladerows interaction, as well as to the hot streak propagation which was described earlier, would be equal to an increase of entropy. A complete analysis of the aerodynamic losses in a turbine should consider investigating the losses arising from the unsteady flow (hot streaks, potential interaction), which may be significant in some cases dependent on the design. In addition to the pressure losses, entropy generation should be enhanced due to the heat transfer across the temperature differences; however, the effects of hot streaks on the entropy production have not been analysed during the current study but could be part of future work.

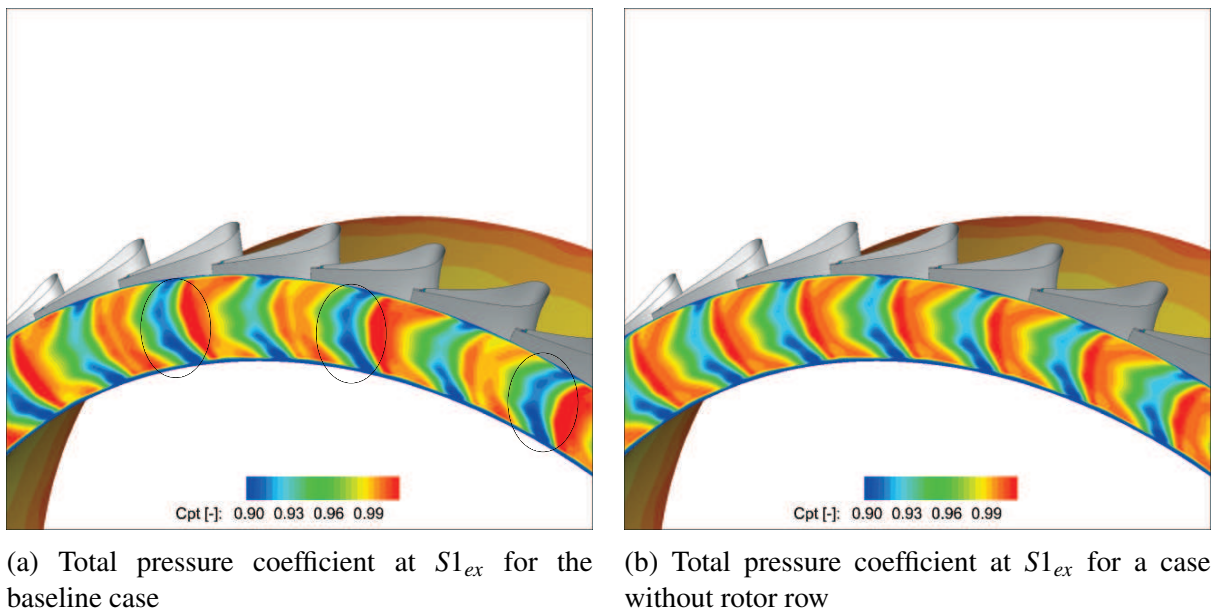


Figure 4.24: Instantaneous total pressure coefficient contours at the exit of 1<sup>st</sup> vane row

## 4.4 Summary

In this chapter the effects of the hot streaks propagation through a two-stage HP turbine were evaluated by means of a 3D unsteady CFD code. The propagation of hot streaks is

an unsteady phenomenon and may be affected by a number of individual and combined parameters.

The kinematics of the six hot streaks, aligned to the first stator midpassage, follows the basic propagation mechanism as has been described in the literature, with the hot fluid migrating towards the rotor blades PS and narrowing around the midspan of blades SS. The preferential heating of the blades PS indicated increased temperature values compared to a case where uniform inlet temperature conditions were applied. Looking into different components, which are related to different flow mechanisms, the presented results showed that effects of vane coolant injection, secondary flows and potential interaction should be taken into account, with regard to the alteration of the hot streak shape and the radial migration of the hot streak centre.

The vane coolant injection, in combination with the stator/rotor interaction, resulted in a circumferentially chopped hot streak profile at first stator exit plane. Secondary flows, enhanced due to the presence of hot streaks, tended to push the hot fluid along the radial direction. Moving through the stages, hot streaks resulted in two distinct peak temperature areas along the blade span. In addition, different hot streak shapes exhibited variation in temperature magnitude and thus, temperature levels appeared elevated at the turbine exit when a concentrated hot streak was applied against an elliptical one.

The presented results in this chapter have shown the influence of specific design parameters on the hot streaks kinematics and the sensitivity of the analysis on the inlet boundary conditions. That is of great importance as most of the relevant studies are based on ideal hot streak shapes to simulate the propagation of the hot fluid through a turbine stage neglecting also the combined effects taking place. Hence, appreciation of the contribution of different sources of interaction to the hot flow path is recommended, with respect to the aerodynamic losses and the design of efficient turbine coolant schemes. The knowledge gained from the current analysis is applied into the following cases where a generic turbine geometry is investigated with regard to the H2-IGCC project.

# **Chapter 5**

## **H2-IGCC Project - Gas Turbine Modification Options for Syngas Operation**

### **5.1 Introduction**

The main objective of the H2-IGCC project is to apply existing gas turbine technology, burning natural gas for power and heat generation, in order to get towards more advanced IGCC power plants burning undiluted hydrogen-rich syngas [21]. Within the frames of the project it is required to demonstrate technical solutions in order to get high-efficiency gas turbine engines under the new operating conditions. The solutions discussed in this thesis are only related to the turbomachinery challenges; however, it should be noted that solutions related to other parts of the power system were also researched by academic and industry partners, including the development of safe and low-emission combustion technology, improved materials, as well as a thermo-economic system analysis.

There are many issues arising from burning syngas fuels compared to conventional natural gas in gas turbines regarding the turbomachinery challenges, some of them have been addressed in Chapter 2 of the thesis. In the last three chapters of the thesis the effects related to the turbine will be discussed further in terms of the aerodynamic and aeromechanical behaviour. Starting with an overview of the baseline geometry and

following with the design modifications, this chapter aims to set the complete picture of the problem, part of which is the scope of the thesis.

### 5.1.1 Baseline Gas Turbine - Overview

For the purposes of comparison between an existing gas turbine engine and an adjusted syngas fired engine, the characteristics of a baseline, natural gas fired turbomachine needed to be established. The suggested design modifications should be based on proven and pre-tested technology; the heavy duty SGT5-4000F was selected (Figure 5.1), the characteristics of which are shown in Table 5.1.

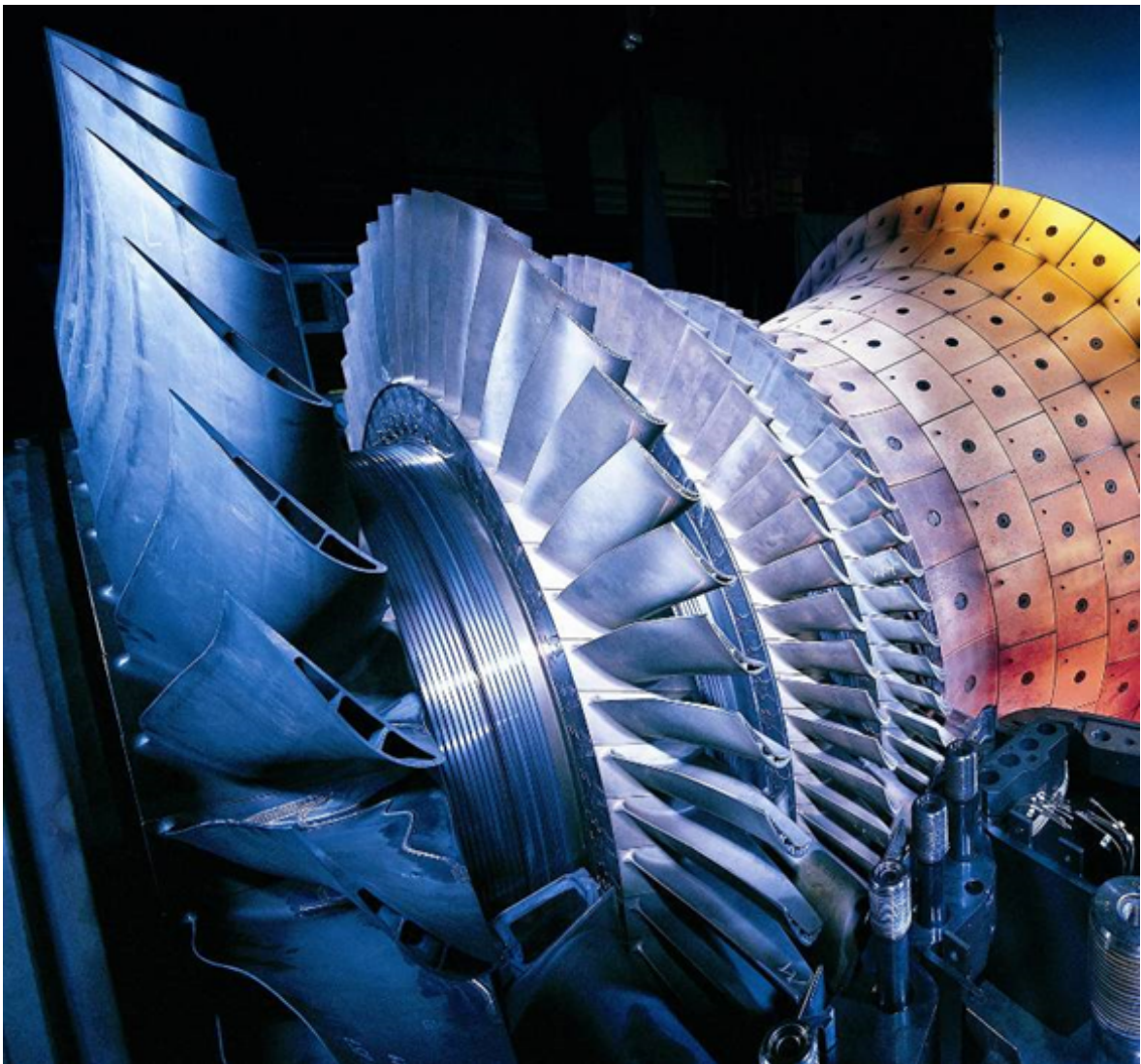


Figure 5.1: SGT5-4000F gas turbine, Siemens Power Generation in Berlin

The SGT5-4000F gas turbine has been in the market since the 1990's and remains a

highly reliable and competitive F-class gas turbine [103]. With regard to the turbine, recent improvements deal with the first and second turbine stages in terms of thermal stresses, applying internal cooling system through a complex array of air channels and external film cooling [104]. Due to the lack of detailed geometric information in open literature though, the baseline, natural gas fired gas turbine engine needed to be re-designed; thus, a generic gas turbine was firstly modelled based on the characteristics of SGT5-4000F, followed by compressor and turbine adjustments to allow for syngas operation. Details on the methodology, based on which the generic machine was designed, have been published by project partners for the cycle and 1D analysis [22], CFD analysis for the compressor [105] and turbine design [23].

Electric power [MW]	292
Grid frequency [Hz]	50
Efficiency	0.398
Exhaust mass flow rate [kg/s]	692
Exhaust temperature [K]	850
Pressure ratio	18.2
Length x width x height [m]	13x6x8

Table 5.1: SGT5-4000F characteristics

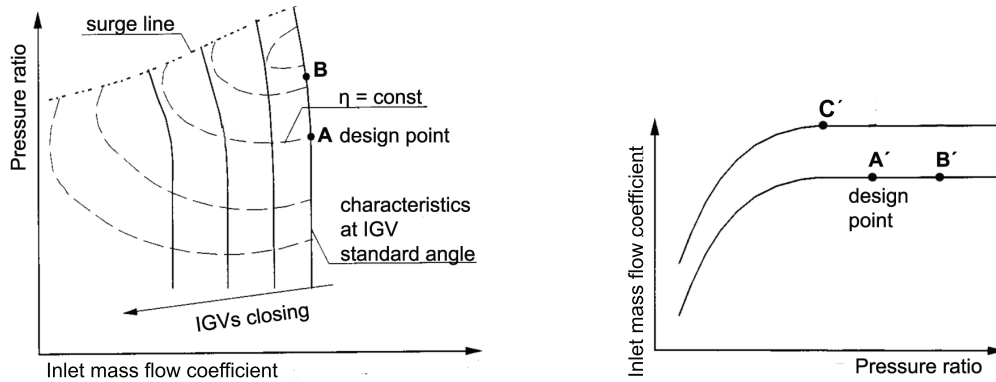
### 5.1.2 Gas Turbine Modifications - Syngas fuel

A main barrier towards the usage of syngas is the difference in composition and the corresponding heating value. Depending on the composition and dilution process, syngas fuels may have medium or significantly lower LHV than natural gas. In agreement with the project partners, a particular undiluted syngas fuel has been chosen, with increased hydrogen content. Details regarding the composition of the two fuels (natural gas and syngas) and the basic thermodynamic characteristics are shown in Table 5.2.

Burning syngas has an impact on the total engine affecting the original compressor/turbine matching. For a single-shaft compressor/turbine arrangement operating at constant rotational speed the dependency of the pressure ratio on the flow capacity is shown in Figure 5.2 where two typical operational characteristics are drawn.

Parameter	Compound	Value	
		Natural Gas	Syngas
Composition [Volume fraction %]	$H_2$	0.00	85.82
	$CO$	0.00	1.17
	$CO_2$	0.00	4.03
	$N_2$	3.50	8.98
	$CH_4$	92.00	0.00
	$C_3H_8$	4.50	0.00
Lower Heating Value [MJ/kg]		50.06	33.4
$C_p$ [ $Jkg^{-1}K^{-1}$ ]		1156.7	1406.6
Gamma [ $\gamma$ ]		1.33	1.28
R [ $Jkg^{-1}K^{-1}$ ]		287	303

Table 5.2: Compositions and properties of selected fuels



(a) Typical compressor characteristic curve at constant rotational speed

(b) Typical turbine characteristic curve at constant rotational speed

Figure 5.2: Compressor and turbine flow characteristics

At a given pressure ratio ( $P_{o3}/P_{o4}$  for the turbine and  $P_{o2}/P_{o1}$  for the compressor) the mass flow function ( or flow capacity) of a choked turbine is described by Equation 5.1

$$\frac{\dot{m}_{in} \sqrt{\frac{TIT}{M}}}{KA_{in}P_{o,in}} = const \quad (5.1)$$

where the subscript "in" refers to the turbine inlet conditions,  $M$  represents the molar mass,  $\dot{m}$  the compressor air and fuel mass flow rate,  $A$  the turbine inlet cross-sectional area,  $P_o$  is the stagnation pressure and  $K = \sqrt{\frac{\gamma}{R} \frac{2}{\gamma+1} \frac{\gamma+1}{\gamma-1}}$ . The flow capacity is controlled

by choking the turbine stator passages which is usually the case for heavy duty gas turbine engines. The flow capacity is then fixed and the mass flow is only dependent on TIT, the turbine inlet pressure, the fuel composition that determines  $\gamma$  and the stator blades stagger angle that controls the flow cross-sectional area.

As the variation of  $\gamma$  between different fuels is less significant compared to the impact of the rest of the parameters in Equation 5.1 [106], a simplified expression of the flow compatibility results (Equation 5.2). In this regard the compressor/turbine matching is associated only with the variations of pressure ratio, the flow area and the volume flow rate for a given TIT.

$$\frac{\dot{m}_{in} \sqrt{\frac{TIT}{M}}}{A_{in} P_{o,in}} = const \quad (5.2)$$

In the case of syngas, the decreased molar mass, that is 27.03 g/mol compared to 28.26 g/mol for natural gas, leads to reduced mass flow and increased turbine inlet pressure in order to satisfy the flow compatibility (Equation 5.2). The problem is described in Figure 5.2 where the two points A and A' have been used to represent the design points of the natural gas fired turbomachine. For the increased pressure ratio the new turbine running point moves from A' to B' and the corresponding compressor point to B. This means that in order to maintain the matching between the two parts, the compressor back-pressure should increase resulting in a reduction of compressor stall margin and consequently, leading to compressor instability [107]. Thus, different running points need to be set in order to maintain the original matching between the compressor and the turbine when switching to syngas fuel.

Potential adjustments can be applied either separately on the compressor and the turbine design or in a combined way. For the purposes of the current project the effects were distinguished between the two parts of the turbomachine and technical solutions were investigated firstly for the compressor and then for the turbine, keeping the other part unaffected. The aspects related to each one of them are presented separately in the following sections.

## **Compressor Modifications**

Investigating the solution strategies with regard to the compressor design, an adjustment through which the compressor operation can be unaffected could be made by closing the Variable Guide Vanes (VGV) and hence reducing the mass flow coefficient. In that case, the turbine is running unaffected, at the original inlet temperature and the design modification applied is only related to the compressor.

Focusing on the solutions to the potential compressor stability, much work has been done investigating the potential geometric modifications of the compressor [105]. During that process a new mean-line compressor design was developed followed by CFD analysis. Restaggering of the compressor front four stator guide vanes was considered in order to adjust the compressor air flow and the compressor surge margin was re-established. Keeping the turbine design point fixed (TIT and volume flow rate), a reduction of about 2.5% of the original compressor inlet mass flow was predicted during that step, without any modifications of the cooling system taken into account. According to the new compressor/turbine matching, the pressure ratio is slightly higher than the original value, which in combination with the syngas higher specific heat leads to greater turbine enthalpy drop. The impact on the original turbine net power output was calculated to be about 7% and was considered as small variation compared to those found in the literature.

## **Turbine Modifications**

Allowing the compressor to operate at the original design point and the TIT being the same as on the natural gas fired machine, matching between the compressor and the turbine may be preserved by the opening of the first turbine bladerow. By restaggering the first stator and increasing the vane cross-sectional area a higher amount of mass flow rate is permitted to pass and turbine will operate at point C' in Figure 5.2. The compressor operating conditions will be then far from the surge line without any stability problems. For the chosen syngas fuel and turbine design, the optimum point for restaggering the first stator was opened by  $0.22^\circ$ . Regarding the turbine efficiency, a small reduction of about 0.2% was found compared to the original design that is related to the higher velocity losses as a result of the higher volume flow rate. That

reduction is consequently reflected to the gas turbine efficiency that was found to be about 0.4% lower than the corresponding natural gas fired turbine.

The new turbine operating conditions may introduce additional aerothermal and aeroelasticity issues. The increased volume flow rate could lead to turbine vibration problems, while the higher specific heat of the combustor gases should affect the turbine hot flow path. The issues related to the turbine aerothermal effects and forced response vibration, are the main objectives of the thesis and are discussed in detail in the following two chapters.

## **5.2 Summary**

The use of undiluted, hydrogen-rich syngas in an existing gas turbine brings about issues related to the compressor/turbine matching. For the purposes of the H2-IGCC project technical solutions were investigated with regard to the compressor and the turbine design. Among the design modifications presented in this chapter the restagging of the first turbine vanes was chosen for the syngas fired gas turbine maintaining the TIT.

# Chapter 6

## Hot Streaks Aerodynamics in 4-Stage Generic Turbine - comparison of fuel conditions

### 6.1 Introduction

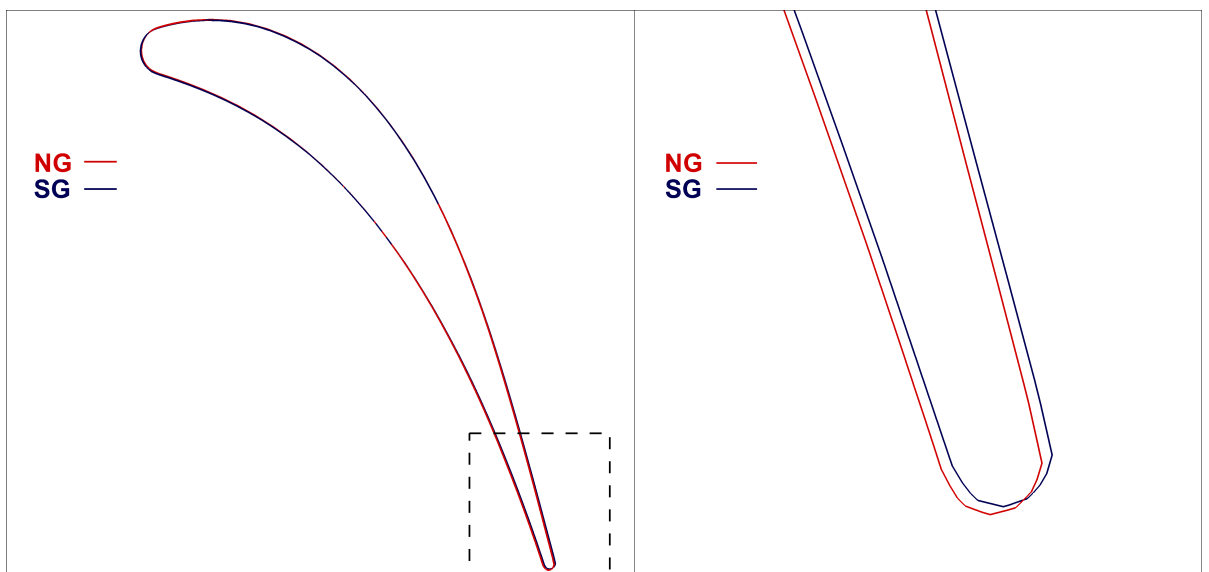
The hot streaks aerodynamics are presented in this chapter for the heavy duty natural gas and syngas fired H<sub>2</sub>-IGCC four-stage gas turbine. As syngas is expected to affect turbine aerodynamics and heat transfer characteristics, the migration behaviour of hot flow path through the stages needs to be investigated. Hot streaks, may exhibit differences of propagation and therefore affect the distribution of cooling and thermal stresses on turbine blades, thus the objective of this chapter is to provide a better understanding of the hot streaks migration pattern with respect to the fuel composition. As it was not possible to obtain a complete hot streak profile for the syngas fuelled machine during this project (no such tests were done by the end of the project), the baseline hot streak profile introduced in Chapter 4 is applied for the CFD analysis presented here which has been scaled in order to achieve the average stagnation temperature corresponding to the TIT. Hence, that study is confined to a known pattern of hot streaks from natural gas combustion that was used in analysis for both natural gas and syngas gas turbines. A boundary condition that consists of 24 non-identical hot streaks is applied at the turbine inlet to simulate the hot flow pattern up to the turbine

exit, with particular focus on the basic mechanisms that affect the turbine aerodynamics including the principal effects of segregation and radial migration. It is expected that a simulation of the hot gases flow pattern in a film cooled turbine will provide a better understanding of the complex nature of the hot gasses migration in a turbine. In addition, the results intent to contribute to a better understanding of the interaction of hot streaks with the coolant scheme as film coolant has not been commonly studied in that respect.

## 6.2 Hot Streaks Case Setup

### 6.2.1 H2-IGCC Turbine Overview

The baseline engine used for this study is a generic gas turbine based on the SGT5-4000F that was modified by opening the first stator blades by  $0.22^\circ$  in order to operate with syngas and maintain the compressor-turbine matching at the same design point (Figure 6.1). The blade configuration is shown in Figure 6.2 and the blade numbers for each stage are given in Table 6.1.



(a) Natural gas and syngas modified first stator blade (b) Closer view on stator TE for natural gas and syngas modification

Figure 6.1: H2-IGCC syngas turbine modification - 1<sup>st</sup> stator blade opening by  $0.22^\circ$

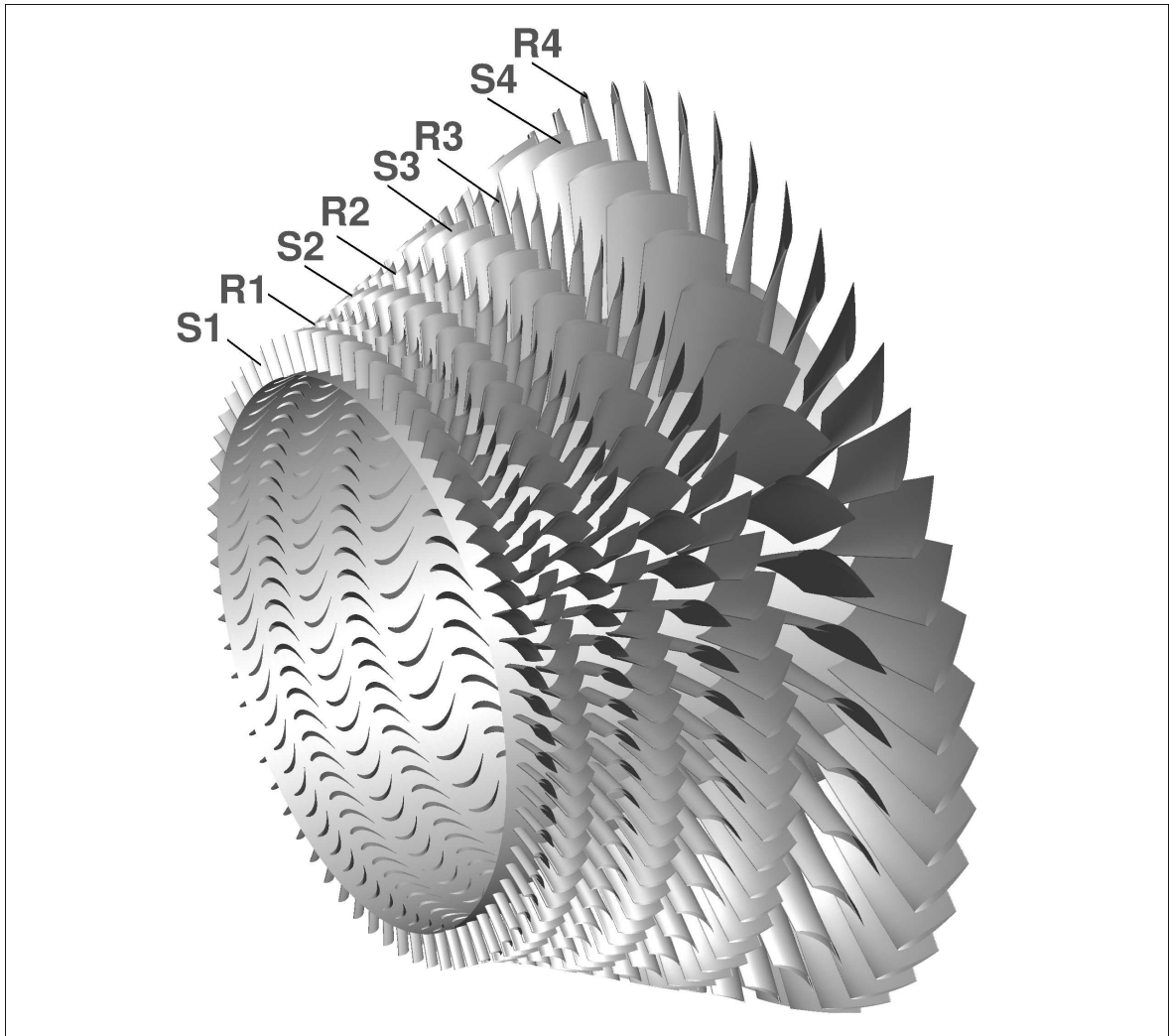


Figure 6.2: H2-IGCC four-stage generic turbine geometry based on SGT5-4000F

Turbine stage	Number of blades (stator/rotor)
1	69/79
2	66/77
3	51/61
4	35/41

Table 6.1: Geometric parameters for H2-IGCC turbine

As previously mentioned a full annulus multi-bladerow CFD analysis is conducted, due to the lack of common factor between the blade numbers and burners, in order to study the propagation of the hot streaks up to the exit of the turbine. Following the same approach as described in Chapter 4, 80 physical time steps were needed, which

based on multiples of the first stator bladerow means that 5520 steps were required to cover one revolution of the rotor for a rotational speed of 3000 rpm. The computational mesh for the whole turbine, shown in Figure 6.2, corresponds to 40 million points and the total wall clock time for one full revolution was about 6 days for a simulation performed in a parallel environment using 72 Intel Xeon cores of 2.5 GHz.

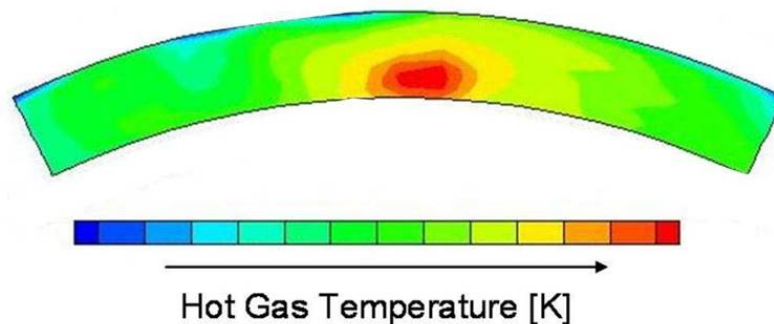
## 6.2.2 Boundary Conditions

For the current project, due to the lack of experimental data, the hot streak profile was calculated based on the data provided by industrial partners and introduced in Chapter 4 (Figure 6.3 (a)). The hot streak profile was randomly adjusted for each of the 24 hot streaks in order to impose variability of the peak temperature in both radial and circumferential directions as shown in Figure 6.3 (b).

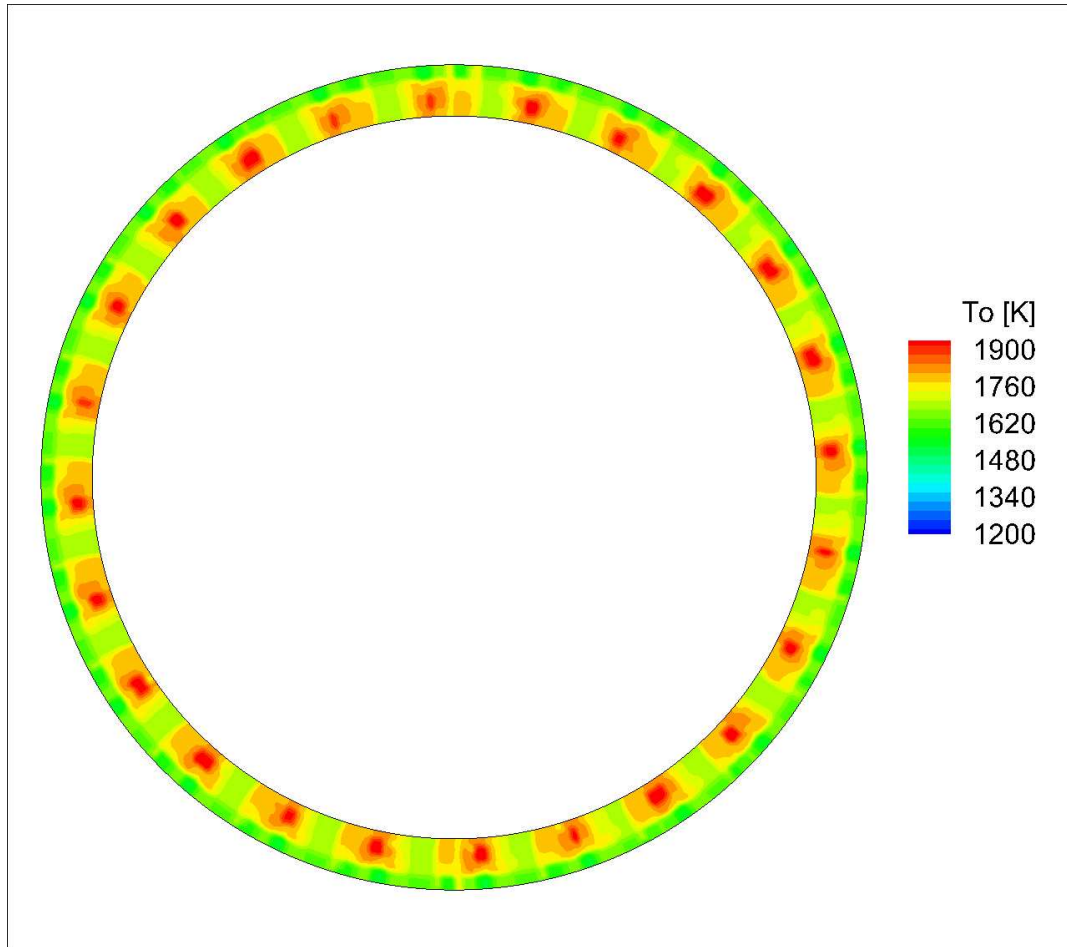
The radial location of the inlet peak temperature is between 20-30% span as shown in Figure 6.4 (a) against the average uniform inlet stagnation temperature. The corresponding Fourier transform of inlet stagnation temperature at 30% span is shown in Figure 6.4 (b) for both fuel conditions (natural gas and syngas). The higher harmonics of 24, 48 and 72 EOs are due to the number of hot streaks, with 24 being the fundamental harmonic and 48, 72 the integer multiples of that.

Fuel	$T_{o,in}$ [K]	$T_{o,out}$ [K]	$P_{o,in}$ [Pa]	$P_{o,out}$ [Pa]	$m_{in}$ [kg/s]	$m_{out}$ [kg/s]
NG	1713	810	1741039	109149	524.3	653.4
SG	1713	877	1743149	112617	516.8	647.3

Table 6.2: H2-IGCC turbine inlet-outlet average values - unsteady CFD results



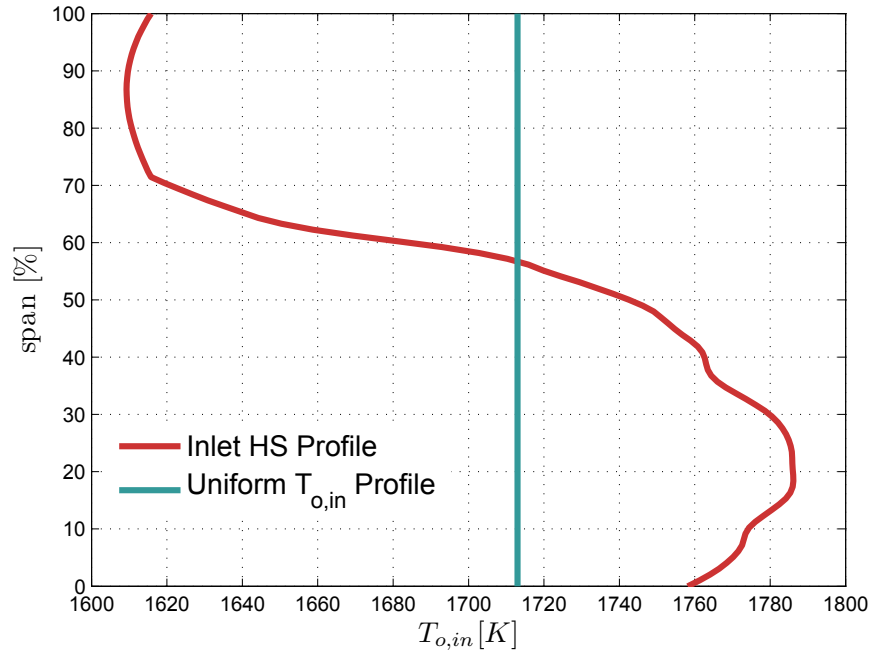
(a) SGT-300 hot gas temperature profile [108]



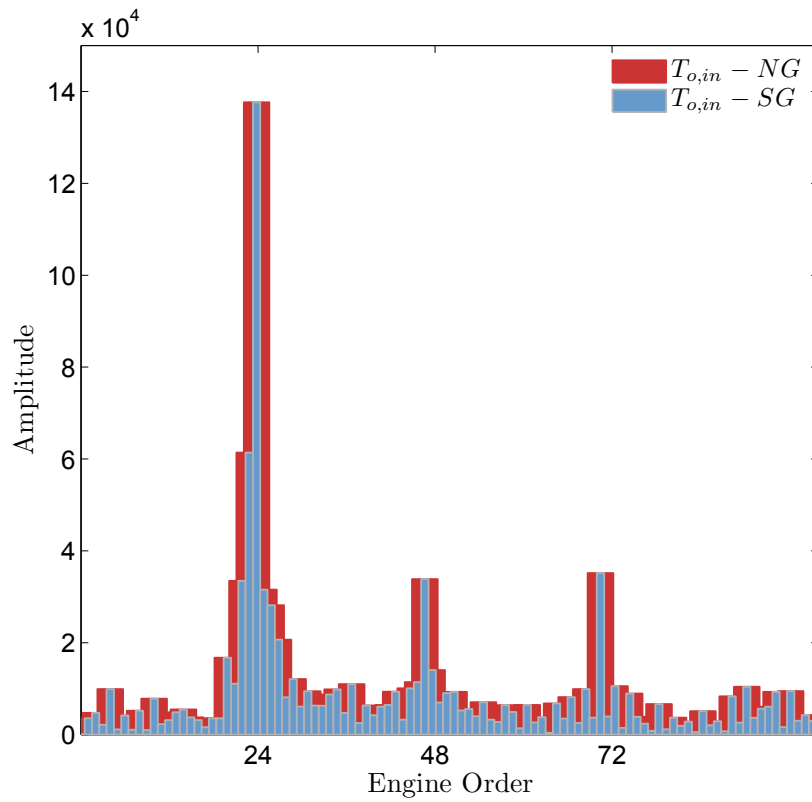
(b) H2-IGCC inlet hot streak profile simulated based on Figure 6.3 (a)

Figure 6.3: Stagnation temperature contours at the turbine inlet plane

For the comparison between the two fuels the temperature levels were kept the same between natural gas and syngas due to the lack of information for the case of syngas. In order to maintain same inlet stagnation temperature levels between the two fuels, density variations were adjusted for syngas using constant values of  $\gamma$  and  $R$ , equal to 1.28 and 307.7 J/kg K, respectively. The values of  $\gamma$  and  $R$  were defined for the average turbine inlet conditions based on NASA-polynomials [109] for the temperature dependence of the specific heat capacity. At the turbine inlet it was assumed that the stagnation pressure of the hot fluid is the same as in the main flow, as discussed in Chapter 4. Averaged values of inlet and outlet are presented in Table 6.2. The inlet stagnation temperature shown in that table is the average temperature after applying the hot streak profile. When uniform temperature conditions are applied, the average value of stagnation temperature at the turbine inlet is kept at the same value (1713 K).



(a) Circumferentially averaged spanwise inlet stagnation temperature profile



(b) Inlet stagnation temperature Fourier transform at 30% span for natural gas and syngas cases

Figure 6.4: H2-IGCC turbine inlet boundary conditions for CFD simulations

### 6.2.3 Film Cooling

For the fuel related comparative study a combustor exit temperature of 1713 K was used regardless the fuel (natural gas or syngas) being considered, as mentioned above. In the case of syngas the higher  $H_2O$  content is expected to change the heat transfer rate and result in increased turbine metal temperature. A solution that has been suggested in order to avoid turbine blade overheating and maintain the same firing temperature is the increase of turbine coolant [19]. For the current study the same percentage of coolant injection is applied in both fuel cases avoiding cross dependences between different parameters when investigating the effects of the fuel composition on the hot streaks aerodynamics.

Bladerow	Coolant		Coolant Temperature [K]
	Mass Flow [kg/s]		
	NG	SG	
S1	33.76	33.88	700
R1	32.57	32.22	700
S2	22.99	23.33	698
R2	18.57	18.96	698
S3	9.17	9.52	579
R3	12.07	12.61	579

Table 6.3: H2-IGCC turbine coolant properties per bladerow for natural gas and syngas

For the purposes of the project, different coolant configurations were investigated considering three values of coolant amount, 32.25 %, 25% and 20% of the compressor's inlet mass flow rate. A coolant mass flow rate of 25% of the compressor's inlet mass flow rate was finally chosen, that corresponds to approximately 130 kg/s [22] to cool the first three of the four turbine stages. Out of that amount 70% was injected to the turbine blades and 30% to end walls. Table 6.3 shows the coolant properties as have been concluded for the investigation of the hot flow path into the turbine for each fuel case. For the current simulation all the airfoils of the first three turbine stages are cooled using a local source term model presented by Romocea et al. [94].

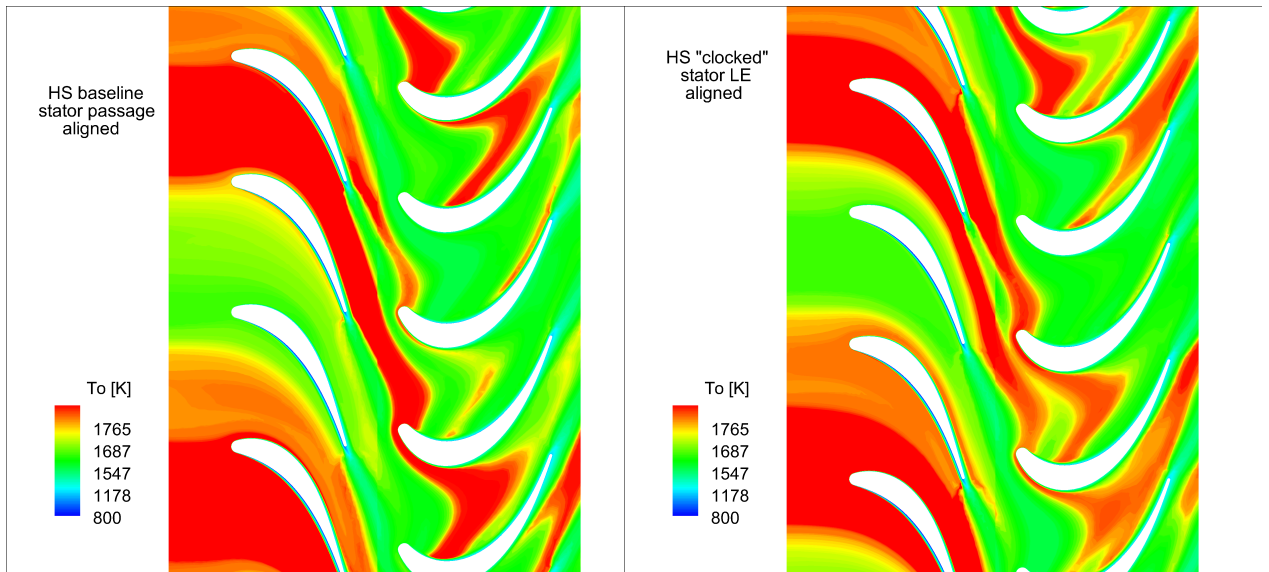
## **6.3 Unsteady CFD Analysis - Results and Discussion**

### **6.3.1 Hot Streaks Migration - Varying Circumferential Inlet Hot Streak Location**

The discussion about unsteady CFD analysis in this chapter is focused on the effects of the fuel composition on the turbine temperature redistribution and hence, the results are mainly presented in comparative basis. Before going into the comparison though, the effect of the circumferential inlet location of the hot streak injection is discussed as a result of the hot streak/stator configuration for the current turbine. The preferential heating of the blades PS downstream the first stator row, as a result of the segregation effect that has been discussed in Chapter 4, is one of the dominant mechanisms of the hot streak redistribution into the turbine. However, the effect is strongly dependent on the alignment of the hot streak to the first stator passage. When there is a common factor between the hot streaks and first stator blades the segregation effect can be controlled by "clocking" the hot streak with respect to the stator blades position. Depending on the exact clocking position and the temperature difference between hot and cold fluid, the segregation phenomenon can be weakened or even reversed, with the hot fluid convecting towards the SS of the first rotor blade.

For both turbines, the generic and the syngas fired, the random differences that have been created between the 24 hot streaks combined with the non-integer ratio between hot streaks and stator blades, result a non-repeating inlet temperature profile. The instantaneous stagnation temperature contour plots at 30% span in Figure 6.5 show the propagation of hot fluid through the first turbine stage for natural gas, while similar observations are made also for syngas (not included here). Assuming the case of hot streak aligned to the first stator passage as the baseline, cases in which the hot streak is shifted towards stator blades or is aligned to the stator LE, are considered as clocking positions. In the baseline case the kinematics of the hot streaks follow the preferential heating effect; Figure 6.5 (a) shows the strongest preferential heating effect. At the exit of first stator row, the cold streak convects towards rotor SS and the hot streak convects towards rotor PS without strongly interacting with each other. In the case where the hot streak is positioned towards the stator blade there is some interaction between the

hot and cold streak.



(a) Hot streak aligned to stator passage

(b) Hot streak aligned to stator LE

Figure 6.5: Zoom on different hot streak clocking positions at 30% span- NG

When the hot streak is aligned to the stator LE, the hot fluid is in phase with the stator wakes and the interaction between them may affect the preferential heating of rotor PS. In Figure 6.5 (b), where the hot streak is aligned to the stator LE, a weakened segregation effect is shown with the hot streak hitting the area around the LE and rotor SS, then forming a V-shape hot fluid as it moves towards the passage. The V-shape results from the effect of coolant injection that leads to slower convection of the hot fluid to the rotor surface boundary layer and is discussed in more detail in the following section.

The effect of the hot streak location with respect to the first stator blades on the downstream bladerows is shown in Figure 6.6. The instantaneous stagnation temperature contours along a half-annulus describe the propagation of hot streaks under different inlet hot streak positions and shapes at 30% span up to the turbine exit. It is clear that the magnitude of the effect on the third and fourth bladerow varies according to the inlet conditions. Two pathlines illustrated in this figure, correspond to the clocked and baseline hot streak positions. The clocked hot streak results a beneficial effect on the downstream blades in terms of hot spots creation, while the neighbour one, that is positioned aligned to the stator mid-passage, gives a stronger effect on the downstream blades with distinct hot spots being formed close to the stator blade of the third

bladerow. One may also observe that same inlet hot streak positions result differences in hot streak propagation and the magnitude of the effect on the last bladerows. This can be attributed to the varied hot streak shapes and sizes, since each one of the hot streaks was simulated independently resulting variations on the hot streak area in both circumferential and radial direction.

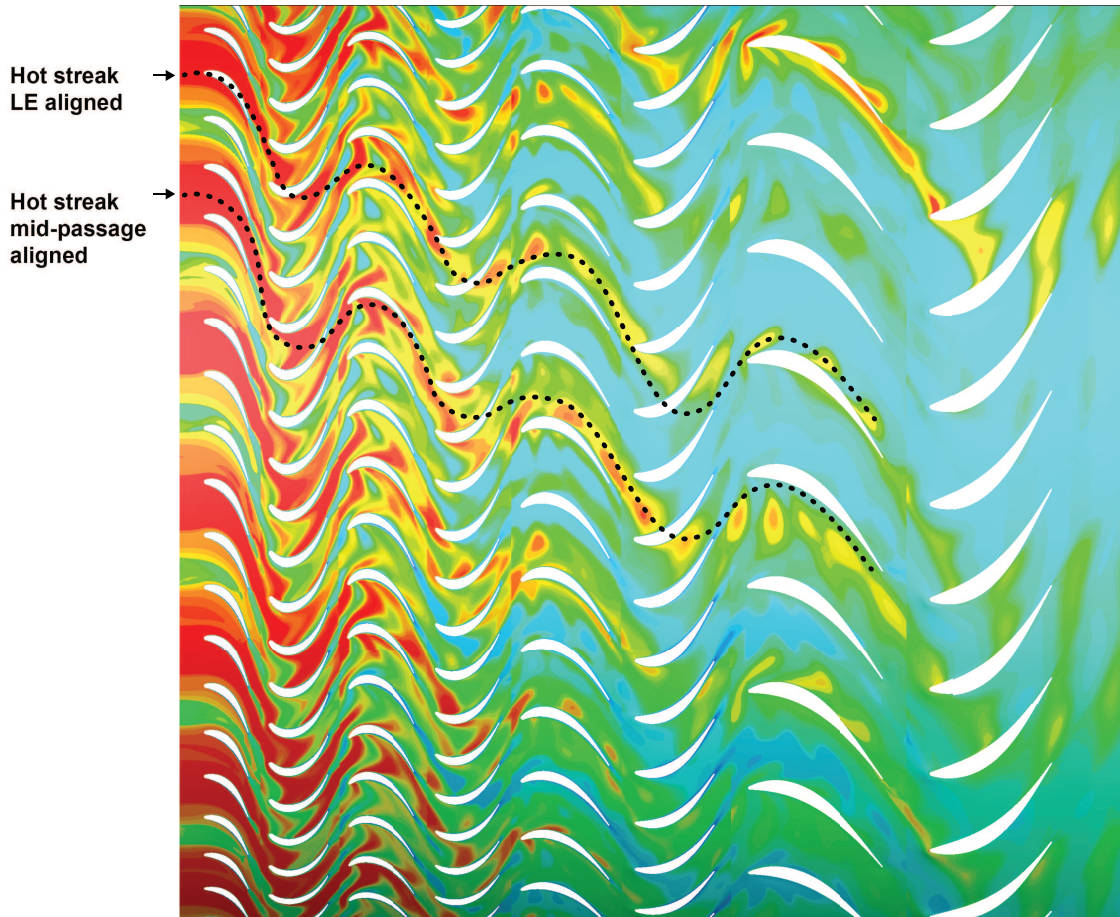
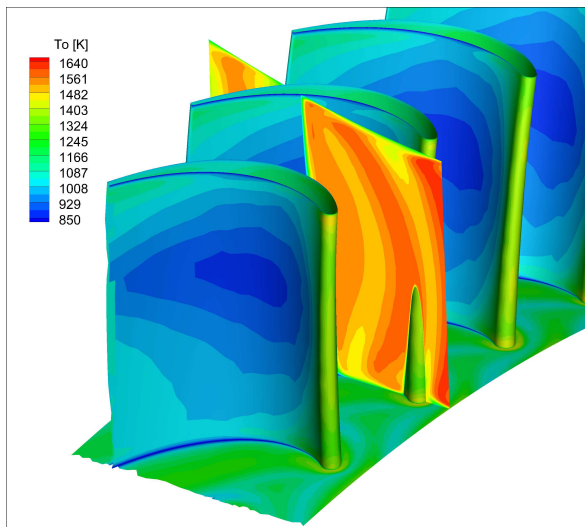


Figure 6.6: Stagnation temperature contours along the four stages at 30% span - NG

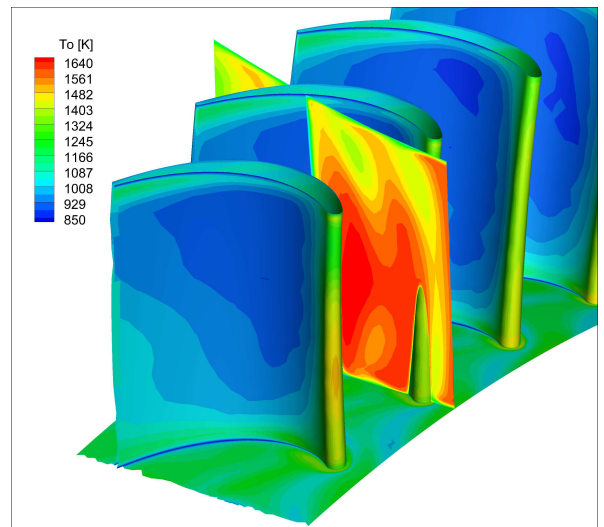
### 6.3.2 Hot Streaks Interaction with Blades Film Coolant

There are not many studies investigating the interaction of film coolant with the hot streaks propagation. The effect of the vane film coolant on the attenuation of the hot streak has been reported by Jenkins et. al [55] where independent regions of coolant injection were investigated, concluded that the vane SS film coolant exhibits the strongest effect on the weakness of the hot streaks. For the current turbine, film coolant is not limited to the first stator bladerow but is injected on the first three stages

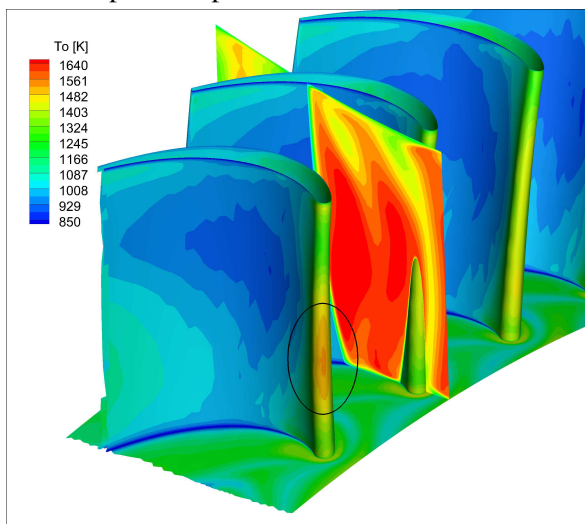
and shows greater effectiveness on the first rotor PS, even in the absence of hot streak injection when uniform inlet stagnation temperature conditions are applied.



(a) Stagnation temperature contours for uniform inlet temperature profile - NG



(b) Stagnation temperature contours for HS inlet profile - NG



(c) Stagnation temperature contours for HS inlet profile - SG

Figure 6.7: Stagnation temperature contours along R1 blade PS for different inlet temperature conditions and fuels

The effect of film coolant on the rotor PS is shown in Figure 6.7 where stagnation temperature contours are shown for different turbine inlet temperature and fuel conditions. The rotor PS remains at low temperature regardless the fuel composition and the inlet temperature profile being applied. The LE is exposed to higher heat loads with syngas exhibiting the greatest effect on that at the span location where the hot streak was injected as shown in Figure 6.7 (c).

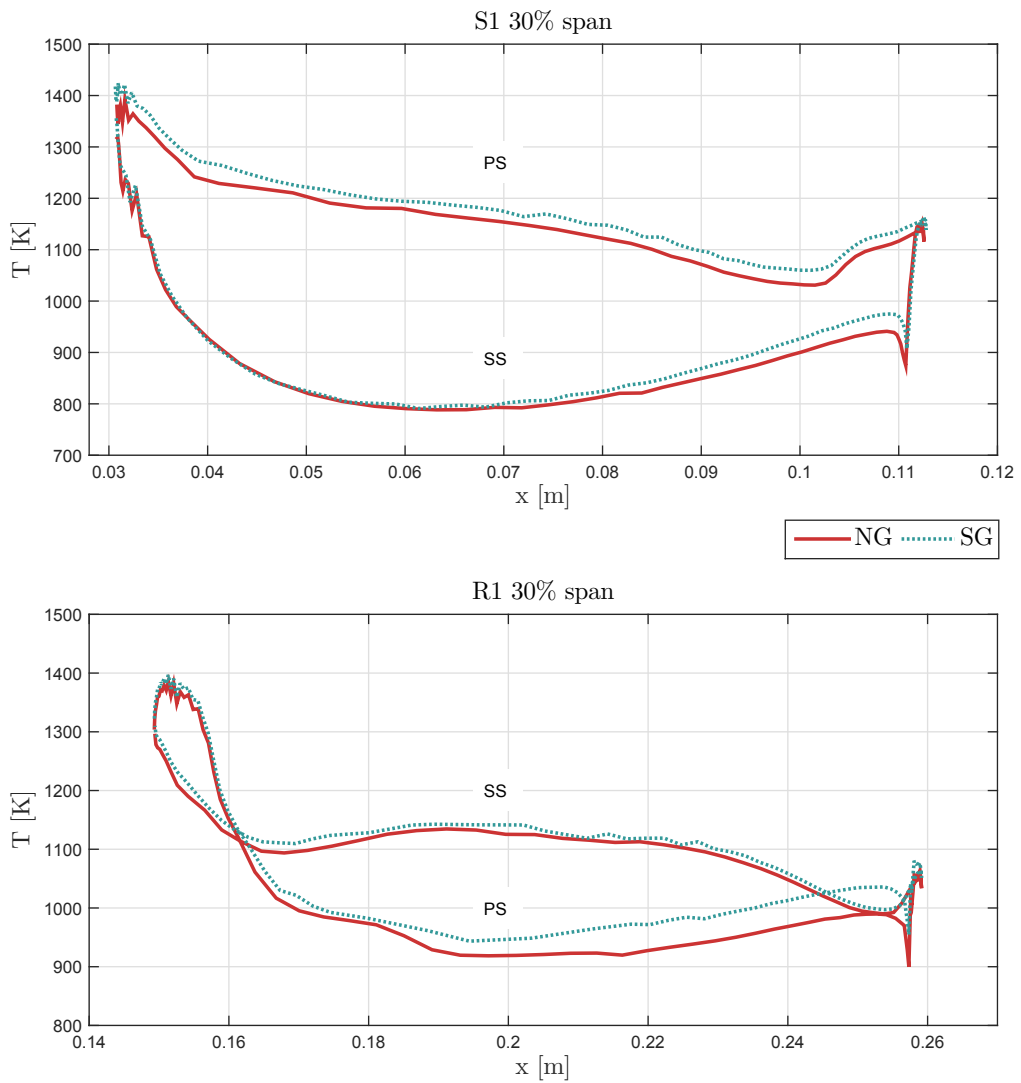


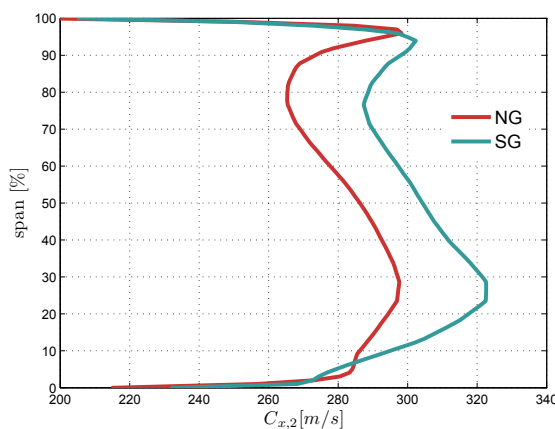
Figure 6.8: Static temperature profile along hot blades of 1<sup>st</sup> turbine stage at 30% span for natural gas and syngas

The increased heat load on the rotor LE can be observed also from the static temperature distribution along rotor hot blades at 30% span shown in Figure 6.8. Downstream the rotor LE area, at about 10% of the blade length, the temperature along the rotor PS exhibits a significant decrease compared to the rotor SS, that is not in agreement to the preferential heating effect of the hot streaks as discussed in Chapter 4. A combination of the circumferential location of the hot streaks injection with the rotor blade film coolant should be the reasons for the reversed effect of hot streaks on the rotor blade surfaces. In terms of fuel composition, syngas exhibits higher temperature val-

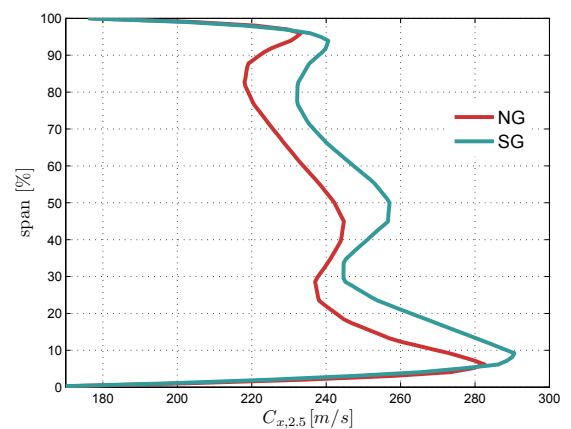
ues along the blades compared to natural gas; however, coolant injection is considered effective for both fuel types with the blade surface temperature meeting the safety margin targets set for each blade row [94].

### 6.3.3 Hot Streaks Propagation - Varying Fuel Composition

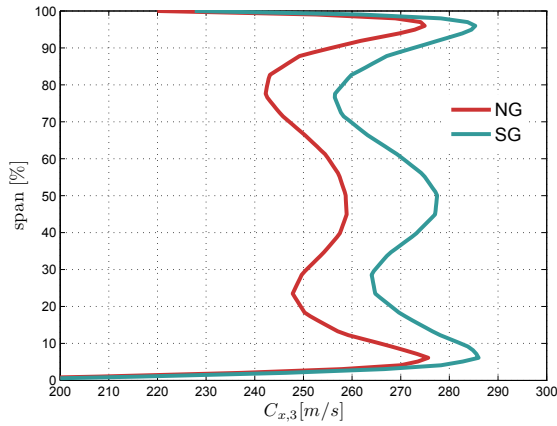
The effect of hot streaks on the shape of velocity triangles has already been discussed in Chapter 4. The hydrogen-rich syngas fuel combustion also influences the velocity triangles at the exit of each bladerow when compared to the natural gas fired gas turbine. The axial component of flow velocity ( $C_x = \sqrt{\gamma RT} Ma$ ) is affected by the fuel composition and the flow temperature, the latter being influenced by the decrease of  $\gamma$  and the geometric modification of the turbine, as the pressure drop is decreased due to the change of the throat area of the first bladerow, consequently increasing the turbine exit temperature. The counteracting effects may result in small or significant changes of the flow velocity depending on the flow conditions such as the syngas composition [18, 82].



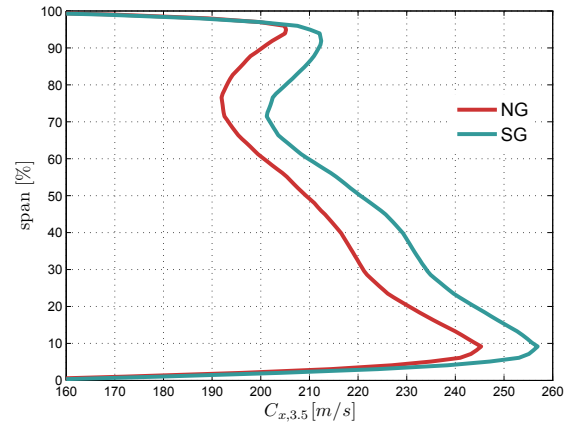
(a) Circumferentially averaged radial absolute velocity at the exit of R1 domain



(b) Circumferentially averaged radial absolute velocity at the exit of S2 domain



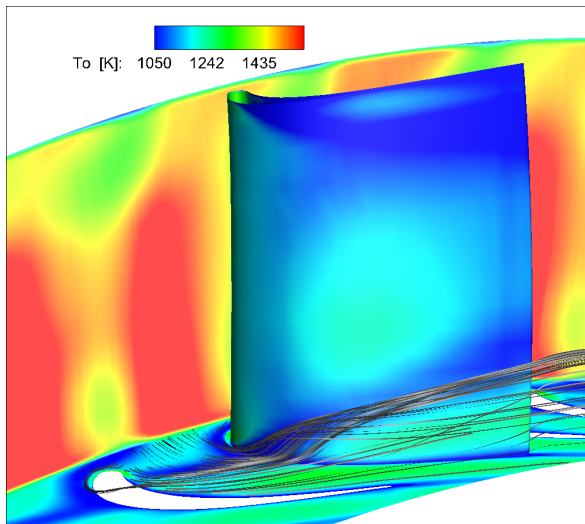
(c) Circumferentially averaged radial absolute velocity at the exit of R2 domain



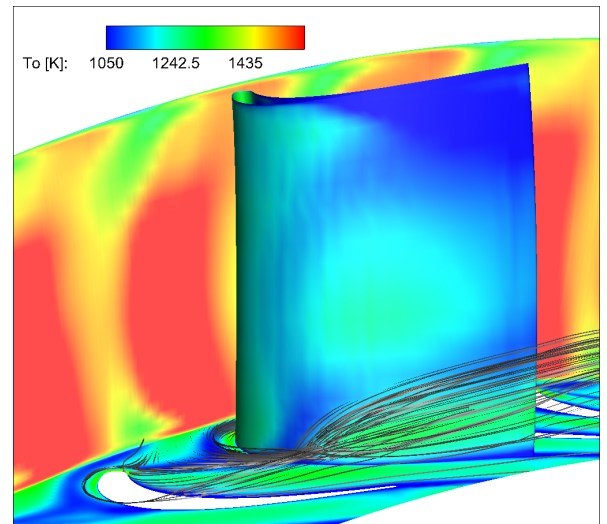
(d) Circumferentially averaged radial absolute velocity at the exit of S3 domain

Figure 6.9: Spanwise axial absolute velocity distribution at bladerows exit plane for natural gas and syngas

Figure 6.9 shows the spanwise distribution of the axial flow velocity at the exit of each bladerow for the reference natural gas fuel and the hydrogen-rich syngas. As discussed in Chapter 4, the spanwise circumferentially averaged velocity profiles were extracted at the exit plane of the absolute frame of reference. The velocity increase of syngas can be observed between 5-95% span along each bladerow exit plane indicating the effect of the increased flow temperature under the same blade coolant conditions. The syngas displays a more intense flow turning that is also slightly moved along span compared to natural gas profile.



(a) Streamlines through R1 passage and stagnation temperature contours - NG



(b) Streamlines through R1 passage and stagnation temperature contours - SG

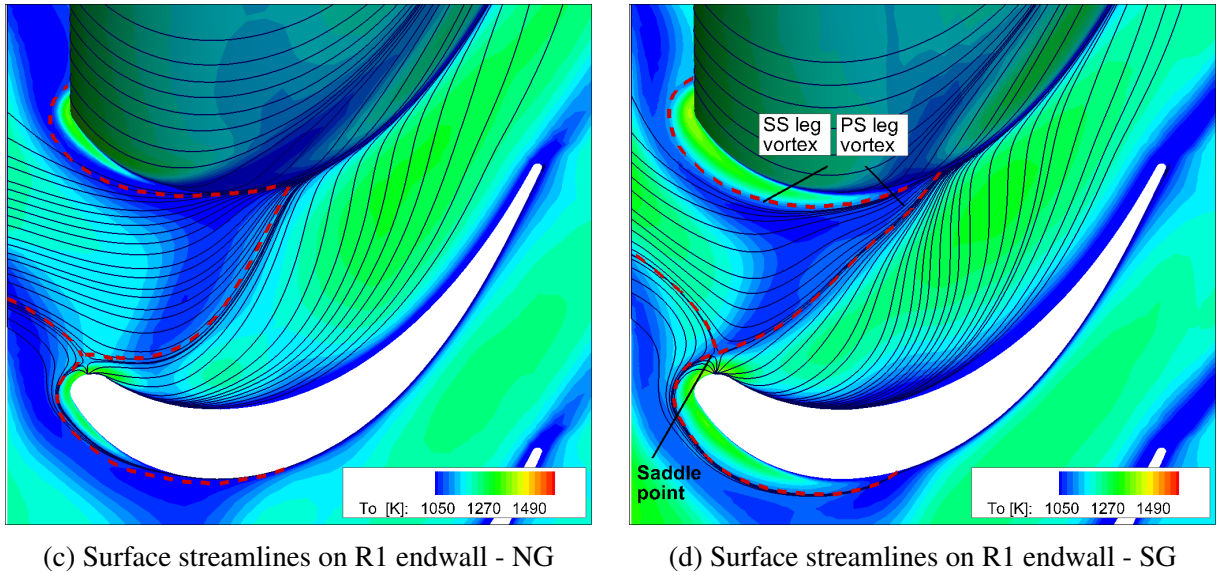


Figure 6.10: Horseshoe vortex system on R1 passage for natural gas and syngas cases

The observation can be better explained in combination with Figure 6.10 (a), (b) where the volume streamlines through one rotor passage show the secondary vortices near the hub endwall and Figure 6.10 (c),(d) where the surface streamlines on the rotor hub endwall identify the saddle point and the horseshoe vortex for natural gas and syngas, respectively. It is well known that upstream variations of axial flow velocity and consequent direction of the approaching flow on the LE of the downstream bladerow has an impact on the saddle point position and the development of the horseshoe vortex. The turning of the streamlines near the rotor LE is higher as well as the distance of the saddle point from the blade LE in case of syngas (Figure 6.10 (d)) compared to natural gas (Figure 6.10 (c)) indicating a smaller horseshoe vortex for the natural gas case. In effect, there is stronger deflection of the streamlines along the SS of the first rotor blade for syngas case compared to natural gas (Figure 6.10 (a), (b)). In addition, the differences in the wake shape which can be observed between Figure 6.10 (c), (d) show a more concentrated wake shape for syngas and will be discussed in more detail in the following section.

The higher flow turning of the horseshoe vortex in syngas case will in turn affect the secondary losses. Previous studies [3] have shown the effect of the horseshoe vortex on the evolution of secondary flow into the blade passage. An illustration of the development of secondary vortices is shown in Figure 6.11 describing the direction and

magnitude of each contributor. The pair of horseshoe vortex legs remains small as it propagates through the blade passage and its sense of rotation is opposite to the rotation of the main hub passage vortex. Although the intensity and length of the horseshoe vortex are relatively small, the vortex pair still affects the evolution of secondary losses and hence, the radial migration of the hot streak centre as it passes through the rotor blade passage.

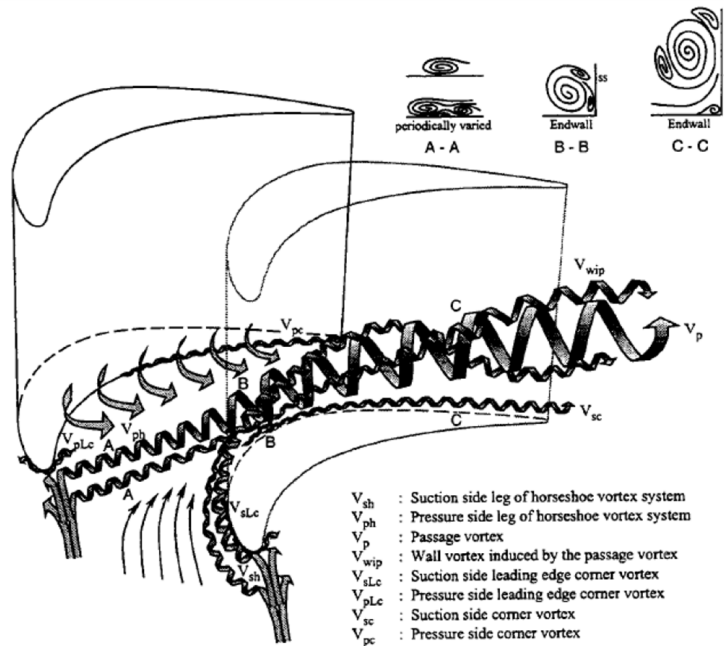
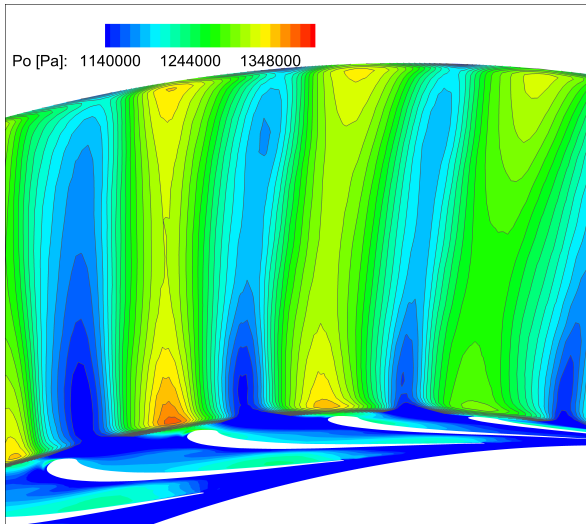
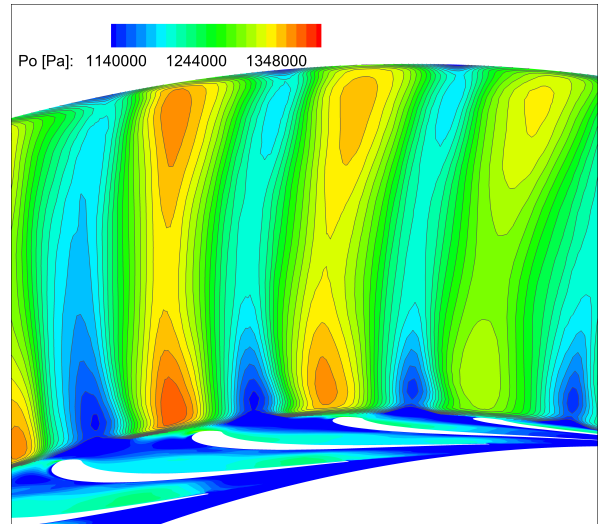


Figure 6.11: Secondary flow development through blade passage [3]

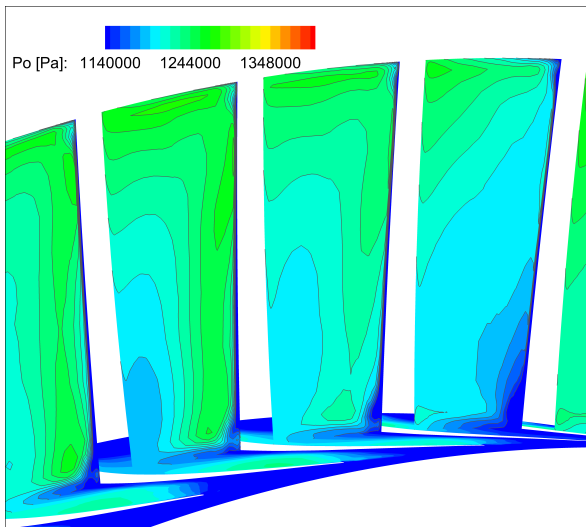
The impact on the secondary losses and the hot streak migration at the exit of the first rotor bladerow for one hot streak position is described in Figures 6.12 - 6.13. The stagnation pressure contours are shown in Figure 6.12 for three axial positions throughout the rotor passage, inlet, mid-chord and outlet, for the two fuel cases. In Figures 6.12 (e), (f) the contour plots indicate the pressure drop and hence, the secondary losses near the hub to be less significant in case of syngas compared to natural gas. As the horseshoe vortex leg propagates through the passage weakens the over turning near the hub because of its opposite direction to the passage vortex. In addition, the centre of the secondary vortex appears in different spanwise location between the two fuel cases, with the minimum stagnation pressure flow region being located closer to the hub endwall for the natural gas case compared to syngas. The interaction with the hot streak and the effect on the hot streak shape is shown in Figure 6.13



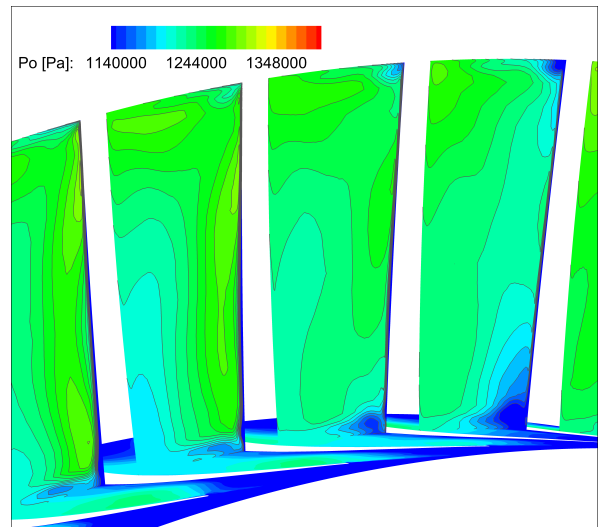
(a) Stagnation pressure contours at R1 inlet,  $x=0.14$  m - NG



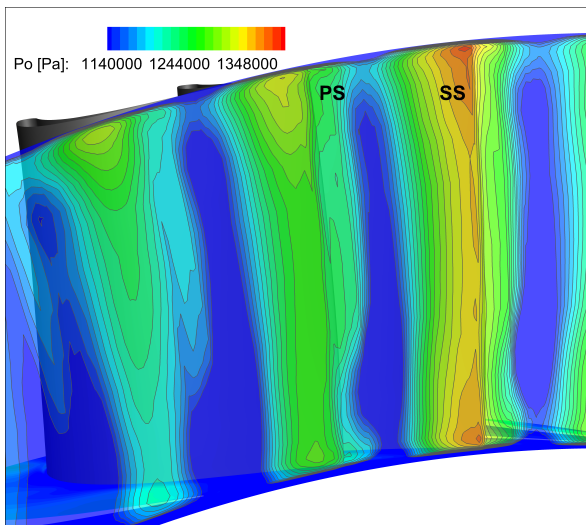
(b) Stagnation pressure contours at R1 inlet,  $x=0.14$  m - SG



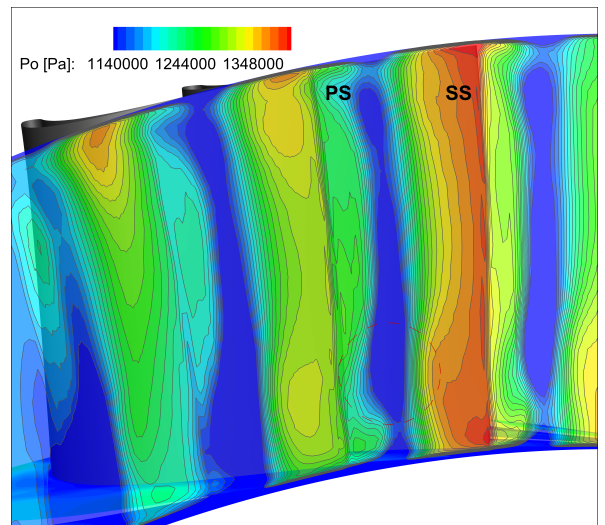
(c) Stagnation pressure contours at R1 mid-chord,  $x=0.20$  m - NG



(d) Stagnation pressure contours at R1 mid-chord,  $x=0.20$  m - SG



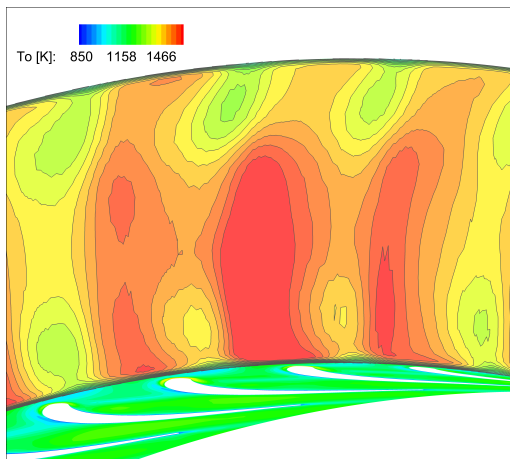
(e) Stagnation pressure contours at R1 outlet,  $x=0.27$  m - NG



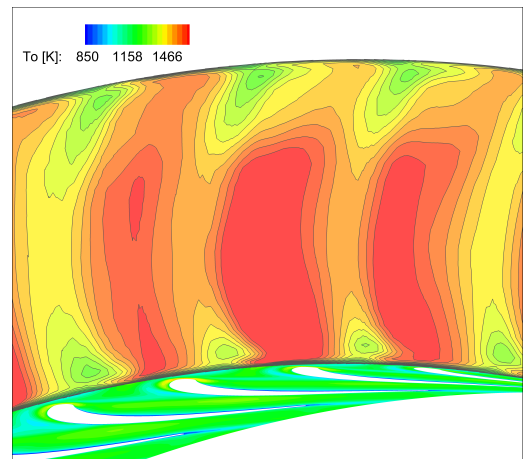
(f) Stagnation pressure contours at R1 outlet,  $x=0.27$  m - SG

Figure 6.12: Stagnation pressure contour plots at R1 exit for natural gas and syngas

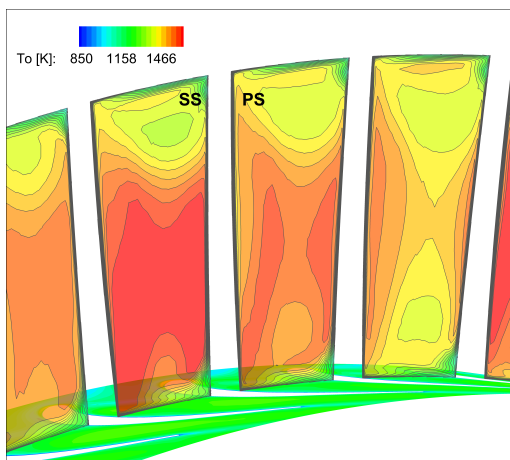
The stagnation temperature contours in Figure 6.13 show the propagation of one hot streak through the rotor passage and the alteration of hot streak shape under the influence of secondary flows for the corresponding to Figure 6.12 locations. The radial migration of the hot streak for the case of syngas is higher with the hot fluid moving radially towards both the hub and tip as it propagated towards the exit of the rotor passage resulting in more stretched shape. In effect, the hub and tip areas should experience higher heat load in syngas case considering also the increased temperature values of syngas compared to natural gas. A similar tendency of the hot streak migration along the span can be observed also for the neighbour bladerow shown in Figure 6.14 where a hot streak propagates throughout a passage of the second stator row.



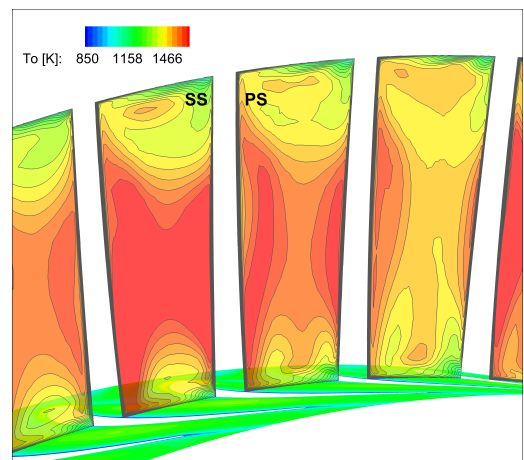
(a) Stagnation temperature contours at R1 inlet,  $x=0.14$  m - NG



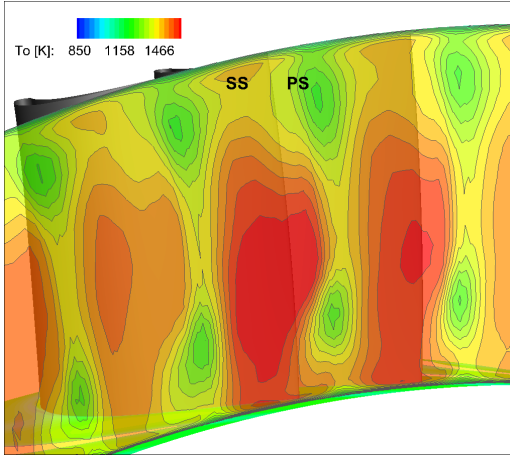
(b) Stagnation temperature contours at R1 inlet,  $x=0.14$  m - SG



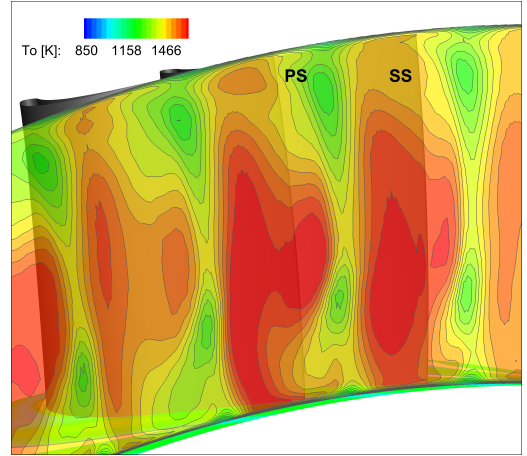
(c) Stagnation temperature contours at R1 mid-chord,  $x=0.20$  m - NG



(d) Stagnation temperature contours at R1 mid-chord,  $x=0.20$  m - SG

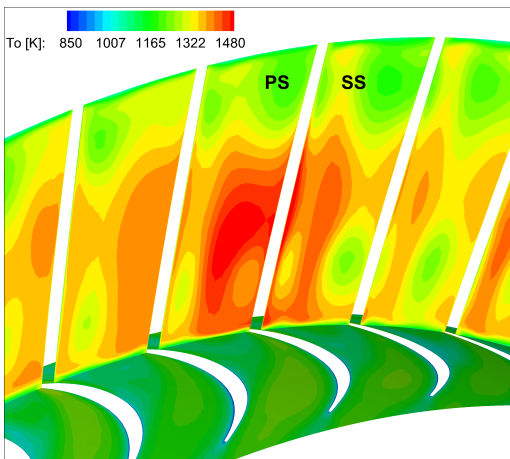


(e) Stagnation temperature contours at R1 outlet,  $x=0.27$  m - NG

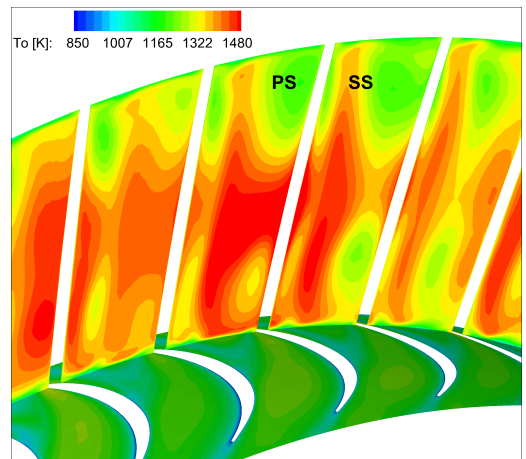


(f) Stagnation temperature contours at R1 outlet,  $x=0.27$  m - SG

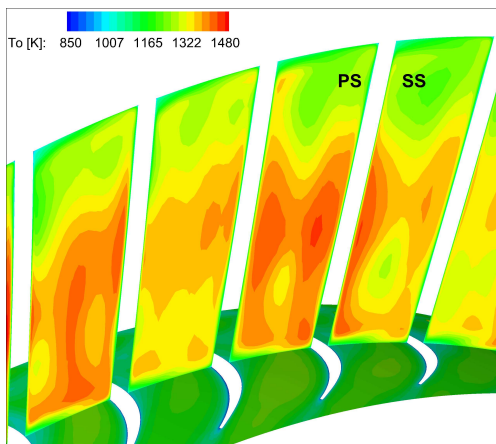
Figure 6.13: Hot streak propagation through R1 passage for natural gas and syngas



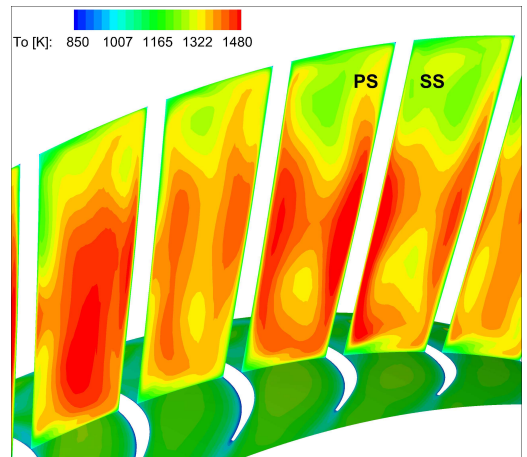
(a) Stagnation temperature contours at S2 inlet,  $x=0.3$  m - NG



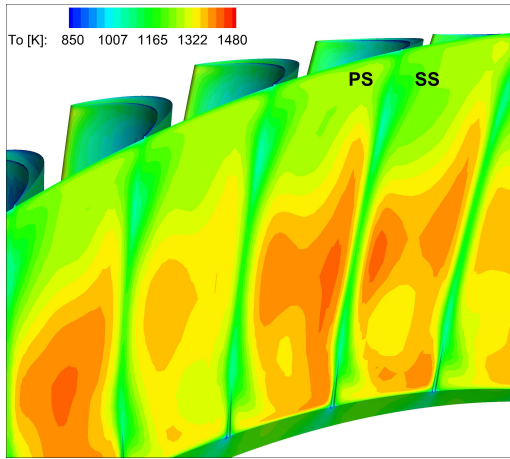
(b) Stagnation temperature contours at S2 inlet,  $x=0.3$  m - SG



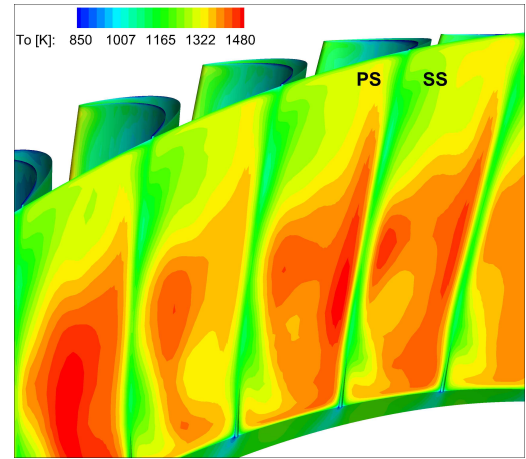
(c) Stagnation temperature contours at S2 mid-chord,  $x=0.35$  m - NG



(d) Stagnation temperature contours at S2 mid-chord,  $x=0.35$  m - SG



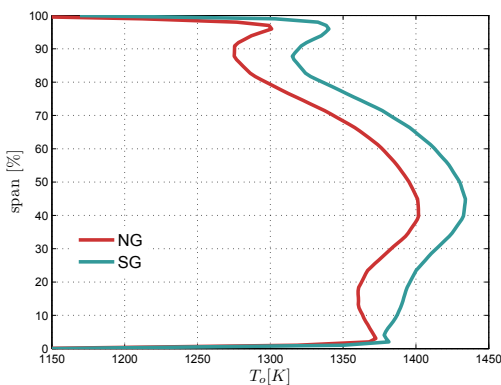
(e) Stagnation temperature contours at S2 outlet,  $x=0.42$  m - NG



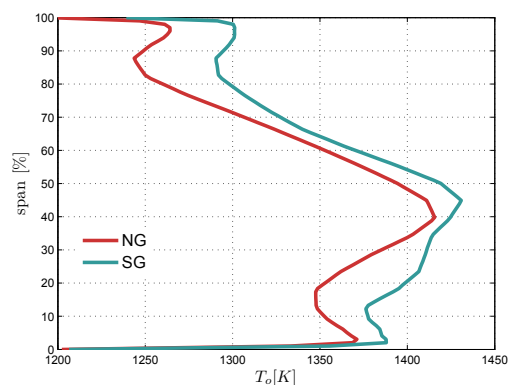
(f) Stagnation temperature contours at S2 outlet,  $x=0.42$  m - SG

Figure 6.14: Hot streak propagation through S2 passage for natural gas and syngas

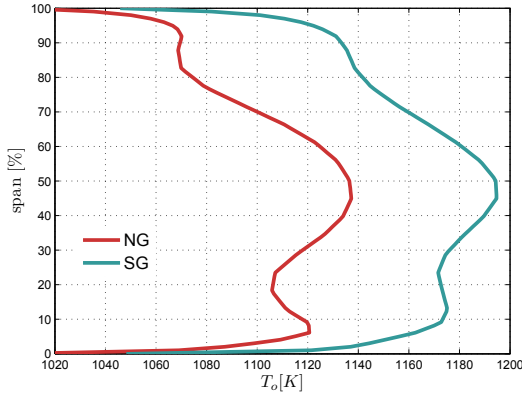
The spanwise distribution of circumferentially averaged stagnation temperature is shown at the corresponding exit planes of each bladerow in Figure 6.15. The syngas hot streak centre moves slightly towards the hub and exhibits a higher spanwise diffusion of the temperature profile compared to natural gas confirming the observations made above for the first rotor and second stator bladerows. The hot streak radial migration is strongly related to the passage secondary flows, as the steeper velocity gradients in syngas case compared to natural gas case, result into increased stretching of the streamwise vorticity structure. In addition, the radial gradient of the stator exit flow angle is affected by the modification of the stator blades and the opening the throat in order to adjust the turbine to the syngas flow conditions, which in turn, alters the radial distribution of circulation into the first rotor passage.



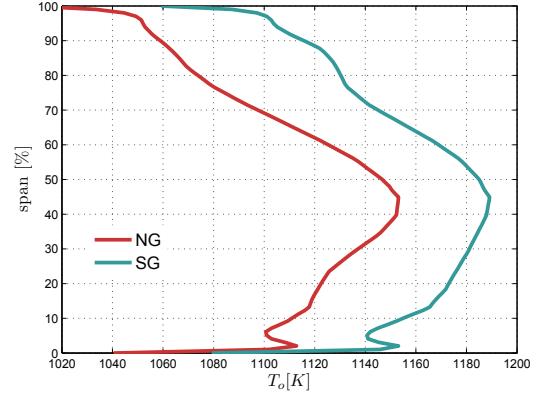
(a) Circumferentially averaged radial stagnation temperature at the exit of R1 domain



(b) Circumferentially averaged radial stagnation temperature at the exit of S2 domain



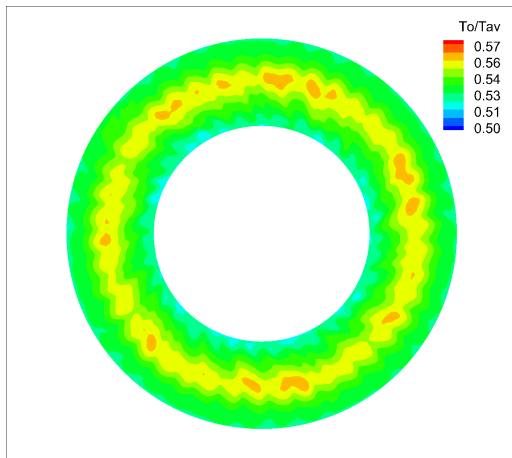
(c) Circumferentially averaged radial stagnation temperature at the exit of R2 domain



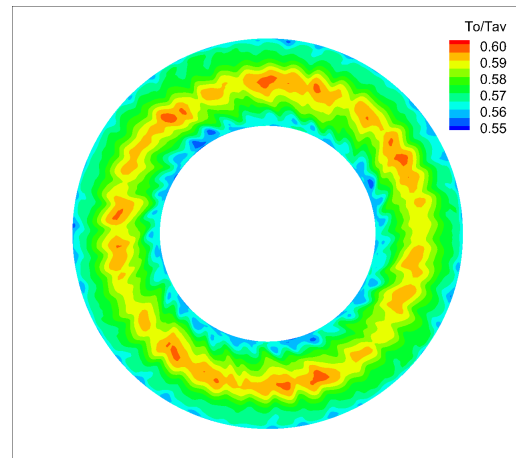
(d) Circumferentially averaged radial stagnation temperature at the exit of S3 domain

Figure 6.15: Spanwise stagnation temperature distribution at bladerows exit plane for natural gas and syngas

At the outlet of the turbine, the peak temperature has been moved radially between 50-60% span with syngas resulting to higher peak temperature compared to natural gas as shown in Figure 6.15 (d) by approximately 8% difference in average temperature levels. Figure 6.16 shows the normalised stagnation temperature contours where circumferentially distinct hot areas are apparent for both fuel types. Hot streaks propagate through the four stages and are still obvious up to the turbine exit with the magnitude of the effect being higher in Figure 6.16 (b) due to the higher temperature levels for syngas compared to natural gas. The values of temperature have been normalised based on the TIT which is the same for both fuels.



(a) Normalised stagnation temperature at R4ex domain - NG



(b) Normalised stagnation temperature at R4ex domain - SG

Figure 6.16: Instantaneous stagnation temperature contours at turbine exit

### 6.3.4 Hot Streaks Effects on Stator Thermal Wakes

Figure 6.17 shows the circumferential stagnation temperature at the exit of first stator at 30% span with a zoom of one hot streak wake, that corresponds to approximately 3 vane wakes. The Fourier transform of the temperature signal at the same spanwise location reveals the main harmonics due to the temperature distribution.

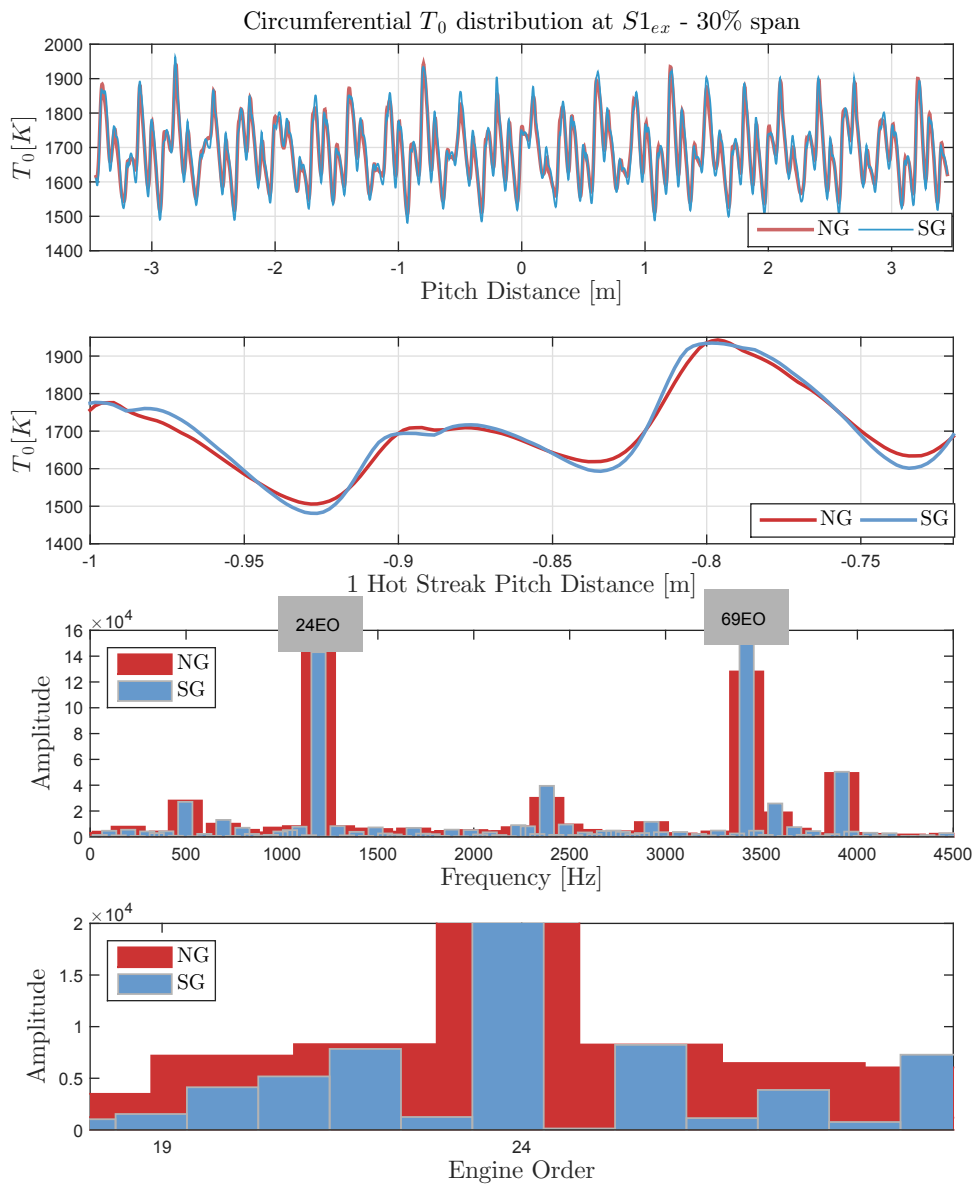


Figure 6.17: Circumferential stagnation temperature profile and FFT at  $S1_{ex}$  plane at 30% section with closer view of one hot streak vane wake and the 19 EO amplitude

A closer view of the lower harmonics in Figure 6.17 reveals a different pattern with slightly higher temperature amplitude for the case of natural gas compared to syngas. That can be explained by the shape of the thermal wake as shown in the same figure (second plot). The wakes that correspond to one hot streak in case of syngas seem to be more concentrated resulting in lower minima and higher maxima which is further explained below.

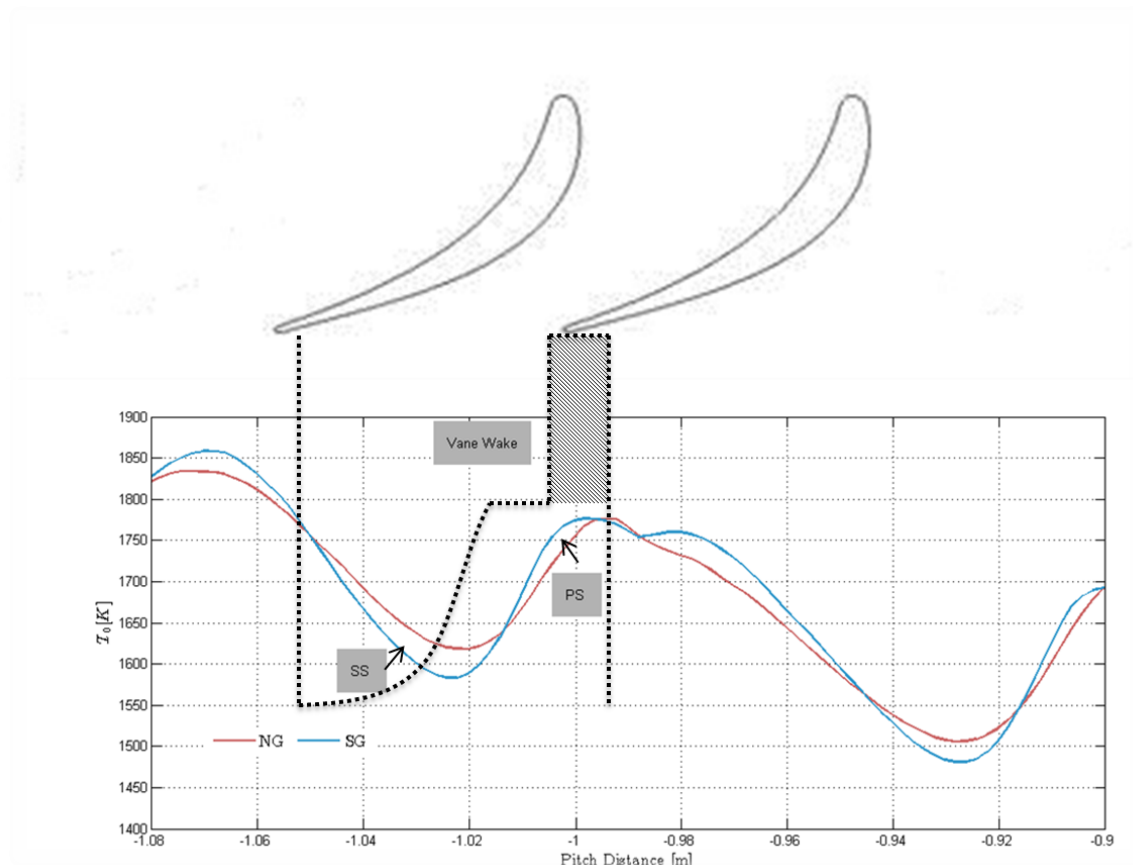


Figure 6.18: Circumferential stagnation temperature profile at  $S1_{ex}$  section at 30% with the theoretically predicted circumferential profile

The 24 EO is related to the 24 combustor cans, the 69 EO is related to the number of stator blades, while additional lower amplitude harmonics are multiples of those two fundamental frequencies. Based on the FFT signal, the syngas case gives slightly higher stagnation temperature amplitudes. Figure 6.18 shows a schematic of the first stator airfoils combined with the stagnation temperature profile at 30% span, as in Figure 6.17. Based on the theory of the thermal wakes transportation as has been described by Kerrebrock and Mikolajczak [38] the theoretically predicted circumferential tem-

perature profile was drawn (dashed line) on top of the CFD results. The main feature of the theoretical profile is a peak temperature near the stator PS, followed by a plateau and a decrease near the SS. The magnitude of the temperature peak (hatched area) increases with tangential Mach number and relative flow angle, with syngas resulting in higher stagnation temperature excess in stator wake. The temperature excess in the wake near the PS times the thickness of the wake gives the energy flux impinging on the stator PS. This means that for syngas there is a higher concentration of high energy fluid near the PS and lower near the SS. The result is of great importance and will be the basis for the analysis of the LEO excitation results presented in the next chapter.

## 6.4 Summary

In this chapter the aerodynamic effects of hot streaks propagation into a heavy duty four-stage HP turbine are discussed with particular attention to the fuel composition. A natural gas fired generic turbine has been compared to a modified syngas fired turbine for the unsteady multi-blade row CFD analysis. Both turbines have been set up under the same inlet boundary conditions and coolant flow scheme.

The effects of the circumferential location of the hot streaks injection is discussed first as the non-integer factor between the hot streaks and stator blades results in different hot streaks alignment configuration. The strength of the segregation effect on the first rotor bladerow is affected by the misalignment of the hot streak with the inlet stator passage that is termed as hot streak "clocking".

The effects of syngas on the propagation of the hot fluid were studied. The hydrogen-rich syngas chosen for this work in combination with the applied turbine modification - opening the first stator bladerow - leads to a lower pressure drop and increased temperature at the exit of the turbine. As an effect of the fuel composition, the hot gas flow path exhibits differences compared to the reference natural gas fuel. The significant changes of the velocity deficit and consequently enhanced secondary flow has been shown with regard to the effects on the hot streak centre migration along the first rotor blade span. In addition, the effects of film coolant on the hot streaks migration are shown with reverse results on the preferential heating effect of the first rotor PS. Observation of the temperature contour plots shows effective prevention of hot fluid

convection to the rotor boundary layer due to the film coolant for both fuels. However, compared to natural gas, syngas blade temperature profiles show higher values by approximately 8% difference in average temperature levels.

Finally, the effects of fuel composition on the thermal wakes exiting the first stationary frame are discussed. Fourier transform of circumferential temperature distribution was applied to describe the difference in amplitude at the exit of first stator row between the two fuels. Syngas results in higher temperature amplitudes for BPFs but not for LEOs. Interpretation of the wake profile at stator exit reveals a different wake shape for syngas that comes more concentrated compared to natural gas as a result of differences in composition and hence in vane exit velocities. That is of great importance as a different flow pattern is created and propagates through the turbine with consequent effects on the structural part of the turbine as well as those will be discussed in the next chapter. However, it is necessary to point out the dependency of the results on the hot flow pattern applied for this study.

# **Chapter 7**

## **Investigation of Low Engine Order Excitation of 1<sup>st</sup> Rotor due to Temperature Distortion**

### **7.1 Introduction**

The unsteady harmonic forcing distribution acting on the rotor blade due to incoming temperature disturbances is related to the LEO forced response excitation. Addressing fuel variability, for the current study of hydrogen-rich syngas, the fuel composition adds an extra parameter related to the turbine hot flow pattern which in turn, will affect the rotor blades vibration due to the inlet temperature non-uniformities. The results presented in Chapter 6 focused on the aerodynamic effects of hot streaks into the H<sub>2</sub>-IGCC generic and syngas turbine. Following the aerodynamic analysis and referring to the same geometric, coolant and boundary conditions, this chapter deals with the effects of hot streaks on the LEO excitation of the downstream rotor blade. The forced response computations were conducted using the unsteady aeroelasticity model described in Chapter 3. The analysis is limited to the first rotor row and is presented in a comparative basis between the syngas and natural gas fired gas turbine.

## 7.2 Overview of the Forced Response Model

The forced response analysis consists of the modal analysis of first rotor blade assembly and the 3D unsteady CFD simulation of the first stages as has been described in Chapter 3. Standard FE analysis techniques are applied to obtain the natural frequencies and mode shapes. In order to predict the frequency-speed Campbell diagram and obtain the associated mode shapes. The prestressed modal analysis is performed taking into account the centrifugal forces. The undamped free vibration modal model is solved to calculate the modal properties of the system at different rotational speeds between 0-3000 rpm. The predicted frequencies are plotted on a Campbell diagram for each ND. Intersections of EO lines with the blades natural frequencies at the speed of interest indicate a potential excitation during the operation of the gas turbine. Based on Campbell diagram the forced response analysis is conducted for the potential resonance conditions (corresponding EO and mode shape) to calculate the amplitude of the aerodynamic forcing under those conditions. Once a crossing between a natural frequency and an EO is identified, close to the design speed (3000 rpm), the corresponding mode shape is mapped into the flow model by interpolation to the CFD mesh. After the mode shapes interpolation into the CFD mesh the modal force is calculated for each iteration from the CFD code. For each one of the interpolated mode shapes the blade excitation is provided by the inlet hot streak profile that is presented in Chapter 6, consisting of 24 NDs. The aim is to provide forced response calculations for different resonant conditions arising from both BPF and LEO excitation sources at the design speed and identify the effects of the fuel composition on the phenomenon. To predict the excitation levels in a forced response analysis a whole annulus, multi-stage unsteady CFD calculation is necessary to deal with the losses of symmetry that give rise especially to LEO excitation.

### 7.2.1 Modal Analysis Setup

#### Boundary Conditions

For the modal cyclic symmetry analysis, one sector of the first rotor disk was modelled to calculate the modal properties. The difference between the stiffness of the simulated

solid rotor blade and the actual one should be mentioned; the actual rotor blade is lighter as there is a number of cooling holes, shown in Figure 7.1. Since the purpose of the study is to provide comparison of the results between the two fuel cases, it was not necessary to add this complication and hence, a solid blade was assumed. The blade geometry was provided by the project partners at RWTH Aachen. The first rotor disk was drawn based on Figure 7.2. where the cross section of the gas turbine is shown. A sketch of the bladed disk FE model is shown in Figure 7.3, including the FE mesh and the boundary conditions.

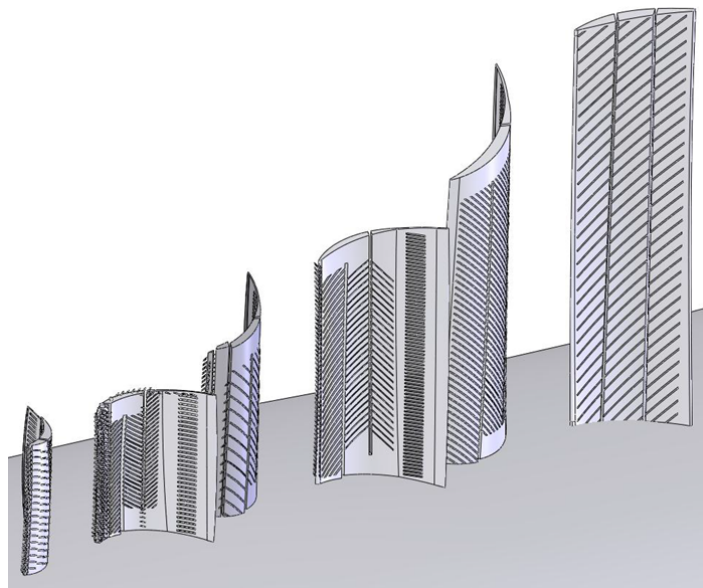


Figure 7.1: H2-IGCC 3-stage cooling geometry overview [4]

In ANSYS the boundary conditions consist of the structural loads and constraints. In order to solve the free response vibration problem the only loads applied for the modal analysis are the inertia loads caused by the rotation of the structure. Boundary conditions include all Degrees Of Freedom (DOF) constraints (displacement constraint in x,y,z direction) at the inner disk diameter plus zero DOF at z direction at the connection between the rotor disk and the neighbouring stator disks. Since the model is symmetric with respect to the rotation axis, cyclic symmetry boundary conditions were applied. By using cyclic symmetry in ANSYS constraint relationships between the high and low edges of the sector are defined for a single sector which is repeated at  $4.557^\circ$  around the axis. The rotor disk sector contains approximately 27,500 20-node solid elements and 43,000 nodes. Taking into account the centrifugal forces, the modal

analysis is conducted for different speeds (0, 1000, 2000, 3000 rpm) in order to draw the Campbell diagram. The material properties, Young's Modulus and Poisson's ratio, for the bladed disk are shown in Table 7.1, while a uniform material density was set, equal to  $8110.21 \text{ kg/m}^3$ .



Figure 7.2: Cross section of the SGT5-4000F gas turbine [5]

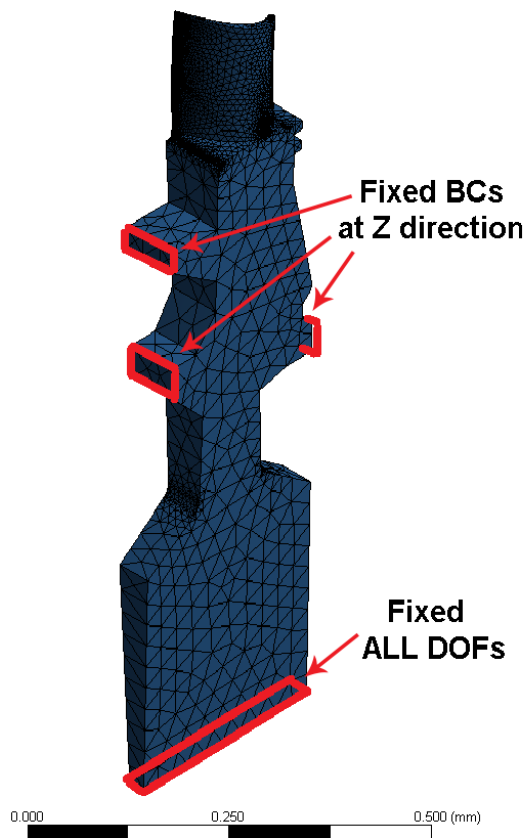


Figure 7.3: 1<sup>st</sup> rotor FE sector model

Temperature [K]	Young's Modulus [GPa]	Poisson's ratio
297.0	200.7	0.28
366.5	195.1	0.27
477.6	190.3	0.27
588.7	184.8	0.28
699.8	179.3	0.28
810.9	175.1	0.30
922.0	167.5	0.30
1033.1	160.0	0.30
1144.3	151.0	0.29
1255.4	140.0	0.30

Table 7.1: Alloy IN-738 properties

## 7.2.2 Modal Analysis Results

In order to solve the free vibration problem firstly the static analysis was performed including the prestressing effect at the design speed that results from the centrifugal forces which are caused by the rotation of the structure. The most significant effect of centrifugal forces has been found to be on the first bending natural frequencies. An increase of the natural frequency of first bending mode is expected with the increase of the rotational speed, while the effect on the torsional mode is negligible. However, due to the effect of temperature in turbines, natural frequency may reduce with the increase of rotational speed and thermal stiffening effects may overtake the stress stiffening effects caused by the inertia. This could be caused by the reduction in Young's modulus values (Table 7.1) with temperature increase. The modal analysis is then solved in the rotating frame, including the prestress effects for 1-24 index numbers calculating the first three modes.

In Figure 7.4, each data series represent the natural frequencies of a mode family depending on the ND. As the number of ND increases, the stiffness matrix of the bladed disk assembly is affected and the system is considered to be disk-dominated. The natural frequency of the corresponding mode family converges to a value after the 6<sup>th</sup> ND when the 1<sup>st</sup> and 2<sup>nd</sup> modes are dominated by the rotor blade motion. All the analyses in this section focuses on the first three modes.

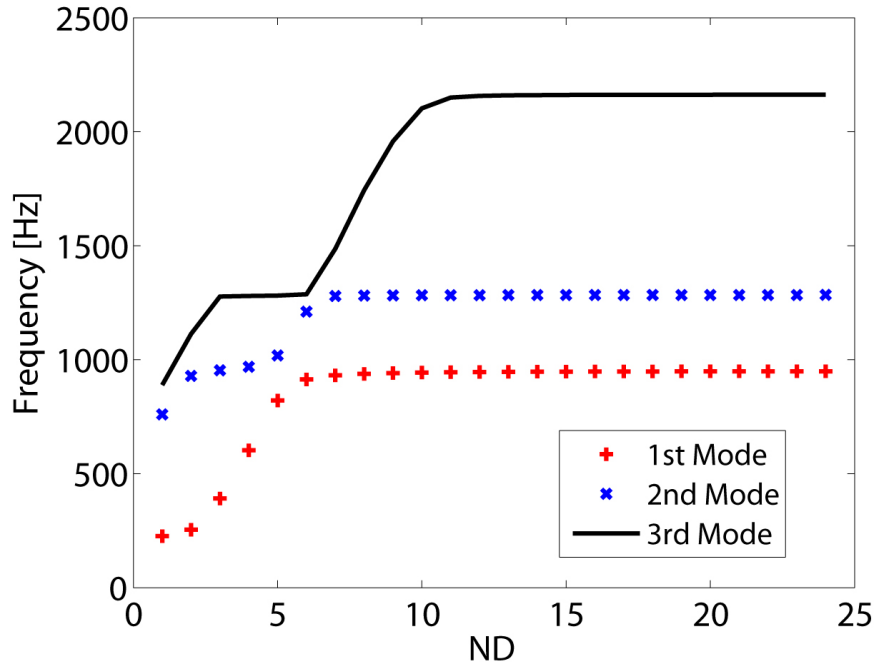
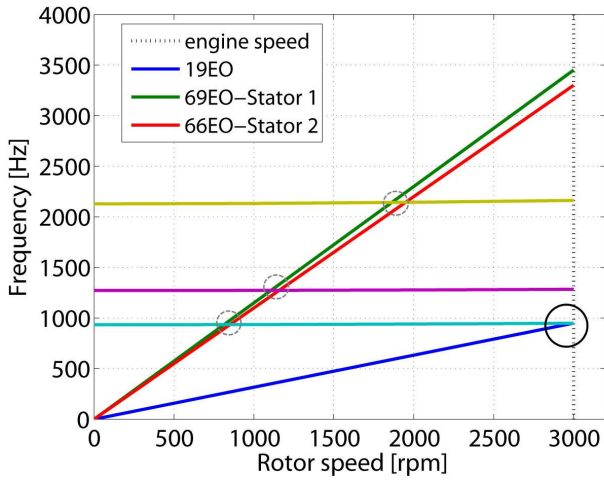


Figure 7.4: Natural frequencies vs. nodal diameters

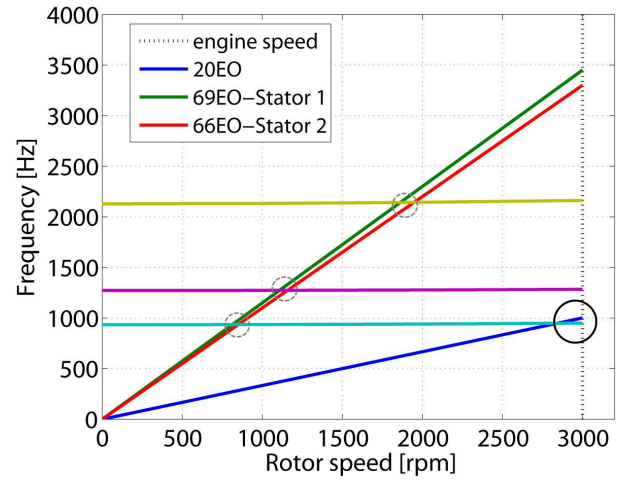
The Campbell diagrams were drawn for each ND in order to assess the potential excitation of the first rotor blade due to the inlet temperature distortion. Campbell diagram has traditionally been used to visualise potential resonance problems. The graph depicts speed of rotation [rpm] on the abscissa versus frequency [Hz] on the ordinate. The excitation frequencies or EO frequencies are multiples of the excitation frequency and correspond to the number of disturbances per revolution.

Six Campbell diagrams are chosen as representative and are shown in Figure 7.5, each one corresponding to a ND <sup>1</sup>. The 24 EO corresponds to the lowest BPF that is related to the number of hot streaks at the combustor exit. Focusing on the LEOs it can be seen that the 19 EO intersects the first mode for the rotational speed (3000 rpm) thus the system's maximum amplitude is expected to occur at that intersection point of first mode and 19 EO excitation. Although the 20 LEO excitation is not an exact intersection it was also considered for the forced response analysis to guarantee a safety margin. The 24 EO has also been considered for the forced response analysis as a BPF excitation compared against the LEO excitation, though there is no intersection shown in Figure 7.5 (e).

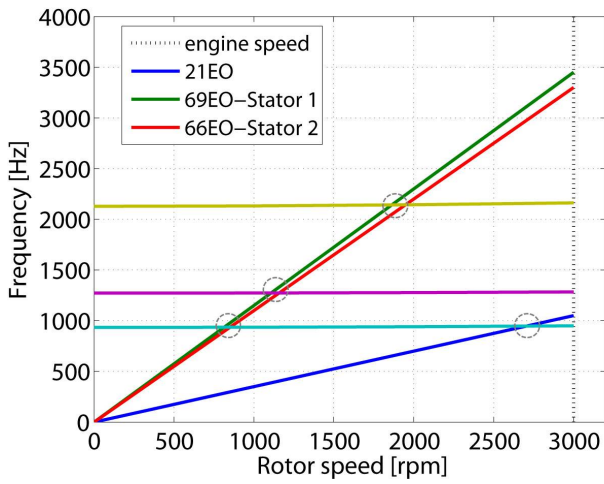
<sup>1</sup>The complete number of Campbell diagrams is provided in Appendix A



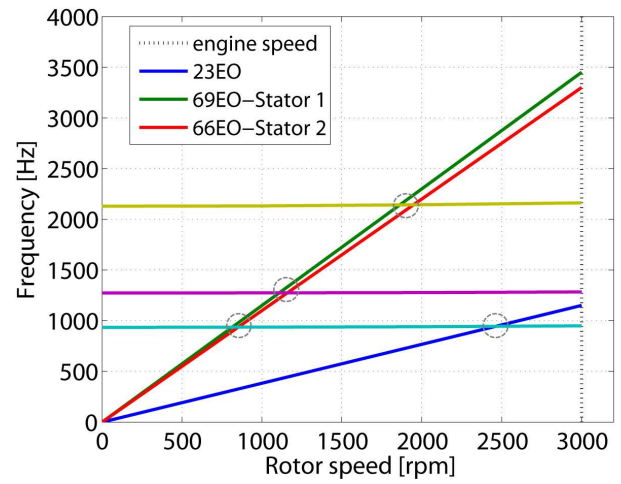
(a) Campbell diagram for 19 ND



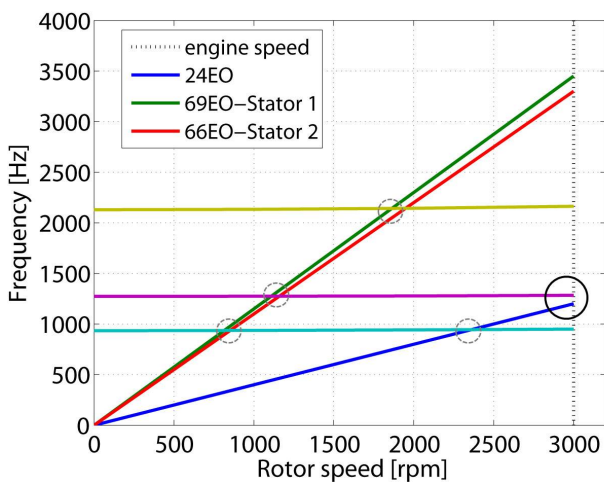
(b) Campbell diagram for 20 ND



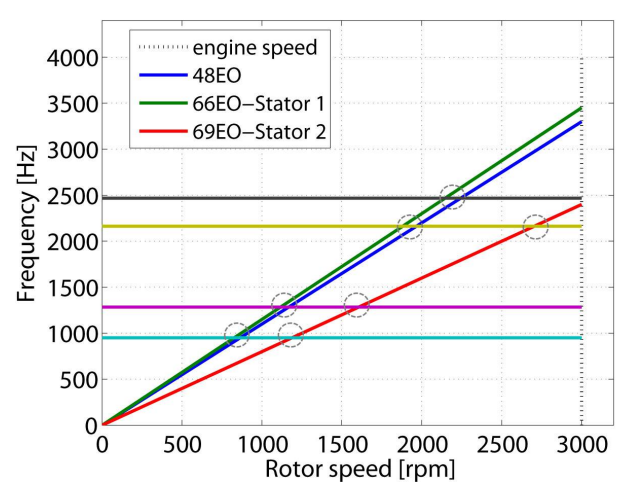
(c) Campbell diagram for 21 ND



(d) Campbell diagram for 23 ND



(e) Campbell diagram for 24 ND



(f) Campbell diagram for 48 ND

Figure 7.5: Campbell diagrams for various NDs

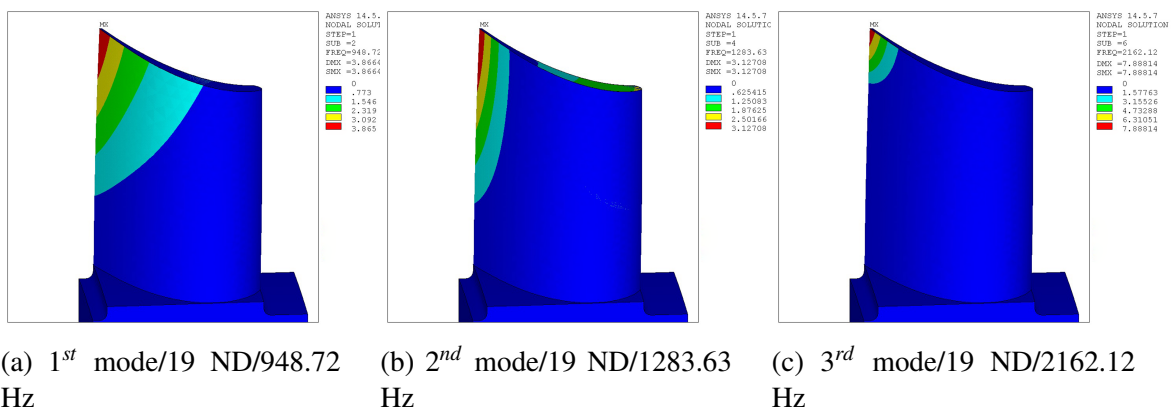
Included in Figure 7.5 are also diagrams that show intersections at lower rotational

speeds. Those intersections have been included in the plots as they should be passed through quickly if possible during the startup or shutdown of the engine in order to ensure that repeat failures will not occur. Based on the Campbell diagrams the 19, 20 and 24 EOs indicate the possible shapes and frequencies of excitation at the engine speed and thus, were chosen for further investigation through a forced response analysis. Table 7.2 presents the natural frequencies of the first rotor disk at 3000 rpm referring to the chosen for further investigation EOs.

Mode	Natural Frequencies [Hz]		
	19 ND	20 ND	24 ND
1 <sup>st</sup>	948.72	948.89	949.36
2 <sup>nd</sup>	1283.63	1283.67	1283.84
3 <sup>rd</sup>	2162.12	2162.23	2162.85

Table 7.2: Natural Frequencies for the first 3 modes of the selected NDs

Figure 7.6 shows the mode shapes contours corresponding to the 19,20 and 24 NDs, while in Figure 7.7 the expanded solution shows the modal response of each rotor blade with an interblade phase angle between adjoin blades for the first mode being excited by the 19 EO. The differences between the frequencies and mode shape contours are quite small for the three chosen NDs; the mode shapes tend to be blade-dominated as discussed previously and thus, the natural frequency remains almost constant and independent of the ND increase.



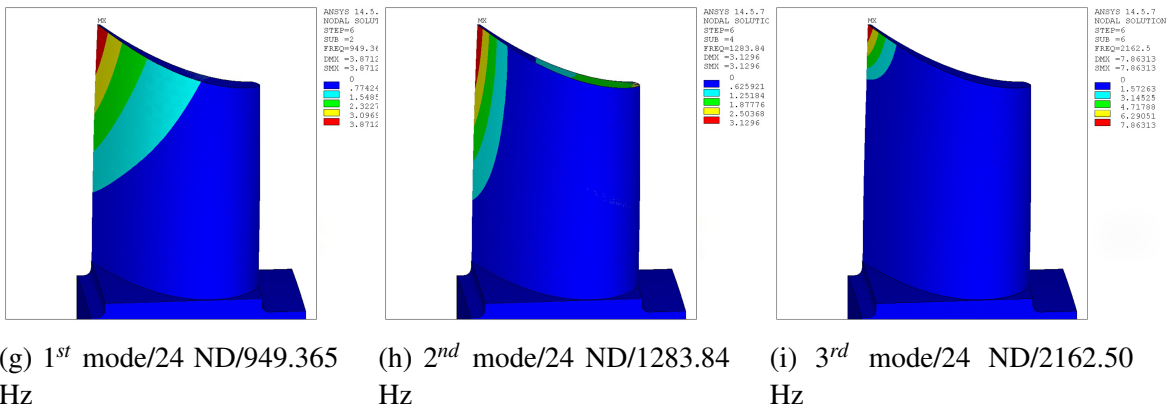
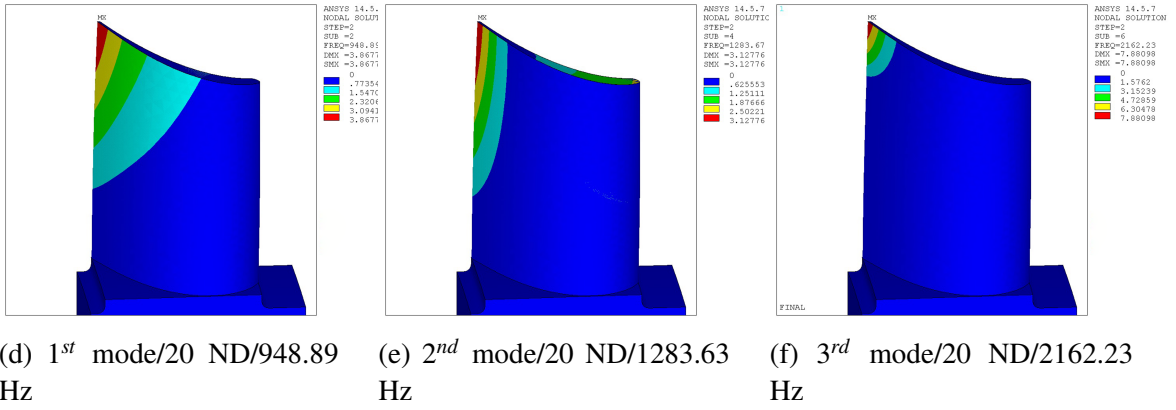


Figure 7.6: Mode shapes contours corresponding to the values presented in Table 7.2

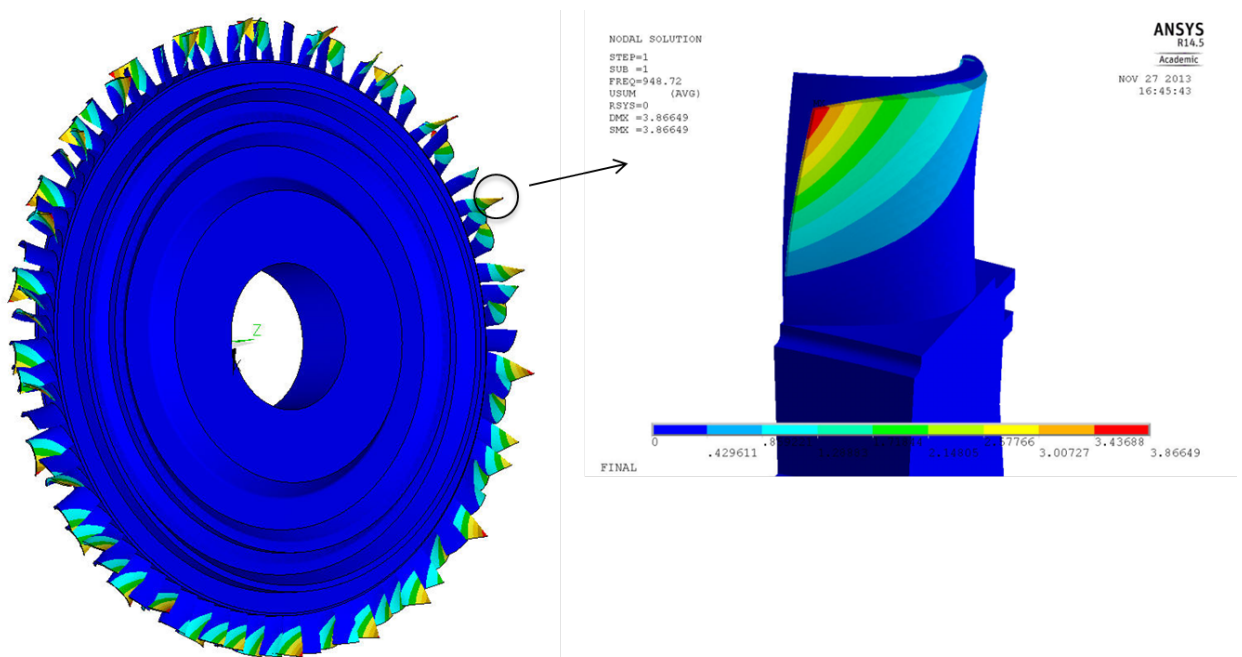


Figure 7.7: Full annulus mode shape for 19 ND and displacement

### 7.2.3 First Stage Forced Response Analysis Setup

In order to compute the excitation due to the turbine inlet temperature distortion, the modal analysis results are used for the uncoupled forced response unsteady analysis as described at Chapter 3. The modal analysis is followed by the FE - CFD interpolation in order to assess the amplitude of the modal force for the resonant modes of interest as those were indicated by the construction of the Campbell diagrams. The two computational grids for the first rotor blade are shown in Figure 7.8. The input to the interpolation process is the real and the imaginary part of the deformation for each grid point as that has been resulted by the modal analysis for the 1<sup>st</sup> mode/19 ND, 1<sup>st</sup> mode/20 ND and 2<sup>nd</sup> mode/24 ND. The FE mesh of the bladed disk consists of 222,012 nodes and the single blade CFD of 109,235 points, while the CFD mesh of the first stage corresponds to 15 million grid points.

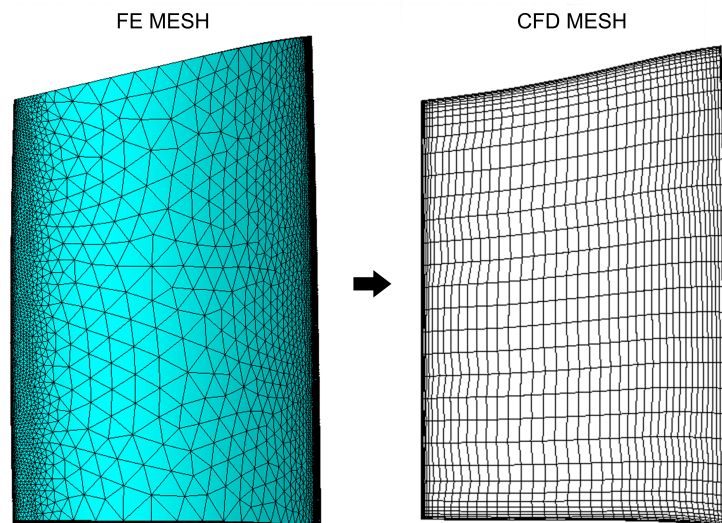


Figure 7.8: FE to CFD mesh interpolation

In Figure 7.9 the contour plots of the first mode shape for the 19 ND are shown, as resulted from the structural analysis and the interpolated to CFD mesh values, respectively. The comparison is made in order to ensure interpolation accuracy which shows fair capture of the deformation especially near the blade tip where the maximum displacement occurs.

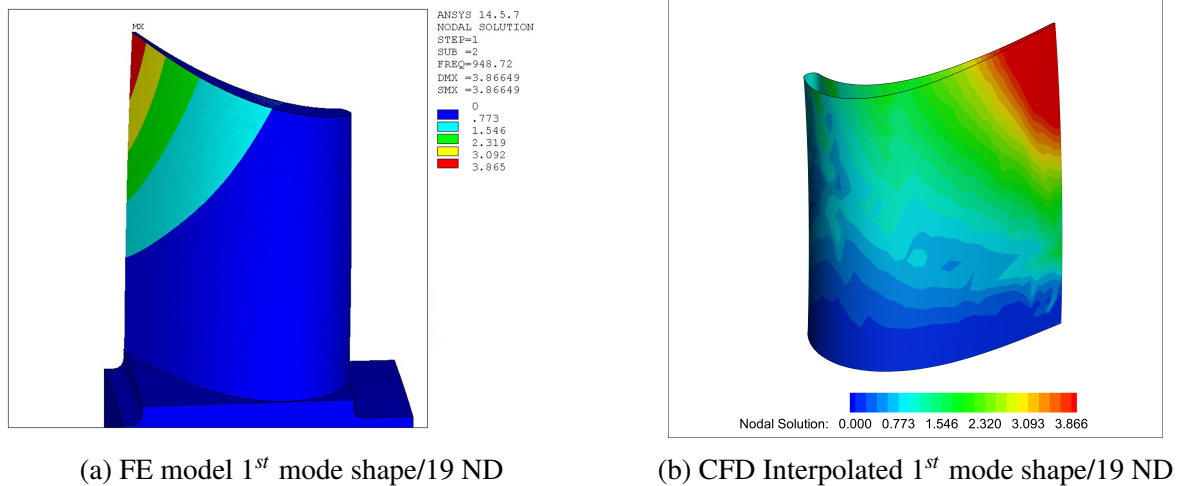


Figure 7.9: Comparison of contour mode shape between the FE modal analysis and the interpolated CFD values for the 19 ND

The CFD boundary conditions of the first turbine stage correspond to those presented in Chapter 6 and the excitation force results from the temperature distortion that is introduced into the flow by the inlet hot streak profile. The forced response analysis is conducted for the full annulus of the first turbine stage. For a fixed rotation speed (50 Hz) on turbine working condition the BPFs related to the first stage can be calculated based on the number of stator blades as well as the number of burners. The BFF corresponding to the first stator bladerow is equal to 3450 Hz (69 stator blades x 50 Hz), while the corresponding to the burners is equal to 1200 Hz (24 hot streaks x 50 Hz).

### 7.2.4 Forced Response Results

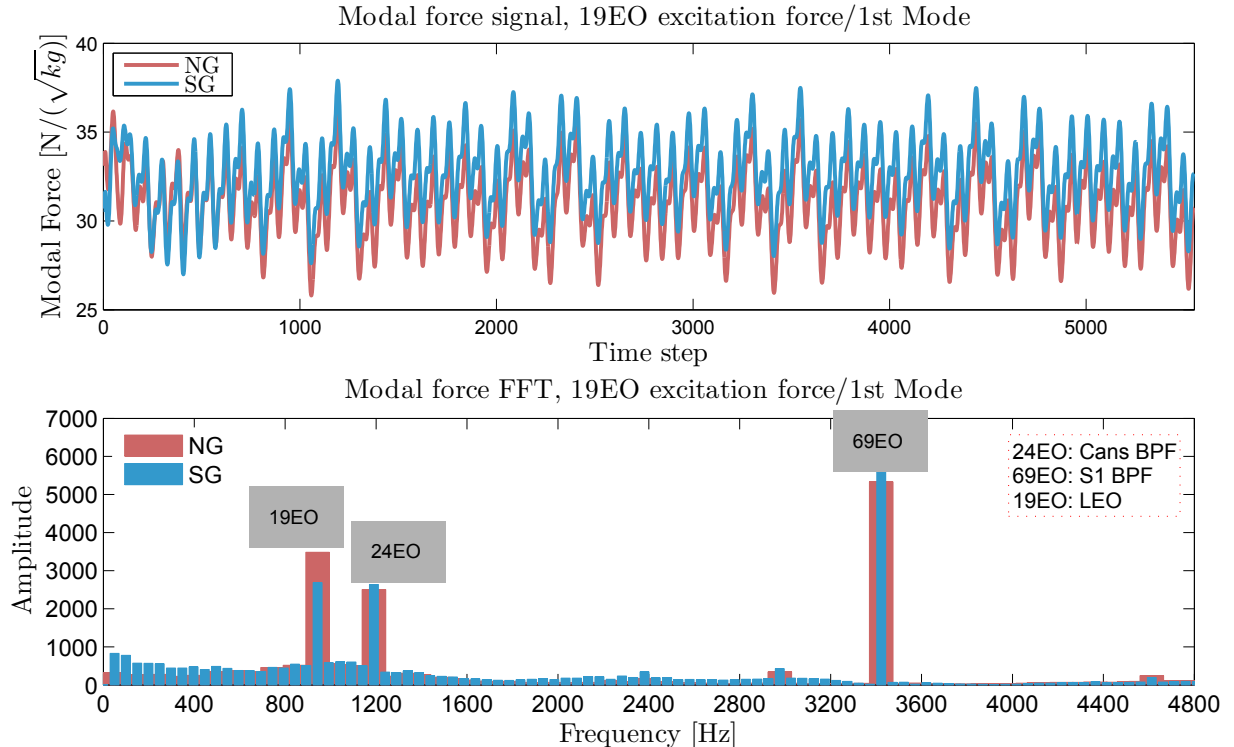
Figure 7.10 shows the modal force signal and the corresponding Fourier transform of the NDs chosen to provide resonant forcing (19 and 24 NDs), for the first mode (19 ND) and second mode (24 ND). The 19 and 20 NDs have been chosen as typical for LEO excitation while the 24 ND as BPF excitation; however, results for the 20 EO are not shown here as the forced response analysis resulted negligible amplitude corresponding to that frequency. For the 19 EO excitation in Figure 7.10 (a) the comparative study between the two fuels reveals a higher amplitude for the case of natural gas, that is in contrast with the BPFs, 24 and 69 EOs, as expected based on the interpretation of the temperature profile in Chapter 6 (Figure 6.17). In case of syngas, the more concen-

trated wake shape at the exit plane of first stator bladerow results higher temperature peaks, giving rise to the excitation of the 24 and 69 EOs while reducing the LEOs.

Regarding the amplitude of modal force in Figure 7.10 (a) it may be also concluded that the LEO and BP forced response amplitudes are comparable. Comparing the 19 LEO to the BPF, the LEO response for the syngas case was found to be about 55% of the S1 BPF and almost equal to the 24 cans BPF, while for the natural gas the difference between the 19 LEO and 60 EO decreases to about 35%. For the 24 EO the impact of syngas on the amplitude of excitation force is higher as shown in both Figures 7.10 (a) and 7.10 (b).

Fuel parameter	Mode	Excitation	Predicted Displacement [mm]
Natural Gas	1 <sup>st</sup> /19ND	19EO	1.135
Syngas	1 <sup>st</sup> /19ND	19EO	0.88

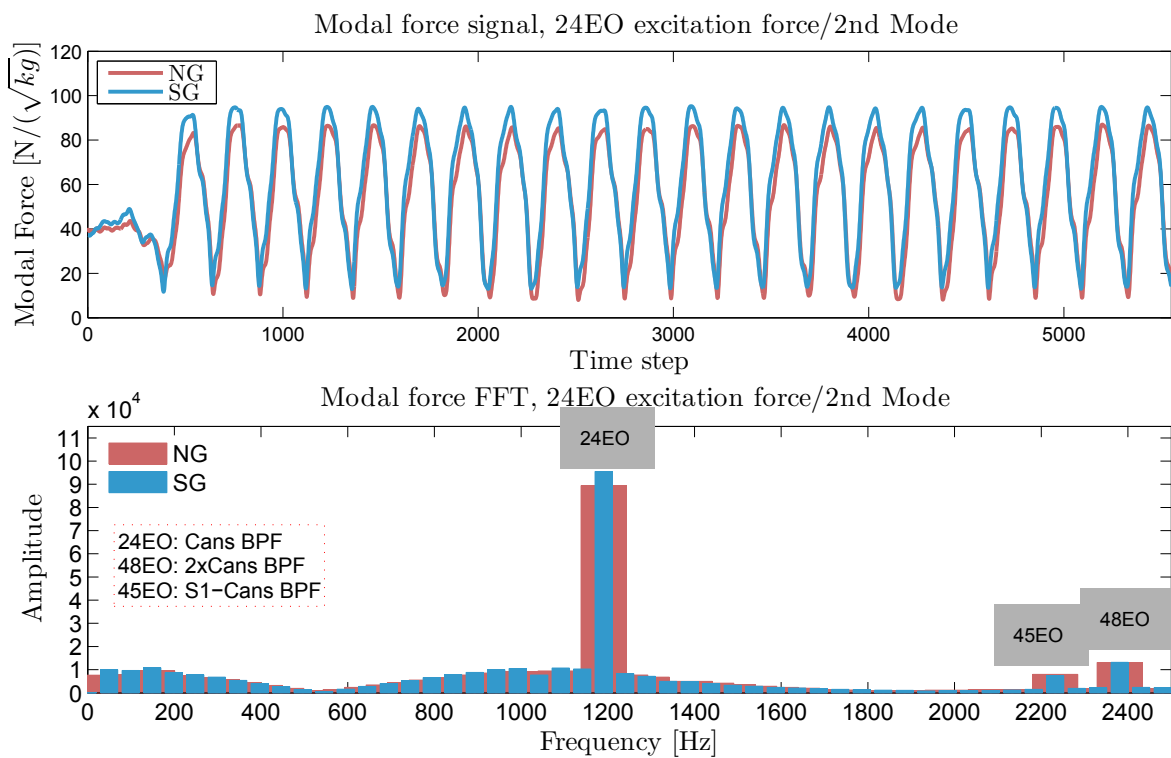
Table 7.3: Syngas and Natural Gas predicted LEO response for R1



(a) Fourier transform of the 1<sup>st</sup> mode/19 ND excitation force

The amplitude of the unsteady aerodynamic forcing can be then used to compute the

maximum resonant displacement for the LEO excitation using Equation 3.12. A typical value of 80 was chosen as representative proportional damping, based on the literature [37] and the value of the largest mode shape element was based on the modal analysis. The results of the computed maximum displacement for both fuels are presented in Table 7.3. Considering that the predicted displacement corresponds to the worst scenario, assuming an exact match between the natural frequency of the blade and the excitation forcing, the results indicate a significant vibration amplitude for the turbine rotor blade, where the blade vibrates with 1.135 mm displacement for the case of natural gas and a lower value of 0.88 mm displacement for the case of syngas fuel.



(b) Fourier transform of the 2<sup>nd</sup> mode/24 ND excitation force

Figure 7.10: Modal force amplitude for compared cases of natural gas and syngas

However, the LEO behaviour is dependent on specific controlling parameters which are likely to be different in actual engine due to the assumptions made for the inlet hot streak profile and thus the excitation forcing. A different hot flow pattern may lead to different excitation levels. What is important from this comparison is the fact that syngas exhibits lower amplitude of the 19<sup>th</sup> low harmonic compared to natural gas and LEO excitation problems related to temperature distortion are not likely to

occur. The findings of the forced response analysis are quite significant as there are no relevant studies on the effects of syngas on the stator wake and the consequent impact on the excitation levels of the downstream bladerows. Before the current analysis the expected enhanced temperature levels of syngas and the affected hot flow path was believed to enhance both the BPF and the LEO excitation levels related to the combustor burners. Moreover, the significant levels of the LEO excitation compared to the burners and stator related BPF indicate the need to consider any potential inlet flow non-uniformities in the design process and obtain forced response predictions with respect to high cycle fatigue limits.

### **7.3 Summary**

In this chapter the full annulus forced response analysis was conducted for the first turbine stage for three LEOs (19, 20, 24) in order to calculate the unsteady aerodynamic force. The FFT analysis of the modal force for comparative fuel compositions (natural gas and hydrogen-rich syngas) shows a slightly lower impact of syngas on the LEO modal force amplitude for the chosen hot streak pattern, that is related to the differences of the wake shape between the two fuels. The modal displacement was also calculated for the LEO excitation, resulting in 1.135 mm for natural gas and 0.88 mm for syngas case. Based on those findings the 19 LEO forced response suggests lower vibration amplitudes for a syngas turbine blade, considering that the predicted displacement corresponds to the worst scenario, assuming an exact match between the natural frequency of the blade and the excitation force. The findings are of great importance, as there are no published studies investigating the effects of the syngas hot flow path on the excitation of the downstream turbine bladerows, this study contributes towards a better understanding of the effects of fuel composition on the forced response problem.

However, the LEO behaviour is dependent on the forcing function; a different hot flow pattern may lead to different excitation levels. Since the original turbine that has been designed for natural gas operates without any aeroelasticity related problems, it is concluded that syngas operation should not raise any combustor cans related LEO problems in terms of blade failure at the turbine running speed. Additional information

is provided for lower speeds, Campbell diagrams exhibit additional crossing areas that should be passed quickly during the startup or shutdown of the machine to avoid any potential excitation of the rotor blades.

# Chapter 8

## Conclusions and Recommendations

### 8.1 Introduction

This chapter summarises the findings that have been presented in this thesis in relation to the stated research objectives, highlighting the conclusions of the aerodynamic and LEO forced response analysis. All three objectives introduced in Chapter 2 have been achieved during the research described in this thesis with particular focus on the effects of syngas combustion on gas turbine. A fundamental understanding of the impact of the fuel composition along with a number of design parameters on the hot streak propagation through a turbine has been gained and the investigation has been extended on the effects on the LEO excitation of the first turbine rotor due to the temperature non-uniformities. The following subsections elaborate further on the achievements of this thesis. Finally some suggestions for improvements and future work are proposed.

### 8.2 Meeting the Objectives: Summary of Thesis Achievement

#### 8.2.1 The aerodynamics of hot streaks in a two-stage HP turbine

The propagation of hot streaks is one of the complex and unsteady phenomena in turbines that cannot be simply accounted for through uniform boundary conditions

and steady CFD simulations. The effects of the hot streaks propagation through a two-stage HP turbine by means of a 3D unsteady CFD code have been discussed in detail in Chapter 4, taking into account a number of individual and combined parameters.

The kinematics of six hot streaks, circumferentially aligned to the first stator mid-passage, follow the basic propagation mechanism as has been described in the literature, with the hot fluid migrating towards the blades PS when entering the rotating frame and narrowing around the midspan of rotor blades SS, under the influence of enhanced secondary flows through the rotor passage. A number of design parameters related to different flow mechanisms was investigated, showing that combined effects of vane coolant injection, secondary flows and potential interaction have an impact on the alteration of the hot streak shape and the migration of the hot streak centre along the blade span with consequent effects on the enhanced local heat transfer on specific areas on the blades surfaces.

The vane coolant injection resulted in a circumferentially chopped hot streak profile at the exit plane of first stator bladerow, while in the absence of vane cooling the alteration of the shape of hot streak has been attributed to the potential interaction of the downstream rotor bladerow. In the rotational frame, enhanced secondary flows due the temperature gradients, interacted with the propagating hot streak pushing the hot fluid along the blade radial direction and migrating the peak temperature areas towards the rotor hub. Moving through the stages, hot streaks resulted in two distinct peak temperature areas along the blade span which are apparent up to the turbine exit. Additionally, comparison between ideal elliptical hot streaks and combustor representative concentrated shapes exhibited variation in temperature magnitude and thus, temperature levels appeared elevated at the turbine exit when a concentrated hot streak was applied against an elliptical one indicating the effect of hot streak area on the propagation mechanism.

Summarising the findings of the analysis carried on the SGT-300-2S gas turbine, the influence of specific design parameters on the hot streaks kinematics and the sensitivity of the analysis on the inlet boundary conditions was shown with the results being in agreement with previous studies providing here a complete overview following more realistic approach. A better understanding and appreciation of the contribution of different sources of interaction to the hot flow path was gained, the knowledge of which

is applied into the generic turbine geometry that was investigated for the purposes of the H2-IGCC project.

### **8.2.2 The aerodynamic of hot streaks in the four-stage H2-IGCC turbine with respect to fuel composition**

After evaluating a number of combined effects on the propagation of hot streaks and establishing realistic hot streak shapes, the aerodynamic effects of hot streaks propagation into the heavy duty four-stage HP turbine were investigated in Chapter 6 with respect to the fuel composition. A natural gas fired generic turbine has been used against a modified syngas fired turbine for the unsteady multi-bladerow CFD analysis using the same inlet conditions with 24 hot streaks circumferentially aligned at the turbine inlet and randomly varied between each other, in terms of the hot area, in order to represent realistic combustor exit conditions.

The effects of the circumferential location of the hot streaks injection were observed due to the non-integer factor between the hot streaks and stator blades that results in different hot streaks alignment configurations. The strength of the segregation effect on the first rotor bladerow was observed to be affected by the misalignment of the hot streak with the inlet stator passage that is termed as hot streak "clocking", as well as by the hot area of the inlet hot streak. An additional input is appended to the comparison between elliptical and concentrated hot streak shapes discussed in Chapter 4, with the smaller hot streaks propagating up to the exit of the four-stage turbine.

The investigation of the effects of syngas on the propagation of the hot fluid consists one of the main contributions of the thesis due to the lack of relevant studies and is discussed in comparison with natural gas that was used as a reference fuel case. The hydrogen-rich syngas chosen for this work in combination with the applied turbine modification re-staggering of the first stator blade - leads to a lower pressure drop and increased temperature at the exit of the turbine that has been observed also in relevant published works. As an effect of the fuel composition, the hot gas flow path exhibits differences compared to the reference natural gas fuel, which constitutes the motivation of the current study. The significant changes of the velocity deficit were shown with consequent changes on the flow angles and development of secondary

flows through the first rotor passage. The flow exiting the first stationary frame in case of syngas exhibited a more concentrated wake shape as a result of differences in composition and hence in vane exit velocities. That is of great importance as the different flow pattern changes the transport mechanism with consequent effects on the structural part of the turbine as it propagates through the turbine.

The interaction of hot streaks with the blade film coolant was also discussed where observation of the temperature contour plots showed effective prevention of hot fluid convection to the rotor boundary layer for both fuels. However, compared to natural gas, syngas temperature levels remained approximately 8% higher and exhibited stronger propagation up to the exit of the turbine. Considering the fact that the same amount of coolant was injected for both fuels, modifications of the blade coolant scheme may need to be taken into account for syngas cases in relevant future work.

### **8.2.3 The effects of fuel composition on the LEO excitation due to inlet temperature non-uniformities**

The final objective of the thesis was completed evaluating the effects of the fuel on the LEO excitation for the H<sub>2</sub>-IGCC turbines in Chapter 7. Following a modal analysis and setting up the corresponding Campbell diagrams to identify any resonance conditions, the full annulus forced response analysis was conducted for the first turbine stage for two chosen LEOs (19, 20) and the cans related 24 EO. The Fourier transform analysis of the modal force for compared fuel compositions (natural gas and syngas) showed a slightly lower impact of syngas on the LEO modal force amplitude for the chosen hot streak pattern. The modal displacement was also calculated for the LEO excitation, resulting in 1.135 mm for natural gas and 0.88 mm for syngas case. Based on those findings the 19 LEO forced response suggested lower vibration amplitudes for a syngas turbine blade. However, comparison of the LEO and the BPF excitation levels showed comparable effects indicating the impact of the LEO excitation on the turbine blade failure and highlighting the importance of investigating any relevant vibration sources during the design process.

## **8.3 Recommendations and Future Work**

The research presented in this thesis has provided information important for the aerodynamic and aeromechanic turbine development in order to prevent from the formation of local hot spots on turbine blades, enhanced secondary losses and low engine order excitation, with the effects being extended into specific applications, such as the IGCC power plants. However, limitations were faced during the research and additional future work could be carried out towards the evaluation of the design parameters in order to interpret the results in a way that may be applied to turbine design regardless the size and the application of the gas turbine.

### **8.3.1 Simulation of full annulus unsteady CFD analysis against experimental data**

One of the limitations faced during this study was the lack of experimental data for validation purposes. Even though the CFD results presented here were compared with a throughflow model case showing very good agreement, as discussed in Chapter 3, and the unsteady flow model has also been validated by other researchers as reported in the literature, the simulation of a whole annulus CFD profile based on experimental measurements and the comparison against the data would add great value on the current study. Due to the high cost there are very few examples of whole-field temperature measurement at the combustor exit that could be used to validate the unsteady CFD results. The scarcity of experimental data is even more significant for the case of syngas fuel. The work presented here is a first step towards the assessment of the effects of syngas on the hot streak propagation. The lack of experimental data though is a significant drawback that leads to assumptions of the hot streak shape and hence, the simulation of syngas hot streaks based on experimental data would enhance the discussion in this thesis.

### **8.3.2 Varied hot flow patterns**

Although considerable effort was spent on the development of a realistic hot streak pattern at the turbine inlet that was based on traverse data of one combustor can, the

results should be evaluated against a variation of hot streak patterns in order to draw general conclusions that could apply to turbine design. Since the hot streak shapes were randomly varied in size and injection location, reliable estimates could be produced applying different variations and analysing the effects on the propagation. However, this can be a time consuming research work and thus probability methods could be applied to minimise the time of conducting the study. Evaluation of the effects on the LEO excitation would be a significant input as the main challenge is the accurate prediction of the inlet flow variations on the excitation of low order nodal diameters.

### **8.3.3 Comparison with other turbulence models**

For complex turbomachinery flows, where the use of unstructured grid becomes very popular due to the advantage of flexibility that offers, the one-equation models have shown sufficient behaviour [110]. For the current study the one-equation Spalart-Allmaras turbulence model is employed for the CFD simulations as discussed in Chapter 3. However, further investigations are recommended towards the implementation of better turbulence models in order to confirm that findings are not dependent on the turbulence model that has been used for this study.

### **8.3.4 LEO excitation of the downstream rotor blades**

Based on the literature [31, 32] indications of LEO excitation on the downstream rotor bladerows has been observed and linked to the temperature gradients at the turbine inlet. Limitations due to time and the lack of accurate designs of the 2<sup>nd</sup>, 3<sup>rd</sup> or 4<sup>th</sup> rotor disks did not allow the complete evaluation of the chosen flow pattern on the effect. Additionally, the simulation of the real turbine blades, including the cooling holes as shown in Chapter 6, would enhance the accuracy of the results and comparison against the current work should reveal any drawback of the solid blade assumption.

# Bibliography

- [1] B. Lakshminarayana. *Fluid Dynamics and Heat Transfer of Turbomachinery*. John Wiley & Sons, Inc., 1996.
- [2] T. Povey and I. Qureshi. Developments in hot-streak simulators for turbine testing. *Journal of Turbomachinery*, 131(3):031009–15, 2009.
- [3] H. P. Wang, S. J. Olson, R. J. Goldstein, and E. R. G. Eckert. Flow visualization in a linear cascade of high performance turbine blades. *Journal of Turbomachinery*, 119:1–8, 1997.
- [4] Cenaero. Temperature distribution through primary and secondary flow path defined. Technical report, 2012.
- [5] Gas turbine sgt5-4000f. <http://www.energy.siemens.com/hq/en/fossil-power-generation/gas-turbines/>.
- [6] S. Gadde, J. Wu, A. Gulati, G. McQuiggan, B. Koestlin, and B. Prade. Syngas capable combustion systems development for advanced gas turbines. *ASME Turbo Expo 2006: Power for Land, Sea, and Air*, 4: Cycle Innovations; Electric Power; Industrial and Cogeneration; Manufacturing:547–554, 2006.
- [7] N. Sipocz, M. Mansouri, P. Breuhaus, and M. Assadi. Development of h<sub>2</sub>-rich syngas fuelled gt for future igcc power plants: Establishment of a baseline. *ASME 2011 Turbo Expo: Turbine Technical Conference and Exposition*, Volume 1: Aircraft Engine; Ceramics; Coal, Biomass and Alternative Fuels; Wind Turbine Technology:563–572, 2011.
- [8] R. Jones, J. Goldmeer, and B. Monetti. Addressing gas turbine fuel flexibility. Technical Report GER4601, GE Energy, 2011.
- [9] European technology platform for zero emission fossil fuel power plants. [www.zeroemissionsplatform.eu](http://www.zeroemissionsplatform.eu).

- [10] Integrated gasification combined cycle (igcc) design considerations for high availability - volume 1: Lessons from existing operations. Technical Report Palo Alto, CA: 1012226, Electric Power Research Institute, 2007.
- [11] R.A. Dennis, W.W. Shelton, and P. Le. Development of baseline performance values for turbines in existing igcc applications. *ASME Turbo Expo 2007: Power for Land, Sea and Air*, page 33, 2007.
- [12] J. G. Speight. Handbook of industrial hydrocarbon processes, 2009.
- [13] R. D. Brdar and R. M. Jones. Ge igcc technology and experience with advanced gas turbines. Technical Report GER-4207, GE Power Systems, 2000.
- [14] J. Karg. Igcc experience and further developments to meet ccs market needs. Technical Report COAL-GEN EUROPE Katowice, Poland, Siemens AG, Energy Sector, Fossil Power Generation Division, 2009.
- [15] E. O. Oluyede. Fundamental impact of firing syngas in gas turbines. Technical report, Electric Power Research Institute, 2006.
- [16] Y. S. Kim, S.K. Park, J. J. Lee, S.W. Kang, and T. S. Kim. Analysis of the impact of gas turbine modifications in integrated gasification combined cycle power plants. *Journal of Energy*, 55:977–986, 2013.
- [17] I. G. Wright and T. B. Gibbons. Recent developments in gas turbine materials and technology and their implications for syngas firing. *International Journal of Hydrogen Energy*, 32:3610–3621, 2007.
- [18] P. Chiesa, G. Lozza, and L. Mazzocchi. Using hydrogen as gas turbine fuel. *Journal of Engineering for Gas Turbines and Power*, 127:73–80, 2005.
- [19] Y. S. Kim, J. J. Lee, T. S. Kim, and J. L. Sohn. Effects of syngas type on the operation and performance of a gas turbine in integrated gasification combined cycle. *Energy Conversion and Management*, 52:2262–2271, 2011.
- [20] P. Nucara and A. Sayma. Effects of using hydrogen-rich syngas in industrial gas turbines while maintaining fuel flexibility on a multistage axial compressor design. *Proceedings of ASME Turbo Expo, Copenhagen, Denmark*, June 11-15 2012.
- [21] Low emission gas turbine technology for hydrogen-rich syngas. Technical report, European Turbine Network, 2008.

- [22] G. Cerri and L. Chennaoui. General method for the development of gas turbine based plant simulators: An igcc application. *ASME Turbo Expo 2013: Turbine Technical Conference and Exposition, 2: Aircraft Engine; Coal, Biomass and Alternative Fuels; Cycle Innovations:V002T03A001–V002T03A015*, 2013.
- [23] R. Kluxen, H. Honen, and P. Jeschke. Gas turbine expander design modifications for h<sub>2</sub>-rich syngas application. *International Gas Turbine Conference*, 2014.
- [24] D. J. Burlet, K. L. G. Dorney. Influence of 3d hot streaks on turbine heat transfer. *International Journal of Turbo and Jet Engines*, 14:123–131, 1997.
- [25] T. Korakianitis, P. Papagiannidis, and N. E. Vlachopoulos. Unsteady flow/quasi-steady heat transfer computations on a turbine rotor and comparison with experiments. *Journal of Turbomachinery*, 124(1):152–159, 2002.
- [26] A. A. Ameri, D. L. Rigby, E. Steinthorsson, J. Heidmann, and J. C. Fabian. Unsteady turbine blade and tip heat transfer due to wake passing. Technical Report 214942, National Aeronautics and Space Administration, 2007.
- [27] P. Jenny, C. Lenherr, A. I. Kalfas, and R. S. Abhari. Effect of hot streak migration on unsteady blade row interaction in an axial turbine. In *ASME Turbo Expo 2010: Power for Land, Sea, and Air*, pages 2573–2584, 2010.
- [28] T. Povey, K. S. Chana, T. V. Jones, and J. Hurrion. The effect of hot-streaks on hp vane surface and endwall heat transfer: An experimental and numerical study. *Journal of Turbomachinery*, 129(1):32–43, 2007.
- [29] O. P. Sharma, G. F. Pickett, and R. H. Ni. Assessment of unsteady flows in turbines. *Journal of Turbomachinery*, 114(1):79–90, 1992.
- [30] V. S. P. Chaluvadi, A. I. Kalfas, H. P. Hodson, H. Ohyama, and E. Watanabe. Blade row interaction in a high- pressure steam turbine. *Journal of Turbomachinery*, 125(1):14–24, 2003.
- [31] S. R. Manwaring and K. L. Kirkeng. Forced response vibrations of a low pressure turbine due to circumferential temperature distortions. In Torsten Fransson, editor, *8th International Symposium on Unsteady Aerodynamics and Aeroelasticity of Turbomachines*, pages 379–392. Kluwer Academic Publishers, 1998.

- [32] M. A. Mayorca, R. Bladh, and U. Ozturk. Estimation of burner can-induced excitation levels in an industrial gas turbine. *ASME Turbo Expo 2013: Turbine Technical Conference and Exposition*, 7B: Structures and Dynamics:V07BT33A013–V07BT33A024, 2013.
- [33] M. E. Goldstein. Unsteady vortical and entropic distortions of potential flows round arbitrary obstacles. *Journal of Fluid Mechanics*, 89(3):443–468, 1978.
- [34] M. F. Platzer and F. O. Carta. Agard manual on aeroelasticity in axial-flow turbomachines. Technical Report 298, Advisory Group for Aerospace Research and Development, June 1988.
- [35] W. Campbell. *Protection of steam turbine disk wheels from axial vibration*. [Schenectady, N.Y.] : General electric company, 1924.
- [36] C. Breard, M. Vahdati, A. Sayma, and M. Imregun. An integrated time-domain aeroelasticity model for the prediction of fan forced response due to inlet distortion. *Journal of Engineering for Gas Turbines and Power*, 124(1):196–208, 2000.
- [37] M. Vahdati, A. I. Sayma, M. Imregun, and G. Simpson. Multibladerow forced response modeling in axial-flow core compressors. *Journal of Turbomachinery*, 129(2):412–420, 2007.
- [38] J. L. Kerrebrock and A. A. Mikolajczak. Intra-stator transport of rotor wakes and its effect on compressor performance. *Journal of Engineering for Power*, 92(4):359–368, 1970.
- [39] M. Munk and R. Prim. On the multiplicity of steady gas flows having the same streamline pattern. *Proceedings of the National Academy of Sciences of the United States of America*, 33(5):137–141, 1947.
- [40] J. R. Schwab, R. G. Stabe, and Whitney W. J. Analytical and experimental study of flow through an axial turbine stage with a nonuniform inlet radial temperature profile. *AIAA Journal* 83-1175, 1983.
- [41] T. L. Butler, O. P. Sharma, H. D. Joslyn, and R. P. Dring. Redistribution of an inlet temperature distortion in an axial flow turbine stage. *Journal of Propulsion and Power*, 5(1):64–71, 1989.

- [42] H. D. Joslyn, G. D. Power, J. M. Verdon, R. Dring, and M. F. Blair. The effects of inlet turbulence and rotor stator interactions on the aerodynamics and heat transfer of a large-scale rotating turbine model. Technical Report CR-4079, NASA, 1987.
- [43] B. Lakshminarayana. Effects of inlet temperature-gradients on turbomachinery performance. *Journal of Engineering for Power-Transactions of the Asme*, 97(1):64–74, 1975.
- [44] M. M. Rai. Navier-stokes analyses of the redistribution of inlet temperature distortions in a turbine. *Journal of Propulsion and Power*, 6(3):272–282, 1987.
- [45] D. J. Dorney, R. L. Davis, D. E. Edwards, and N. K. Madavan. Unsteady analysis of hot streak migration in a turbine stage. *Journal of Propulsion and Power*, 8(2):520–529, 1992.
- [46] B. Lakshminarayana and J. H. Horlock. Generalized expressions for secondary vorticity using intrinsic coordinates. *Journal of Fluid Mechanics*, 59:97–115, 1972.
- [47] J. H. Horlock and B. Lakshminarayana. Secondary flows: Theory, experiment, and application in turbomachinery aerodynamics. *Annual Review of Fluid Mechanics*, 5:247–280, 1973.
- [48] K. S. Hermanson and K. A. Thole. Effect of inlet conditions on endwall secondary flows. *Journal of Propulsion and Power*, 16:286–296, 2000.
- [49] T. Shang and A. H. Epstein. Analysis of hot streak effects on turbine rotor heat load. *Journal of Turbomachinery*, 119(3):544–553, 1997.
- [50] R.J. Boyle and P.W. Giel. Prediction of nonuniform inlet temperature effects on vane and rotor heat transfer. Technical Report NASA TM-107539, National Aeronautics and Space Administration, September 1997.
- [51] K. S. Hermanson and K. A. Thole. Effect of nonuniform inlet conditions on endwall secondary flows. *Journal of Turbomachinery*, 124(4):623–631, 2002.
- [52] D. Prasad and G. J. Hendricks. A numerical study of secondary flow in axial turbines with application to radial transport of hot streaks. *Journal of Turbomachinery*, 122, 2000.

- [53] A. M. Basol, P. Jenny, M. Ibrahim, A. I. Kalfas, and R. S. Abhari. Hot streak migration in a turbine stage: Integrated design to improve aerothermal performance. *Journal of Engineering for Gas Turbines and Power*, 133:061901–1–10, 2011.
- [54] J. Ong and R. J. Miller. Hot streak and vane coolant migration in a downstream rotor. *Journal of Turbomachinery*, 134(43161):051002–0510012, 2012.
- [55] S. Jenkins, K. Varadarajan, and G. Bogard. The effects of high mainstream turbulence and turbine vane film cooling on the dispersion of a simulated hot streak. *Journal of Turbomachinery*, 126:203–211, 2004.
- [56] K. L. Lewis. Spanwise transport in axial-flow turbines: part 1—the multistage environment. *Journal of Turbomachinery*, 116(2):179–186, 1994.
- [57] John J. Adamczyk. Aerodynamic analysis of multistage turbomachinery flows in support of aerodynamic design. *Journal of Turbomachinery*, 122(2):189–217, 2000.
- [58] A. Zilli, V. Pachidis, A. Jackson, and P. Pilidis. Cfd investigation of the performance of a military hp axial turbine subjected to inlet temperature distortion. *ASME Turbo Expo 2005: Power for Land, Sea and Air*, 2005:1107–1116, 2005.
- [59] R.J. Roback and R.P. Dring. Hot streaks and phantom cooling in a turbine rotor passage: Part 1—separate effects. *Journal of Turbomachinery* —, 115:657–666, 1993.
- [60] L. Castillon, E. Laroche, and O. Sgarzi. Unsteady three-dimensional navier-stokes analysis of a hot streak transport through an axial high pressure turbine stage. *16th INTERNATIONAL SYMPOSIUM ON AIR BREATHING ENGINES (ISABE 2003)*, 2003.
- [61] L. He, V. Menshikova, and B. R. Haller. Influence of hot streak circumferential length-scale in transonic turbine stage. In *ASME Turbo Expo 2004: Power for Land, Sea, and Air*, volume 2004, pages 1117–1126, 2004.
- [62] B.-T. An, J.-J. Liu, and H.-D. Jiang. Numerical investigation on unsteady effects of hot streak on flow and heat transfer in a turbine stage. *Journal of Turbomachinery*, 131(3):031015–15, 2009.

- [63] W. Yi, L. Ji, and Y. Xiao. Unsteady numerical simulation of hot streak/blades interaction and film cooling. *Journal of Thermal Science*, 19(5):402–409, 2010.
- [64] R. M. Mathison, C. W. Haldeman, and M. G. Dunn. Aerodynamics and heat transfer for a cooled one and one-half stage high-pressure turbine—part iii: Impact of hot-streak characteristics on blade row heat flux. *Journal of Turbomachinery*, 134(1):011008–9, 2012.
- [65] S. Pyliouras, H.-P. Schiffer, E. Janke, and L. Willer. Effects of non-uniform combustor exit flow on turbine aerodynamics. *ASME Turbo Expo 2012: Power for Land, Sea and Air*, pages 1–11, 2012.
- [66] S. Simone, F. Montomoli, F. Martelli, K. S. Chana, I. Qureshi, and T. Povey. Analysis on the effect of a nonuniform inlet profile on heat transfer and fluid flow in turbine stages. *Journal of Turbomachinery*, 134(1):011012–14, 2012.
- [67] D. J. Dorney, K. L. G. Burlet, and D. L. Sondak. A survey of hot streak experiments and simulations. *International Journal of Turbo and Jet Engines*, 16:1–15, 1999.
- [68] D. J. Dorney and K. L. G. Burlet. Effects of hot streak shape on rotor heating in a high-subsonic single-stage turbine. *International Journal of Turbo and Jet Engines*, 18:15–29, 2001.
- [69] T. Povey, K. S. Chana, and T. V. Jones. Heat transfer measurements on an intermediate-pressure nozzle guide vane tested in a rotating annular turbine facility, and the modifying effect of a non-uniform inlet temperature profile. *Proceedings of the Institution of Mechanical Engineers, Part A: Journal of Power and Energy*, 217(4):421–432, 2003.
- [70] E. M. Greitzer, A. H. Epstein, J. L. Kerrebrock, and C. S. Tan. Unsteady and three-dimensional flow in turbomachines. Technical report, Massachusetts Institute of Technology, 1996.
- [71] A. I. Sayma, M. Vahdati, and M. Imregun. An integrated nonlinear approach for turbomachinery forced response prediction. part i: Formulation. *Journal of Fluids and Structures*, 14(1):87–101, 2000.

- [72] B. Elliott, A. I. Sayma, and M. Imregun. Aeromechanical design of damped high pressure turbine blades subject to low engine order forcing. Technical Report 0704-0188, Rolls-Royce plc, 1 October 2005.
- [73] R. Rzadkowski, V. Gnesin, and L. Kolodyazhnaya. *Stator-Rotor Aeroelastic Interaction for the Turbine Last Stage in 3D Transonic Flow*, chapter IX Rotor Stator Interaction, pages 569–580. Springer, 2006.
- [74] M. Jcker, A. Kessar, T. Fransson, G. Kahl, and H.-J. Rehder. *Comparison of Models to Predict Low Engine Order Excitation in a High Pressure Turbine Stage*, chapter II Forced Response, pages 145–159. Springer, 2006.
- [75] J. Aschenbruck, C. E. Meinzer, L. Pohle, L. Panning-von Scheidt, and J. R. Seume. Regeneration-induced forced response in axial turbines. *ASME Turbo Expo 2013: Turbine Technical Conference and Exposition*, 7B: Structures and Dynamics:V07BT33A010–V07BT33A022, 2013.
- [76] C. Breard, J. Green, and M. Imregun. Low-engine-order excitation mechanisms in axial-flow turbomachinery. *Journal of Propulsion and Power*, 19:704–712, 2003.
- [77] M. A. Mayorca, J. A. D. Andrade, D. M. Vogt, H. Mrtensson, and T. Fransson. Effect of scaling of blade row sectors on the prediction of aerodynamic forcing in a highly loaded transonic compressor stage. *Journal of Turbomachinery*, 133:021013–021023, 2010.
- [78] M. Vahdati, A. I. Sayma, and M. Imregun. An integrated nonlinear approach for turbomachinery forced response prediction. part ii: Case studies. *Journal of Fluids and Structures*, 14(1):103–125, 2000.
- [79] Ed Bancalari, Pedy Chan, and Ihor S. Diakunchak. Advanced hydrogen gas turbine development program. In *ASME Turbo Expo 2007: Power for Land, Sea, and Air*, pages 977–987, 2007.
- [80] O. Maurstad. An overview of coal based integrated gasification combined cycle (igcc) technology. Technical report, Massachusetts Institute of Technology, Laboratory for Energy and the Environment, 2005.

- [81] T. B. Gibbons and I. G. Wright. A review of materials for gas turbines firing syngas fuels. Technical report, U.S. Department of Energy, Fossil Energy Program, 2007.
- [82] R. Chacartegui, D. Snchez, J.M. Muoz de Escalona, B. Monje, and T. Snchez. On the effects of running existing combined cycle power plants on syngas fuel. *Fuel Processing Technology*, 103(0):97 – 109, 2012. 4th International Congress of Energy and Environment Engineering and Management.
- [83] A. S. Sabau and I. G. Wright. The effects of changing fuels on hot gas path conditions in syngas turbines. *Journal of Engineering for Gas Turbines and Power*, 131:044501–044508, 2009.
- [84] S. Colantoni, F. Fantozzi, U. Desideri, S. D. Gatta, R. D. Prosperis, and A. Russo. Gas turbines fired with biomass pyrolysis syngas: Analysis of the overheating of hot gas path components. *Journal of Engineering for Gas Turbines and Power*, 132:061401–061409, 2010.
- [85] Z. N. Wang and X. Yuan. Concurrent effects of hot streak and gas species concentration on aerothermal characteristics in a turbine stage. *ASME Turbo Expo 2012: Turbine Technical Conference and Exposition*, 8:1431–1441, 2012.
- [86] A. I. Sayma, M. Vahdati, L. Sbardella, and M. Imregun. Modelling of 3d viscous compressible turbomachinery flows using unstructured hybrid grids. *AIAA Journal*, pages 945–954, 2000.
- [87] A. Sayma, M. Vahdati, and M. Imregun. Turbine forced response prediction using an integrated non-linear analysis. *Proceedings of the Institution of Mechanical Engineers, Part K: Journal of Multi-body Dynamics*, 214(1):45–60, 2000.
- [88] A. Sayma, M Vahdati, and M. Imregun. Multi-bladerow fan forced response predictions using an integrated three-dimensional time-domain aeroelasticity model. *Journal of Mechanical Engineering Science*, 214:1467–1483, 2000.
- [89] M. M. Rai. An implicit, conservative, zonal-boundary scheme for euler equation calculations. *Computers & Fluids*, 14(3):295–319, 1986.
- [90] L. Sbardella, A. I. Sayma, and M. Imregun. Semi-structured meshes for axial turbomachinery blades. *International Journal for Numerical Methods in Fluids*, 32(5):569–584, 2000.

- [91] P. R. Spalart and S. R. Allmaras. One-equation turbulence model for aerodynamic flows. *Recherche aerospaciale*, (1):5–21, 1994.
- [92] Y.-L. Li. *Numerical Simulations of Rotating Stall in Axial Flow Compressors*. PhD thesis, Department of Engineering and Design, University of Sussex, 2013.
- [93] M. M. Rai. Three-dimensional navier-stokes simulations of turbine rotor-stator interaction; part i - methodology. *Journal of Propulsion and Power*, 5(3):305–311, 1989.
- [94] A. A. Romocea, A. M. R. Elbaz, and Sayma. A. I. Application of a cfd film cooling model to a high pressure multistage axial turbine fueled with hydrogen rich syngas. *Eleventh International Conference of Fluid Dynamics, Alexandria, Egypt*, (ICFD11-EG-4069), 2013.
- [95] T. Kampe and S. Volker. Application of a cfd-based film cooling model to a gas turbine vane cascade with cylindrical and shaped hole endwall film cooling. *ASME 2011 Turbo Expo: Turbine Technical Conference and Exposition*, 5:35–44, June 610, 2011.
- [96] J. P. Clark. Design strategies to mitigate unsteady forcing. Technical report, Air Force Research Lab., Wright-Patterson AFB, 2008.
- [97] D. Lastiwka. Influence of rotor blade scaling on the numerical simulation of a high pressure gas turbine. Master’s thesis, University of Ottawa, 2008.
- [98] M. H. Rahman, S. I. Kim, and I. Hassan. Effects of inlet temperature uniformity and nonuniformity on the tip leakage flow and rotor blade tip and casing heat transfer characteristics. *Journal of Turbomachinery*, 134:021001–021011, 2011.
- [99] J. Ong, R. J. Miller, and J. D. Denton. The prediction of hot streak migration in a high-pressure turbine. *Proceedings of the Institution of Mechanical Engineers, Part A: Journal of Power and Energy*, 224(1):119–128, 2010.
- [100] D. J. Dorney, R. L. Davis, and O. P. Sharma. Two-dimensional inlet temperature profile attenuation in a turbine stage. *ASME, International Gas Turbine and Aeroengine Congress and Exposition, 36th, Orlando, FL*, 1991.

- [101] D. L. Cizmas P. G. A. Dorney, D. J. Sondak. Effects of hot streak/airfoil ratio in a high-subsonic single-stage turbine. *International Journal of Turbo and Jet Engines*, 17:119–131, 2000.
- [102] J. D. Denton. Loss mechanisms in turbomachines. *Journal of Turbomachinery*, 115:621–655, 1993.
- [103] H. Ceric, J. Slad, and T. Johnke. Latest performance upgrade of the siemens gas turbine sgt5-4000f. Power-Gen Europe 2008, June 03 05 2008.
- [104] Siemens gas turbine sgt5-4000f. Brochure, 2008.
- [105] P. Nucara. *Design of Gas Turbine Axial Compressors for Fuel Flexibility*. PhD thesis, University of Sussex, School of Engineering and Informatics, Thermo-Fluid Mechanics Research Centre, 2013.
- [106] D. Sanchez, R. Chacartegui, M. Munoz, J., T. Munoz, and T. Sanchez. Performance analysis of a heavy duty combined cycle power plant burning various syngas fuels. *International Journal of Hydrogen Energy*, 35:337–345, 2009.
- [107] R. Chacartegui, D. Sanchez, J. M. Munoz, T. Munoz, and T. Sanchez. Gas and steam combined cycles for low calorific syngas fuels utilisation. *Applied Energy*, 101:81–92, 2013.
- [108] K. K. Lam, K. Liu, Ch. Jayatunga, and D. Helas. Siemens sgt-300 twin-shaft dle engine combustion system from design to engine validation. *ASME Turbo Expo 2013: Turbine Technical Conference and Exposition*, 1A: Combustion, Fuels and Emissions:V01AT04A027–V01AT04A037, 2013.
- [109] B. J. McBride, S. Gordon, and M. A. Reno. Coefficients for calculating thermodynamic and transport properties of individual species. Technical report, NASA Technical Memorandum 4513, 1993.
- [110] D. G. Koubogiannis, A. N. Athanasiadis, and K. C. Giannakoglou. One- and two-equation turbulence models for the prediction of complex cascade flows using unstructured grids. *Computers & Fluids*, 32(3):403–430, 2003.
- [111] M. A. Mayorca. *Numerical Methods for Turbomachinery Aeromechanical Predictions*. PhD thesis, School of Industrial Engineering and Management, Royal Institute of Technology, Stockholm, Sweden, 2011.

[112] M. Imregun. Basics of blade and disk vibration. Lectures Series Programme,  
Von Karman Institute for Fluid Dynamics, Belgium, May 3-7 1999.

# Appendix A

## Harmonic Index and Nodal Diameter

The free response mode shapes of bladed disks can be considered as a combination of disk-alone and blade-alone mode shapes. The nomenclature often used to refer to different blade mode shapes is analogue to beam like modes as shown in Figure A.1 [111]. The blade modes are flapwise, edgewise and torsional with 1F and 1T being the abbreviations of the 1<sup>st</sup> flap mode and 1<sup>st</sup> torsion mode, respectively.

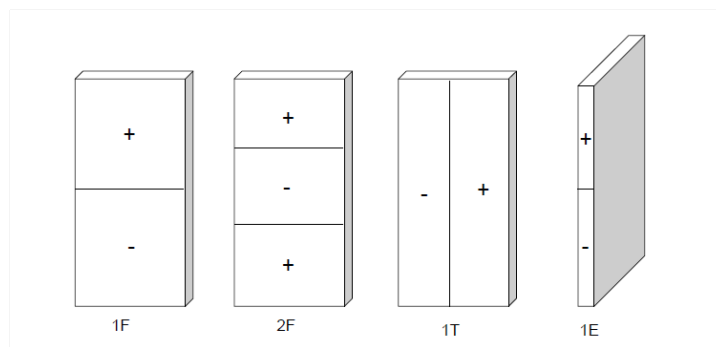


Figure A.1: Beam mode shapes

The disk mode shapes are named as Nodal Diameters (ND) due to the radial lines which cross the disk entire disk and form the zero out-of-plane displacement. The vibration can take place in axial, radial or tangential directions as shown in Figure A.2 [112].

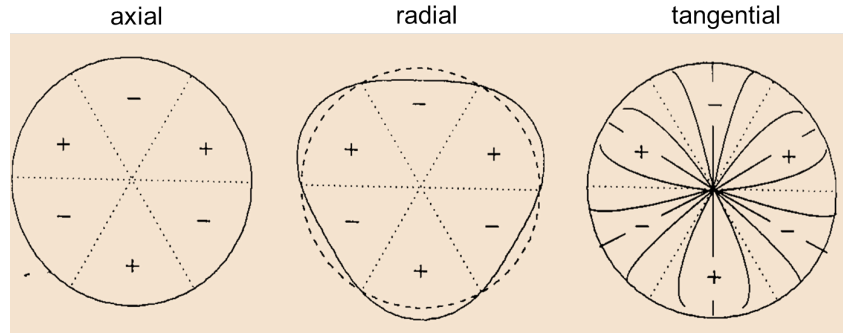


Figure A.2: Disk mode shapes

The maximum number of NDs that a bladed disk can have is related to the number of blades as described by Equations A.1-A.2:

$$ND_{max} = \frac{N}{2}, N : even \quad (A.1)$$

$$ND_{max} = \frac{N-1}{2}, N : odd \quad (A.2)$$

The deflection shapes of a turbine bladed disk are usually described by the same nomenclature that is used to refer to the disk and blade mode shapes. In the thesis the beam nomenclature was not mentioned and only the ND that was associated to the excitation pattern was used to investigate the LEO excitation problem.

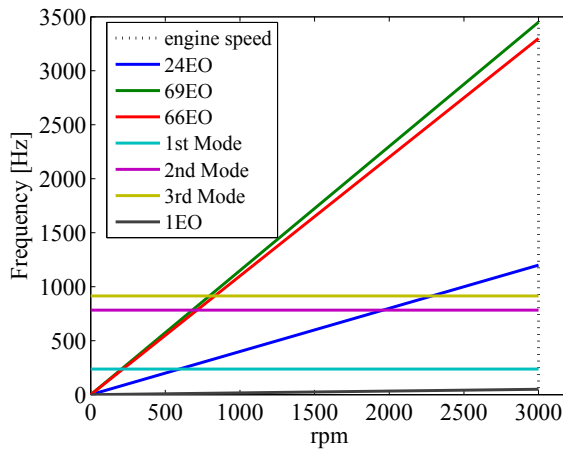
In order to solve a modal cyclic symmetry analysis in ANSYS the harmonic index needs to be specified as a representative of the ND. The relationship between the harmonic index  $k$  and ND for a model consisting of  $n$  sectors, is given by the following equation:

$$ND = m * n \pm k \quad (A.3)$$

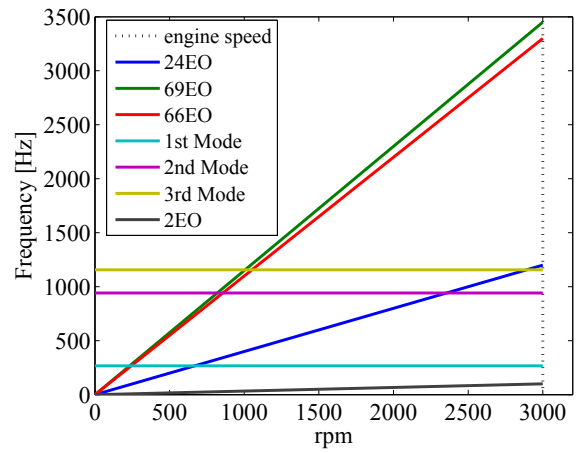
where  $m = 0, 1, 2, 3, \dots, \infty$

For the modal analysis presented in Chapter 7, the rotor model consists of 79 blades ( $n=79$ ) then for the specified harmonic index  $k = 19$  ANSYS solves for nodal diameters 19, 60, 98, 139, 177 and so on. The harmonic index range can be from 0 to  $ND/2$ , hence the modal analysis was conducted for a range of  $k = [0, 39]$  and the correspond-

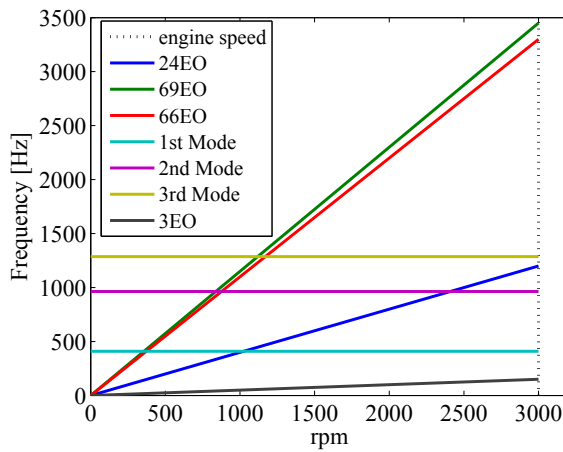
ing to the excitation source of the 24 combustor cans Campbell diagrams were drawn for each ND up to the 24<sup>th</sup> as shown in Figure A.3.



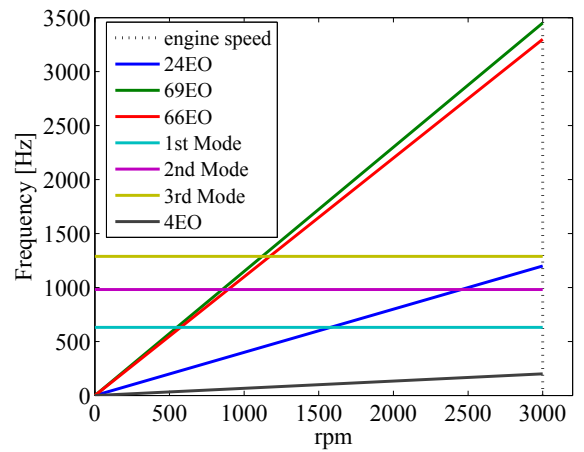
(a) Campbell diagram for 1 ND



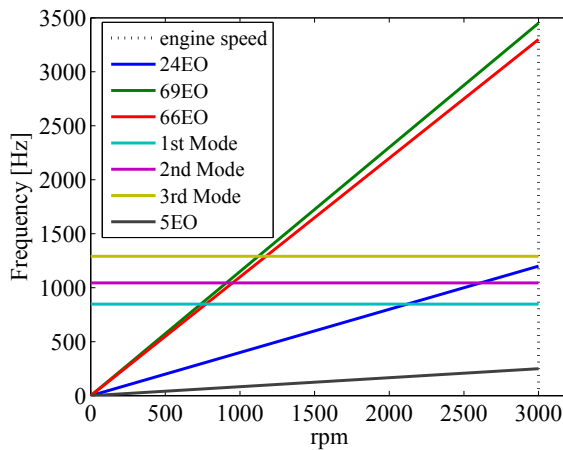
(b) Campbell diagram for 2 ND



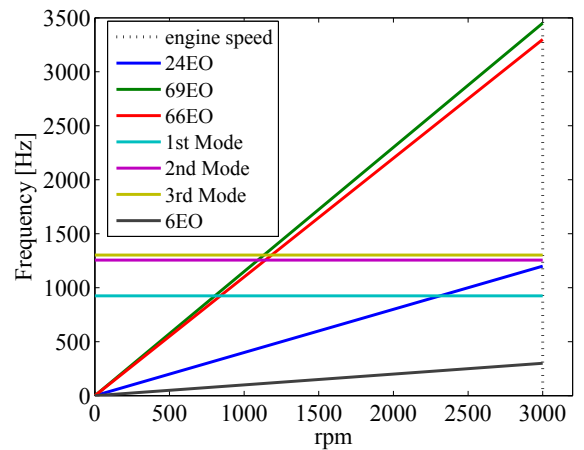
(c) Campbell diagram for 3 ND



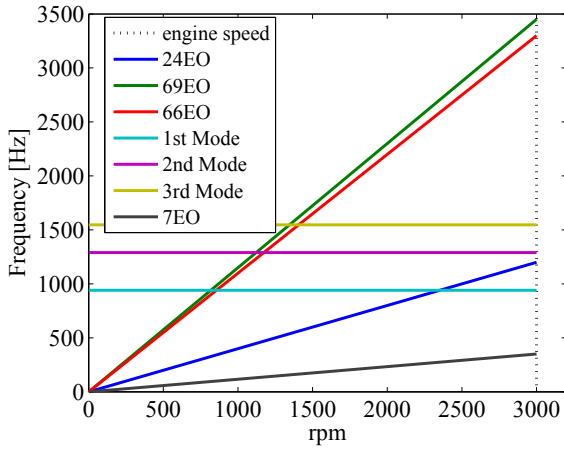
(d) Campbell diagram for 4 ND



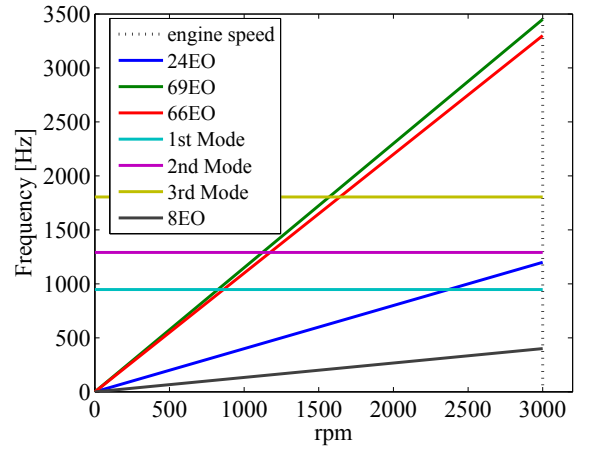
(e) Campbell diagram for 5 ND



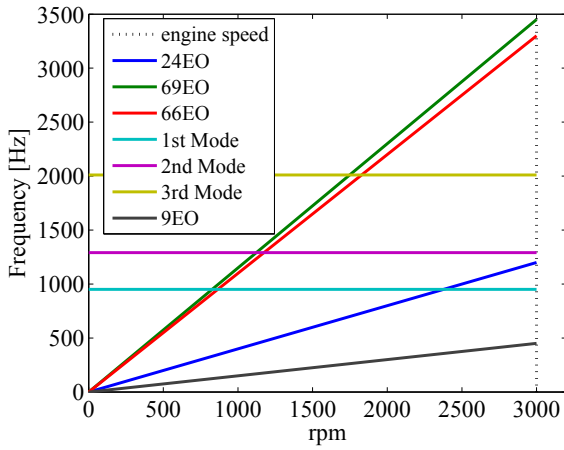
(f) Campbell diagram for 6 ND



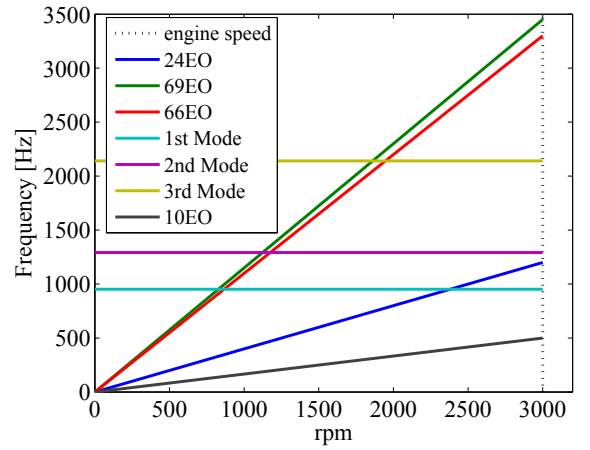
(g) Campbell diagram for 7 ND



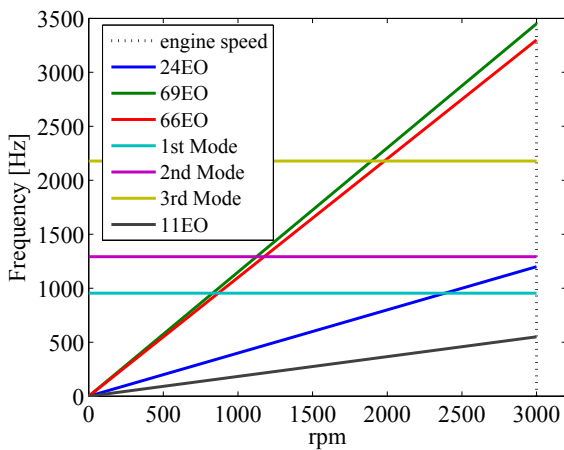
(h) Campbell diagram for 8 ND



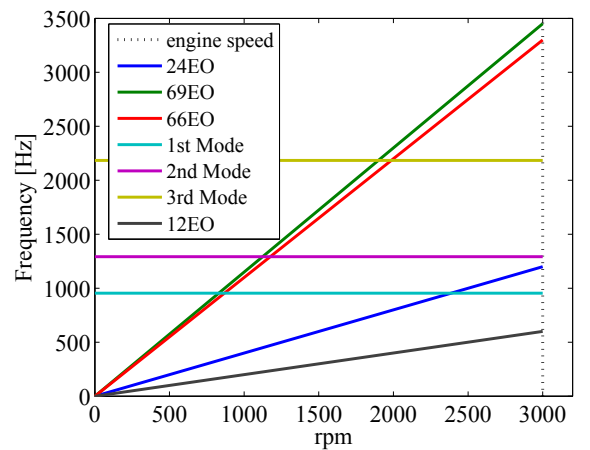
(i) Campbell diagram for 9 ND



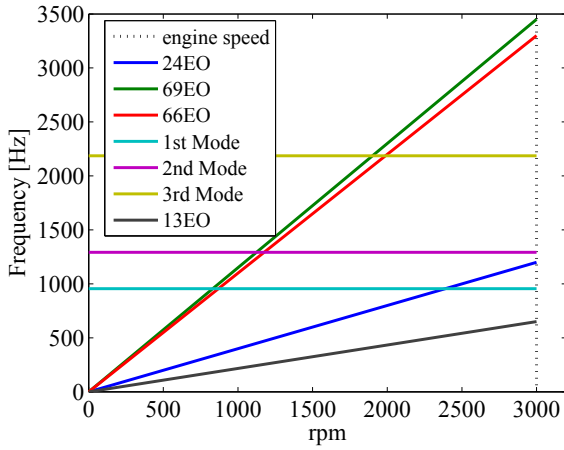
(j) Campbell diagram for 10 ND



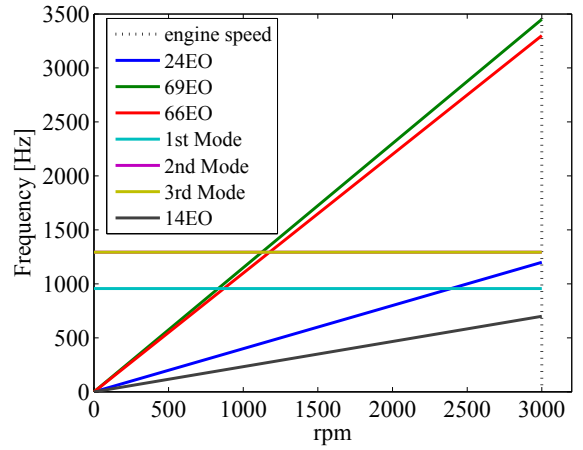
(k) Campbell diagram for 11 ND



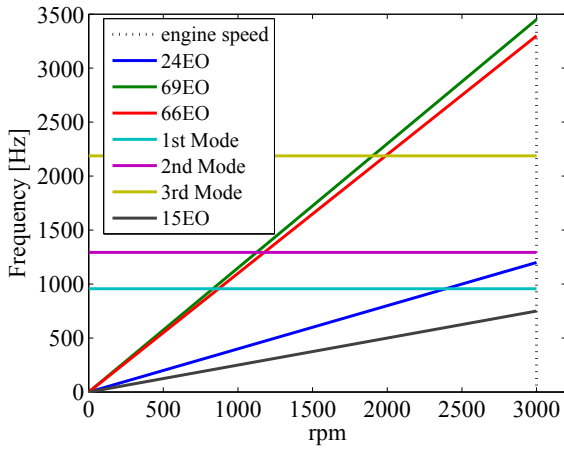
(l) Campbell diagram for 12 ND



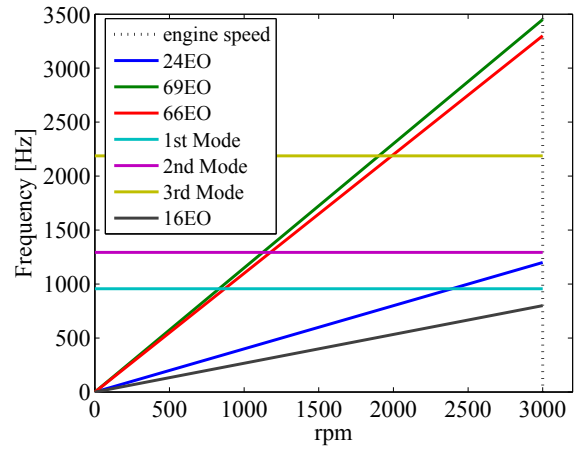
(m) Campbell diagram for 13 ND



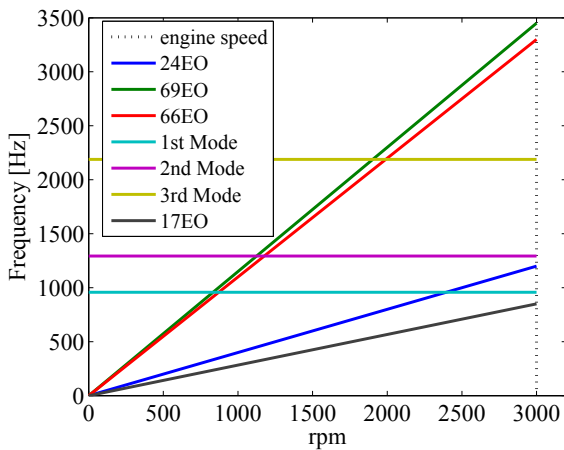
(n) Campbell diagram for 14 ND



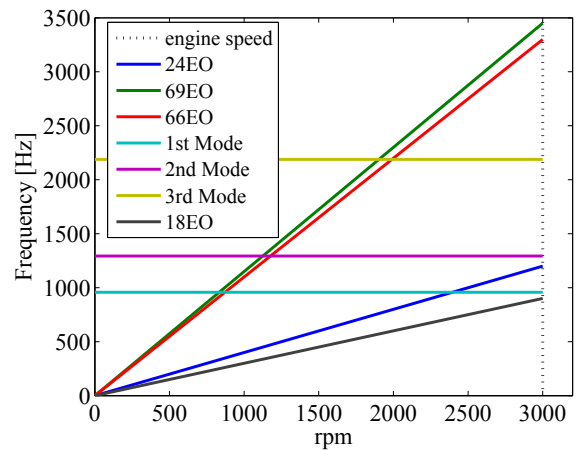
(o) Campbell diagram for 15 ND



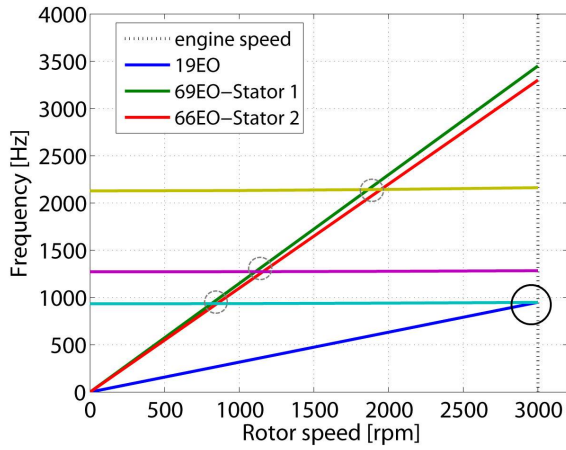
(p) Campbell diagram for 16 ND



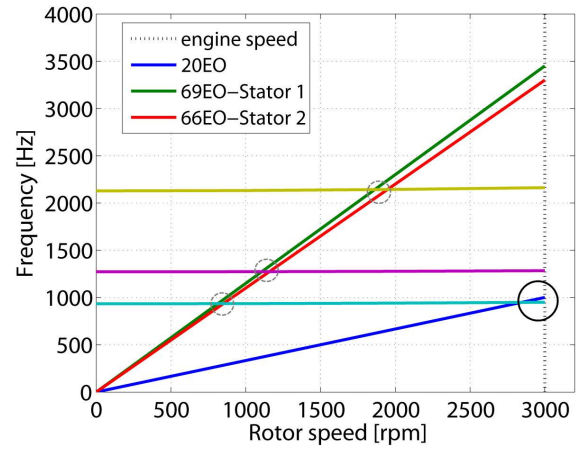
(q) Campbell diagram for 17 ND



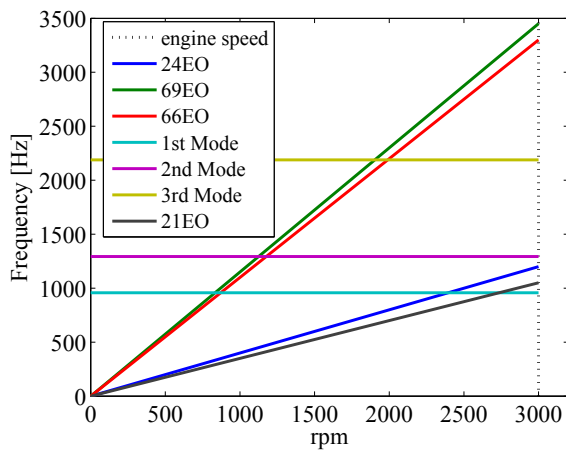
(r) Campbell diagram for 18 ND



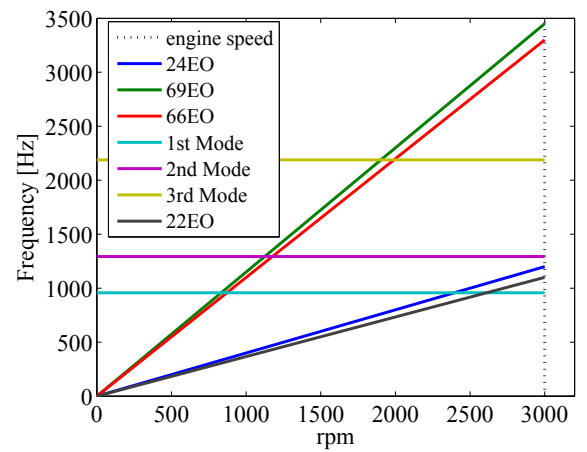
(s) Campbell diagram for 19 ND



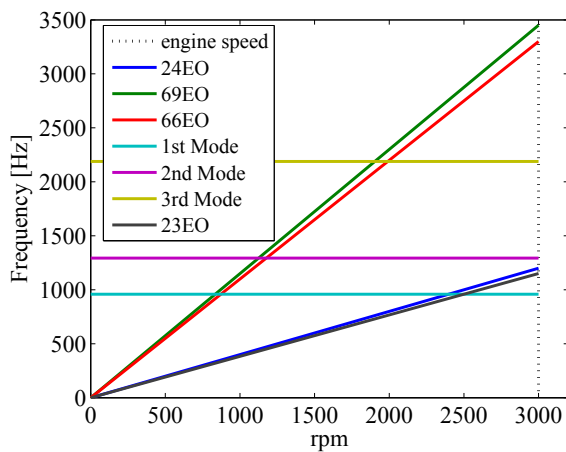
(t) Campbell diagram for 20 ND



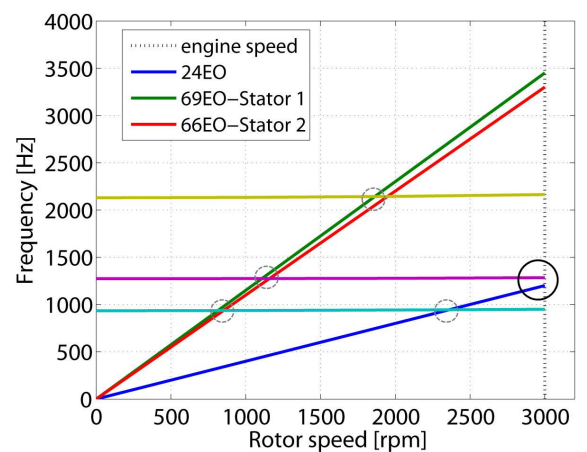
(u) Campbell diagram for 21 ND



(v) Campbell diagram for 22 ND



(w) Campbell diagram for 23 ND



(x) Campbell diagram for 24 ND

Figure A.3: Campbell diagrams for 1-24 ND